



Friedrich-Schiller-Universität Jena

Chemisch-Geowissenschaftliche Fakultät

Depth-Sensing Indentation of Soft Matter

Dissertation

zur Erlangung des akademischen Grades
doctor rerum naturalis (Dr. rer. nat.)

vorgelegt dem Rat der Chemisch-Geowissenschaftlichen Fakultät
der Friedrich-Schiller-Universität Jena

von Diplom-Chemiker Erik Franz-Josef Rettler
geboren am 20.05.1981 in Essen

Gutachter:

1. Prof. Ulrich S. Schubert, Friedrich-Schiller-Universität Jena
2. Prof. Heinz W. Siesler, Universität Duisburg-Essen

Tag der öffentlichen Verteidigung: 02.10.2013

Gefördert durch das Dutch Polymer Institute (DPI, Technology Area HTE, projects #502 & #604)

To my grandma

„Zeit meines Lebens habe ich es immer geliebt, zu lernen.“

- Margot Kötteritzsch -

Table of contents

Documentation of authorship	3
Introduction	5
Depth-sensing indentation: Examples, theory and limitations	9
Mechanical properties and water uptake behavior of polyoxazolines	15
Application of depth-sensing indentation to crosslinking studies and industrial polymers	25
Summary	33
Zusammenfassung	36
References	39
Curriculum vitae	42
Publication list	43
Acknowledgements / Danksagung	46
Declaration of authorship / Selbständigkeitserklärung	48
Publications P1-P8	49

Documentation of authorship

This section contains a list of the individual authors' contributions to the publications reprinted in this thesis.

- P1 Erik F.-J. Rettler, Stephanie Hoepfener, Bernd W. Sigusch, Ulrich S. Schubert, "Mapping the mechanical properties of biomaterials on different length scales: Depth-sensing indentation and AFM based nanoindentation", *J. Mater. Chem. B* **2013**, *1*, 2789-2806.

E. Rettler: Preparation of the manuscript
S. Hoepfener: Preparation of the manuscript
B.W. Sigusch: Correction of the manuscript
U.S. Schubert: Conceptual contribution, correction of the manuscript

- P2 Erik Rettler, Johannes M. Kranenburg, Stephanie Hoepfener, Richard Hoogenboom, Ulrich S. Schubert, "Verification of key assumptions for the analysis of depth-sensing indentation data", *Macromol. Mater. Eng.* **2013**, *298*, 88-89.

E. Rettler: Measurements, preparation of the manuscript
J. Kranenburg: Measurements, preparation of the manuscript
S. Hoepfener: AFM measurements, correction of the manuscript
R. Hoogenboom: Discussions on the manuscript
U.S. Schubert: Correction of the manuscript

- P3 Kristian Kempe, Erik F.-J. Rettler, Renzo M. Paulus, Anette Kuse, Richard Hoogenboom, Ulrich S. Schubert, "A systematic investigation of the effect of side chain branching on the glass transition temperature and mechanical properties of aliphatic (co-)poly(2-oxazoline)s", *Polymer* **2013**, *54*, 2036-2042.

K. Kempe: Synthesis of the samples, preparation of the manuscript
E. Rettler: Indentation measurements, preparation of the manuscript
R. Paulus: DSC measurements
A. Kuse: Synthesis of the samples
R. Hoogenboom: Correction of the manuscript
U.S. Schubert: Correction of the manuscript

- P4 Erik F.-J. Rettler, Miriam V. Unger, Richard Hoogenboom, Heinz W. Siesler, Ulrich S. Schubert, "Water uptake of poly(2-N-alkyl-2-oxazoline)s: Temperature-dependent FTIR spectroscopy and two-dimensional correlation analysis", *Appl. Spectrosc.* **2012**, *10*, 1145-1155.

E. Rettler: Measurements and data analysis, preparation of the manuscript
M. Unger: Data analysis, preparation of the manuscript
R. Hoogenboom: Synthesis of the samples, correction of the manuscript
H. Siesler: Discussions on analysis, correction of the manuscript
U.S. Schubert: Correction of the manuscript

- P5 Erik Rettler, Tobias Rudolph, Andreas Hanisch, Stephanie Hoepfener, Markus Retsch, Ulrich S. Schubert, Felix H. Schacher: "UV-induced crosslinking of the polybutadiene domains in lamellar polystyrene-block-polybutadiene block copolymer films – An in-depth study", *Polymer* **2012**, *53*, 5641–5648.
- E. Rettler: Measurements and data analysis, preparation of the manuscript
T. Rudolph: Preparation of the manuscript
A. Hanisch: Synthesis of the samples
S. Hoepfener: AFM measurements, correction of the manuscript
M. Retsch: Discussions, correction of the manuscript
U.S. Schubert: Correction of the manuscript
F.H. Schacher: SAXS measurements, correction of the manuscript
- P6 Erik F.-J. Rettler, Hanneke M. L. Lambermont-Thijs, Johannes M. Kranenburg, Richard Hoogenboom, Miriam V. Unger, Heinz W. Siesler, Ulrich S. Schubert, "Water uptake of poly(2-*N*-alkyl-2-oxazoline)s: Influence of crystallinity and hydrogen-bonding on the mechanical properties", *J. Mater. Chem.* **2011**, *21*, 17331–17337.
- E. Rettler: Measurements, preparation of the manuscript
H. Lambermont-Thijs: Water-uptake measurements
J. Kranenburg: Correction of the manuscript
R. Hoogenboom: Synthesis of the samples, correction of the manuscript
M. Unger: Discussions, correction of the manuscript
H. Siesler: Correction of the manuscript
U.S. Schubert: Correction of the manuscript
- P7 Laszlo I. Majoros, Bernard Dekeyser, Nancy Haucourt, Pieter Castelein, Johan Paul, Johannes M. Kranenburg, Erik F.-J. Rettler, Richard Hoogenboom, Ulrich S. Schubert, "Preparation of polyurethane elastomers (PUEs) in a high-throughput workflow", *J. Polym. Sci., Part A: Polym. Chem.* **2011**, *49*, 301–313.
- L. Majoros: Synthesis of the samples, preparation of the manuscript
B. Dekeyser: Preparation of the manuscript
N. Haucourt: Synthesis of the samples
P. Castelein: Synthesis of the samples
J. Paul: Synthesis of the samples
J. Kranenburg: Characterization and data analysis
E. Rettler: Characterization and data analysis
R. Hoogenboom: Correction of the manuscript
U.S. Schubert: Conceptual contribution
- P8 Erik F.-J. Rettler, Johannes M. Kranenburg, Hanneke M. L. Lambermont-Thijs, Richard Hoogenboom, Ulrich S. Schubert, "Thermal, mechanical, and surface properties of poly(2-*N*-alkyl-2-oxazoline)s", *Macromol. Chem. Phys.* **2010**, *211*, 2443–2448.
- E. Rettler: Measurements and data analysis, preparation of the manuscript
J. Kranenburg: Correction of the manuscript
H. Lambermont-Thijs: Surface energy measurements
R. Hoogenboom: Synthesis of the samples, correction of the manuscript
U.S. Schubert: Correction of the manuscript

Chapter 1

Introduction

The efficient testing of the mechanical properties of materials has a long tradition in science and materials research. Conventional testing is mostly based on standardized tensile tests, rheology or indentation techniques.^[1-4] These methods are usually destructive techniques and/or require large amounts of material or significant efforts in sample preparation, which limit their routine applicability, in particular for a fast screening or high-throughput experimentation approach. The mechanical properties of materials depend on a large variety of parameters which have a tremendous influence on the material's characteristics. This holds, in particular, for polymer materials, which can be tuned to cover a broad range of mechanical materials properties,^[5-9] e.g., by the introduction of side chain functionalization, fine-tuning of the degree of crystallinity or by varying the composition of copolymers^[10] and blend systems.^[11, 12] The investigation of structure-property relationships to predict the resulting materials properties has therefore gained strong interest,^[13] in particular, as significant improvements in the synthesis of polymer materials have been made due to the introduction of controlled and living polymerization techniques.^[14] These permit the synthesis of well-defined polymers and copolymers with low polydispersity index (PDI) values. Thus, it is nowadays possible to correlate the molecular properties and the influences of the polymer architecture independently of uncertainties which arise from the variation of the molar masses within the sample system. However, frequently the synthesis of such polymer systems is in the first instance performed in lab-scale quantities, i.e., the available material for mechanical testing is small (typically 100 to 500 mg). While traditionally employed characterization techniques require rather large amounts of sample material, e.g., dog-bone shaped samples for tensile testing, alternative characterization tools are highly desired which require only small quantities of material.

Depth-sensing indentation (DSI) was introduced in the 1970s^[15] and was developed as a measurement technique for small volumes of material, but it was not until the ground-breaking publication by Oliver and Pharr that it became commonly used.^[16] The authors developed an analysis method that allows, under certain assumptions, the simultaneous measurement of the elastic modulus and hardness of small samples with the same device setup. The elastic modulus is regarded as a true material property which enables the direct comparison of the tested materials independent of the measurement parameters. Thus, the contribution by Oliver and Pharr is regarded as a milestone for the development of indentation analysis which opened the field of indentation to the wide range of materials testing applications, mainly because of the low requirements towards the test specimens. In this respect depth-sensing indentation (DSI) is a non-destructive, high-throughput capable testing method, that requires only very small quantities of material (for soluble materials, usually a few tens of milligrams are sufficient). However, it is still not a routinely employed method as no standardized testing conditions exist. Furthermore, it was originally designed for hard materials, like metals or ceramics, and the developed models for the material's behavior are frequently not directly applicable for polymers and other soft (bio-)materials.^[17]

The goal of this thesis is to determine the critical parameters for the investigation of soft polymer samples by DSI and complementary techniques, the correlation of molecular architectures and intermolecular interactions to develop structure-property relationships as well as to evaluate the applicability of DSI for the monitoring of kinetic processes and the high-throughput characterization of polymer libraries. These investigations include first an introduction to the investigation of soft (bio-)materials with an in-depth discussion of the uncertainties which arise for soft sample systems. In the course of this discussion the verification of key parameters of the commonly utilized analysis model by Oliver and Pharr for the investigation of soft polymers is introduced (Chapter 2). This study defines a set of measurement conditions which can be applied for the investigation of soft sample systems, in

particular, of poly(2-oxazoline)s. This polymer class has recently received significant attention for biomedical applications^[18-20] due to their structural similarities with polypeptides, their high biocompatibility and thermo-responsiveness which make them ideal compounds for potential drug delivery and biotechnological applications,^[7, 21] where the mechanical properties are of importance, e.g., to stimulate cell division in cell culturing, etc..^[22-24] A library of poly(2-oxazoline)s, which are facilitated with different side chains was chosen and was utilized to study the influence of the molecular architecture of the polymers on the mechanical properties. The introduction of side chains manipulates the mechanical properties and fundamental structure-property relationships could be elucidated by combining depth-sensing indentation, DSC, FT-IR and TGA measurements (Chapter 3). Finally, the implementation of DSI for the investigation of the time-dependent crosslinking of polystyrene/polybutadiene (PS/PB) and the high-throughput analysis of the mechanical properties of semi-industrially synthesized polyurethane elastomers (PUE) was performed (Chapter 4).

As such, the presented studies evaluate the applicability of DSI as a valuable, easily accessible and fast analysis tool in polymer science. The individual contributions are summarized in Figure 1-1 and highlight the significance of the individual studies in the context of this thesis; ranging from the determination of fundamental parameters up to the integration of DSI in a high-throughput experimentation approach of industrially relevant polymer formulations.

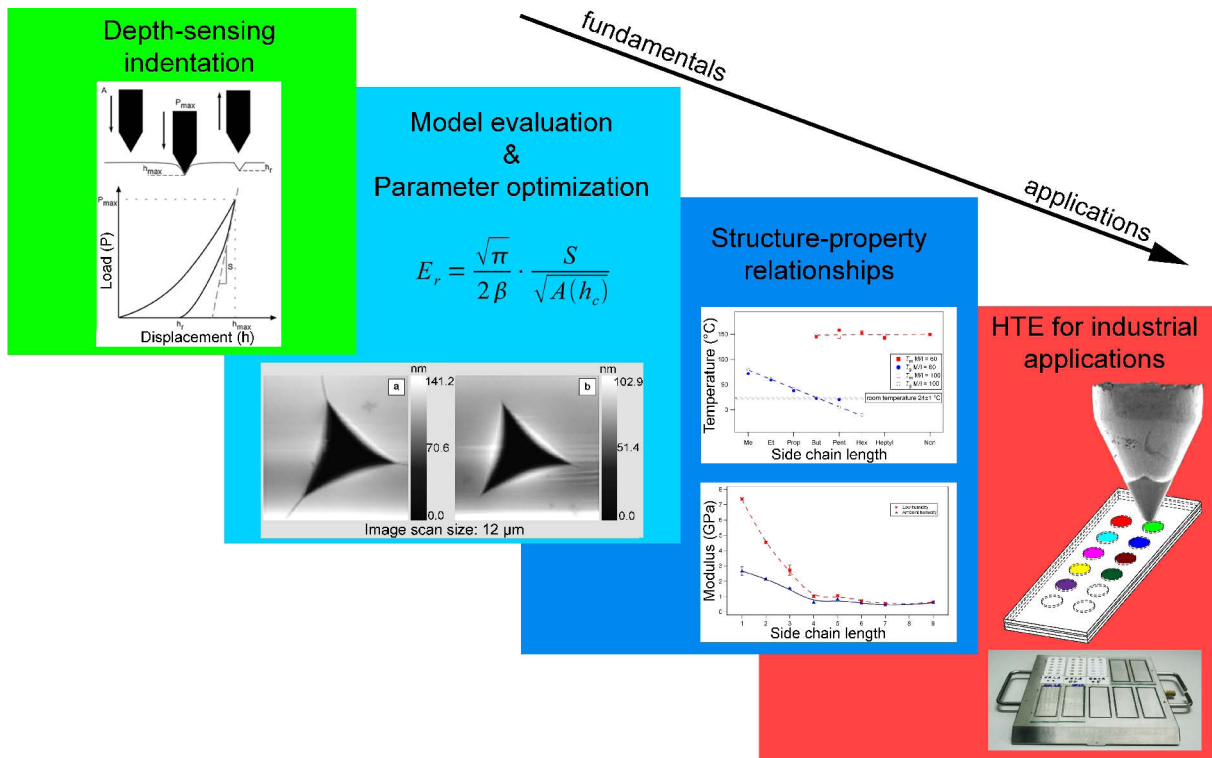


Figure 1-1: Applications of depth-sensing indentation as discussed within this thesis.

Chapter 2

Depth-sensing indentation: Examples, theory and limitations

Parts of this chapter have been or will be published: P1) E. F.-J. Rettler, S. Hoepfener, B. W. Sigusch, U. S. Schubert, "Mapping the mechanical properties of biomaterials on different length scales: Depth sensing indentation and AFM based nanoindentation", *J. Mater. Chem. B* **2013**, *1*, 2789-2806. P2) E. Rettler, J. M. Kranenburg, S. Hoepfener, R. Hoogenboom, U. S. Schubert, "Verification of key assumptions for the analysis of depth-sensing indentation data", *Macromol. Mater. Eng.* **2013**, *298*, 88-89.

Originally, depth-sensing indentation techniques have been developed for the investigation of the mechanical properties of hard materials like metals or ceramics, which behave either fully plastic or elastic.^[25, 26] While data analysis for hard samples is well understood and reliable models have been developed, the situation becomes more complex if soft samples, i.e., polymers and biological materials, are measured. As a main criterion for the applicability of DSI on soft materials the development of consistent analysis models is required that take into account the specific characteristics of this class of samples. In practice, the classical models for the materials behavior start to fail if, e.g., the investigated materials become too soft for indentation measurements or show unexpected behavior during the experiment, i.e., viscoelastic creep or adhesion or the material becomes inhomogeneous, which is frequently observed for biological samples as well as for polymers.^[27] Such materials cover a wide range of mechanical properties from brittle to viscous and, therefore, show a different behavior under the application of load compared to metals or ceramics. There are examples where depth-sensing indentation is utilized to directly investigate the viscoelastic and viscoplastic behavior, e.g., to study the response of biomaterials. In such experiments long loading times have been applied to investigate the creep behavior to determine the properties of, e.g., human enamel.^[28] As a result the indentation creep rate sensitivity could be determined and it can be demonstrated that a similar viscoelastic and viscoplastic behavior of enamel as well as of bone are observed.^[29] The analysis

of the indentation creep at maximum load and the creep recovery at the minimum load are in this case measured and fitted to a double-exponential function which can be compared to classic viscoelastic models. These results can explain the excellent wear and crack resistance of natural tooth structures.

However, when testing polymer materials, these effects may invalidate the measurements of the mechanical properties, e.g., of the hardness and Young's modulus. For softer materials the tip/sample adhesion can also result in an additional load, pulling the indenter probe onto the material, as described for various conditions by the Derjaguin-Muller-Topov model or the Johnson-Kendall-Roberts model.^[30, 31] Moreover, the adhesion may result in friction, which may also influence the load-displacement response obtained by indentation.^[3, 32] Ito *et al.*^[33] also showed the dependence of the mechanical properties of dental resins on the hydrophilicity of the respective materials. Thus, different models and analysis techniques are required to be applied for the characterization of such materials.^[34]

In standard polymer analysis, the classical Oliver and Pharr model is conventionally applied, which is based on three key assumptions:

1. the unloading is predominantly elastic (which implies that the time-dependent displacement of the tip into the sample material due to creep is small),
2. the tip/sample adhesion and friction are so small that they do not influence the load-displacement response,
3. no cracks are formed around the indent or at the indent corners.

The verification of these key assumptions represents an important step to ensure reliable data analysis as well as to define suitable measurement parameters for polymeric samples. Validation tests were performed on poly(2-oxazoline)s to determine the limitations of the Oliver and Pharr model and to optimize the investigation conditions for this special class of polymers.

The first and the second assumption listed above have been investigated using copolymers of 2-ethyl-2-oxazoline (Et) and 2-(3-ethylheptyl)-2-oxazoline (EHe). It was shown that amorphous, non-crosslinked polymers of relatively low molar mass close to their glass transition may give rise to unreliable results when the unloading responses are analyzed using the protocol proposed by Oliver and Pharr. Due to substantial time-dependent deformation, the assumption that the unloading is predominantly elastic can be violated. Increasing the unloading rate improved the reliability of the analysis results. It could be demonstrated that an unloading displacement rate exceeding the creep rate by a factor of five is suitable to minimize the influence of creep on the obtained reliable E_i values. Moreover, the pull-off force, where the indenter probe breaks loose from the sample surface, indicates that the extent of adhesion is no longer negligible for materials close to their glass transition. Therefore, apart from the creep, also the increased adhesion and tip-sample friction reduces the accuracy of the analysis results for such copolymers tested very close to, or above, their T_g . The second assumption is usually met for glassy polymers, like polycarbonate (PC) or polymethylmethacrylate (PMMA), as evidenced by the good agreement between modeling and experimental results ignoring adhesion and friction.^[35]

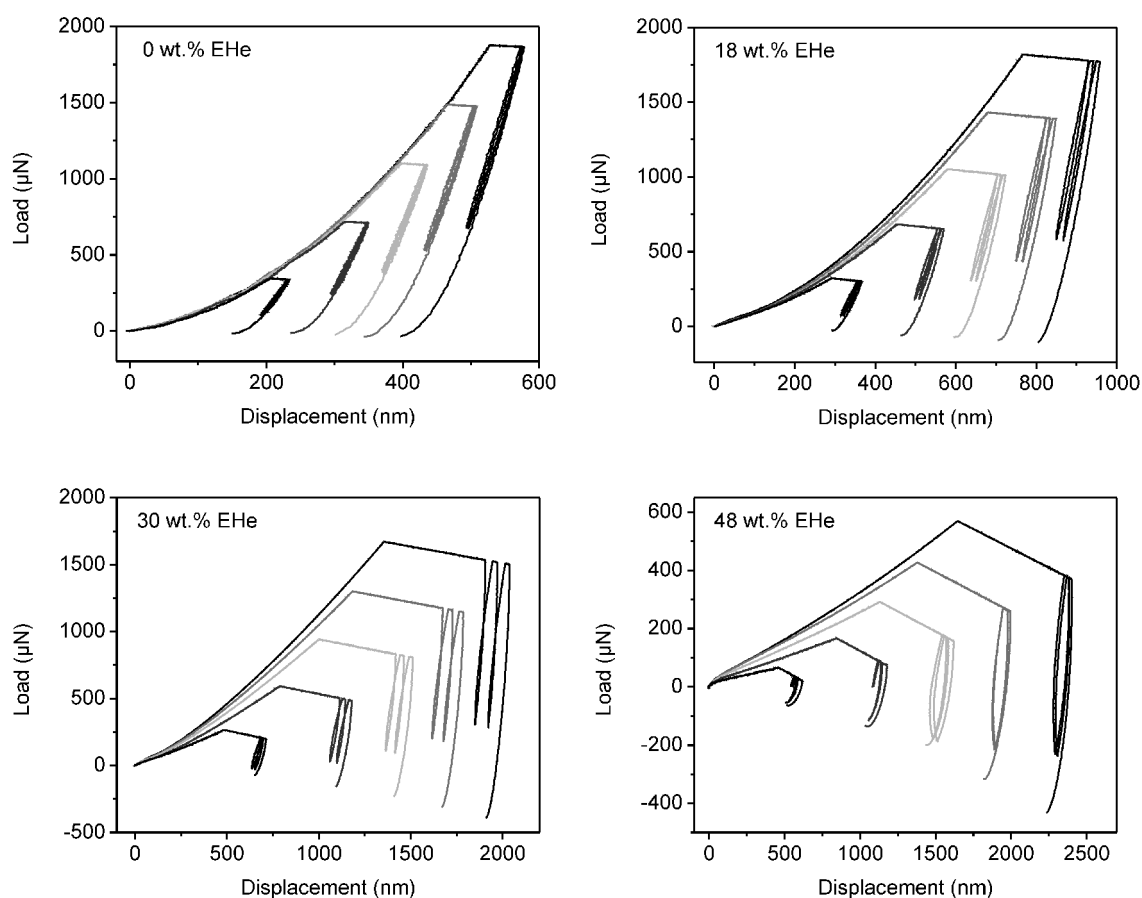


Figure 2-1: Representative indentation curves of experiments with a loading/unloading/reloading pattern on copolymers with different 2-(3-ethylheptyl)-2-oxazoline (EHe) content. Material creep is visualized by the continuing penetration of the tip into the material during the hold period and adhesion by the negative force on the tip at the end of the unloading segment.

Compliance with the third assumption can be ensured by imaging some of the indents on materials that may behave brittle. For indentation depths well in the micrometer range, optical imaging can be applied,^[36] while for shallower indents, topographic imaging is most suitable. As polystyrene (PS) is well-known for its (macroscopic) brittleness, compliance with the last assumption was investigated using polystyrene. The PS sample was subjected to several heating/cooling cycles to increase its brittleness for this study.

Cracks could be visualized by imaging with a Berkovich tip even though the cracks resulted in only modest changes in the load-displacement response.

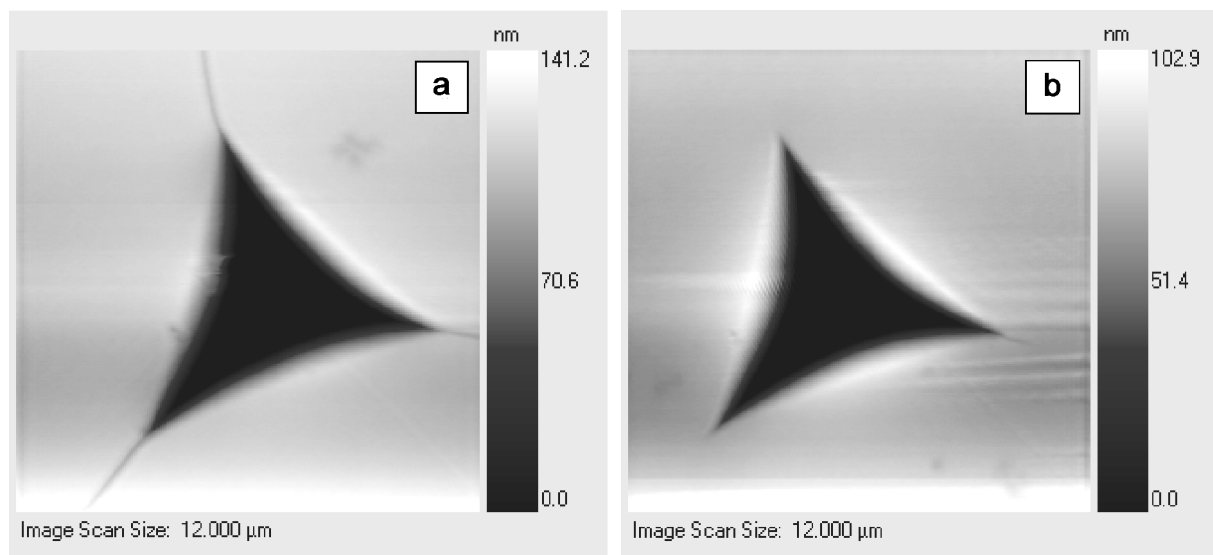


Figure 2-2: *In-situ* imaging with the (Berkovich) indenter tip after making indents in polystyrene at high force. a) Severe cracking occurred at the corners of the indent. b) Only minor cracks are found.

It shall be noted that no cracking was observed in any other of the investigated systems within this thesis.

These fundamental studies of the key assumption verification represent important tests of the polymer systems, which have been studied in the following investigations, and essentially define the parameters which can be applied during the depth-sensing indentation measurements. For all subsequent studies data analysis could be performed utilizing the Oliver and Pharr method taking into account the parameters determined in the validation study.

Chapter 3

Mechanical properties and water uptake behavior of polyoxazolines

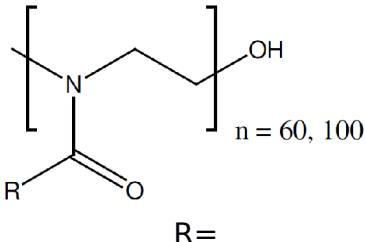
Parts of this chapter have been or will be published: P3) K. Kempe, E. F.-J. Rettler, R. M. Paulus, A. Kuse, R. Hoogenboom, U. S. Schubert, "A systematic investigation of the effect of side chain branching on the glass transition temperature and mechanical properties of aliphatic (co-)poly(2-oxazoline)s", *Polymer* **2013**, *54*, 2036-2042. P4) E. F.-J. Rettler, M. V. Unger, R. Hoogenboom, H. W. Siesler, U. S. Schubert, "Water uptake of poly(2-*N*-alkyl-2-oxazoline)s: Temperature-dependent FTIR spectroscopy and two-dimensional correlation analysis", *Appl. Spectrosc.* **2012**, *10*, 1145-1155. P6) E. F.-J. Rettler, H. M. L. Lambermont-Thijs, J. M. Kranenburg, R. Hoogenboom, M. V. Unger, H. W. Siesler, U. S. Schubert, "Water uptake of poly(2-*N*-alkyl-2-oxazoline)s: Influence of crystallinity and hydrogen-bonding on the mechanical properties", *J. Mater. Chem.* **2011**, *21*, 17331-17337. P8) E. F.-J. Rettler, J. M. Kranenburg, H. M. L. Lambermont-Thijs, R. Hoogenboom, U. S. Schubert, "Thermal, mechanical, and surface properties of poly(2-*N*-alkyl-2-oxazoline)s", *Macromol. Chem. Phys.* **2010**, *211*, 2443-2448.

Poly(2-oxazoline)s have been chosen as a suitable system to investigate structure-property relationships in systematically varied polymer libraries because their synthesis via a living cationic polymerization method allows a good control over the main chain length and the introduction of side groups.^[13] Earlier work on 2-oxazoline copolymers showed that the mechanical properties strongly depend in particular on the side chains;^[37] e.g., the type of side chain governs the glass transition temperature of the polymer,^[P8] as well as the presence of crystallinity, and, therefore, the modulus of elasticity of the resulting material.^[38-42] Furthermore, the mechanical properties also depend on the humidity of the surrounding atmosphere.^[P6, 43] For some poly(2-oxazoline)s, small amounts of water still present in the samples at low humidity induce hydrogen bonding and/or polar interactions between the polymer chains, resulting in relatively high elastic moduli.

To investigate these influences in more detail the thermal, mechanical and water-uptake behavior was investigated for a library of poly(2-oxazoline)s, where the linear side chains have been systematically varied. Two different series prepared with monomer over initiator (M/I) ratios of 60 and 100 were investigated.

This investigation has been extended on copolymers with different ratios of poly(2-ethylloxazoline) (EtOx) content to obtain information on the effect of branching in the side chain functionalization. Investigations were performed in a high-throughput fashion and only small amounts of sample material of ~50 mg were utilized to complete the studies.

Table 3-1: Schematic representation of the chemical structures of the investigated poly(2-oxazoline) homopolymers and their abbreviations used in the text.

	Abbreviation
-CH ₃	MeOx
-C ₂ H ₅	EtOx
-C ₃ H ₇	PropOx
-C ₄ H ₉	ButOx
-C ₅ H ₁₁	PentOx
-C ₆ H ₁₃	HexOx
-C ₇ H ₁₅	HeptylOx
-C ₉ H ₁₉	NonOx
-CH(CH ₃) ₂	<i>i</i> -PrOx
-CH ₂ -CH(CH ₃) ₂	<i>i</i> -ButOx

As summarized in Figure 3-1, glass transition temperatures are observed for the MeOx up to the PentOx linear side chain functionalized samples. For ButOx up to the NonOx, endothermal peaks around 150 °C were found. Since these peaks only occur within the polymers with longer side chains, they are attributed to side chain crystallization. While the glass transition temperatures constantly decrease with increasing length of the side chain (MeOx through

PentOx), the melting temperatures of the semicrystalline polymers (ButOx to NonOx) stay constant at around 150 ± 10 °C, indicating that T_m is independent of the side chain length. Up to the PropOx sample no melting peaks were observed, reflecting the fact that a minimum length of the side chain is required to induce crystallization. From these results, it was concluded that MeOx, EtOx, and PropOx side chain functionalized samples are completely amorphous, while the rest of the library is semi-crystalline.

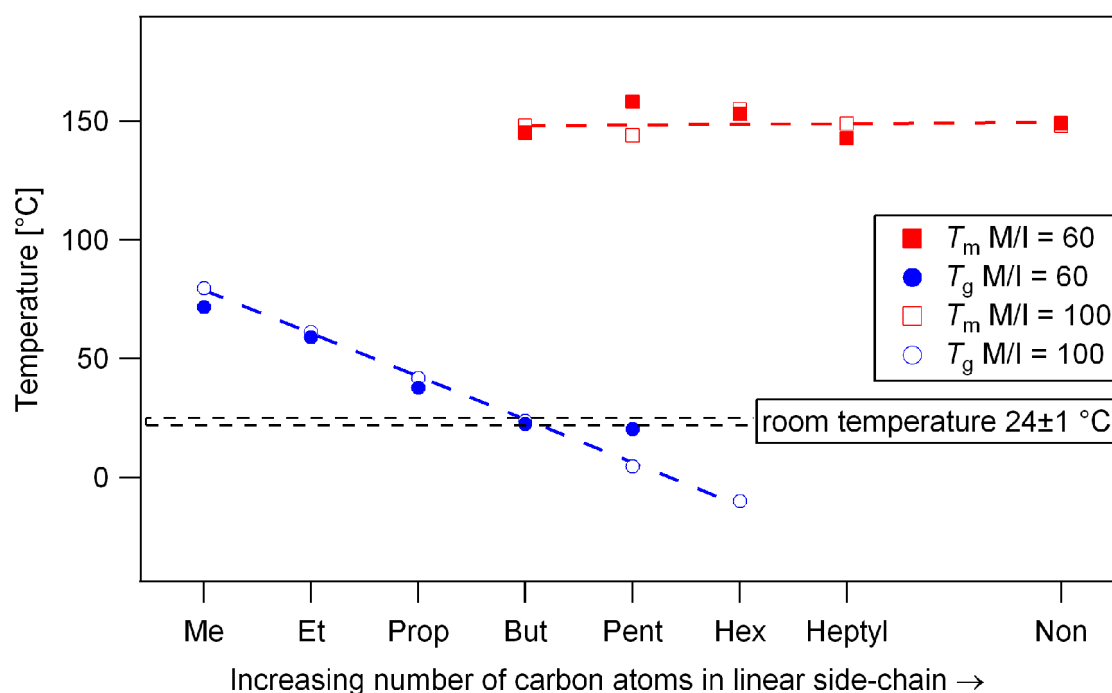


Figure 3-1: Thermal properties of the investigated poly(2-oxazoline)s with linear side chains prepared with M/I ratios of 60 and 100 respectively.

Water-uptake causes a swelling of the polymers, thus increasing the interchain volume which results in a higher flexibility of the polymer chains. As a result the elastic modulus of the hygroscopic materials is significantly decreased. Under ambient conditions, the indentation moduli drop by almost 50% for the hygroscopic materials compared to the dried state, while for the semi-crystalline materials, the decrease is very small up to negligible. As can be seen in Figure 3-2, the indentation moduli linearly decrease with increasing

length of the side chain until the T_g is below room temperature. After that the values stay more or less constant. This trend holds true for both testing conditions at low and ambient humidity. As the measurements have been performed at room temperature, MeOx up to PropOx are still in the glassy state, while the T_g of the rest of the library is at (for ButOx) or below room temperature.

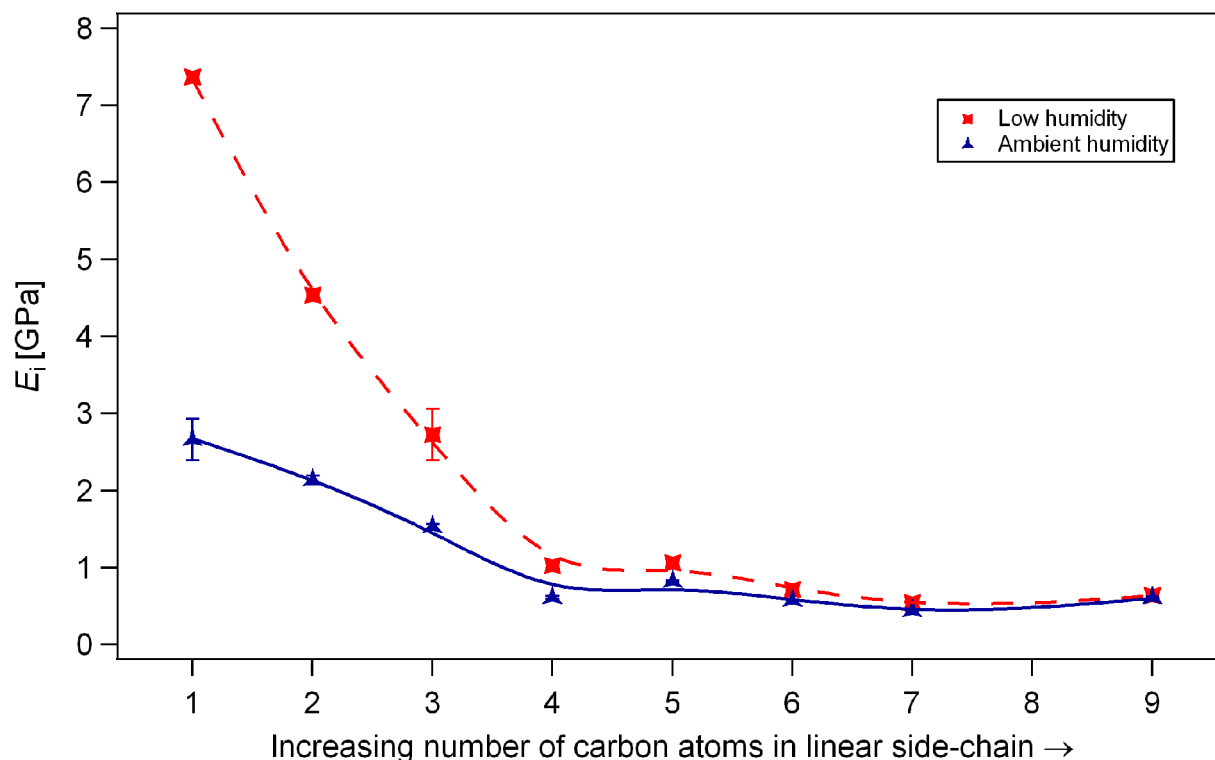


Figure 3-2: Indentation moduli of the investigated poly(2-oxazoline)s with linear side chains at ambient (~40% r.h.) and dry conditions (~5% r.h.).

For comparison of the hygroscopicity of the different polyoxazolines, thermogravimetric analysis (TGA) has been performed on water-saturated samples from the M/I=60 series. For MeOx, EtOx, and *i*-PrOx, smaller mass losses were observed due to the evaporation of water. This confirms earlier water-uptake measurements^[P6] that also showed these samples to be hygroscopic.

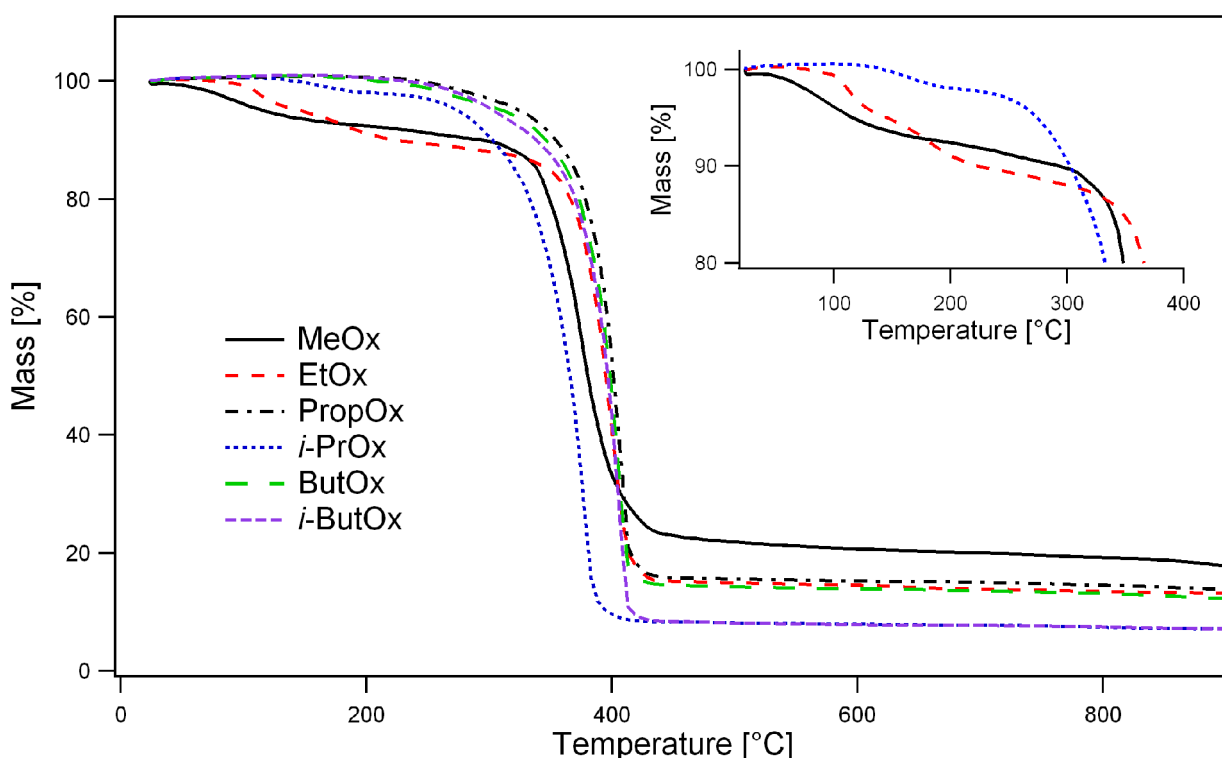


Figure 3-3: TGA analysis of the water-saturated polyoxazolines prepared with a M/I ratio of 60. The inset shows an enlarged view of the most hygroscopic samples.

Temperature-dependent IR-measurements have proven to be a more precise indicator for crystallinity as well as hygroscopicity than DSC or TGA measurements and were utilized to reveal the underlying molecular processes. The full width at half-maximum (FWHM) values of the C=O peak are highly sensitive towards changes in the material upon variation of the temperature, thus, crystalline behavior could even be detected for the PropOx sample, where neither DSC showed a melting peak, nor a water loss could be detected by TGA. However, the standard analysis of the spectra did not reveal water-uptake in the PropOx. By using advanced analysis techniques (2-dimensional correlation analysis (2DCOS) and perturbation-correlation moving-window 2-dimensional (PCMW2D) correlation) also the weak interaction of water with the C=O functionality of the polymer could be detected. This is shown by the

correlation of the water and polymer peaks in the synchronous as well as the asynchronous spectrum (Figure 3-4 A and B). The water loss can also be followed in the PCMW2D spectrum by the negative peak around $\sim 1625 \text{ cm}^{-1}$ which disappears with increasing temperature and the corresponding strengthening of the C=O peak at $\sim 1660 \text{ cm}^{-1}$.^[P4]

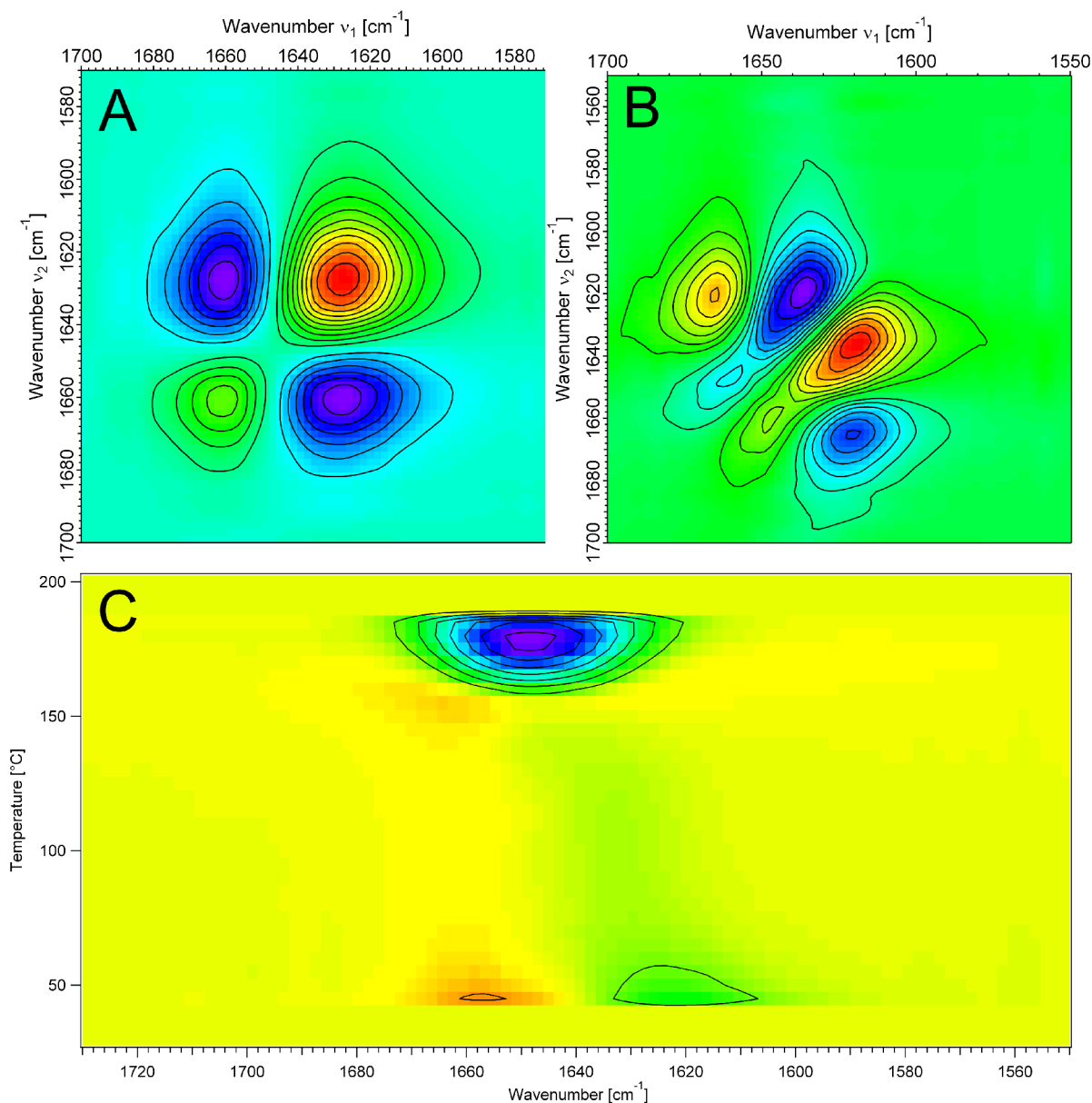


Figure 3-4: A) Synchronous and B) asynchronous correlation spectra of the PropOx $\nu(\text{C}=\text{O})$ region calculated from the FT-IR spectra in the temperature range 30 to 170 $^{\circ}\text{C}$. C) Synchronous PCMW2D correlation spectrum in the temperature range 30 to 200 $^{\circ}\text{C}$. Red color indicates positive, blue color indicates negative peak intensities.

At ambient conditions, the water-saturated samples exhibit lower moduli in depth-sensing indentation than under dry conditions due to a plasticising effect of the incorporated water.^[44] The water molecules are hydrogen-bonded to the polymer as shown by FTIR-spectroscopy, thus increasing the interchain volume. Furthermore, crystalline behavior of the carbonyl-band was observed for poly(2-oxazoline)s with a linear side chain of at least three carbon atoms in length. Both effects can be studied by the observation of the C=O stretching vibration which is the dominant feature of the spectrum and represents the “junction point” between the side chains and the polymer backbone. Therefore, it can be concluded that the crystalline behavior found for the C=O vibration results from side chain crystallization for ButOx and longer side chains (which correlates with the melting peaks found in the DSC), whereas for shorter side chains, the crystalline behavior is dominated by an alignment of the polymer backbones.

Next to poly(2-oxazoline)s which are functionalized with linear side chains also branched side chains can be introduced into the polymers.^[45-46] As industrially produced polymers usually exhibit branching, this effect is of significant importance for practical applications. As shown above, the homo poly(2-oxazoline)s with longer side chains (allowing branching) all exhibit glass transition temperatures below room temperature, aggravating the mechanical characterization and comparison of samples with each other. Therefore, copolymers of different branched poly(2-oxazoline)s with decremental amounts of EtOx have been investigated. Figure 3-5 shows the schematic representation of these copolymer systems and the resulting moduli. These copolymers can be seen as hard/soft composite materials, where the EtOx always represents the “hard” component. The thermal properties of the homopolymers as well as of the copolymer series were determined by DSC and were compared to the known PEHOx and P(EHOx-*r*-EtOx) system. PEPOx and P3EPOx exhibit the same number of carbon atoms in the side chain and the same branching group but different branching positions. Both polymers were found to be amorphous, i.e.,

revealing only a glass transition and no melting point. In a similar fashion as for the PEHOx homopolymer the crystallinity of the polymers is suppressed in comparison to their linear analogs with the same number of carbon atoms in the side chain. Thus, the incorporation of branching points in the side chain changes the thermal behavior from semi-crystalline to amorphous. Furthermore, the position of the branching point and the length of the side chain influence the T_g values significantly.

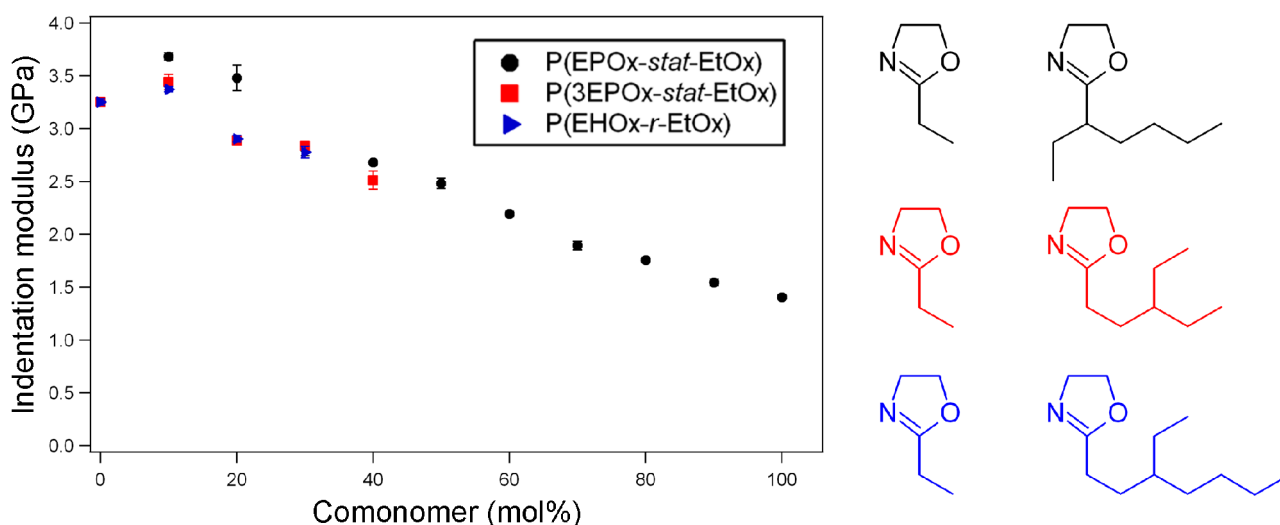


Figure 3-5: Indentation moduli of the different copolymer systems with decreasing EtOx content.

Within each library, the moduli linearly decrease with increasing comonomer content as reflected by the linear decrease in the glass transitions. When comparing the different libraries with each other, it is observed that upon changing the position of the ethyl-group in the side chain from the 1- to the 3-position, the effect on the mechanical properties is more prominent than upon elongation of the main side chain by another ethyl-unit as it is also observed in the T_g values. As a possible reason for this behavior the steric hindrance of the branched side chain structure can be assumed. Considering the number of stiff 'junction' points per repeating unit, the P(EPOx-stat-EtOx) only has one connection point between the main chain and the two side chains (considering one ethyl- and one butyl-side chain starting from the branching point), while

the P(3EPOx-*stat*-EtOx) has two junction points, one between main and side chain and one where the side chain branches.

When comparing the P(3EPOx-*stat*-EtOx) with the P(EHOx-*r*-EtOx), the moduli do not significantly differ, contrary to the difference in the glass transition temperatures. As the steric hindrance is already high due to the second junction point, an increase in one of the secondary side chains does not significantly increase the interchain distance any further. The unexpectedly lower modulus of the pure EtOx is thus a result of the hygroscopicity of that particular sample as discussed above.

By utilization of a combination of DSI, TGA, DSC and advanced FT-IR spectroscopic techniques it was possible to relate the changes of the mechanical properties within libraries of systematically varied poly(2-oxazoline)s to intermolecular processes, such as crystallization and hygroscopicity. It could be explained how water incorporated in the material decreases the mechanical properties. Furthermore it was shown that branching also has a strong effect on the mechanical properties and that changing the branching point from the 1- to the 3-position has a stronger effect than the elongation of the branched chain.

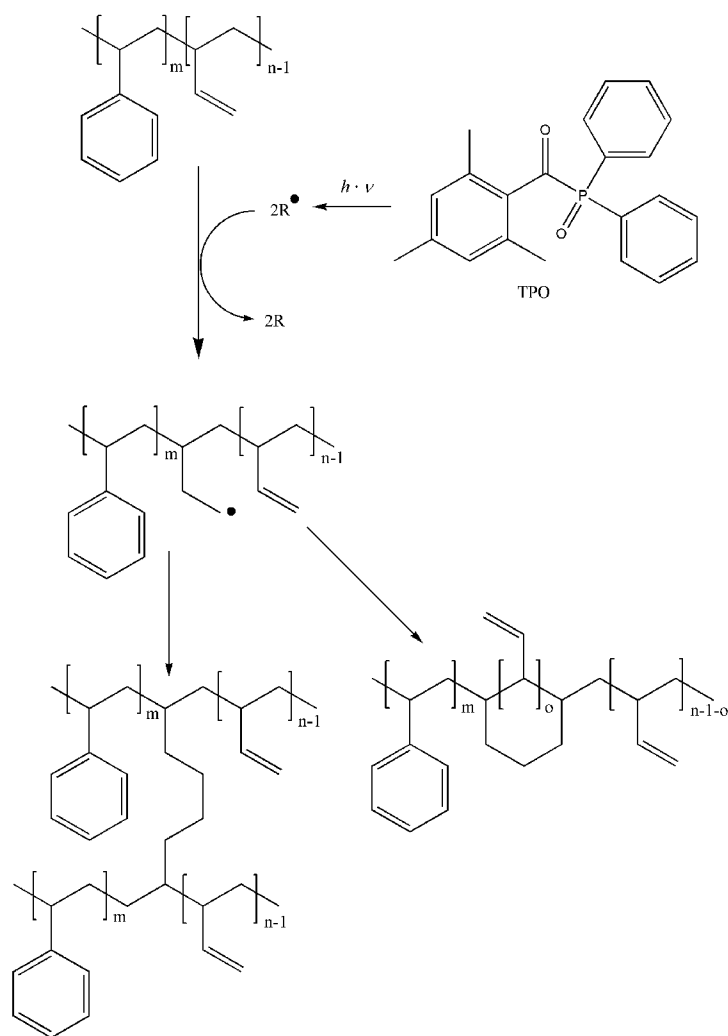
Chapter 4

Application of depth-sensing indentation to crosslinking studies and industrial polymers

Parts of this chapter have been published: P5) E. Rettler, T. Rudolph, A. Hanisch, S. Hoepfener, M. Retsch, U. S. Schubert, F. H. Schacher: "UV-induced crosslinking of the polybutadiene domains in lamellar polystyrene-*block*-polybutadiene block copolymer films – An in-depth study", *Polymer* **2012**, *53*, 5641–5648. P7) L. I. Majoros, B. Dekeyser, N. Haucourt, P. Castelein, J. Paul, J. M. Kranenburg, E. F.-J. Rettler, R. Hoogenboom, U. S. Schubert, "Preparation of polyurethane elastomers (PUEs) in a high-throughput workflow", *J. Polym. Sci. Part A: Polym. Chem.* **2011**, *49*, 301–313.

The main advantages of depth-sensing indentation (DSI) investigations are in particular the low amount of material and the fact that essentially no demanding sample preparation is required. These features make DSI interesting not only for kinetic but also for screening applications.

The possibility to investigate time-dependent processes, i.e., polymerizations, crosslinking and vulcanization processes, was demonstrated on a polystyrene / polybutadiene (PS / PB) 50:50 copolymer, where the crosslinking of the PB domains was triggered by UV light irradiation in the presence of different amounts of a crosslinking initiator (Scheme 4-1).



Scheme 4-1: Schematic representation of the crosslinking of the PB domains in films of $PS_{51}\text{-}b\text{-}PB_{49}$ ^{73,3} induced via photolysis of an UV-photoinitiator, Lucirin-TPO®.

The phase separation observed in this system exhibits a periodicity of approximately 50 nm, which is far smaller than the typical indentation size, thus, it is validated that a combined elastic modulus for the material is obtained.^[47] Moreover, the system permits to follow the crosslinking process not only by DSI, as mechanical hardening of the samples will occur, but can be also spectroscopically monitored by Raman spectroscopy, analyzing the ratio of the C=C stretching vibrations and the aromatic C-H signals. Both measurements were performed in an *ex-situ*, step-wise fashion in time intervals

of 1 h. Exemplarily DSC measurements were added into the analysis cycle for 20 wt% initiator addition. Figure 4.1 depicts the DSI data for systems with different initiator concentrations.

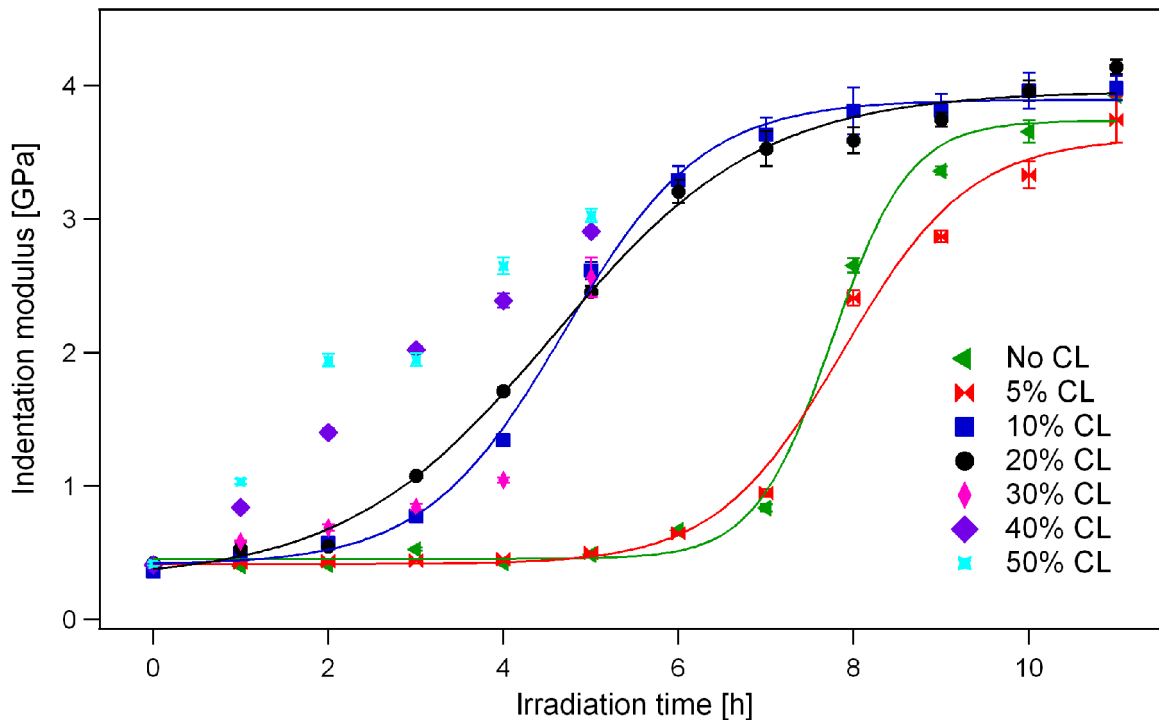


Figure 4-1: Development of the crosslinking process over time followed by depth-sensing indentation for different amounts of crosslinking agents.

For low initiator concentrations a slow crosslinking is found which reflects the formation of radicals in the initial stage of irradiation. However, no essential change of the mechanical properties of the polymer is observed.^[48-50] After the initiation period, the material undergoes a transition in which crosslinks are formed. The radicals then migrate until they react with a double bond in one of the polymer chains, forming a larger macro-radical. These macro-radicals can either undergo recombination reactions or lead to intra- or interchain crosslinking. In this stage changes of the mechanical properties can be observed, which are mainly attributed to interchain crosslinking, as a dense polymer network with lower degrees of freedom is formed. This model was confirmed by the in-depth investigation of a 20 wt% initiator system, which is depicted in Figure 4-2.

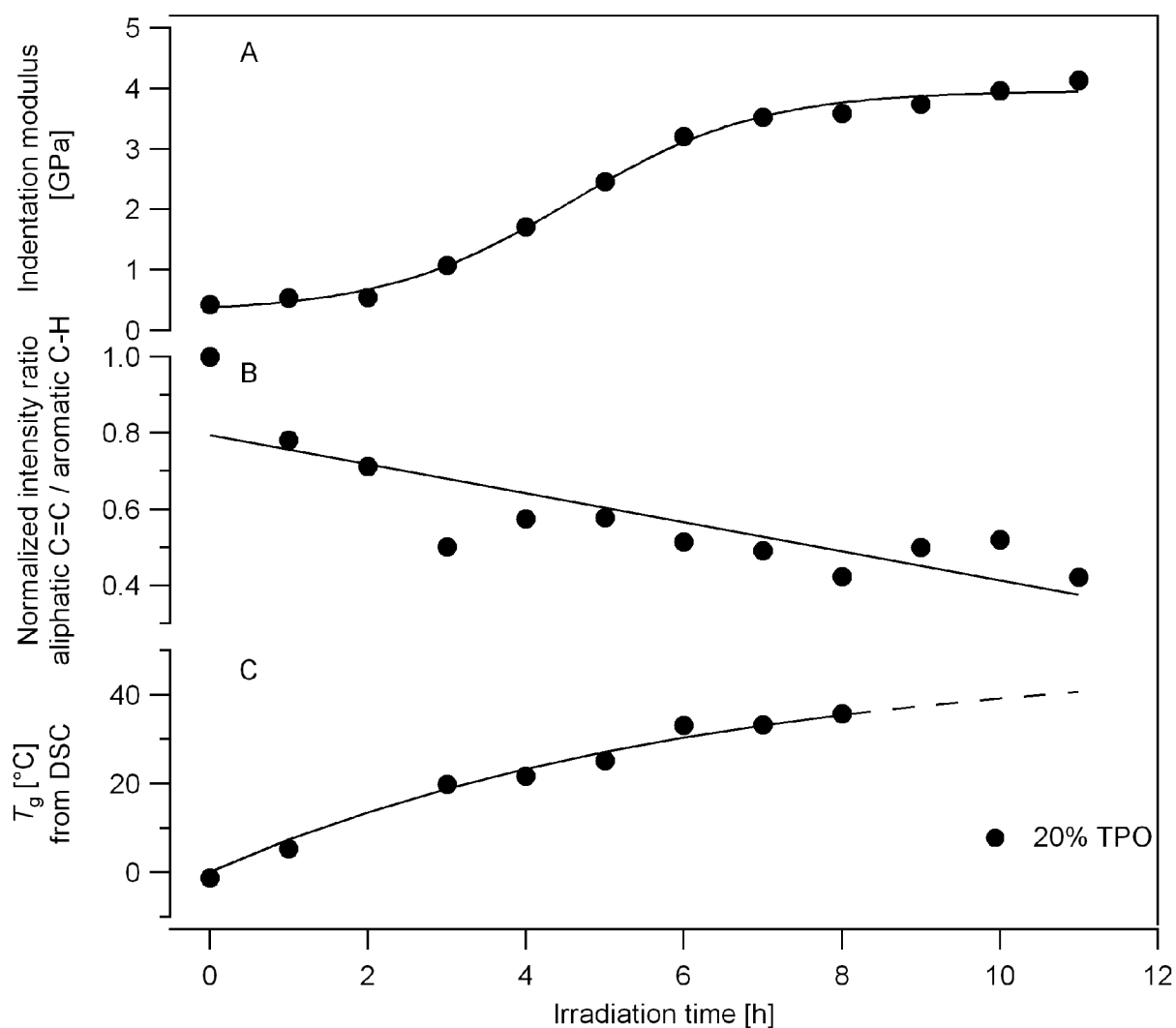
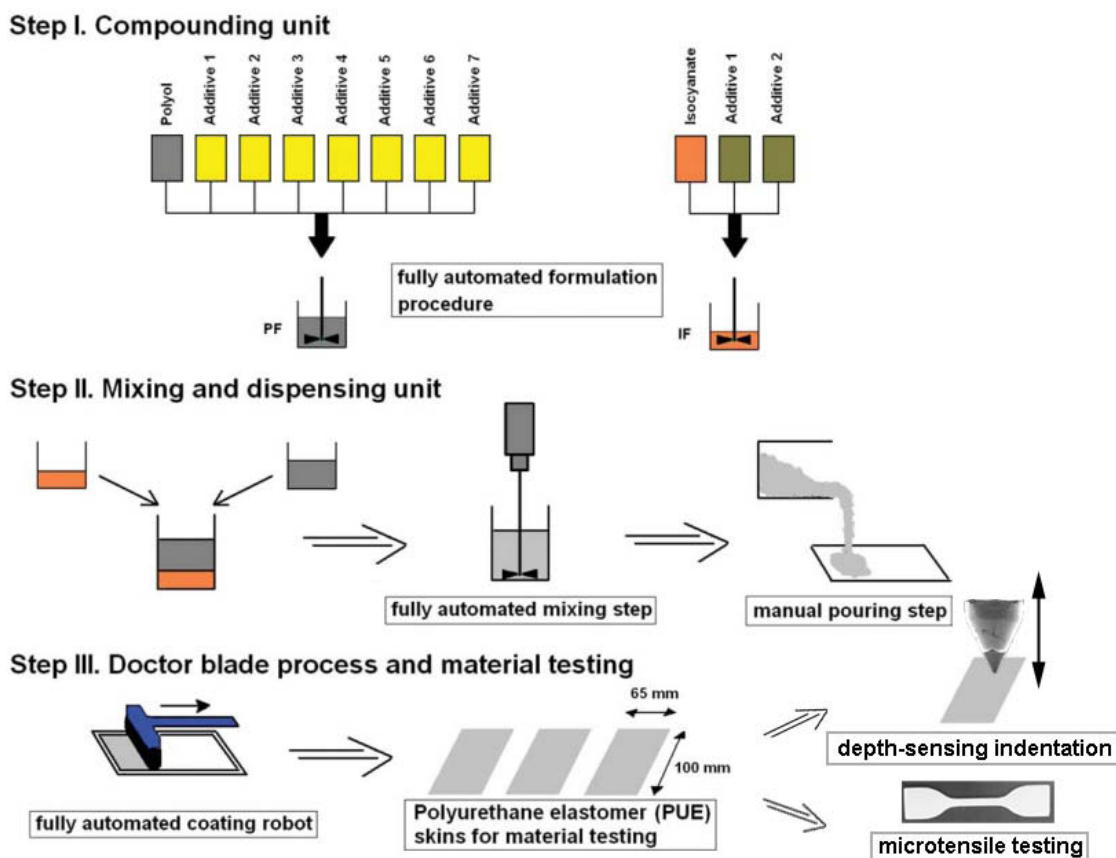


Figure 4-2: The crosslinking process of a sample containing 20 wt.% crosslinker followed by DSI, Raman spectroscopy and DSC.

Raman and T_g data indicate the start of the crosslinking after 1 h, whereas the mechanical hardening can be observed only after 3 h of UV-irradiation until after 8 hours a complete crosslinking of the polymer is observed. Thus, it could be demonstrated that the time-dependent investigation of the crosslinking of PS-PB copolymer could in principle be easily analyzed in a time-resolved fashion with a low amount of material as well as without excessive sample preparation. The combination with complementary investigation techniques, moreover, confirmed the underlying network formation.

The ease of analysis represents moreover an attractive feature for the integration of depth-sensing indentation into high-throughput workflow schemes. Also the amount of material which is required is much lower as it would be necessary for, e.g., tensile testing, where the samples have to be cut into standardized shapes of defined size. An example for such a high-throughput characterization approach was implemented on semi-industrially produced PUEs which were synthesized in a high-throughput synthesis approach (see Scheme 4-2).



Scheme 4-2: Implementation of depth-sensing indentation into a high-throughput experimentation workflow.

A set of 40 PUEs with different compositions was synthesized. The final goal was here to implement DSI as a high-throughput characterization tool to allow the efficient screening of structure-property relationships as well of an economic way of integrating quality control.

The sample preparation for the indentation as well as the measurement itself could be carried out in 12 h in an automated fashion for all 40 PUEs prepared in the workflow, demonstrating that such mechanical tests will not be a bottleneck in the complete high-throughput workflow.

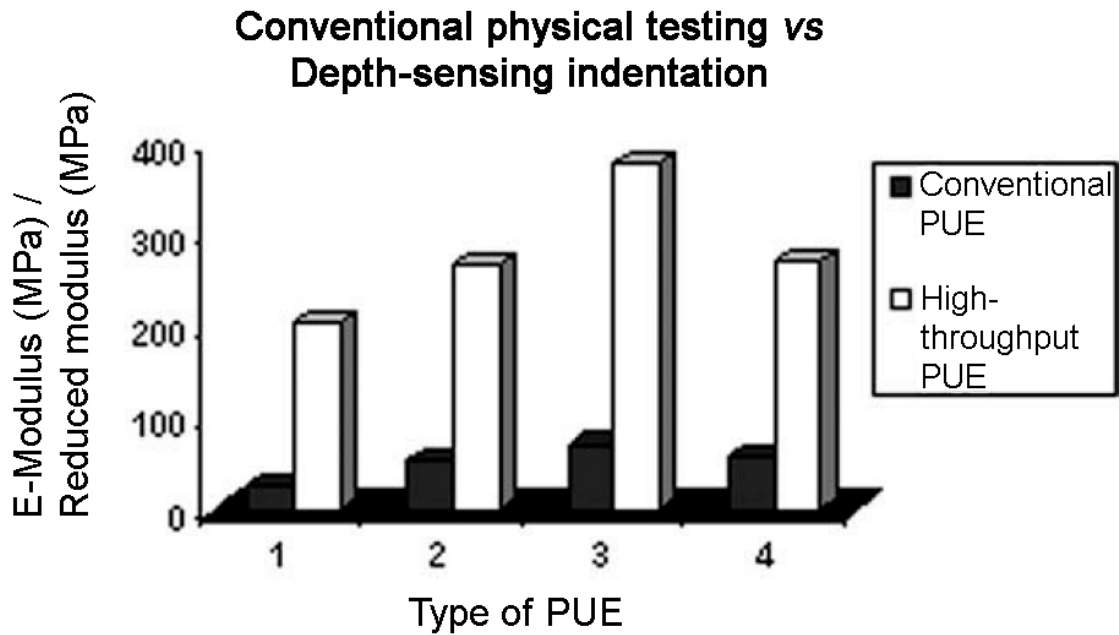


Figure 4-3: Comparison of mechanical properties determined by conventional mechanical analysis and depth-sensing indentation.

First of all it is observed that values differ by an order of magnitude from those measured by the conventional testing method (see also Figure 4-3). In general, the values obtained from indentation experiments were found to be higher than those obtained from bending tests. This is probably due to material creep and to pile-up around the indent.

The reduced modulus is calculated from the unloading stiffness S and the contact area A (which is a function of the contact depth h_c) *via*:

$$E_r = \frac{\sqrt{\pi}}{2\beta} \cdot \frac{S}{\sqrt{A(h_c)}}, \quad (4.1)$$

where β is a coefficient for the indenter geometry with a value slightly larger than 1.

Creep results in an overestimated stiffness obtained from the unloading response of the indenter, while pile-up additionally results in an increased contact area. As the values for the contact area are used from a reference material, the values obtained from a measurement where pile-up occurs will always underestimate the contact area. Therefore, the resulting reduced modulus is overestimated. These obstacles in the analysis routine limit the significance of the quantitative values of the obtained material properties. In addition, the surface roughness might influence the results. Careful optimization of the sample surface is not compatible with the targeted high-throughput experimentation approach, thus, only a qualitative screening was obtained. However, the uncertainties in data analysis do not obscure the observed trends. In general, the indentation data represented the same trends as the results obtained by conventional physical testing for the modulus. Even small deviations in the macroscopic properties, for example, PUE2 vs PUE4 could be detected with this technique. Therefore, it could be demonstrated that for a qualitative evaluation of structure property relationships depth-sensing indentation can be integrated into high-throughput experimentation workflows as an additional high-value investigation tool.

Summary

The advantages and current limitations of depth-sensing indentation (DSI) as a characterization tool for polymer materials are discussed throughout this thesis. It could be demonstrated that depth-sensing indentation studies of soft polymers are still a challenging field which is up to now only in its infancy. Within the summarized studies a base for the reliable characterization of mainly poly(2-oxazoline) libraries was created. This included a careful verification of suitable indentation parameters, a cross-evaluation of the obtained results with complementary techniques, i.e., Fourier-transform infrared spectroscopy (FTIR), differential scanning calorimetry (DSC), thermogravimetric analysis (TGA) and Raman spectroscopy, which ultimately allowed not only to determine the underlying intermolecular changes of the sample system, which are responsible for the macroscopic mechanical properties of the sample systems, but also verified the level of precision which can currently be obtained by DSI.

Particular problems arise for soft sample systems due to the material behavior that does not comply with the typical characteristics of hard samples, like metals or ceramics, for which DSI was originally used. Problems resulting from unexpected material behavior have been discussed in the context of this thesis. The application of DSI to soft polymers requires new analysis models to represent the specific material's properties of soft polymers. While metals or ceramics behave mostly elastic-plastic, polymers frequently show (visco-)elastic behavior, meaning they deform nonlinearly under the applied load. This material creep may significantly influence the measured properties, thus falsifying the obtained results. Furthermore, during contact, the material can create pile-up around the indenter tip. This leads to an underestimation of the contact area and, therefore, the calculated modulus is overestimated.

In Chapter 2 practical solutions for the investigation of soft polymers are provided. In particular the adjustment of the unloading cycle turned out to be sufficient to improve the data integrity significantly. In general for soft

polymers, a long hold segment and a high unloading rate are recommended. The long hold at the maximum load allows the material to equilibrate itself to the applied force and the quick unloading minimizes the effect of creep on the measurement.

The determined measurement protocol was applied in Chapter 3 to a polymer library consisting of poly(2-oxazoline)s with different molecular architecture. The aim of this study was to generate structure-property relationships which ultimately allow the tailor-made synthesis of polymer systems with predefined mechanical signatures. Different aspects which influence the mechanical properties could be determined: The crystallinity, branching and the influence of adsorbed water molecules. The indentation measurements provided valuable information in addition to the thermal properties investigated by DSC and TGA, which showed a linear dependence of the mechanical properties on the distance of the individual polymer T_g to room temperature. Furthermore, with the help of temperature-dependent FT-IR spectroscopic techniques, the processes of crystallization and hydrogen-bonding could be followed. This study was performed on a systematically varied library, where only small quantities (~50 mg) of the individual samples were available. As the polymers could all be prepared similarly, the fabrication of a library of samples on a microscopy glass slide allowed a consecutive measurement in an automated run. This enabled a quick comparison of the samples and resulted in the extraction of structure-property relationships.

However, as demonstrated in Chapter 4 it turned out that reliable quantitative mechanical data can only be obtained on optimized material systems – a prerequisite which is hardly achievable, in particular in semi-industrial high-throughput experimentation, where the preparation of the individual samples cannot be adapted each time. In this particular case only a qualitative correlation of the mechanical properties is possible. Therefore, an additional standardized preparation routine is highly advised for larger sample batches.

As shown in Chapter 4, creep and pile-up influences may falsify the obtained values by one order of magnitude and should therefore be avoided where possible. However, it could be demonstrated that DSI can be implemented in the high-throughput workflow as a primary evaluation tool which provides clearly the qualitative trends of the mechanical properties and even small changes can be tracked. These possibilities are frequently sufficient during industrial quality control applications.

Additionally, it was demonstrated in Chapter 4 that DSI can also be used to investigate time-dependent processes, like UV-induced crosslinking. A polystyrene / polybutadiene (PS/PB) copolymer system with varying amounts of crosslinking agent was used to investigate this process by a stepwise irradiation/measurement cycle. It was shown that the optimum amount of crosslinker is approximately 10 wt.% of the crosslinkable PB amount. The crosslinking starts after around 3 hours of irradiation and is completed after about 7 to 8 hours for sample films with a thickness of approximately 200 μm . Here, DSI was the main investigation tool for following this process. The results were confirmed by Raman spectroscopy which showed the decrease of the corresponding C=C bands from the PB block which are consumed during crosslinking.

The presented studies clearly show that DSI on soft sample systems inherently suffers from non-ideal sample behavior and future work has to focus on a better understanding of these influences. A standardized application of DSI will certainly rely on an implementation of refined models to extract the mechanical properties. Nonetheless, it can be expected that DSI will gain more importance as can be clearly seen also in the large research interest which is strongly accelerating during the last years. In particular the possibility to obtain quantitative material parameters in a local fashion with micrometer resolution, the small sample area and amount of material which is required as well as the ease and speed of data acquisition make DSI a promising tool for materials research.

Zusammenfassung

Die Vorteile und gegenwärtigen Limitierungen von Nanoindentationsmessungen als Werkzeug für die Polymeranalyse werden in dieser Arbeit diskutiert. Es konnte gezeigt werden, dass Nanoindentationsstudien an sehr weichen Polymeren ein herausforderndes Forschungsgebiet darstellen, welches immer noch in den Kinderschuhen steckt. Mit den hier zusammengefassten Studien wurde eine solide Basis für die weitere Erforschung von Poly-2-oxazolin gelegt. Dies umfasst eine vorsichtige Validierung der Messparameter, einen Vergleich der Ergebnisse mit komplementären Techniken, wie z. B. Fourier-Transformations Infrarotspektroskopie (FTIR), Differentialthermoanalyse (DSC), Thermogravimetrie (TGA) und Raman Spektroskopie, erlaubt schließlich nicht nur die Bestimmung von intermolekularen Änderungen innerhalb des betrachteten Probensystems, die letztendlich für die makroskopischen mechanischen Eigenschaften der Probe verantwortlich sind, sondern zeigt weiterhin die derzeitige Genauigkeit von Nanoindentationsmessungen.

Indentationsmessungen an weichen Polymeren stellen eine besondere Herausforderung dar, da deren Verhalten nicht dem Schema harter Materialien, wie z. B. Metallen oder keramischen Werkstoffen, folgt, für die diese Methode ursprünglich entwickelt wurde. Einige Probleme die aus unvorhergesehenen Materialeigenschaften resultieren werden in dieser Arbeit diskutiert. Die standardisierte Anwendung von Nanoindentationsmessungen in der Polymeranalytik erfordert neue Analysemodelle, die das tatsächliche Verhalten der Materialien beschreiben. Während Metalle und Keramiken elastisch-plastisch verformt werden, zeigen Polymere häufig visco-elastisches Verhalten, was bedeutet, dass ihre Verformung unter Druck nicht linear verläuft. Dieses Verhalten kann die gemessenen Eigenschaften in hohem Maße beeinflussen und die Messergebnisse somit verfälschen. Des Weiteren kann sich die Polymeroberfläche im Kontakt mit der Indenterspitze nach Außen wölben, was eine größere Kontaktfläche gegenüber der Kalibration zur Folge hat. Dies führt wiederum zu einem verfälschten Wert für den E-Modul.

In Kapitel 2 werden praktische Lösungen für die angesprochenen Probleme bei Indentationsmessungen an Polymeren vorgestellt. Die Anpassung des Rückzugssegmentes der Messung hat sich als besonders geeignet herausgestellt, um Meßfehler zu minimieren. Im allgemeinen wird für weiche Materialien ein Indentationsmuster mit langer Halteperiode bei maximaler Kraft und einer hohen Rückzugsrate der Spitze empfohlen. Die lange Halteperiode erlaubt es dem Werkstoff, sich der aufgebrachten Kraft anzupassen und der

schnelle Rückzug der Spitze minimiert zusätzlich den Effekt des Kriechens des Materials.

Das entwickelte Meßprotokoll wurde in Kapitel 3 an einer Probenbibliothek von Poly-2-oxazolinen mit unterschiedlichen molekularen Strukturen angewandt. Das Ziel dieser Studien war es, Struktur-Eigenschafts-Beziehungen ableiten zu können, was es zukünftig erlauben soll, Polymere mit maßgeschneiderten mechanischen Eigenschaften herzustellen. Verschiedene Aspekte mit Einfluss auf die mechanischen Eigenschaften konnten identifiziert werden: Kristallinität, Verzweigungsgrad und die Anlagerung von Wassermolekülen. Die Indentationsmessungen lieferten zusätzlich zu den thermischen Eigenschaften, die mittels DSC und TGA bestimmt wurden, wertvolle Informationen. Diese zeigten einen linearen Zusammenhang zwischen mechanischen Eigenschaften und der jeweiligen Glasübergangstemperatur. Des Weiteren konnte mit temperaturabhängigen FT-IR Messungen die Kristallisation sowie der Einfluss von Wasserstoffbrückenbindungen verfolgt und aufgezeigt werden. Diese Studie wurde an einer Probenbibliothek mit systematischer Variation der Seitenkettenlänge durchgeführt, für die nur sehr geringe Mengen an Material (jeweils ca. 50 mg) zur Verfügung standen. Da die Probenpräparation für alle Polymere ähnlich erfolgen konnte, war es möglich, alle Proben automatisiert zu messen. Dies ermöglichte einen schnellen Vergleich der Proben untereinander und die Extraktion von Struktur-Eigenschaftsbeziehungen.

Wie Kapitel 4 jedoch zeigt, ist es nur möglich quantitative mechanische Daten zu sammeln, wenn ein optimiertes Probensystem zur Verfügung steht. Dies ist im allgemeinen nur unter hohem Aufwand zu erreichen und limitiert daher die Anwendung der Methode für (semi-)industrielle Hochdurchsatzanwendungen. Im gezeigten Beispiel war nur ein qualitativer Vergleich der mechanischen Eigenschaften möglich. Daher ist ein zusätzlicher, standardisierter Präparationsschritt für größere Proben-mengen unabdingbar.

Zudem konnte gezeigt werden, das die Messergebnisse durch Kriechen und Adhäsion sogar um eine Zehnerpotenz verfälscht werden können. Trotzdem lassen sich Nanoindentationsmessungen leicht in ein Hochdurchsatzschema integrieren und bilden sowohl die mechanischen Trends als auch sehr kleine Variationen innerhalb der Probenbibliothek korrekt ab. Diese Möglichkeit sollte meist schon ausreichend für die Anwendung in der industriellen Qualitätskontrolle sein.

Zusätzlich konnte in Kapitel 4 gezeigt werden, dass Nanoindentationsmessungen ebenso verwendet werden können, um zeitabhängige Prozesse, wie z. B. die UV-induzierte Quervernetzung von Polymeren, zu untersuchen. Ein Copolymersystem aus Polystyrol und Polybutadien mit variierendem Anteil an

Vernetzungsreagenz wurde für diese Studie verwendet. Die Proben wurden zyklisch wechselweise belichtet und gemessen. Es konnte gezeigt werden, dass die optimale Menge an Vernetzungsreagenz bei etwa 10 Gewichtsprozent liegt, bezogen auf den Anteil an Polybutadien. Die Vernetzung startet nach ca. 3 Stunden Belichtungszeit und wird nach 7 bis 8 Stunden vervollständigt bei den gemessenen Probenfilmen von ca. 200 µm Dicke. Nanoindentation diente hier als hauptsächliche Charakterisierungsmethode um den Prozess anhand der Änderung der mechanischen Eigenschaften zu verfolgen. Die Ergebnisse wurden mit Hilfe der Ramanspektroskopie bestätigt. Diese Messungen zeigten die Verringerung der Intensität der C=C Doppelbindung des Polybutadien-Blocks, welche im Verlauf der Vernetzung zu Einfachbindungen reduziert werden.

Die präsentierten Studien zeigen klar, dass Nanoindentationsmessungen an sehr weichen Proben durch Abweichungen vom idealen Verhalten erschwert werden, und dass weitere Studien für ein besseres Verständnis dieser Abweichungen nötig sind. Eine zukünftige standardisierte Anwendung der Nanoindentation wird wahrscheinlich auf neuen Modellen zur Extraktion der mechanischen Eigenschaften basieren. Trotz alledem ist zu erwarten, dass der Nanoindentationstechnik künftig eine größere Rolle bei der Messung von mechanischen Eigenschaften zukommt, was auch dem stark wachsenden Forschungsinteresse in den letzten Jahren geschuldet ist. Von besonderem Interesse ist hier die Möglichkeit, quantitativ die Materialeigenschaften mit einer lokalen Auflösung im Mikrometerbereich bestimmen zu können, sowie allgemein die geringe Menge an benötigtem Probenmaterial und die Möglichkeit zur Automatisierung der Messung. All diese Eigenschaften machen die Nanoindentationstechnik zu einem wertvollen und vielversprechenden Werkzeug für die Materialforschung.

References

- [1] ASTM D882.
- [2] D. T. N. Chen, Y. Wen, P. A. Janmey, J. C. Crocker, A. G. Yodh, *Ann. Rev. Cond. Matt. Phys.* **2010**, *1*, 301-322.
- [3] R. L. Smith, G. E. Sandland, *Proc. Inst. Mech. Eng.* **1922**, *1*, 623-641.
- [4] S. P. Rockwell, *Transactions of the American Society for Steel Treating* **1922**, *2*, 1013-1033.
- [5] R. Hoogenboom, *Angew. Chem. Int. Ed.* **2009**, *48*, 7978-7994.
- [6] A. Makino, S. Kobayashi, *J. Polym. Sci., Part A: Polym. Chem.* **2010**, *48*, 1251-1270.
- [7] H. Schlaad, C. Diehl, A. Gress, M. Meyer, A. L. Demirel, Y. Nur, A. Bertin, *Macromol. Rapid Commun.* **2010**, *31*, 511-525.
- [8] N. Adams, U. S. Schubert, *Adv. Drug Deliv. Rev.* **2007**, *59*, 1504-1520.
- [9] D. G. Anderson, C. A. Tweedie, N. Hossain, S. M. Navarro, D. M. Brey, K. J. Van Vliet, R. Langer, J. A. Burdick, *Adv. Mater.* **2006**, *18*, 2614-2618.
- [10] J.-S. Park, K. Kataoka, *Macromolecules* **2006**, *39*, 6622-6630.
- [11] J. Schellenberg, J. Vogel, *J. Polym. Sci., Part B: Polym. Phys.* **1994**, *32*, 1969-1975.
- [12] C. G. Simon, N. Eidelman, Y. Deng, N. R. Washburn, *Macromol. Rapid Commun.* **2004**, *25*, 2003-2007.
- [13] R. Hoogenboom, M. W. M. Fijten, H. M. L. Thijs, B. M. van Lankvelt, U. S. Schubert, *Design. Monom. Polym.* **2005**, *8*, 659-671.
- [14] R. Hoogenboom, *Macromol. Chem. Phys.* **2007**, *208*, 18-25.
- [15] B. Poon, D. Rittel, G. Ravichandran, *Int. J. Solids Struct.* **2008**, *45*, 6018-6033.
- [16] W. C. Oliver, G. M. Pharr, *J. Mater. Res.* **1992**, *7*, 1564-1583.
- [17] C. G. N. Pelletier, J. M. J. Den Toonder, L. E. Govaert, N. Hakiri, M. Sakai, *Philos. Mag.* **2008**, *88*, 1291-1306.
- [18] D. C. Webster, *Macromol. Chem. Phys.* **2008**, *209*, 237-246.

- [19] C. A. Tweedie, D. G. Anderson, R. Langer, K. J. Van Vliet, *Adv. Mater.* **2005**, *17*, 2599–2604.
- [20] J. M. Kranenburg, C. A. Tweedie, K. J. Van Vliet, U. S. Schubert, *Adv. Mater.* **2009**, *21*, 3551–3561.
- [21] Y. S. Park, Y. S. Kang, D. J. Chung, *e-Polymers* **2002**, no.016.
- [22] V. Vogel, M. Sheetz, *Nat. Rev. Mol. Cell Biol.* **2006**, *7*, 265–275.
- [23] J. H.-C. Wang, B. P. Thampatty, J.-S. Lin, H. J. Im, *Gene* **2007**, *391*, 1–15.
- [24] C. M. Lo, H. B. Wang, M. Dembo, Y. L. Wang, *Biophys. J.* **2000**, *79*, 144–152.
- [25] L. Cheng, X. Xia, L. E. Scriven, W. W. Gerberich, *Mech. Mater.* **2005**, *37*, 213–226.
- [26] J. M. J. den Toonder, Y. Ramone, A. R. van Dijken, J. G. J. Beijer, G. Q. Zhang, *J. Electron. Packag.* **2005**, *127*, 267–285.
- [27] M. L. Oyen, *Philos. Mag.* **2006**, *86*, 5625–5631.
- [28] L.-H. He, M. V. Swain, *J. Biomed. Mater. Res. A* **2009**, *91A*, 352–359.
- [29] L.-H. He, Y. Xu and D. G. Purton, *Arch. Oral Biol.* **2011**, *56*, 512–519.
- [30] C. Müller, A. Lüders, W. Hoth-Hannig, M. Hannig, C. Ziegler, *Langmuir* **2009**, *26*, 4136–4141.
- [31] S. Bechtle, S. F. Ang, G. A. Schneider, *Biomaterials* **2010**, *31*, 6378–6385.
- [32] P. W. Lucas, R. Cook, T. K. Lowrey, *MRS Proceedings* **2006**, *975*, 0975-DD0908-0907.
- [33] S. Ito, M. Hashimoto, B. Wadgaonkar, N. Svizero, R. M. Carvalho, C. Yiu, F. A. Rueggeberg, S. Foulger, T. Saito, Y. Nishitani, M. Yoshiyama, F. R. Tay, D. H. Pashley, *Biomaterials* **2005**, *26*, 6449–6459.
- [34] M. L. Oyen, R. F. Cook, *J. Mech. Behav. Biomed.* **2009**, *2*, 396–407.
- [35] M. L. Oyen, R. F. Cook, *J. Mater. Res.* **2003**, *18*, 139–150.
- [36] H. G. H. van Melick, O. F. J. T. Bressers, J. M. J. den Toonder, L. E. Govaert, H. E. H. Meijer, *Polymer* **2003**, *44*, 2481–2491.

- [37] J. M. Kranenburg, H. M. L. Thijs, C. A. Tweedie, S. Hoepfener, F. Wiesbrock, R. Hoogenboom, K. J. Van Vliet, U. S. Schubert, *J. Mater. Chem.* **2009**, *19*, 222–229.
- [38] H. K. Reimschuessel, *J. Polym. Sci., Part A: Polym. Chem.* **1979**, *17*, 2447–2457.
- [39] J. M. Kranenburg, C. A. Tweedie, R. Hoogenboom, F. Wiesbrock, H. M. L. Thijs, C. E. Hendriks, K. J. Van Vliet, U. S. Schubert, *J. Mater. Chem.* **2007**, *17*, 2713–2721.
- [40] M. W. M. Fijten, J. M. Kranenburg, H. M. L. Thijs, R. M. Paulus, B. M. van Lankvelt, J. de Hullu, M. Springintveld, D. J. G. Thielen, C. A. Tweedie, R. Hoogenboom, K. J. Van Vliet, U. S. Schubert, *Macromolecules* **2007**, *40*, 5879–5886.
- [41] M. Litt, J. Herz, *J. Colloid Interface Sci.* **1969**, *31*, 248–252.
- [42] M. Litt, F. Rahl, L. G. Roldan, *J. Polym. Sci., Part A-2* **1969**, *7*, 463–473.
- [43] L. Cabedo, J. M. Lagaron, D. Cava, J. J. Saura, E. Gimenez, *Polym. Test.* **2006**, *25*, 860–867.
- [44] A. L. Demirel, M. Meyer, H. Schlaad, *Angew. Chem. Int. Ed.* **2007**, *46*, 8622–8624.
- [45] S. Tsuchida, K. Tadano, S. Yano, *Polym. Bull.* **1996**, *37*, 97–104.
- [46] K. Kempe, S. Jacobs, H. M. L. Lambert. Thijs, M. M. W. M. Fijten, R. Hoogenboom, U. S. Schubert, *Macromolecules* **2010**, *43*, 4098–4104.
- [47] G. Constantinides, K. S. Ravi Chandran, F. J. Ulm and K. J. Van Vliet, *Mater. Sci. Eng. A-Struct.* **2006**, *430*, 189–202.
- [48] C. Decker, T. N. T. Viet, *Macromol. Chem. Phys.* **1999**, *200*, 358–367.
- [49] C. Decker, T. N. T. Viet, *Macromol. Chem. Phys.* **1999**, *200*, 1965–1974.
- [50] C. Decker, K. Zahouily, D. Decker, T. Nguyen, T. Viet. *Polymer* **2001**, *42*, 7551–7560.

Curriculum vitae

- 20-05-1981 Born in Essen, Germany
- 1987 - 1991 Primary School Josefschule in Essen, Germany
- 1991 - 2000 Carl-Humann-Gymnasium in Essen, Germany
Degree: Abitur, A-levels equivalent
- 2001 - 2008 Study of Chemistry, University of Duisburg-Essen, Germany
2004 Vordiplom (equivalent to B.Sc.)
2008 Scientific degree: Diplom-Chemiker (equivalent to M.Sc.)
03. - 06.2005 Foreign semester at the Capital University of Medical Sciences, Beijing, VR China (Prof. Peng Shiqui)
Project: "Study on the Synthesis of 1,4-dioxo-2,3,6,7,12,12a hexahydropyrazino-[1',2':1,6]-pyridino[3,4-b]indoles"
- 04.2008-04.2009 PhD student at Eindhoven University of Technology, The Netherlands (Prof. U. S. Schubert)
"Depth-sensing Indentation of Soft Polymers"
- Since 04.2009 PhD student at the Institute of Organic Chemistry and Macromolecular Chemistry (Prof. U. S. Schubert), Friedrich-Schiller-Universität Jena, Germany
"Depth-sensing Indentation of Soft Polymers"

Publication list

PEER-REVIEWED PUBLICATIONS

- 2013 E. F.-J. Rettler, S. Hoepfener, U. S. Schubert, "Mapping the mechanical properties of biomaterials on different length scales: depth sensing indentation and AFM based nanoindentation", *J. Mater. Chem. B* **2013**, *1*, 2789-2806.
- K. Kempe, E. F.-J. Rettler, R. M. Paulus, A. Kuse, R. Hoogenboom, U. S. Schubert, "A systematic investigation of the effect of side chain branching on the glass transition temperature and mechanical properties of aliphatic (co-)poly(2-oxazoline)s", *Polymer* **2013**, *54*, 2036-2042.
- E. F.-J. Rettler, J. M. Kranenburg, S. Hoepfener, U. S. Schubert, "Verification of key assumptions for the analysis of depth-sensing indentation data", *Macromol. Mater. Eng.* **2013**, *298*, 78-88.
- 2012 E. F.-J. Rettler, T. Rudolph, A. Hanisch, S. Hoepfener, M. Retsch, U. S. Schubert, F. H. Schacher, "UV-induced crosslinking of the polybutadiene domains in lamellar polystyrene-*block*-polybutadiene block copolymer Films – An in-depth study", *Polymer* **2012**, *53*, 5641-5648.
- E. F.-J. Rettler, M. V. Unger, R. Hoogenboom, H. W. Siesler, U. S. Schubert, "Water uptake of poly(2-*N*-alkyl-2-oxazoline)s: Temperature-dependent FT-IR spectroscopy and two-dimensional correlation analysis", *Appl. Spectrosc.* **2012**, *22*, 1145-1155.
- 2011 E. F.-J. Rettler, H. M. L. Lambermont-Thijs, J. M. Kranenburg, R. Hoogenboom, M. V. Unger, H. W. Siesler, U. S. Schubert, "Water uptake of poly(2-*N*-alkyl-2-oxazoline)s: Influence of crystallinity and hydrogen-bonding on the mechanical properties", *J. Mater. Chem.* **2011**, *21*, 17331-17337.
- L. I. Majoros, B. Dekeyser, N. Haucourt, P. Castelein, J. Paul, J. M. Kranenburg, E. F.-J. Rettler, R. Hoogenboom, U. S. Schubert, "Preparation of polyurethane elastomers (PUEs) in a high-throughput workflow", *J. Polym. Sci., Part A: Polym. Chem.* **2011**, *49*, 301-313.

- 2010 E. F.-J. Rettler, J. M. Kranenburg, H. M. L. Lambermont-Thijs, R. Hoogenboom, U. S. Schubert, "Thermal, mechanical, and surface properties of poly(2-*N*-alkyl-2-oxazoline)s", *Macromol. Chem. Phys.* **2010**, *211*, 2443-2448.

PREVIOUS PUBLICATIONS

- 2009 Y. Duan, M. Thunga, R. Schlegel, K. Schneider, E. F.-J. Rettler, R. Weidisch, H. W. Siesler, M. Stamm, J. W. Mays, N. Hadjichristidis, "Morphology and deformation mechanisms and tensile properties of tetrafunctional multigraft copolymers", *Macromolecules* **2009**, *42*, 4155-4164.
- 2008 Y. Duan, E. F.-J. Rettler, K. Schneider, R. Schlegel, M. Thunga, R. Weidisch, H. W. Siesler, M. Stamm, J. W. Mays, N. Hadjichristidis, "Deformation behavior of sphere-forming trifunctional multigraft copolymer", *Macromolecules* **2008**, *41*, 4565-4568.

ORAL PRESENTATIONS

- 2011 E. F.-J. Rettler, E. Koc, U. S. Schubert, "High-throughput characterization of PE copolymers by depth-sensing indentation and vibration spectroscopy", DPI Cluster Meeting, Darmstadt, Germany, 06/2011.
- 2009 E. F.-J. Rettler, B. Garipcan, K. Kempe, U. S. Schubert, "High-throughput characterization of PDMS and poly(2-oxazoline)s by depth-sensing indentation", DPI Cluster Meeting, Darmstadt, Germany, 09/2009.
- 2008 E. F.-J. Rettler, J. M. Kranenburg, U. S. Schubert, "High-throughput characterization by depth-sensing indentation", DPI Cluster Meeting, Eindhoven, The Netherlands, 11/2008.

POSTER PRESENTATIONS

- 2011 E. F.-J. Rettler, D. Linde, G. Schneider, T. Körbs, P. Litschko, S. Hoepfner, U. S. Schubert, "Modulus mapping of bone implant microcomposites", Nanomechanical Testing in Materials Research and Development, Lanzarote, Spain, 10/2011.
- 2010 E. F.-J. Rettler, J. M. Kranenburg, R. Hoogenboom, U. S. Schubert, "Nanomechanical investigations on poly(2-oxazoline)s", Nanobrücken, Saarbrücken, Germany, 02/2010.
- 2009 E. F.-J. Rettler, J. M. Kranenburg, R. Hoogenboom, U. S. Schubert, "Nanomechanical investigations on poly(2-oxazoline)s", Nanomechanical Testing, Barga, Italy, 10/2009.
- E. F.-J. Rettler, J. M. Kranenburg, R. Hoogenboom, U. S. Schubert, "Nanomechanical investigations on poly(2-oxazoline)s", Deformation, Yield and Fracture of Polymers, Kerkrade, The Netherlands, 04/2009.
- 2008 E. F.-J. Rettler, J. M. Kranenburg, E. Koc, R. Duchateau, U. S. Schubert, "Nanomechanical investigations on polyolefins", Nanomech 9, Hückelhoven, Germany, 09/2008.
- E. F.-J. Rettler, J. M. Kranenburg, E. Koc, R. Duchateau, U. S. Schubert, "Nanomechanical investigations on polyolefins", Hysitron European Workshop and User Meeting, Ismaning, Germany, 10/2008.

Acknowledgements / Danksagung

First of all, I would like to thank Prof. Dr. Ulrich S. Schubert for the opportunity to do my PhD project at two totally different universities. Thank you for all the places I could visit due to conferences and all the people I met. The experiences and impressions I earned during this time are unique and priceless. Thank you for making all this possible.

I would also like to thank my supervisor in Eindhoven, Dr. Johannes M. Kranenburg, for introducing me to the field of depth-sensing indentation and tutoring me during my first year in the Netherlands. Mine eyes are open.

I am greatly indebted to my supervisor in Jena, Dr. Stephanie Höppener, not only for the help she provided me with the manuscripts, the AFM measurements or the chocolates she brought to the office, but also for all the non work-related activities. Thank you for never giving up your hope in me. Wish you all the best for the future!

Furthermore, I would like to thank Prof. Dr. Heinz W. Siesler for the cooperation and the time in his lab. It was a great pleasure to come to Essen for two weeks and take data back to Jena worth for one and a half publications. Thank you and also Dr. Miriam Unger for the continuous support and the discussions regardless of being in Germany, Japan, America or South Africa.

I also want to express my gratitude to Gabriele Sentis for the introduction to the IR spectrometer in Jena and sharing her measurement time, even though the results did not make it into this thesis.

I greatly thank all the new friends I made during my PhD time for all the barbecue evenings, volleyball and other sports events, crazy travels (Eyjafjallajökull!), concerts and parties. Vashe zdorovie!

I would also like to thank a lot of people “behind the scenes”. As I sometimes do not even know them personally (and also fear to forget somebody), I will not give names here:

First of all, many thanks to all the secretaries in the administration departments both in Eindhoven and Jena. It may have been troublesome to go through all the registration processes twice, but you always had time for me and my problems.

Also many thanks to everyone who provided samples for the different projects. Then of course also a big thank you to all the people (usually in the sub-group meetings) who discussed the problems arising during the measurements of their own or somebody else's samples. Thanks for the ideas and suggestions that helped to improve the thesis!

Special thanks go to the Jena biking group. Thank you Jürgen for the statistics and always finding a “track” and Steffi for the barbecues on your awesome roof terrace.

At the end, I would like to thank my friends and family for all the energy you gave me to complete this work.

Declaration of authorship / Selbständigkeitserklärung

Hiermit erkläre ich, dass ich die vorliegende Arbeit selbständig und unter Verwendung der angegebenen Hilfsmittel, persönlichen Mitteilungen und Quellen angefertigt habe.

I certify that the work presented here is, to the best of my knowledge and belief, original and the result of my own investigations, except as acknowledged, and has not been submitted, either in part or whole, for a degree at this or any other university.

Jena, den

Publications P1-P8

- P1: Reproduced by permission of The Royal Society of Chemistry.
<http://pubs.rsc.org/en/content/articlelanding/2013/tb/c3tb20120a>
- P2: Reprinted with permission. Copyright 2012 WILEY-VCH Verlag GmbH & Co. KG, Weinheim.
- P3: Reprinted with permission. Copyright © 2013 Elsevier.
- P4: Reprinted with permission. Copyright © 2012 Society for Applied Spectroscopy.
- P5: Reprinted with permission. Copyright © 2012 Elsevier.
- P6: Reproduced by permission of The Royal Society of Chemistry.
<http://pubs.rsc.org/en/content/articlelanding/2011/JM/c1jm12541a>
- P7: Reprinted with permission. Copyright © 2010 Wiley Periodicals, Inc.
- P8: Reprinted with permission. Copyright © 2010 WILEY-VCH Verlag GmbH & Co. KGaA, Weinheim

P1 Mapping the mechanical properties of biomaterials on different length scales: Depth sensing indentation and AFM based nanoindentation

Erik F.-J. Rettler, Stephanie Hoepfener, Ulrich S. Schubert,

J. Mater. Chem. B **2013**, *1*, 2789-2806.

Mapping the mechanical properties of biomaterials on different length scales: depth-sensing indentation and AFM based nanoindentation

Cite this: *J. Mater. Chem. B*, 2013, **1**, 2789

Erik Rettler,^{ab} Stephanie Hoepfener,^{*ac} Bernd W. Sigusch^d and Ulrich S. Schubert^{abc}

The micro- and nanomechanical properties of biomaterials are of central importance as surface elasticity, surface elastic response and adhesion play a central role in a large number of biological processes. They influence, e.g. morphogenesis, self-healing abilities and restoration processes, focal adhesion, motility, mechano-transduction, metastasis and are important for drug delivery applications, and others. These processes address fundamental questions in biology, medicine and diagnostics, pharmaceutical research, archaeology, dental as well as cosmetic applications. With nanoindentation as well as AFM force spectroscopic techniques suitable investigation tools are at hand, which can provide mechanical information on different length scales. The development of both techniques resulted in a broad applicability and the number of examples where both techniques have been used to study (soft) biomaterials rapidly increased during the last years.

Received 25th January 2013
Accepted 19th March 2013

DOI: 10.1039/c3tb20120a

www.rsc.org/MaterialsB

Introduction

The mechanical properties of materials represent essential parameters for their applicability as their hardness, next to their

chemical composition and surface topography, has a significant impact on many different research directions. Biological systems frequently consist (partially) of soft matter materials, such as hydrogels, polymers, nanocomposites, *etc.*, which impose demanding requirements on the utilized analysis tools. The role of mechano-responsive and -stimulated responses of biological tissues is an area of growing interest and it was discovered that the mechanical properties, *e.g.*, of cells, play a crucial role in biological processes.^{1–3} In addition, changes of the mechanical properties of cells can be regarded as characteristic signatures of ill-regulated biochemical and biophysical processes.^{4,5} These fields of research represent an active area where recently the

^aLaboratory of Organic and Macromolecular Chemistry (IOMC), Friedrich Schiller University Jena, Humboldtstr. 10, 07743 Jena, Germany. E-mail: s.hoepfener@uni-jena.de; Fax: +49 3641948202; Tel: +49 3641948261

^bDutch Polymer Institute (DPI), John F. Kennedylaan 2, 5612 AB Eindhoven, The Netherlands

^cJena Center for Soft Matter (JCSM), Friedrich Schiller University Jena, Philosophenweg 7, 07743 Jena, Germany

^dDepartment of Conservative Dentistry, Jena University Hospital, An der alten Post 4, Jena D-07743, Germany



Erik Rettler was born in Essen, Germany, where he later also studied Chemistry. He graduated from the University of Duisburg-Essen in 2008. After that, he joined the group of Prof. Ulrich S. Schubert at the Eindhoven University of Technology, The Netherlands and later at the Friedrich Schiller University Jena, Germany for his PhD project on depth-sensing indentation of soft polymers.



Stephanie Hoepfener studied physics at the Westfälische Wilhelms-University Münster, Germany, where she earned her PhD degree in 2001 under the supervision of Prof. H. Fuchs and Prof. L.F. Chi. After her PhD studies she joined the group of Prof. J. Sagiv at the Weizmann Institute of Science, Israel, as a Minerva fellow. In 2003 she moved to the group of Prof. U.S. Schubert, Eindhoven University of Technology, The Netherlands. Since 2009 she is the project leader for Nanolithography and responsible for electron microscopy in the Jena Center for Soft Matter at the Friedrich Schiller University Jena, Germany.

implementation of different technologies has become an important issue to investigate, *e.g.*, the local mechanical properties of biomaterials. Other applications relate to the mechanical and surface properties of biomaterials, *e.g.*, for their application as bone replacement or dental implant materials.⁶⁷ In clinical studies biocompatibility of replacement materials, their stability with respect to the biological environment (pH, temperature stability, *etc.*), their ability to facilitate cell growth around or even into the material are subject of investigation. Recently, the utilization of mechanical properties as a tool for diagnosis has been increasingly discussed. The early stage diagnosis of osteoporosis, *e.g.*, can be related to a change of the mechanical properties of the bone material; however, with commonly applied diagnostic tools, a severe decrease of the bone density has to have taken place already, before significant changes can be measured. Guglielmi *et al.*^{8,9} recently reviewed the most common diagnostic techniques and explicitly pointed out the necessity of a more accurate and early diagnostic instrument. New research strategies therefore try to relate local micro- and nanomechanical changes of the properties of the bone to the early stage diagnosis and progression of osteoporosis.³⁰

In particular, for biomaterials it has been observed that the mechanical performance of materials depends on properties of very different length scales, ranging from the micrometer to the nanometer range. By integrating Atomic Force Microscopy (AFM) and depth-sensing indentation (DSI) investigations the micro- and nanomechanical properties can be obtained. In particular, biological sample systems resemble complex biochemical and biophysical architectures.

This review article summarizes recent research developments with the main focus being placed on the testing of mechanical properties of biomaterials and biological systems by DSI and AFM spectroscopy in different ranges of dimension. Applications as well as fundamental questions for the investigation of biological processes are highlighted. These studies are frequently complemented by additional spectroscopic and microscopic tools, which are, however, beyond the scope of this review article. For comprehensive summaries of these technologies we refer readers to additional literature articles.^{11–17}

Determination of mechanical properties

The classical determination of the mechanical properties of materials is usually performed by means of standardized procedures, such as tensile and compression testing. In such tests the sample specimen is stretched or compressed at a defined force, while the deformation of the material is recorded. Classical hardness testing, like Vicker's¹⁸ or Rockwell hardness tests,¹⁹ utilizes a stylus of standardized geometry which is driven into the sample material and the hardness is calculated from the residual imprint. Very soft materials, *i.e.*, soft rubber or hydrogels, are tested by rheology.²⁰ These tests require the availability of a relatively large quantity of material. Such testing frequently is difficult to apply on biomaterials, either due to the availability of only small quantities of material, due to the demanding material's properties, or due to the nature of the material which limits the possibilities for sample preparation. Thus, there is a strong desire to develop and to apply alternative measurement techniques which can be performed on small



Bernd W. Sigusch is the head of the clinic of Conservative Dentistry and Full-Professor for Conservative Dentistry and Periodontology at the Jena University Hospital. He is head of the WHO Collaborating Center for Prevention of Oral Disease, Germany. Since 2008 he has been the CME-editor for 'ZWR-Das Deutsche Zahnärzteblatt' and was the chairman of the Society for Basic Dental Research of the DGZMK (Mainz).



Ulrich S. Schubert was born in Tübingen (Germany) in 1969. He studied chemistry in Frankfurt and Bayreuth (both Germany) and the Virginia Commonwealth University, Richmond (USA). His PhD studies were performed at the Universities of Bayreuth and South Florida/Tampa. After postdoctoral training with J.-M. Lehn at the University in Strasbourg (France), he moved to the TU München (Germany) and obtained his Habilitation in 1999. During 1999–2000 he was a professor at the Center for Nano-Science, University of Munich (Germany), and during 2000–2007 Full-Professor at TU Eindhoven. Since April 2007, he has been Full-Professor at the Friedrich Schiller University Jena (Chair of Organic and Macromolecular Chemistry), Germany. His awards include the Bayerischen Habilitations-Förderpreis, the Habilitandenpreis of the GDCh (Makromolekulare Chemie), the Heisenberg-Stipendium of the DFG, the Dozenten-Stipendium of the Fonds der Chemischen Industrie, the VICI award of the NWO, the Piet-Lemstra innovation award of the DPI and the BPG biannual international award.

quantities of the sample material, preferentially providing information on different length scales and in the native environment of the sample. The discussion presented here mainly focuses on two analysis tools for investigating the mechanical properties of biomaterials with micro- and nanometer resolution. Recent developments and investigation performed with depth-sensing indentation (DSI) as well as AFM spectroscopy and force volume mapping will be summarized. We will highlight important measurement tools, limitations, as well as perspectives of the introduced methods referring to selected reports from the literature.

Depth-sensing indentation and AFM force spectroscopy

DSI and AFM spectroscopy are measurement tools which are based on a probe assisted methodology. For depth-sensing indentation diamond tips are utilized with effective radii down to a few microns. Different tip geometries are available, like (cono-)spherical, Berkovich, flat punch or Vicker's probes and the choice of the tip is strongly dependent on the properties of the sample under investigation.²¹ For soft materials, like polymers and biomaterials, typically a (cono-)spherical tip of small radius or a flat punch indentation tip is used.

In the construction of the nanoindenter, the displacement of the tip is recorded by a capacitive sensor. With this setup, displacements down to 0.002 nm with a force resolution of 1 nN can be measured. Fig. 2A shows the schematic representation of a single depth-sensing experiment.

The tip approaches the surface until a pre-defined minimum force for surface detection is reached. The corresponding displacement is registered and the tip is retracted for a few nanometers. The tip re-approaches the surface and is pushed into the material until the maximum force is reached, resulting in both plastic and elastic deformation of the sample. After an optional hold period at maximum load, the tip is retracted. A typical load-displacement diagram is shown in Fig. 2A (bottom).

In the AFM (Fig. 1B), the probe is usually a very sharp tip with an effective radius of 10 nm mounted on a soft flexible cantilever. Any deflection of the cantilever is detected by means of a position sensitive photodiode allowing for an accurate registration of the tip movement across the surface. Depending on the stiffness of the chosen cantilevers a typical force resolution

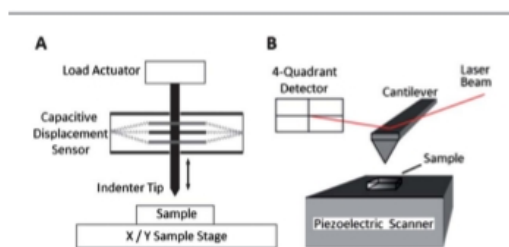


Fig. 1 Typical schematic setup for depth-sensing indentation (A) and AFM spectroscopy (B). In both cases force-displacement curves are obtained which allow the extraction of mechanical information.

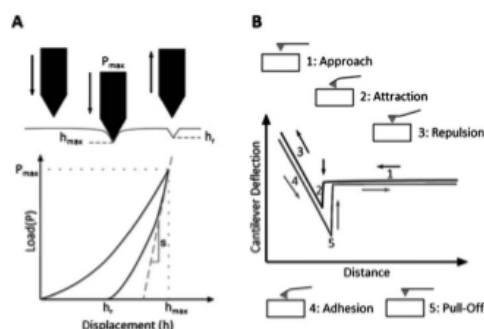


Fig. 2 Schematic representation of a single (A) indentation and (B) force spectroscopic experiment. The resulting force-displacement curves are illustrated below.

down to few pN can be achieved with a vertical distance resolution better than 0.1 nm.

A typical AFM based force spectroscopic experiment is depicted in Fig. 2B. Most frequently the probe is mounted on a soft cantilever, which is used as a bending sensor to determine the force exerted between the tip and the sample. In the case of soft samples or elastic and plastic deformation of the sample, a deviation from the linear slope of the force-displacement curve (3 and 4) can be measured, which directly provides access to the mechanical properties of the material itself.

By performing a raster-like array of measurements property maps can be generated both by means of DSI and AFM spectroscopy. This raster-scanning can be combined with very shallow indentation experiments by superimposing an oscillatory force over the normal load signal. These so-called dynamic mechanical analysis (nano-DMA) measurements significantly reduce the measurement time compared to the quasistatic mapping approach, where single indentation measurements are performed for each data point, but simultaneously reduce the mapped area to the XY scan range of the instrument. In addition to the indentation moduli and hardness information obtained from quasistatic measurements, this technique allows the determination of storage, loss and complex modulus, as well as $\tan \delta$ values and their spatial distribution over the mapped area.

These measurements can be performed also in liquid environments, such that biological samples can be investigated in their natural condition (living cells, biomembranes without dehydration, etc.).²² Furthermore, repeated indentation experiments can be carried out to investigate changes of the sample properties in a time-resolved fashion.²³ With these possibilities suitable tools are at hand to study the mechanical properties on the micro- and even nanometer scale and several examples can be found in the literature where these techniques were applied to study biological materials. However, these materials pose special limitations and requirements on the measurements due to the demanding mechanical properties of soft materials. While depth-sensing indentation was originally designed for the characterization of hard materials in the last decade, the

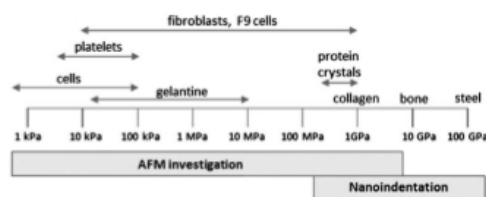


Fig. 3 Summary of the Young's moduli for different biomaterials in comparison to steel. Next to a remarkable range of different hardnesses considerable differences are also found within cells. Adapted from ref. 24 with permission from Elsevier.

field is also moving into the direction of softer materials. Fig. 3 summarizes the Young's moduli of different biomaterials²⁴ and it is evident that most biomaterials are representatives of soft and even very soft materials. This fact requires the understanding and integration of shortcomings of the nano-indentation method, *e.g.*, regarding the nonlinear material behavior. These have to be integrated into the data analysis models. These are highlighted in the works of Oyen and Cook^{25–27} and have been recently reviewed by Franke *et al.*²⁸ In particular, effects of, *i.e.*, viscous flow and/or creep and adhesion have to be taken into account. These uncertainties can be seen as a major reason why DSI of biomaterials is still a non-standard tool in materials research.

Essential for the interpretation of the force–displacement curves, both in depth-sensing indentation as well as in the AFM based studies, is the choice of a proper model system to calculate the respective mechanical properties. Depending on the utilized tips as well as on the overall properties of the sample systems a proper model has to be chosen taking into account several considerations. A summary of the most commonly utilized analysis model is presented in Table 1.

In some cases adaptations are made to these models or data evaluation is performed with complementary analysis routines to carefully evaluate the obtained results.³³ Finite element analysis is additionally used to understand and describe the tip–sample interaction.³⁴ For a more detailed view on the

different analysis techniques the reader is referred to the literature.²¹

Probing biomaterials by nanoindentation

In the literature there are a number of examples where depth-sensing indentation has been applied to study the mechanical behavior of biological samples and biomaterials. These include, *e.g.*, the mapping of the mechanical properties of tooth enamel and dentin,^{35–38} the behavior of tissue in the direct proximity of a dental implant or the mapping of the dentin–enamel junction in human teeth.³⁹ Many researchers have used different indentation approaches to measure the mechanical properties of biomaterials at different length scales. Examples are highlighted, *e.g.*, in an overview provided by Thurner,¹³ who summarized the results of several clinical studies on the indentation of human and animal bone. Furthermore, fruit seeds,¹⁷ nacre,^{40,41} insect cuticles,^{41–44} gecko seta,⁴⁵ fish scales,⁴⁶ shells,^{47,48} bovine hoof wall,^{41,43} sclera,⁴⁹ hair,⁴⁹ bone,^{50–53} shark teeth⁵⁴ and mineralized tissue⁵⁵ and cartilage⁵⁶ were studied by depth-sensing indentation techniques.

Depth-sensing indentation on bone samples

Bone is regarded as a complex material with hierarchical organization on different length scales. Several examples are found for the mechanical testing of human and animal bone by indentation of different length scales,^{14,57–60} as well as the combination with other complementary techniques, such as μ CT,^{61–63} Raman micro-spectroscopy,^{23,39,64} SEM⁶⁵ or conventional mechanical testing. Budyn and Hoc⁶⁶ developed a multiscale method using 3-point bending, modeling and optical microscopy approaches to determine the tensile strength at the millimeter scale, the stress field in the tens to hundreds of microns scale and the crack growth at the micron scale.

Srinivasan *et al.* compared nanoindenter-based moduli images with strain elastograms of thin slices of tissue-mimicking phantoms.⁶⁷ Beef slices, canine prostates, ovine kidneys and breast cancers grown in mice were used to demonstrate the qualitative correspondence between modulus images and strain elastograms. Experiments on real tissue

Table 1 Summary of the most common analysis models utilized in DSI and AFM spectroscopy

Model	Equations	Applications/limitations
Hertz ²⁹	$P = \frac{4}{3} E^* \sqrt{R} h_c^{\frac{3}{2}}, \frac{1}{E^*} = \frac{1 - \nu_1^2}{E_1} + \frac{1 - \nu_2^2}{E_2}, E^*:$ reduced modulus, h_c : indentation depth, R : radius of the tip	Only elastic deformation of the sample
Oliver and Pharr ³⁰	$P = \frac{2}{\pi} E^* h_c^2 \tan \alpha, \alpha:$ cone angle of the indenter tip	Predominantly elastic unloading; no adhesion or friction
Johnson–Kendall–Roberts ³¹	$P = P_1 - P_A, P_A:$ adhesion force $P = \frac{4}{3} E^* \frac{a^3}{R} - \sqrt{8\pi a^3 2\gamma E^*}, a:$ contact radius of the tip	Adhesion only in the area of contact; soft materials; large radius
Derjaguin–Muller–Topov ³²	$P = \frac{4}{3} E^* \frac{a^3}{R} - 4\pi R \Delta\gamma, \Delta\gamma:$ surface energy of both materials in contact	Adhesion just slightly outside of contact; small contact radius; rigid materials

slices showed a decrease in the correlation of both methods, possibly due to additional confounding factors such as time-dependent mechanical properties and geometrical distortions in the tissue during imaging. Also anisotropies of the material itself have to be taken into account frequently. This counts in particular for the directional organization of the bone tissue, which has to be controlled, by defining the cutting direction (parallel or perpendicular to the lamellar structure of the collagen fibrils). This anisotropy of the bone tissue⁶⁸ is also addressed and modeled in terms of indentation measurements by Fan *et al.*,⁶⁹ Carnelli *et al.*⁷⁰ and Chevalier *et al.*⁷¹ Bone is inherently a material with a complex hierarchical architecture. Haversian systems or 'osteons' are cylindrical structures, formed by bone lamellae, which make up the major part of human cortical bone. Despite their early discovery, their mechanical properties are still only poorly understood. Faingold *et al.* recently investigated the Young's modulus of individual lamellae around a single bone osteon.⁷² The authors measured three orthogonal planes utilizing dynamic nano-indentation. Perpendicular to the osteon axis the lamella closest to the canal showed the highest modulus compared to the other lamellae. These differences were not observed in measurement planes parallel to the osteon axis, but an asymmetry in the modulus was found on opposing sides of the canal. These findings support the rotated plywood structure model of bone lamellae. Reisinger *et al.*, however, reported on an approach to measure indentations in three planes on a single osteon too.⁷³ The authors found anisotropic mechanical properties with a preferential alignment of the stiffness along the axial direction with a small helical winding around the osteon axis. The authors claim that these findings do not comply with the commonly accepted models of compact bone microstructures.

Besides the investigation of the structural anisotropies, fundamental studies of the structural and microelastic properties during bone development and aging have been studied.

Feng *et al.* investigated the development of bone by indentation and found that the mechanical hardening of the bone material proceeds at different rates for different microstructural components of the bone.⁷⁴ Porcine femoral cortical bone was investigated under hydrated conditions. Samples from three different age groups ranging from 6 to 42 months were investigated as representatives of young up to mature animals. Longitudinal as well as transverse cross-sectional surfaces were tested and the elastic modulus and hardness of lamellae within the bone structure were determined. Within the sample system the hardness as well as the elastic moduli increased, whereby the individual microstructures showed different increases. In general the longitudinal moduli were higher than the transverse ones.

Pathak *et al.* utilized the dynamic indentation technique (nano-DMA) to investigate the viscoelastic properties of hydrated bone samples at lamellar length scales in a 'frequency-sweep' mode.⁷⁵ The probe is oscillated at different frequencies while being scanned over the sample in a raster like fashion.⁷⁶ The resulting amplitude, displacement amplitude and the phase lag are analyzed to calculate the loss modulus, the storage modulus as well as $\tan \delta$. They

investigated two different inbred mouse strains regarding their viscoelastic properties. The authors normalized for the anatomical location relative to the biological growth patterns (Fig. 4) in the anteromedial cortex and found that bone tissue from samples known to have a lower mineral-to-matrix ratio show a higher viscoelastic response. Newer bone regions with higher collagen content, located closer to the endosteal edge of the anteromedial cortex, also showed a trend towards a larger viscoelastic response. The authors discussed moreover the possibility to study the porosity of wet hydrated samples. This work is also expected to have an impact on other sample systems, *i.e.*, to readily correlate details of local porosity (*e.g.*, osteocyte lacunae, primary vascular canals, Haversian canals) and local tissue behavior in order to study the effects of aging and diseases on (non-)dehydrated specimens.

All these investigations have in common that only sample specimens are measured disconnected from the living organism. Hansma *et al.* developed an indentation device for the direct *in vivo* measurements of bone.^{77–79} Here, the mechanical probe head, in the form of a syringe needle, is driven through the skin onto the bone. Then, the actual indentation stylus is pressed in the bone tissue through the channel of the needle. The goal of this research is the development of a prediction model to estimate bone failure risk as a method for the early diagnosis and monitoring of osteoporosis, based solely on the mechanical properties of the bone. Osteoporosis significantly alters the structure of the bone material. Common diagnostic tools require the presence of a certain amount of decay (approximately 30% of bone loss) before osteoporosis can be accurately diagnosed. DSI would present an alternative with the appealing possibility to detect small areas in which decay of the bone mineral density starts at an early stage of disease progression. Osteoporosis significantly alters the structure of the bone material. Fan *et al.* studied the changes of the mechanical properties of bone tissue from children with type III Osteogenesis Imperfecta.⁶⁹ In contrast to normal bone tissue the samples showed more isotropic material properties. The deformation of the samples during DSI was observed to be similar to those of normal adult bone based on the ratio of modulus to hardness.

Tjhia *et al.* investigated atypical fractures of patients on long term bisphosphonate therapy, a frequently applied treatment for osteoporosis patients.⁸⁰ It is generally observed that the type, fashion and sites of bone fracture are different from the usually

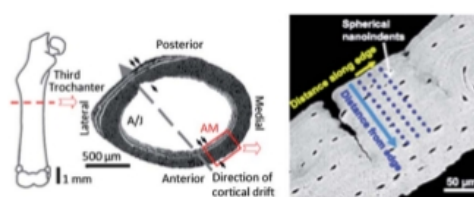


Fig. 4 Sample preparation for DSI measurements of a mouse bone sample. The indents are placed on the surface perpendicular to the orientation of the tissue fibrils. Reprinted from ref. 75 with permission from Elsevier.

observed fractures caused by osteoporosis. A comparative study including fracture samples from patients with severely suppressed bone turnover (SSBT) associated with long-term bisphosphonate therapy, age-matched treatment-naïve osteoporotic patients with vertebral fracture, age-matched normals and young normals was performed. The authors found only different plastic deformation resistances for cortical bone by DSI within the four groups with the highest resistance found in the SSBT group whereas other mechanical parameters did not change. The latter group also showed harder trabecular bone compared to the other groups, stiffer bone compared to the osteoporotic and young normal groups, and a trend of higher mineral density compared to the age-matched normal and osteoporotic groups. Lower heterogeneity of modulus and contact hardness for cortical bone of the SSBT and trabecular bone of the osteoporotic fracture groups, respectively, compared to the non-fractured groups, may contribute to fracture susceptibility due to a lowered ability to prevent crack propagation. In a later study the authors investigated the relationship between the mineral content and mechanical properties.⁸¹ They found differences between the fracture and the normal group as well as between the young and old normal group. The observed atypical fractures were suspected to be caused by changes of the microstructural material properties and tissue level mineralization compared to osteoporotic patients with vertebral fracture and the normal subjects, respectively. The authors suggest that the tissue level bone quality might be an important factor in fracture risk.

Besides the structural features the overall development of the bone material is of fundamental importance also with respect to the healing of bone fractures (for a general overview on biological and synthetic self-healing systems see ref. 82). The extent to which stability is regained after injury strongly depends on the tissue formed during the healing process. Leong and Morgan utilized DSI at multiple locations across a thin, longitudinal section of a rat fracture callus 35 days post fracture.⁸³ The indentation moduli varied over three orders of magnitude and variations could be related to the presence of different tissue types: granulation tissue, chondroid tissue and woven bone. The identified areas were subsequently stained to determine the mineral content of the tissue. The authors found a positive correlation between the staining intensity and the indentation modulus in woven bone. Additionally, they found an increasing indentation modulus along the periosteal aspect of the cortex for woven bone.

DSI on dental samples

Another natural system which represents an important biomedical materials class is the natural tooth. It shows, *e.g.*, an extreme hardness, excellent wear resistance, antifatigue, and crack resistant abilities. Understanding of the individual properties as well as a detailed investigation on the architecture, chemical composition as well as on factors diminishing the performance of the tooth material is of tremendous importance. Similar to bone, also in teeth a hierarchical structure in the material's architecture is found. DSI and AFM studies have

been extensively employed to investigate the features of the tooth material. Balooch *et al.*³⁵ determined the material properties at different locations on a tooth sample and investigated the characteristic changes of the hardness and elastic moduli, when crossing, *e.g.*, the dentin–enamel junction (DEJ) (Fig. 5).

Studies performed, *e.g.*, by Braly *et al.* investigate the gradual change of the mechanical properties of human molar enamel.⁸⁴ Their study was motivated by reports that the hardness and Young's modulus decrease by more than 50% when moving from the occlusal surface to the dentin–enamel junction on cross-sectional samples. Among other possible reasons the hydroxyapatite prism orientation was suspected, thus, the authors performed DSI tests at two different orientations relative to the prisms. The experiments showed only very small differences within a single sample volume and it was concluded that changes in the local chemistry, the degree of mineralization, organic matter and water content, as well as changes in the microstructure (differences in the volume fraction of inorganic crystals and organic matrix) are responsible for the local variation of the hardness parameters rather than the prism orientation itself.

Darnell *et al.* studied the inhomogeneity of the enamel on axial cross-sections of an unworn permanent third molar, a worn permanent first molar and a worn deciduous first molar of *Alouatta palliata*.⁸⁵ The hardness and Young's modulus varied with location throughout the cross-sections from the occlusal surface to the dentin–enamel junctions, from the buccal to lingual sides and also from one tooth to another. The mechanical changes were correlated with changes in the organic content which varied between 6 and 20% close to the dentin–enamel junction.

In particular the soft region right below the dentin–enamel junction is suspected to play an important role in tooth function, strain distribution and fracture resistance during chewing.

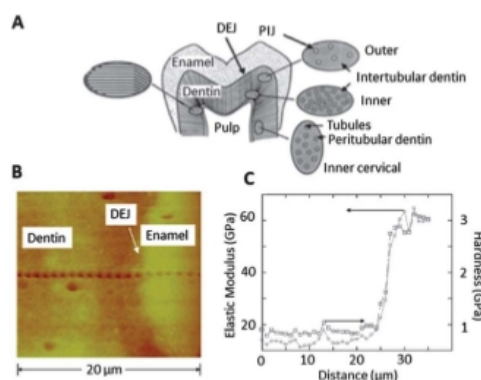


Fig. 5 (A) Schematic representation of the architecture of tooth with important interfaces being highlighted. (B) AFM topography image of indentations performed across the dentin–enamel junction (DEJ). (C) Corresponding elastic moduli and hardnesses found for the different locations across the junction. Reprinted from ref. 35 with the permission of Elsevier.

Brauer *et al.* tried to relate the asymmetry in mechanical properties with tooth function. A similar asymmetry like the one found for the enamel is also found in the softer dentin region.⁸⁶ The authors investigated the buccal and lingual side of extracted teeth using micro- and nanoindentation. The influence of the surface and dentin depth was measured from the dentin–enamel junction in crown dentin and from the cementum–dentin junction (CDJ) in root dentin. Coronal dentin presented a higher elastic modulus and hardness on the lingual side of the teeth for all measurements, whereas root dentin was harder on the buccal side, an effect which might be ascribed to the compensatory functions of both tooth sides.

Also other important properties of teeth can be assessed by DSI experiments, *e.g.*, viscoelastic properties can be studied by creep measurements.

He *et al.* applied long loading times to investigate the creep behavior of human enamel. The authors succeeded in determining the indentation creep rate sensitivity and could demonstrate the viscoelastic and viscoplastic behavior of the enamel.⁷⁹ Therefore, the authors performed indentation experiments using a Berkovich indenter in a one-step loading and unloading approach. A constant hold time at maximum load, as well as at minimum load during unloading was introduced. The indentation creep at maximum load and the creep recovery at the minimum load were extracted and could be fitted to a double-exponential function which was compared to classic viscoelastic models. These results are of special interest as they can serve as an explanation for the excellent wear and crack resistance of natural tooth structures. The enamel may inelastically deform in case of the entrapment of particulates between teeth under functional loading and sliding wear conditions, but can recover after its release.

A similar investigation was performed by Schneider *et al.* The authors tried to interpret the creep during indentation of the enamel by a model which considers the basic shape of the apatite crystallites and describes the thin protein layer in between the crystals as a viscous fluid.⁸⁷ This allowed determining the main flow plane in the anisotropic enamel as well as a study of the influence of the volume fraction of the apatite crystals.

Degenerative processes frequently impair the properties of teeth. These can be related to mechanical defects, the chemical environment or due to diseases.

He *et al.* investigated the demineralization of the cervical region of human teeth in the development of a non-carious cervical lesion.⁸⁸ The authors included nanoindentation as well as electron microscopy to study the demineralization process in a solution of pH 4.5 for 1 and 2 days, respectively. DSI experiments were performed at the cementum–enamel junction with a lateral spacing of 30 μm and a mechanical property map was obtained. The authors observed a dramatic degeneration of the mechanical properties by $\sim 50\%$ and $\sim 90\%$ at the junction and SEM and optical imaging could reveal the artificial demineralization in typical zones of the enamel close to the cementum–enamel junction (Fig. 6). After 2 days, moreover, the demineralization also penetrated the sound enamel at the junction and the dentin beneath was undermined. This could

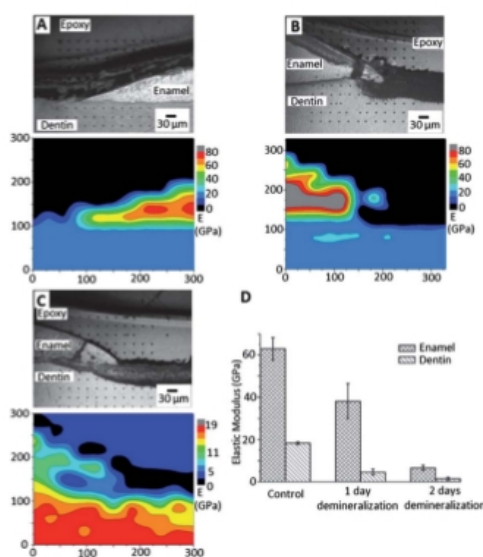


Fig. 6 Light microscopy (top) and elasticity contour maps obtained in the area of the cementum–enamel junction (CEJ). (A) Control sample, (B) sample after 1 day of demineralization in acid and (C) after 2 days of demineralization. After one day the surface of the enamel and root dentin were demineralized. After 2 days a heavy demineralization of the enamel near the CEJ and the adjacent dentin was observed. The overall mechanical performance significantly decreased. Reprinted from ref. 88 with permission from Elsevier.

compromise the mechanical properties of the teeth in such a way that even toothbrush abrasion could produce non-carious cervical lesions.

Barbour *et al.* investigated the dissolution process of the enamel in a time dependent fashion and could deduce a model for the process.^{89,90} Compared to the untreated enamel the authors found a change in the enamel hardness after only 120 s and a change of the elastic modulus at 300 s exposure to citric acid solutions. The rate of change of both measures decreases with increasing exposure time due to a diffusion-limited dissolution process.

Cosmetical and restorative dental indications are increasingly performed. Also in this respect the influence of the applied treatments as well as the associated changes in material properties as well as on the micromechanical performance is of utmost importance. This certainly applies also to interfaces, *e.g.*, created during the repair of defects by filling materials *etc.* Nanoindentation was also used to study the influence of bleaching agents on the properties of human premolars.⁹¹ Despite the fact that bleaching is a popular cosmetic means, the impact of the bleaching agent, which contains 30% hydrogen peroxide, on the mechanical properties of the enamel is largely unknown. Harul Nizam *et al.* compared the Young's modulus and hardness before and after bleaching on sliced enamel as well as on dentin and care was taken to perform nanoindentation measurements in the same sample region.

Significant differences in the hardness and Young's modulus of the control enamel were found. Even though the mechanism of property degradation is not yet known the authors could reveal an undermining effect on the nanomechanical properties of the teeth by the hydrogen peroxide.

For the durability of tooth fillings and replacements the contact mechanical properties of the enamel biocomposite are of special importance. He and Swain investigated the mechanical response of enamel with dental-used metals.⁹² The authors compared cast alloy, gold alloy, titanium and amalgam and compared them to a pure hydroxyapatite as a ceramic analogue of enamel. It is suggested from this study that metallic-like dental restorative materials are a better choice for tooth fillings, to sustain the severe cyclic contact behavior experienced and to protect the opposing teeth from damages due to their similar properties compared to enamel.

A recent example investigated by our group is the study of dental implant materials.⁹³ The sample specimens consist of a methacrylate-based polymer matrix with a calcium phosphate (TCP) filler. DSI measurements were performed in a grid-like fashion. Based on this dataset a contour map is generated by nearest-neighbor-interpolation, spatially displaying the mechanical properties of the indented area. The result is a map of the mechanical properties (Fig. 7B), which shows good correlation with the optical image and, therefore, allows for the identification of the TCP-rich phases of the material, which are present in the darker areas of the optical image. Each of the datapoints is associated with a corresponding indentation curve, which has a characteristic shape in the different domains, shown in Fig. 7C.

This property map also allows for a rough estimation of the domain size of the composite material.

When trying to generate such property maps care has to be taken to not place the individual indents in too close proximity

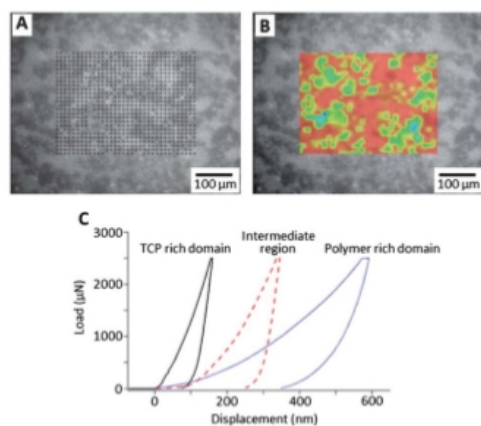


Fig. 7 Optical image of a TCP/polymer microcomposite with (A) valid indentation measurement points, (B) interpolated modulus-heatmap. (C) Typical indentation curves from TCP-rich, polymer-rich and intermediate regions.

to each other, as each measurement usually plastically deforms the surface around itself. The actual stress field of the indentation experiment is several times larger than the residual imprint of the surface and spreads out radially from the point of measurement.

When testing a biphasic material with small domains, the size of the indentation may cover not only one phase at a time, resulting in a combined modulus of a "homogenized" material with properties from both phases. For example when using a Berkovich tip, the material probed in a single indent is roughly a volume of three times the indentation depth. These issues have been addressed in detail by Constantinides *et al.*⁹⁴

The critical part of the data processing is in particular the analysis process. In general, DSI data have to be handled with care due to a manifold of obstacles which have to be taken into account. Zhou *et al.* discussed the effects of the DSI conditions with respect to the indent depth on the enamel.⁹⁵ The authors found that in a depth range from 100 to 2000 nm the elastic moduli continuously decreased from approximately 104 to 70 GPa and the hardness respectively from 5.7 to 3.6 GPa. The authors applied a model for fiber-reinforced composites to quantify the upper and lower values of the elastic moduli. As a result similar hardness and moduli compared to the literature were obtained. Thus, the authors could attribute the dependence of the hardness and modulus as an effect of the nanoindenter tip.

Ang *et al.* utilized nanoindentation to investigate the elastic/plastic deformations of human enamel on the length scale of several hundreds of hydroxyapatite crystallites within one enamel rod.⁹⁶ An indentation yield point of 1.5 GPa and 0.6% strain was preset and it was found that the corresponding indentation depth is limited to only 7 nm. Due to this special situation the authors specifically mention the necessity to calibrate the indenter tip particularly for this region to be able to extract meaningful elastic moduli from the penetration curves by applying the Hertz model.

Sadr *et al.* applied nanoindentation on typical dental adhesives.⁹⁷ These systems showed a strong viscoelastic behavior and the authors compare different fitting algorithms to determine the mechanical properties. They highlight explicitly that the standard models integrated in the instrument's software were not able to determine the modulus values correctly and overestimated them up to 2.5 times due to the time-dependent material properties, which were not implemented in standard analysis routines. The load-displacement curves were fitted to obtain best fit parameters for a generalized Kelvin viscoelastic model, from which creep compliance and Young's modulus were calculated.

DSI on soft biomaterials

While bone and enamel represent relatively hard materials, much softer biomaterials can also be investigated by means of depth-sensing indentation. However, the number of reports on soft tissue is rather limited. In general it can be observed that the uncertainties and additional aspects which have to be taken into account gradually emerge if softer sample systems are investigated.

Ebenstein and Pruitt discussed in particular the challenges associated with DSI of soft biological samples.⁹⁸ The authors introduced practical solutions and considerations on an agarose gel, serving as a model system. They developed a hydration system which allows maintenance of hydration for more than 8 h, suggested the utilization of a 100 μm conical tip and demonstrated the efficient alignment procedure on the backlight-illuminated agarose gel. The authors point out that such agarose gels exhibit similar properties to soft biological tissues, *i.e.* vascular tissue.

The importance of verifying experimental results obtained by DSI is discussed in the study of Akhtar *et al.*⁹⁹ The authors utilized spatially resolved nanoindentation mapping to investigate 5 mm thick sections of ferret aorta and vena cava and to determine the histological distribution of fluorescent fibers within the tissue sections. An extended Oliver and Pharr method was used to minimize the substrate's effect on the mechanical properties of the tissue and the results were correlated with hematoxylin and eosin stained samples. As a result a clear correlation of the tissue stiffness related to the elastic fiber density could be obtained. They found a progressive decrease of the elastic modulus from the adventitial (outermost) to the intimal (innermost) layer whereas for vena cava a generally high elastic modulus was observed across the complete section with a decrease of the elastic modulus in the highly cellularized medial layer in the center of the structure (Fig. 8).

This decrease was inversely correlated with the elastic fiber density of the extracellular matrix-rich regions of the vena cava. The mechanical properties of dynamic and compliant tissues, *i.e.* large blood vessels, have an important impact on the tissue function, morbidity and mortality; *e.g.* the *in vivo* gross arterial stiffness increases with age, but also with cardiovascular risk factors, *i.e.*, hypertension, diabetes mellitus and end-stage renal failure. This increase in stiffness is also an issue for the storage of arterial tissue. DSI was utilized by Hemmasizadeh *et al.* to evaluate the common cold storage practice for arterial tissues, which represents an essential step in various clinical and experimental processes.¹⁰⁰ Such cold storage techniques have significant effects on the post-cryosurgical or post-

cryopreservation mechanical behavior of arteries. The authors utilized a custom-made nanoindentation device to measure changes to the local viscoelastic properties of porcine thoracic aorta wall at three common storage temperatures. They found a clear preference for the storage at $-80\text{ }^{\circ}\text{C}$, since in these samples no significant alteration of the instantaneous Young's modulus and their permanent average relaxation amplitude was found.

Huang *et al.*¹⁰¹ recently studied the process of myelination by DSI. This process represents an important step in the development and regeneration of the nervous system with tremendous importance for the transmission of nerve impulses and, thus, also for the healing of the nervous system, *e.g.*, after central or peripheral injuries. The development of a set of factors that influence the myelination process could be furthermore the key in also treating demyelinating diseases such as the Guillain-Barré syndrome or multiple sclerosis. The authors investigated co-cultures of Schwann cells and PCL2 cells from a rat pheochromocytoma cell line after different times of cultivation by *in vivo* indentation of a multilayered myelin sheath structure. The authors observed three different stages of development, which are associated with different mechanical properties of the myelin sheaths. Utilizing this approach the authors introduced DSI as a suitable investigation tool to access the myelination process.

The transport of drugs and genes through the skin's outer layer (stratum corneum (SC)) into the underlying abundant immunologically sensitive viable epidermal cells is a crucial point in the development of vaccines and drug delivery systems. Kendall *et al.* utilized a modified nanoindenter setup with customized tungsten tips of different nominal diameters of 5 and 2 μm respectively, to study the mechanical properties of fresh mammalian skin and quantified these properties.¹⁰² The authors determined the Young's modulus, storage modulus and stress at different indentation depths through the SC and the viable epidermis of freshly excised murine skin by continuous stiffness measurements (CSM). Different indentation velocities resulted in characteristic storage modulus plots, which show significant differences in the utilized tip shape (Fig. 9).

The different characteristic storage moduli obtained by the different indentation tips were interpreted as model experiments that allowed simulating two essential drug delivery mechanisms: the micro-nanoprojection patch and ballistic delivery.

Yang *et al.* investigated the nanomechanical changes of cholesterol-depleted and -restored cell membranes by DSI.¹⁰³ Cholesterol is known to be a major component of eukaryotic cell membranes and the depletion of the cholesterol content triggers a complex cascade of biochemical reactions which influence cell processes. The authors performed DSI on the lamellipodium of adherent NIH-3T3 fibroblasts with normal, depleted and restored cholesterol contents. They extracted the contact stiffness of the cells by utilizing the DMC mode and performed indentation tests with a depth of 20 nm. An exponential decay with the cholesterol depletion time resulted in a decrease of the cell stiffness. On the other hand a different kinetics was observed for the cholesterol restoration process;

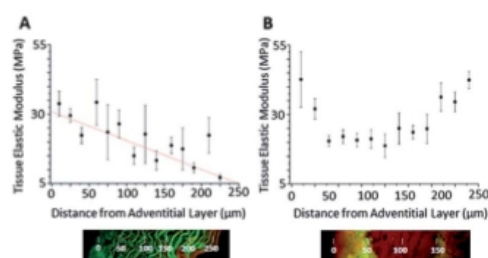


Fig. 8 Elastic modulus of (A) ferret aorta and (B) vena cava. The elastic moduli are determined as a function of the distance from the adventitial region of the tissue. Nanoindentation results (top) are correlated with hematoxylin and eosin stained histological investigation by fluorescence microscopy (bottom). Reprinted from ref. 99 with permission from Materials Research Society/Cambridge Journals.

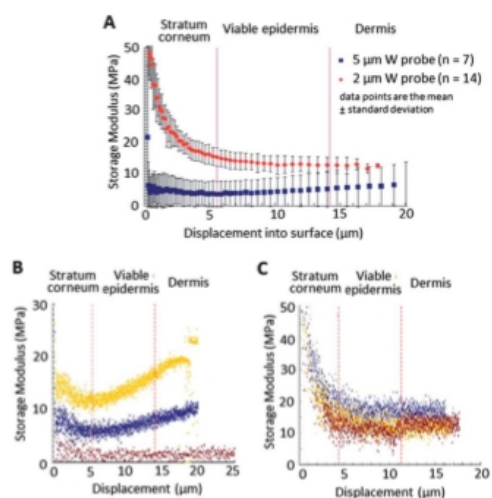


Fig. 9 Storage moduli as a function of the displacement measured with microprobe indenter tips into murine ears. (A) Comparison of the characteristic storage moduli obtained with tips of 5 μm and 2 μm probes. Selected storage moduli raw data curves obtained with (B) a 5 μm tip (lower, upper and near average curves) and (C) 2 μm tip. Reprinted from ref. 102 with permission from Elsevier.

nonetheless, it could be demonstrated that restoration reverses the effect of cholesterol depletion both on the cellular morphology as well as on the membrane stiffness. The authors moreover compared the obtained results with accompanying AFM measurements and found a good correlation of the Young's modulus and the contact stiffness measurements.

As can be seen from the large number of different examples, depth-sensing indentation is still a method which is mainly employed for the investigation of relatively hard sample systems. The selected examples highlight the diversity of fundamental studies that can be performed to relate different aspects, like aging, degradation, influence of environment on material properties, *etc.*, to the micro- and nanomechanical performance. Next to the micro- and nanomechanical properties functional design concepts can also be elucidated by nanoindentation. AFM can also address investigation of the mechanical properties of much softer materials. Illustrative examples of this investigation technique and the information accessible are summarized in the next paragraphs.

Probing mechanical material properties by AFM spectroscopy and force volume mapping

In general for AFM spectroscopy and force volume mapping a much higher lateral resolution at lower force loads can be applied. This allows measurements down to the scale of individual molecules, as exemplified by different groups investigating the structure and stretching characteristics of DNA, RNA, proteins, *etc.* and to map the interaction and adhesion of biomaterials on substrates.^{104,105} This approach can also be used

to investigate protein misfolding and aggregation which are the very first and critical steps in development of various neurodegenerative disorders, including Parkinson's disease induced by misfolding of alpha-synuclein.^{40,41} However, these are special applications which are beyond the scope of this review article. Therefore, we only refer here to a number of review articles which summarize recent developments in this field.^{106–108} The focus of this review is placed on the discussion of micro- and nanomechanical as well as viscoelastic property maps. The range of materials that can be investigated covers also softer materials, including membranes, hydrogels and soft (bio-) polymers due to the higher force resolution that can be obtained by AFM spectroscopic methods. This makes AFM based elasticity measurement a very attractive tool for biological sample systems and the range of applications in the literature is very broad. A few representative examples are highlighted here.

In general AFM based studies can be divided into an indentation-type microsphere approach and a pure AFM tip based approach. To avoid complicated fitting models, which would be required for commercially available pyramidal shaped AFM tips, several studies follow an approach which utilizes AFM cantilevers that are facilitated with glass spheres used as the actual probe head. Cantilevers with different sphere diameters are commercially available. For example a tip with a 5 μm sphere on a 0.06 N m⁻¹ cantilever can detect sample shear moduli between 100 Pa and 50 kPa. Spherical glass tips ranging from 0.6 to 12 μm diameter and spring constants from 0.01 to 0.58 N m⁻¹ are available. The tip characteristics of course also determine the indentation characteristics. A 5 μm tip provides a theoretical contact area between the tip and tissue of about 5 to 9 μm² for 400 to 700 nm indentation depth. Smaller or larger tips can be used to provide smaller or larger scales of spatial resolution. Also pyramidal tips have been used in AFM indentation,^{109–112} providing in general smaller contact areas and, thus, increasing spatial resolution in mapping; however, data fitting is more complex for this tip geometry. AFM elasticity measurements performed with pyramidal tips can yield elasticities 2 to 3 fold larger than spherical tips, an effect which is attributed to the larger contact area of spherical tips.¹¹³ Thus, a careful choice of the model for the evaluation of mechanical properties will be required. Measured force–displacement curves can be fitted with, *e.g.*, the Bilodeau model¹¹⁴ to calculate the apparent Young's modulus of indented samples. These improvements have led to a strong research activity in the field of biomaterials being investigated by AFM related techniques and several methods can be utilized to obtain information on the degeneration, function of biological tissue and cells as well as provide information on characteristic changes of cell stiffness related to diseases.

AFM based micro- and nanoindentation on cartilage

The pathological changes in osteoarthritis – a degenerative joint disease prevalent among older people – start at the molecular scale and spread to the higher levels of the architecture of articular cartilage to cause progressive and irreversible structural and functional damage.

Stolz *et al.* investigated the properties of articular cartilage and found a scale dependent dynamic stiffness by indentation-type atomic force microscopy.^{115,116} Utilization of micrometer-sized spherical tips revealed a unimodal microstiffness distribution, whereas indentations performed with a nanometer-sized pyramidal tip resulted in a bimodal distribution of the nanostiffness. The authors interpreted the presence of the bimodal character of the nanostiffness as a result of the cartilage's soft proteoglycan gel which is first compressed, whereas the higher stiffness value results from the deformation of the collagen fibrils. They verified this interpretation by an additional study of a gel-microfiber composite.¹¹⁶ Both sample systems revealed the same characteristics and the authors propose to utilize the nanostiffness as a new biomarker to analyze structure–function relationships in normal, diseased, and engineered cartilage. Measurements of the cartilage samples revealed a digestion of, *e.g.*, elastase following an enzyme action with a clearly lowered modulus of collagen in the micrometer scale, whereas the digestion of proteoglycans by Cathepsin D can be only monitored by a stiffening in the nanometer dimension. The authors applied the methodology also to reveal early changes of the structure and mechanical properties of normal aging and osteoarthritic articular cartilage in mice and patients.¹¹⁷ They suggest that their measurement approach will open the possibility to construct a simple nano-device as a clinical tool.

Darling *et al.* utilized stiffness mapping to investigate articular cartilage.¹¹⁸ In this sample system chondrocytes are surrounded by the pericellular matrix and the mechanical properties were *in situ* investigated to quantify the mechanical properties of the pericellular and extracellular matrix of human, porcine and murine articular cartilage. The authors quantified the microscale elastic moduli using stiffness mapping and force volume mapping (Fig. 10). The results obtained on the cartilage samples were in good agreement with studies of mechanically isolated chondrons and demonstrated that AFM stiffness mapping is a versatile tool to *in situ* determine microscale inhomogeneities in mechanical properties.

A recent review exclusively dealing with the investigation of the properties of cartilage assessed by different techniques including nanoindentation and AFM studies is presented by Han *et al.*¹¹⁹

Nanoindentation on dental samples

A similar micro- and nanomechanical analysis to that of enamel was performed using SEM and atomic force microscopy (AFM). Mechanical properties of dentin were characterized with respect to hardness and elasticity, utilizing nanoindentation with a modified AFM to elucidate further influences on the enamel material (Fig. 10). Transgenic mouse models which drive over-expression of an activated form of TGF- β 2 under the control of osteocalcin promoters were investigated by Saeki *et al.* to study the role of TGF- β 2 in the dental mesenchyme on the enamel formation.¹²⁰ The authors found that the elastic modulus of dentin measured with a modified AFM was significantly reduced in male transgenic mice. This was further associated

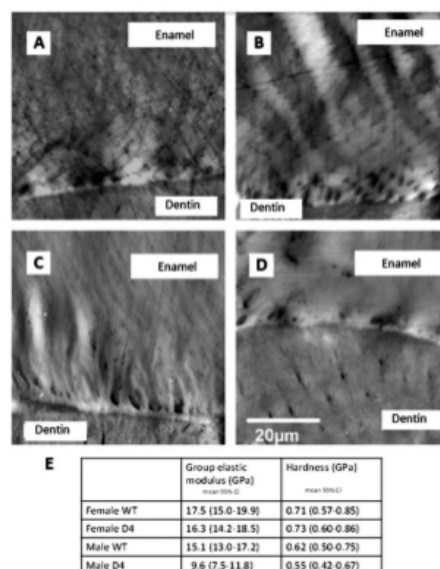


Fig. 10 AFM topographic images of the occlusal area of the enamel near the DEJ. (A) WT male, (B) D4 male, (C) WT female, and (D) D4 female. More pores were apparent in D4 male. (E) Table of the obtained elastic moduli and hardness in the individual test groups. Reprinted from ref. 120 with the permission of Elsevier.

with the presence of pores in the enamel. On the other hand no distinct differences were found in female mice. *In situ* hybridization of the continuously erupting incisor confirmed that osteocalcin expression was limited to the odontoblast cell layer at all stages of tooth formation.

Lippert *et al.* utilized AFM based nanoindentation to study the nanomechanical and structural properties of polished enamel samples to investigate the re-hardening of surface softened enamel *in vitro* by demineralization/remineralization cycles under physiologically relevant conditions.¹²¹ While the AFM studies could reveal a mineral deposition after remineralization of the softened enamel, no re-hardening of the enamel could be measured. The protective effect of the layer was also not observed. Exposure of the softened enamel samples to a remineralizing solution or mineral water led to an improved acid resistance. A significantly higher nanohardness of erosive enamel after the application of alginate and gum arabic polymers added to citric acid solutions was also observed by Beyer *et al.*¹²² As the results show the treated enamel regions generally exhibit a smoother surface compared to those treated with citric acid solutions alone. The authors hypothesized that the polymers possibly adsorb on the eroded enamel surface resulting in an increase of nanohardness.

Indentation experiments on cells

A very active field of research is the stiffness analysis of cells. This area promises new diagnostic tools which require a high

force sensitivity best obtained by AFM force mapping and force spectroscopy. Advantage is taken here of the fact that the spatial and temporal changes of the mechanical properties of living cells may reflect complex underlying physiological processes. Following these changes could provide valuable insight into the biological importance of cellular mechanics and its regulation. A central question to be addressed is how the stiffness variations within a tissue can be related to disease processes that result in tissue remodeling and how local mechanical properties of tissue vary across space and disease progression. For these measurements a spatial resolution in the scale relevant to resident cells is required.

Liu and Tschumperlin¹²³ reported on measurements of lung tissue, which is inherently highly compliant and elastic remodeling is a predominant feature in diseases such as asthma, emphysema, hypertension and fibrosis. A systematic sampling of tissue strips provided maps of mechanical properties of tissue that reveal local spatial variations in the shear modulus (Fig. 11). Correlations between the mechanical properties and the underlying anatomical and pathological features illustrate how stiffness varies with matrix deposition in fibrosis. Corresponding macro-scale measurements in normal and fibrotic lung tissue indicated an approximately 2 to 3 fold increase in elasticity for tissue with fibrosis, while AFM micro-indentation could demonstrate a strong increase in local tissue stiffening, with some regions exhibiting up to ~30 fold increase in the shear modulus compared to the average normal lung tissue.¹²⁴ The authors discuss important short-comings of the invasive character of the AFM as the lung architecture is altered due to the loss of the air-liquid interface, that normally exists in the air-filled lung, and the loss of pre-stress that maintains lung partial inflation upon relaxation of respiratory muscles. The

authors found that the median stiffness measured in the parenchyma of normal lung tissue does not differ substantially from estimates based on punch-indentation of intact lungs at resting volumes.

Dulińska *et al.* investigated the stiffness of human red blood cells (erythrocytes).^{125–127} The authors measured the Young's modulus of erythrocyte samples from patients with different diseases. It was found that pathological erythrocytes showed significantly higher stiffness values. The authors relate this increase in stiffness to possible changes in the structure of the cell cytoskeleton associated with the diseases.

An increase in the Young's modulus was also observed on other abnormal human blood cells from human subjects with the genotype for sickle cell trait.¹²⁸ The increase could be a direct result of the polymerization of sickle cell hemoglobin or of the mentioned changes in the cytoskeleton.

In contrast to the observed hardening of cells as a consequence of diseases, cancerous cells show a significant softening by a factor of four. An AFM study on living metastatic cancer cells taken from the lung, chest and abdominal cavities of patients demonstrated this effect. The results were in good agreement with earlier *in vitro* studies and also correlate well with established testing methods, such as antibody labeling. The cell softening is attributed to the ability of cancer cells to metastasize or to spread.¹²⁹ It is hoped that the characteristic mechanical signature of cancerous as well as of diseased cells will result in a useful and reliable tool to complement clinical settings. However, the field is still in its infancy and the reasons for characteristic changes are still not entirely clear. A crucial question will be if different influences can be reliably separated from each other.

Surface hydrated cells of *Staphylococcus epidermidis* were investigated by Méndez-Vilas *et al.*¹³⁰ The authors report on force measurements which were acquired on the surface of bacteria, which represent chemically as well as mechanically heterogeneous systems. The obtained different characteristic force curves were related to cell properties, sub-surface properties, and irreversible destruction of the surface. Also, oscillations in the retraction curve were related, e.g., to rupture phenomena within the multilayered cell wall architecture typical of Gram-positive bacteria such as *Staphylococcus epidermidis*, which results in irreversible surface damage. Volle *et al.* studied both elasticity and adhesion of environmental and laboratory strains of Gram-negative as well as Gram-positive bacteria by AFM force spectroscopy with a silicon nitride tip.¹³¹ These bacteria formed biofilms on glass surfaces which revealed different spring constants. The Gram-positive cells showed significantly larger spring constants and a depletion of the extension curve was observed to be correlated with the biomolecules present on the cell surface. Gram-negative strains with long lipopolysaccharides showed a larger nonlinear region than rough bacterial strains with shorter lipopolysaccharides. Additionally, differences of the adhesion of the cells to the tip were observed.

Wagh *et al.* studied the mechanism of lung epithelial wound healing.¹¹² This process progresses *via* cell spreading, migration of cells into the wounded area and, finally, cell proliferation. These studies were performed on bronchial epithelial cells

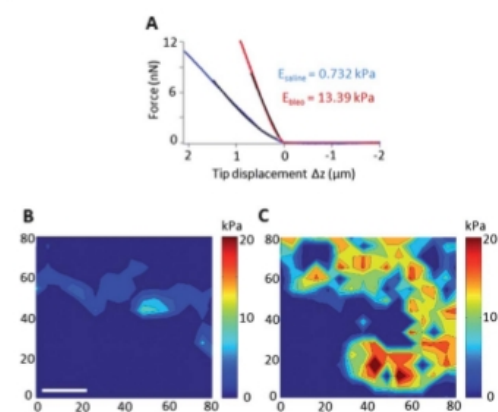


Fig. 11 (A) Representative force-displacement curves collected from saline (blue) and bleomycin-treated (red) mouse lung parenchyma, respectively. Black lines are the best fit resulting from the spherical Hertz model and are labeled with their corresponding calculated Young's moduli. (B and C) Elastographs from saline (B) and bleomycin-treated (C) mouse lung parenchyma depicting the shear moduli distribution. Scale bar: 20 μm . Reprinted from ref. 123.

(16HBE) after a scratch wound was applied. 2 h after scratching contact mode AFM measurements were performed. The authors identified different regions which exhibit characteristic elastic moduli around the wound edges. Far away from the scratch variations in the elastic modulus in specific cellular regions were observed with a median value averaged over several $1.5 \mu\text{m}$ square regions of $<5 \text{ kPa}$. Directly at the wound edge a reduced cell stiffness was observed within a distance of $5 \mu\text{m}$; at larger distances the cell stiffness decreases again. The authors concluded that cells near the wound edge undergo localized changes in their cellular stiffness, which might be a suitable trigger signal to initiate the spreading and migration of cells during the healing process. The success of cell-based tissue engineering approaches in restoring biological function will be facilitated by a comprehensive fundamental knowledge of the temporal evolution of the structure and properties of the newly synthesized tissue. Ludwig *et al.* addressed the effect that the function of cells strongly depends on their extracellular micro-environment that includes, *e.g.*, the stiffness and fiber orientation in the surrounding matrix. This will influence the cell adhesion as well as migration. The authors reviewed important contributions of AFM (elasticity mapping) and related techniques to investigate these effects.¹³² The understanding of the pericellular proteolytic activity and the adaptation of the migration behavior of the cells play a crucial role in many biological processes, *i.e.* tissue maintenance, wound repair and cancer cell invasion. To establish such functions the cell needs to be able to actively sense and remodel according to its surroundings.

The mobility of cells is usually a result of the interplay between lamellipodia and filopodia at their protrusion sites. The actin cytoskeleton rearranges during the movement from a highly branched short filamentous network to well aligned extended bundles from lamellipodia to filopodia, respectively. This process is regulated by the actin binding proteins VASP and fascin. Swei *et al.* utilized AFM to determine the Young's modulus of phalloidin stabilized comets grown under different conditions.¹³⁴ The authors found a linear increase in the Young's modulus for comets grown in the presence of fascin above a critical threshold and a decrease of the initial velocity of the comets. VASP and fascin, in combination, resulted in a stronger increase of the Young's modulus compared to only one of the two proteins, in particular for low concentrations.

Li and Logan measured the stickiness of bacteria by force curve spectroscopy and pointed out the crucial difficulties in defining the distance between the AFM tip and the surface of the bacterium.¹³⁵ This uncertainty derives from the elasticity of the bacterial surface and the resulting deformation during force imaging. The result of this deformation is a highly nonlinear contribution in the force–displacement curves. The authors studied three different bacteria samples of *Escherichia coli* which showed different sticking coefficients to glass. To calibrate these values measurements of packed bed flow through a column were performed. Sample analysis was performed by a gradient force curve analysis method and a model for the interactions between a colloidal probe and the surface was developed. The measured sticking coefficients could be directly

correlated with the length of the noncontact phase rather than with the properties of the other phases. The authors conclude that gradient analysis is a valuable tool for studying the effect of the length of the exopolymers on the cell surface to bacterial adhesion to glass surfaces.

Eaton *et al.* investigated the antimicrobial effect of different chitosan coatings on Gram-positive (*Staphylococcus aureus*) and Gram-negative (*Escherichia coli*) bacteria.¹³⁶ The authors utilized AFM measurements to study the antibacterial effect but also could verify the response strategies used by the bacteria. The cell walls tend to collapse and morphology changes reveal cell death; on the other hand clustering indicated a strategy for the bacteria to survive. Nanoindentation experiments revealed that besides small modifications observed in the Gram-positive samples, mechanical changes in the cell walls of the bacteria occurred.

Pericytes surround capillary endothelial cells and are able to exert contractile forces modulating microvascular tone and endothelial growth. The underlying mechanisms mediating adhesion-dependent shape changes and the contractile force transduction are still not entirely clear. Kotecki *et al.* utilized AFM nanoindentation to study the modulation of pericyte contraction by the neutral cysteine protease, calpain, and report on the cellular stiffening upon the application of talin, an integrin-binding and F-actin associating protein.¹³⁷ The effect is diminished when calpain-cleavage resistant mutant talin L432G or vinculin are expressed. Measurements performed with the cell-penetrating calpain-specific inhibitor CALPASTAT reverse the talin-enhanced contractility. The authors found that CALPASTAT but not its inactive mutant alters contractile cell-driven substrate deformations while increasing the mechanical stiffness of the subcellular contractile regions of these pericytes. The calpain-dependent cleavage of talin as a modulating trigger for the contractile dynamics was suggested to be involved in normal capillary function or microvascular pathophysiology.

Ross and Wuite utilized AFM based nanoindentation to study the mechanical properties of viruses.¹³³ They measured the Young's moduli of capsids, the maximal force viruses can withstand (Fig. 12) and explored the material fatigue in these nanosized objects. The authors specifically investigated prokaryotic (bacteriophages) as well as eukaryotic viruses. Moreover, they discussed the impact of internalized materials and the effect of alterations to the capsid proteins on the viruses' mechanical strength. Their studies are important, since viruses are now increasingly used as templates for constructing specific nanocontainers, *etc.*

These illustrative examples of applying nanoindentation and AFM mapping demonstrate the vast number of systems which can be investigated and show, moreover, the tremendous importance of understanding the micro- and nanomechanical properties of biomaterials with respect to biophysical and biochemical processes. Not only fundamental understanding, but also suitable ways to integrate new diagnostic tools represent extremely interesting means where both techniques can provide a valuable contribution – despite the still prevalent difficulties and obstacles. In particular, for soft and heterogeneous sample systems improvements and adaptations are still required on the route to standard integration and routine

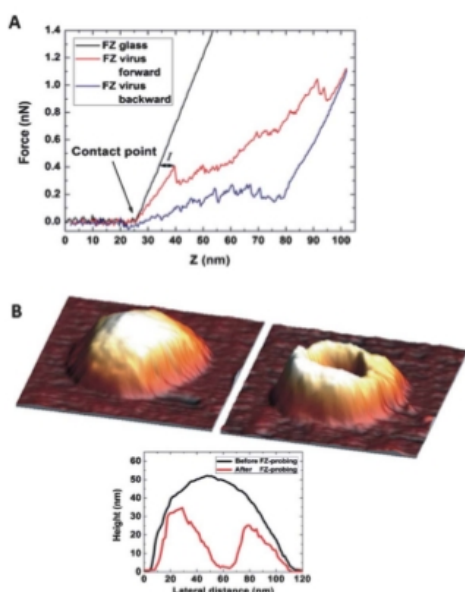


Fig. 12 (A) AFM indentation force–distance curves obtained on viral capsids. A single forward and backward scan on an empty bacteriophage capsid. At a relatively low force of 0.4 nN the capsid breaks. Further indentation proceeds with a smaller slope, indicating the higher flexibility of the capsid after breaking. The corresponding backward curve shows a strong hysteresis of the indentation curve. (B) AFM images and corresponding line profiles of a capsid before (left, black) and after an indentation experiment, which resulted in breaking of the capsid. Reprinted from ref. 133 with the permission of Wiley-VCH.

applicability. These cover innovations and developments both in the interpretation as well as in the instrumental implementation.

Challenges and future perspectives

The micro- and nanomechanical investigation of biological and soft materials still places a number of challenges, which are partially controversially discussed in the recent literature. However, improvements of the experimental and instrumental setup continuously increase the applicability as well as the user-friendliness of the investigation methods. Key points in these innovations include the implementation of new measurement modes, the vertical indentation setup in particular for the available AFM equipment, the combination of indentation setups with complementary investigation techniques, *i.e.* fluorescence and phase microscopy, *etc.* and, finally, the refinement of the analysis models to complex sample systems.

In particular the analysis requires the choice of a proper model and shortcomings in these models have to be taken into account. A careful evaluation of the chosen model and optimization for each investigated sample model have to be carried out. Particularly, refined models are required for AFM based

devices, which will allow the quantitative analysis of mechanical properties.

In contrast to classical phase imaging in tapping mode (non-contact or ac-mode), where quantification of the obtained contrast is effectively impossible, other techniques are developed which utilize a frequency modulation technique that can be applied during 'normal' scanning and allows probing of the mechanical properties at high data acquisition times. Examples include loss tangent and amplitude-modulated force-modulated viscoelastic AFM.^{138–142} In the loss tangent imaging mode the interpretation of the obtained phase images is summarized into one term that includes both the dissipated and stored energy of the tip–sample interaction. Simultaneously, the tip–sample interaction affects the frequency and results in a modulation of the frequency of the second resonant mode. The frequency shift essentially depends on the sample stiffness and can be analyzed by a variety of different models, which largely depend on the experimental setup (size and shape of the tip) as well as on the characteristics of the sample system. This method can be applied simultaneously with the low force imaging in tapping mode and provides quantitative elasticity and loss tangent images. The AM-FM Viscoelastic Mapping mode is a two pass technique where the first scan is run in conventional tapping mode. The second pass operates at a resonance frequency which is adjusted to keep the phase at 90° in resonance. The z-feedback loop is operating independently, in contrast to conventional FM modes, and not used as a detection signal, which allows for an easier and more reliable separation of the conservative and dissipative contributions of the tip–sample interaction. The second resonance frequency is a very sensitive measure of the tip–sample interaction, which is shifted to a higher frequency in stiffer sample regions and to lower frequencies on softer samples. These frequencies are converted into a quantitative modulus measurement and mapping. Alternatively, the loss tangent can be determined when the sample is vibrated normal to the surface at different frequencies. Recording of the amplitude and phase signal of the cantilever response allows determination of the loss tangent. Another technique which can be applied is the conventional contact resonance force microscopy mode. At high frequency modulation the feedback loop cannot counterbalance the resulting topographical modulations. In the dynamic measurement mode this causes an amplitude modulation of the cantilever oscillation; in contact mode the deflection of the lever is periodically altered with the modulation frequency. The amplitude modulation is then analyzed by the interferometer signal at the modulation frequency and yields quantitative measurements of the elastic modulus. This approach was introduced already in the late 1990s and was – originally in a spectroscopic fashion – developed into a quantitative imaging (mapping) of elastic modulus. Contact resonance techniques have been further modified for their application on more demanding and sensitive soft materials (modulus ~1 GPa to 10 GPa) and for measurements of viscoelastic properties.¹³⁹

Recently, Sweers *et al.* compared different AFM based methods to determine the nanomechanical properties of amyloid fibrils of human alpha-synuclein protein. These fibrils

are strongly associated with Parkinson's disease.¹⁴³ They determined the elastic moduli of the alpha-synuclein fibrils by different AFM based measurement modes: force spectroscopy and the relatively newly introduced surface mapping techniques harmonic force microscopy and peakforce measurements. The authors critically discussed the advantages, disadvantages and difficulties of the applied methods.

Other improvements address, *e.g.*, solutions to suppress instrumental uncertainties, *i.e.* the tip rolling effect in AFM cantilever detection, improved detection and the integration of phase locked loop systems, *etc.*

Harris *et al.* found a way to validate some general aspects of the assumptions that are generally applied in the course of the force-curve analysis.¹⁴⁵ The authors utilized a combined AFM-confocal microscopy approach to measure epithelial cells expressing a GFP-tagged membrane marker. This allowed direct visualization of the indentation geometry and depth of the indentation event. A careful comparison of the obtained results for spherical and pyramidal tips demonstrated a good agreement with the generally applied models for spherical tips; however, for pyramidal tips the contact area is underestimated at forces larger than 0.2 nN, which results in a two-fold overestimated elasticity. As a result of this dramatic uncertainty the authors suggest that a large number of literature data should be critically re-examined and highlight the importance of defining guidelines for avoiding elasticity artifacts.

The limitations in terms of surface resolution of sensitive AFM techniques are mostly given by thermal fluctuations, tip contamination and, if imaging in air, by the fluid layers adsorbed on the surfaces. Additionally, the probing surface and the tip material must be chemically inert. The tip size and profile are the most important intrinsic factors enabling higher magnification and imaging of deep cavities, but eventually also give rise to artifacts.

Depth-sensing indentation as well as AFM force volume mapping approaches are slow techniques and produce large datasets. The temporal resolution of the AFM is dependent on the scan speed and the size of the substrate to be probed; the scan speed is mainly dependent on the electronic feed-back loop. For a scanning area of one square micrometer and at a resolution of 512×512 points about 5 min are required at a scanning speed of about $2 \mu\text{m s}^{-1}$. For techniques based on the static indentation measurements both the temporal as well as the spatial resolution are limited. This limits the investigation of rather slow bio-chemical and -mechanical processes. A recently introduced approach was suggested by Raman *et al.*¹⁴⁴ The authors suggested utilizing dynamic atomic force microscopy to map quantitatively the nanomechanical properties of living cells with a data acquisition rate which is 10 to 1000 times faster than with quasi-static measurement methods. The local properties, such as the local stiffness, stiffness gradients and viscoelastic dissipation are extracted from the 0th, 1st, and 2nd harmonic components of the Fourier spectrum of the AFM cantilevers which are interacting with the sample. The approach is compatible with commercial AFM systems and measurements can be performed in liquids. Lin *et al.* introduced an automated routine for the determination

of the Young's modulus of soft samples with inhomogeneities at the microscopic scale. Their first contribution towards the development of an automated high-throughput analysis routine is based on the Hertz analysis on samples which are compatible with the assumptions of this model. Local elasticities of tissue-engineered cartilage were investigated by AFM and a set of 1024 force-displacement curves were automatically analyzed.¹⁴⁵ The obtained Young's moduli were compared to macroscopically measured values as well as by direct compression of synthetic gels and were found to be in good agreement. The automated analysis of force-displacement curves holds for a minimized subjectivity, improved consistency as well as minimized user intervention and renders the method of force-curve and elasticity mapping much more user-friendly. In a second step the process was refined for soft, inhomogeneous materials, which are not compatible with simple Hertz model fitting procedures.¹⁴⁶ Application of adhesive contact models and the automated scheme to the retraction curves yielded average values of Young's modulus close to those obtained with Hertzian models for the extension curves.

Conclusions

The presented discussion and examples stress the usefulness of DSI and AFM spectroscopic techniques to determine the micro- and nanomechanical properties of biomaterials. Given the fact that this research area is highly interdisciplinary and several uncertainties as well as important factors have to be taken into account, we intended to assemble a comprehensive overview which highlights recent developments and shines light on the difficulties which might be involved during the study of real systems. Potential room for improvement is seen in the development of model systems to extract the mechanical properties in a quantitative fashion which can be applied to complex biological systems and in the development of new measurement techniques, which directly provide access to the mechanical properties of samples on different length scales.

In particular, during the last few years a large number of new studies were published on very different sample materials and new approaches to understand the mechano-responsive behavior of living tissue were developed. Both methods provide unprecedented possibilities to obtain information on such systems which are not accessible by other methods. While depth-sensing indentation is still a method which is preferentially applied to relatively hard sample systems, AFM based force measurements opened the possibility to study also soft biological systems and enabled new methods to relate the nanomechanical behavior of tissue as well as even cells to the fundamental underlying physiological and biochemical processes. This field of research is in particular of high interest as alternative diagnostic tools might emerge from the fundamental understanding of the relationship between mechanical properties and diseases which are influencing these properties. This approach might open up new tools for the early stage diagnosis as well as for analysis of the progression of the disease

and possibly also might allow judgement of the success of therapeutical treatments.

Acknowledgements

This work was financially supported by the technology area HTE of the Dutch Polymer Institute (DPI).

Notes and references

- V. Vogel and M. Sheetz, *Nat. Rev. Mol. Cell Biol.*, 2006, **7**, 265–275.
- J. H.-C. Wang, B. P. Thampatty, J.-S. Lin and H.-J. Im, *Gene*, 2007, **391**, 1–15.
- C. M. Lo, H. B. Wang, M. Dembo and Y. L. Wang, *Biophys. J.*, 2000, **79**, 144–152.
- S. Suresh, J. Spatz, J. P. Mills, A. Micoulet, M. Dao, C. T. Lim, M. Beil and T. Seufferlein, *Acta Biomater.*, 2005, **1**, 15–30.
- E. L. Baker, J. Lu, D. Yu, R. T. Bonnecaze and M. H. Zaman, *Biophys. J.*, 2010, **99**, 2048–2057.
- C. Müller, A. Lüders, W. Hoth-Hannig, M. Hannig and C. Ziegler, *Langmuir*, 2009, **26**, 4136–4141.
- N. Schwender, K. Huber, F. A. Marrawi, M. Hannig and C. Ziegler, *Appl. Surf. Sci.*, 2005, **252**, 117–122.
- G. Guglielmi, G. Scalzo, F. de Terlizzi and W. C. G. Peh, *Radiol. Clin.*, 2010, **48**, 577–588.
- G. Guglielmi and G. Scalzo, *Diagn. Imag. Eur.*, 2010, **26**, 7–11.
- G. Guglielmi, S. Muscarella and A. Bazzocchi, *RadioGraphics*, 2011, **31**, 1343–1364.
- E. Heurich, M. Beyer, K. D. Jandt, J. Reichert, V. Herold, M. Schnabelrauch and B. W. Sigusch, *Dent. Mater.*, 2010, **26**, 326–336.
- J. Currey, *Clin. Orthop. Relat. Res.*, 2009, **467**, 1948–1954.
- P. J. Thumer, *Wiley Interdiscip. Rev.: Nanomed. Nanobiotechnol.*, 2009, **1**, 624–649.
- K. S. Katti, D. R. Katti and R. Dash, *Biomed. Mater.*, 2008, **3**, 034122.
- S. Lin-Gibson, L. Sung, A. M. Forster, H. Hu, Y. Cheng and N. J. Lin, *Acta Biomater.*, 2009, **5**, 2084–2094.
- S. Bechtle, S. F. Ang and G. A. Schneider, *Biomaterials*, 2010, **31**, 6378–6385.
- P. W. Lucas, R. Cook and T. K. Lowrey, *Proc. Mater. Res. Soc.*, 2006, vol. 975, 0975-DD0908-0907.
- R. L. Smith and G. E. Sandland, *Proc. - Inst. Mech. Eng.*, 1922, **1**, 623–641.
- S. P. Rockwell, *Trans. Am. Soc. Steel Treat.*, 1922, **2**, 1013–1033.
- D. T. N. Chen, Y. Wen, P. A. Janmey, J. C. Crocker and A. G. Yodh, *Annu. Rev. Condens. Matter Phys.*, 2010, **1**, 301–322.
- A. C. Fischer-Cripps, *Nanoindentation*, Springer, 2004.
- T. Cohen-Bouhacina and A. MaAli, in *Soft-Matter Characterization*, ed. R. Borsali and R. Pecora, Springer, New York, 2008, pp. 1379–1438.
- S. Hoepfener, J. H. K. van Schaik and U. S. Schubert, *Adv. Funct. Mater.*, 2006, **16**, 76–82.
- J. L. Alonso and W. H. Goldmann, *Life Sci.*, 2003, **72**, 2553–2560.
- M. L. Oyen and R. F. Cook, *J. Mater. Res.*, 2003, **18**, 139–150.
- M. L. Oyen and R. F. Cook, *J. Mech. Behav. Biomed. Mater.*, 2009, **2**, 396–407.
- M. L. Oyen, *Philos. Mag.*, 2006, **86**, 5625–5641.
- O. Franke, M. Göken and A. Hodge, *JOM*, 2008, **60**, 49–53.
- H. Hertz, *J. Reine Angew. Math.*, 1881, **92**, 156–171.
- W. C. Oliver and G. M. Pharr, *J. Mater. Res.*, 1992, **7**, 1564–1583.
- K. L. Johnson, K. Kendall and A. D. Roberts, *Proc. R. Soc. A*, 1971, **324**, 301–313.
- B. V. Derjaguin, V. M. Muller and Y. P. Toporov, *J. Colloid Interface Sci.*, 1975, **53**, 314–326.
- D. Maugis, *Langmuir*, 1995, **11**, 679–682.
- J. Mackerle, *Eng. Comp.*, 2004, **21**, 23–52.
- G. Balooch, G. W. Marshall, S. J. Marshall, O. L. Warren, S. A. S. Asif and M. Balooch, *J. Biomech.*, 2004, **37**, 1223–1232.
- J. L. Cuy, A. B. Mann, K. J. Livi, M. F. Teaford and T. P. Weihs, *Arch. Oral Biol.*, 2002, **47**, 281–291.
- L. H. He and M. V. Swain, *J. Mech. Behav. Biomed. Mater.*, 2008, **1**, 18–29.
- G. M. Guidoni, M. V. Swain and I. Jäger, *Wear*, 2009, **266**, 60–68.
- R. R. Gallagher, M. Balooch, G. Balooch, R. S. Wilson, S. J. Marshall and G. W. Marshall, *J. Dent. Biomech.*, 2010, **1**, 256903(1–7).
- F. Barthelat, C.-M. Li, C. Comi and H. D. Espinosa, *J. Mater. Res.*, 2006, **21**, 1977–1986.
- J.-Y. Sun and J. Tong, *Journal of Bionic Engineering*, 2007, **4**, 11–17.
- N. Barbakadze, S. Enders, S. Gorb and E. Arzt, *J. Exp. Biol.*, 2006, **209**, 722–730.
- J. Y. Sun, Y. J. Guo and J. Tong, *J. Terramech.*, 2006, **43**, 355–364.
- D. Klocke and H. Schmitz, *Acta Biomater.*, 2011, **7**, 2935–2942.
- G. Guber, S. Orso, R. Spolenak, U. G. K. Wegst, S. Enders, S. N. Gorb and E. Arzt, *Int. J. Mater. Res.*, 2008, **99**, 1113–1118.
- B. J. F. Bruet, J. Song, M. C. Boyce and C. Ortiz, *Nat. Mater.*, 2008, **7**, 748–756.
- T. Sumitomo, H. Kakisawa and Y. Kagawa, *J. Struct. Biol.*, 2011, **174**, 31–36.
- S. W. Lee, G. H. Kim and C. S. Choi, *Mater. Sci. Eng., C*, 2008, **28**, 258–263.
- V. T. Nayar, J. D. Weiland and A. M. Hodge, *Mater. Sci. Eng., C*, 2011, **31**, 796–800.
- J. Y. Rho, M. E. Roy, T. Y. Tsui and G. M. Pharr, *J. Biomed. Mater. Res.*, 1999, **45**, 48–54.
- J.-Y. Rho, T. Y. Tsui and G. M. Pharr, *Biomaterials*, 1997, **18**, 1325–1330.
- A. J. Bushby, V. L. Ferguson and A. Boyde, *J. Mater. Res.*, 2004, **19**, 249–259.
- A. J. Rapoff, R. G. Rinaldi, J. L. Hotzman and D. J. Daegling, *Am. J. Phys. Anthropol.*, 2008, **135**, 100–109.

- 54 L. B. Whitenack, D. C. Simkins Jr, P. J. Motta, M. Hirai and A. Kumar, *Arch. Oral Biol.*, 2010, **55**, 203–209.
- 55 M. L. Oyen, *J. Biomech.*, 2006, **39**, 2699–2702.
- 56 V. L. Ferguson, A. J. Bushby and A. Boyde, *J. Anat.*, 2003, **203**, 191–202.
- 57 K. Tai, M. Dao, S. Suresh, A. Palazoglu and C. Ortiz, *Nat. Mater.*, 2007, **6**, 454–462.
- 58 U. Wolfram, H. J. Wilke and P. K. Zysset, *J. Mech. Med. Biol.*, 2010, **10**, 139–150.
- 59 G. J. Miller and E. F. Morgan, *Osteoarthritis Cartilage*, 2010, **18**, 1051–1057.
- 60 S.-Y. Lee, Y.-L. Lai and T.-S. Hsu, *Eur. J. Oral Sci.*, 2002, **110**, 179–183.
- 61 S. Judex, S. Boyd, Y.-X. Qin, L. Müller, R. Müller and C. Rubin, *Curr. Osteoporosis Rep.*, 2003, **1**, 11–19.
- 62 M. Matsuura, F. Eckstein, E.-M. Lochmüller and P. Zysset, *Biomech. Model. Mechanobiol.*, 2008, **7**, 27–42.
- 63 L. M. Miller, W. Little, A. Schirmer, F. Sheik, B. Busa and S. Judex, *J. Bone Miner. Res.*, 2007, **22**, 1037–1045.
- 64 T. Buchwald, K. Niciejewski, M. Kozieleski, M. Szybowicz, M. Siatkowski and H. Krauss, *J. Biomed. Opt.*, 2012, **17**, 017007.
- 65 E. Verné, M. Ferraris, C. Jana and L. Paracchini, *J. Eur. Ceram. Soc.*, 2000, **20**, 473–479.
- 66 É. Budyn and T. Hoc, *Int. J. Numer. Meth. Eng.*, 2010, **82**, 940–965.
- 67 S. Srinivasan, T. Krouskop and J. Ophir, *Ultrasound Med. Biol.*, 2004, **30**, 899–918.
- 68 J. G. Swadener, J.-Y. Rho and G. M. Pharr, *J. Biomed. Mater. Res.*, 2001, **57**, 108–112.
- 69 Z. Fan, P. A. Smith, E. C. Eckstein and G. F. Harris, *J. Biomed. Mater. Res., Part A*, 2006, **79**, 71–77.
- 70 D. Camelli, R. Lucchini, M. Ponzoni, R. Contro and P. Vena, *J. Biomech.*, 2011, **44**, 1852–1858.
- 71 Y. Chevalier, D. Pahr, H. Allmer, M. Charlebois and P. Zysset, *J. Biomech.*, 2007, **40**, 3333–3340.
- 72 A. Faingold, S. R. Cohen and H. D. Wagner, *J. Mech. Behav. Biomed. Mater.*, 2012, **9**, 198–206.
- 73 A. G. Reisinger, D. H. Pahr and P. K. Zysset, *J. Mech. Behav. Biomed. Mater.*, 2011, **4**, 2113–2127.
- 74 L. Feng, M. Chittenden, J. Schirer, M. Dickinson and I. Jasiuk, *J. Biomech.*, 2012, **45**, 1775–1782.
- 75 S. Pathak, G. J. Swadener, S. R. Kalidindi, H.-W. Courtland, K. J. Jepsen and H. M. Goldman, *J. Mech. Behav. Biomed. Mater.*, 2011, **4**, 34–43.
- 76 S. A. S. Asif, K. J. Wahl, R. J. Colton and O. L. Warren, *J. Appl. Phys.*, 2001, **90**, 1192–1200.
- 77 P. K. Hansma, P. J. Turner and G. E. Fantner, *Rev. Sci. Instrum.*, 2006, **77**, 075105–075106.
- 78 P. Hansma, P. Turner, B. Drake, E. Yurtsev, A. Proctor, P. Mathews, J. Lulejian, C. Randall, J. Adams, R. Jungmann, F. Garza-de-Leon, G. Fantner, H. Mkrchyan, M. Pontin, A. Weaver, M. B. Brown, N. Sahar, R. Rossello and D. Kohn, *Rev. Sci. Instrum.*, 2008, **79**, 064303–064308.
- 79 C. Randall, P. Mathews, E. Yurtsev, N. Sahar, D. Kohn and P. Hansma, *Rev. Sci. Instrum.*, 2009, **80**, 065108.
- 80 C. K. Tjhia, C. V. Odvina, D. S. Rao, S. M. Stover, X. Wang and D. P. Fyhrie, *Bone*, 2011, **49**, 1279–1289.
- 81 C. K. Tjhia, S. M. Stover, D. S. Rao, C. V. Odvina and D. P. Fyhrie, *Bone*, 2012, **51**, 114–122.
- 82 M. D. Hager, P. Greil, C. Leyens, S. van der Zwaag and U. S. Schubert, *Adv. Mater.*, 2010, **22**, 5424–5430.
- 83 P. L. Leong and E. F. Morgan, *Acta Biomater.*, 2008, **4**, 1569–1575.
- 84 A. Braly, L. A. Darnell, A. B. Mann, M. F. Teaford and T. P. Weihs, *Arch. Oral Biol.*, 2007, **52**, 856–860.
- 85 L. A. Darnell, M. F. Teaford, K. J. T. Livi and T. P. Weihs, *Am. J. Phys. Anthropol.*, 2010, **141**, 7–15.
- 86 D. S. Brauer, J. F. Hilton, G. W. Marshall and S. J. Marshall, *J. Biomech.*, 2011, **44**, 1626–1629.
- 87 G. A. Schneider, L. H. He and M. V. Swain, *J. Appl. Phys.*, 2008, **103**, 014701–014705.
- 88 L.-H. He, Y. Xu and D. G. Purton, *Arch. Oral Biol.*, 2011, **56**, 512–519.
- 89 M. E. Barbour, D. M. Parker and K. D. Jandt, *J. Colloid Interface Sci.*, 2003, **265**, 9–14.
- 90 M. E. Barbour, D. M. Parker, G. C. Allen and K. D. Jandt, *Eur. J. Oral Sci.*, 2003, **111**, 258–262.
- 91 B. R. Hairul Nizam, C. T. Lim, H. K. Chng and A. U. J. Yap, *J. Biomech.*, 2005, **38**, 2204–2211.
- 92 L. H. He and M. V. Swain, *J. Dent.*, 2007, **35**, 431–437.
- 93 E. Rettler and U. S. Schubert, unpublished results, 2013.
- 94 G. Constantinides, K. S. Ravi Chandran, F. J. Ulm and K. J. Van Vliet, *Mater. Sci. Eng., A*, 2006, **430**, 189–202.
- 95 J. Zhou and L. L. Hsiung, *J. Biomed. Mater. Res., Part A*, 2007, **81**, 66–74.
- 96 S. F. Ang, T. Scholz, A. Klocke and G. A. Schneider, *Dent. Mater.*, 2009, **25**, 1403–1410.
- 97 A. Sadr, Y. Shimada, H. Lu and J. Tagami, *Dent. Mater.*, 2009, **25**, 13–19.
- 98 D. M. Ebenstein and L. A. Pruitt, *J. Biomed. Mater. Res., Part A*, 2004, **69**, 222–232.
- 99 R. Akhtar, N. Schwarzer, M. J. Sherratt, R. E. B. Watson, H. K. Graham, A. W. Trafford, P. M. Mummery and B. Derby, *J. Mater. Res.*, 2009, **24**, 638–646.
- 100 A. Hemmasizadeh, K. Darvish and M. Autieri, *Ann. Biomed. Eng.*, 2012, **40**, 1434–1442.
- 101 W.-C. Huang, J.-D. Liao, C.-C. K. Lin and M.-S. Ju, *Nanotechnology*, 2011, **22**, 275101.
- 102 M. A. F. Kendall, Y.-F. Chong and A. Cock, *Biomaterials*, 2007, **28**, 4968–4977.
- 103 Y.-T. Yang, J.-D. Liao, C.-C. K. Lin, C.-T. Chang, S.-H. Wang and M.-S. Ju, *Soft Matter*, 2012, **8**, 682–687.
- 104 N. B. Holland, C. A. Siedlecki and R. E. Marchant, *J. Biomed. Mater. Res.*, 1999, **45**, 167–174.
- 105 S. Chirasatitsin and A. J. Engler, *J. Phys.: Condens. Matter*, 2010, **22**, 194102.
- 106 E. M. Puchner and H. E. Gaub, *Curr. Opin. Struct. Biol.*, 2009, **19**, 605–614.
- 107 A. Fuhrmann and R. Ros, *Nanomedicine*, 2010, **5**, 657–666.
- 108 T. E. Fisher, M. Carrion-Vazquez, A. F. Oberhauser, H. Li, P. E. Marszalek and J. M. Fernandez, *Neuron*, 2000, **27**, 435–446.

- 109 F. Rehfeldt, A. J. Engler, A. Eckhardt, F. Ahmed and D. E. Discher, *Adv. Drug Delivery Rev.*, 2007, **59**, 1329–1339.
- 110 M. F. Berry, A. J. Engler, Y. J. Woo, T. J. Pirolli, L. T. Bish, V. Jayasankar, K. J. Morine, T. J. Gardner, D. E. Discher and H. L. Sweeney, *Am. J. Physiol.*, 2006, **290**, H2196–H2203.
- 111 E. U. Azeloglu, J. Bhattacharya and K. D. Costa, *J. Appl. Physiol.*, 2008, **105**, 652–661.
- 112 A. A. Wagh, E. Roan, K. E. Chapman, L. P. Desai, D. A. Rendon, E. C. Eckstein and C. M. Waters, *Am. J. Physiol.*, 2008, **295**, L54–L60.
- 113 A. R. Harris and G. T. Charras, *Nanotechnology*, 2011, **22**, 345102.
- 114 G. G. Bilodeau, *J. Appl. Mech.*, 1992, **59**, 519–523.
- 115 M. Stolz, R. Raiteri, A. U. Daniels, M. R. VanLandingham, W. Baschong and U. Aebi, *Biophys. J.*, 2004, **86**, 3269–3283.
- 116 M. Loparic, D. Wirz, A. U. Daniels, R. Raiteri, M. R. VanLandingham, G. Guex, I. Martin, U. Aebi and M. Stolz, *Biophys. J.*, 2010, **98**, 2731–2740.
- 117 M. Stolz, R. Gottardi, R. Raiteri, S. Miot, I. Martin, R. Imer, U. Staufer, A. Raducanu, M. Duggelin, W. Baschong, A. U. Daniels, N. F. Friederich, A. Aszodi and U. Aebi, *Nat. Nanotechnol.*, 2009, **4**, 186–192.
- 118 E. M. Darling, R. E. Wilusz, M. P. Bolognesi, S. Zauscher and F. Guilak, *Biophys. J.*, 2010, **98**, 2848–2856.
- 119 L. Han, A. J. Grodzinsky and C. Ortiz, *Annu. Rev. Mater. Res.*, 2011, **41**, 133–168.
- 120 K. Saeki, J. F. Hilton, T. Alliston, S. Habelitz, S. J. Marshall, G. W. Marshall and P. DenBesten, *Arch. Oral Biol.*, 2007, **52**, 814–821.
- 121 F. Lippert, D. M. Parker and K. D. Jandt, *Caries Res.*, 2004, **38**, 464–472.
- 122 M. Beyer, J. Reichert, E. Heurich, K. D. Jandt and B. W. Sigusch, *Dent. Mater.*, 2010, **26**, 831–839.
- 123 F. Liu and D. J. Tschumperlin, *J. Visualized Exp.*, 2011, e2911.
- 124 F. Liu, J. D. Mih, B. S. Shea, A. T. Kho, A. S. Sharif, A. M. Tager and D. J. Tschumperlin, *J. Cell Biol.*, 2010, **190**, 693–706.
- 125 I. Dulińska, M. Targosz, W. Strojny, M. Lekka, P. Czuba, W. Balwierz and M. Szymoński, *J. Biochem. Biophys. Methods*, 2006, **66**, 1–11.
- 126 M. Fomal, M. Lekka, G. Pyka-Fościak, K. Lebed, T. Grodzicki, B. Wizner and J. Styczeń, *Clin. Hemorheol. Microcirc.*, 2006, **35**, 273–276.
- 127 M. Lekka, M. Fornal, G. Pyka-Fościak, K. Lebed, B. Wizner, T. Grodzicki and J. Styczeń, *Biorheology*, 2005, **42**, 307–317.
- 128 J. L. Maciaszek and G. Lykotrafitis, *J. Biomech.*, 2011, **44**, 657–661.
- 129 S. E. Cross, Y.-S. Jin, J. Rao and J. K. Gimzewski, *Nat. Nanotechnol.*, 2007, **2**, 780–783.
- 130 A. Méndez-Vilas, A. Gallardo-Moreno and M. L. González-Martín, *Antonie van Leeuwenhoek*, 2006, **89**, 373–386.
- 131 C. B. Volle, M. A. Ferguson, K. E. Aidala, E. M. Spain and M. E. Núñez, *Colloids Surf., B*, 2008, **67**, 32–40.
- 132 T. Ludwig, R. Kirmse, K. Poole and U. Schwarz, *Pflugers Arch – Eur. J. Physiol.*, 2008, **456**, 29–49.
- 133 W. H. Roos and G. J. L. Wuite, *Adv. Mater.*, 2009, **21**, 1187–1192.
- 134 S. Swei, J. Plastino and L. Kreplak, *J. Struct. Biol.*, 2012, **177**, 40–45.
- 135 X. Li and B. E. Logan, *Langmuir*, 2004, **20**, 8817–8822.
- 136 P. Eaton, J. C. Fernandes, E. Pereira, M. E. Pintado and F. Xavier Malcata, *Ultramicroscopy*, 2008, **108**, 1128–1134.
- 137 M. Kotecki, A. S. Zeiger, K. J. Van Vliet and I. M. Herman, *Microvasc. Res.*, 2010, **80**, 339–348.
- 138 B. A. Smith, B. Tolloczko, J. G. Martin and P. Grütter, *Biophys. J.*, 2005, **88**, 2994–3007.
- 139 P. A. Yuya, D. C. Hurley and J. A. Turner, *J. Appl. Phys.*, 2008, **104**, 074916–074917.
- 140 R. Garcia and E. T. Herruzo, *Nat. Nanotechnol.*, 2012, **7**, 217–226.
- 141 N. F. Martinez, S. Patil, J. R. Lozano and R. Garcia, *Appl. Phys. Lett.*, 2006, **89**, 153115.
- 142 R. Proksch and D. G. Yablon, *Appl. Phys. Lett.*, 2012, **100**, 073106.
- 143 K. Sweers, K. van der Werf, M. Bennink and V. Subramaniam, *Nanoscale Res. Lett.*, 2011, **6**, 270.
- 144 A. Raman, S. Trigueros, A. Cartagena, A. P. Z. Stevenson, M. Susilo, E. Nauman and S. Contera Antoranz, *Nat. Nanotechnol.*, 2011, **6**, 809–814.
- 145 D. C. Lin, E. K. Dimitriadis and F. Horkay, *J. Biomech. Eng.*, 2007, **129**, 430–440.
- 146 D. C. Lin, E. K. Dimitriadis and F. Horkay, *J. Biomech. Eng.*, 2007, **129**, 904–912.

P2 Verification of key assumptions for the analysis of depth-sensing indentation data

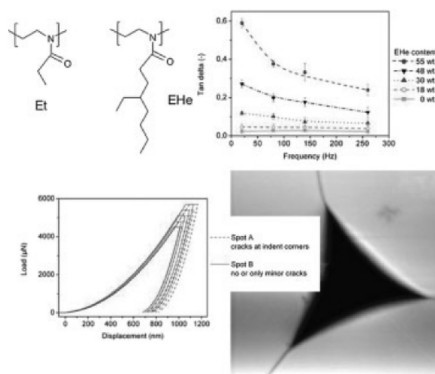
Erik Rettler, Johannes M. Kranenburg, Stephanie Hoepfener,
Richard Hoogenboom, Ulrich S. Schubert,

Macromol. Mater. Eng. **2013**, 298, 88-89.

Verification of Selected Key Assumptions for the Analysis of Depth-Sensing Indentation Data^a

Erik Rettler, Johannes M. Kranenburg, Stephanie Hoepfener, Richard Hoogenboom, Ulrich S. Schubert*

Methods for indentation analysis involve assumptions that may be problematic for visco-elastic materials. Three assumptions are discussed: (1) the unloading is predominantly elastic, (2) tip/sample adhesion and friction are negligible, and (3) no cracking occurs around the indent. A series of copolymers is investigated by indentation at room temperature, just below their glass transitions. Closer to the glass transition assumptions (1) and (2) were violated. Erroneous analysis due to extensive creep was identified by comparison of the creep rate at the end of the hold period with the unloading displacement rate and from the power of the fit to the unloading response. Assumption (3) was studied by scanning the indenter tip over the residual indent in polystyrene, which is known to be susceptible to stress localization.



E. Rettler, J. M. Kranenburg, S. Hoepfener, R. Hoogenboom, U. S. Schubert
Laboratory of Macromolecular Chemistry and Nanoscience, Eindhoven University of Technology, Den Dolech 2, P.O. Box 513, 5600 MB Eindhoven, The Netherlands
E. Rettler, J. M. Kranenburg, U. S. Schubert
Dutch Polymer Institute (DPI), P.O. Box 902, 5600 AX Eindhoven, The Netherlands
E. Rettler, S. Hoepfener, U. S. Schubert
Laboratory of Organic and Macromolecular Chemistry (IOMC), Friedrich-Schiller-University Jena, Humboldtstr. 10, 07743 Jena, Germany
E-mail: ulrich.schubert@uni-jena.de
E. Rettler, S. Hoepfener, U. S. Schubert
Jena Center for Soft Matter (JCSM), Humboldtstr. 10, 07743 Jena, Germany

^a Supporting Information for this article is available from the Wiley Online Library or from the author.

1. Introduction

Depth-sensing indentation (DSI) or instrumented indentation is more and more used for the investigation of mechanical properties of polymers. Various methods exist to analyze the load and displacement responses.^[1] Several analysis methods obtain the modulus and the visco-elastic behavior from the loading response. For these analyses, a material model is used where for instance non-linear elastic deformation and plastic deformation are supposed to be absent,^[2,3] or all viscous behavior is attributed to viscoplasticity and visco-elasticity is supposed to be negligible.^[4] Often (but not always^[4,5]) the occurrence of plastic deformation is suppressed by ensuring low strain levels by using a spherical indenter and keeping the indentation depth small compared to the radius of the sphere.

Apart from these indenter geometries, also the Berkovich geometry is often used due to historical reasons and reasons

of experimental convenience. Compared to a spherical indenter, the Berkovich geometry is for instance easier to calibrate (frame compliance of the instrument, tip shape), less affected by sample surface roughness,^[6] adhesion or deviating mechanical behavior of the top layer of the material,^[7] and more suitable for imaging of the residual imprint. One disadvantage of the Berkovich geometry is that plastic deformation during loading cannot be ignored. This can be overcome by obtaining the indentation modulus E_i from the load-displacement response upon unloading, as proposed by Oliver and Pharr.^[8–10]

It is known that for polymers, E_i obtained from the Oliver and Pharr method overestimates the true elastic modulus.^[11] However, for obtaining an estimate for the elastic modulus, e.g., in a high-throughput setting where a large set of materials is screened for one or more properties,^[1,11,12] that does not need to be a severe problem as long as the ratio between the obtained E_i and the true elastic modulus stays approximately constant.

In the method proposed by Oliver and Pharr, E_i is obtained from the projected contact area A_c and the slope S of the load-displacement response at the start of the unloading using^[9]

$$\frac{(1 - \nu_{\text{sample}}^2)}{E_{i,\text{sample}}} = \frac{2\beta}{S} \left(\frac{A_c}{\pi}\right)^{1/2} - \frac{1 - \nu_{\text{probe}}^2}{E_{\text{probe}}} \quad (1)$$

Here, E_{probe} is the elastic modulus of the indenter probe, β is a constant slightly larger than unity, and ν represents the Poisson's ratio of the indenter probe and the sample material, respectively. Considering that the diamond probe is much stiffer than the polymer, $E_{\text{probe}} \gg E_i$, Equation 1 can be simplified to

$$E_{i,\text{sample}} \approx (1 - \nu_{\text{sample}}^2) \frac{S}{2} \left(\frac{\pi}{A_c}\right)^{1/2} \quad (2)$$

For the determination of the contact area, elastic deflection of the surface around the indent is assumed, while also pile-up may occur.^[4,9] Moreover, the Oliver and Pharr method implicitly assumes that:

1. the unloading is predominantly elastic (which implies that the time-dependent displacement of the tip into the sample material due to creep is small);
2. the tip/sample adhesion and friction are so small that they do not influence the load-displacement response;
3. no cracks are formed around the indent or at the indent corners.

To assure that assumption (1) is met, i.e., that the unloading response is predominantly elastic and not affected by creep, the slope of the unloading response can be corrected for the creep,^[13] or the unloading can be

performed quickly.^[14] In order to assess when unloading is performed quick enough, a criterion is needed. Such a criterion could be based on a comparison of the displacement rate during the unloading to that at the end of a hold period at constant load just prior to the unloading. In earlier work, we proposed that the displacement rate upon unloading should exceed the displacement rate at the end of the hold period by at least a factor of five (and should have the opposite direction).^[15] This somewhat arbitrary choice deserves some more attention and is discussed in this work.

The second assumption is usually met for glassy polymers, as evidenced by the good agreement between modeling and experimental results ignoring adhesion and friction.^[5] However, for softer materials the tip/sample adhesion results in an additional load, pulling the indenter probe onto the material, as described for various conditions by the Derjaguin-Muller-Topov model or the Johnson-Kendall-Roberts model.^[6,16] Moreover, the adhesion may result in friction, which may also influence the load-displacement response obtained by indentation.^[17,18]

Compliance with the third assumption may be ensured by imaging some of the indents on materials that may behave brittle. For indentation depths well in the micrometer range, optical imaging can be applied,^[19] while for shallower indents (as discussed here), topographic imaging is most suitable. However, in order to be able to rely on the obtained topographic data, it should be investigated whether the sensitivity of imaging with the indenter is sufficient to reveal the presence of cracks.

The first and the second assumption listed above are investigated using copolymers of 2-ethyl-2-oxazoline (Et) and 2-(3-ethylheptyl)-2-oxazoline (EH θ). The schematic representation of the chemical structure of both monomer repeat units, which are randomly distributed over the polymer chain, is shown in Figure 1. During the study of these copolymers, dynamic DSI was also performed. The thereby obtained loss tangent nicely showed the proximity of the glass transition. As polystyrene is well-known for its (macroscopic) brittleness, compliance with the last assumption was investigated using polystyrene.

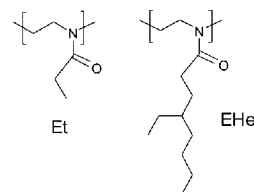


Figure 1. Schematic representation of the monomer repeat units in the random copolymer poly((2-ethyl-2-oxazoline)-*ran*-[2-(3-ethylheptyl)-2-oxazoline]), Et-*r*-EH θ .

2. Experimental Section

The synthesis and structural characterization of the Et-*r*-EHe copolymers is reported elsewhere.^[20] The glass transition temperatures (midpoints) of these random copolymers were determined by differential scanning calorimetry (DSC) on a Netzsch DSC 204 F1 Phoenix under nitrogen atmosphere from -50 to $+200$ °C with a heating rate of $20\text{ K} \cdot \text{min}^{-1}$ (the first heating run to 200 °C, which was followed by a cooling run at $40\text{ K} \cdot \text{min}^{-1}$, was not considered for analysis). 20 – 26 mg of each copolymer were dissolved in $80\text{ }\mu\text{L}$ chloroform (Biosolve LTD). Several droplets from each solution, each $\approx 4\text{ }\mu\text{L}$, were pipetted onto a glass slide using a pipetting robot (AnalytikJena Fastrans system, Jena, Germany), in line with high-throughput experimentation concepts.^[1] The glass slides were subsequently dried under reduced pressure at 40 °C for 2 weeks and then transferred into the enclosure of the TriboIndenter (Hysitron Inc., MN, USA). The samples resided for 1 week at $<7\%$ relative humidity (RH) as measured using a Hygrometer testo 608-H2. Subsequently, indentation experiments were performed at $5.2 \pm 0.4\%$ RH and 24 ± 2 °C employing a nanoDMA (1D) transducer and a diamond Berkovich indenter. Before every indent, the indenter was held in contact with the surface, to allow for piezoactuator stabilization (35 s) and drift correction (40 s) at a contact load of only $0.5\text{ }\mu\text{N}$ to prevent any deformation of the polymer surface prior to the indentation experiment. The drift rate (typically $0.1\text{ nm} \cdot \text{s}^{-1}$) was automatically determined over the last 20 s of the 40 s period.

Quasistatic experiments in load control were performed by lifting the tip 30 nm prior to the measurement, re-approaching the surface (surface detection at a load of $0.5\text{ }\mu\text{N}$), loading to maximum load in 10 s, holding at maximum load for 10 s and unloading in 2 or 0.4 s. The maximum load was reduced in steps of $300\text{ }\mu\text{N}$ from 2100 to $300\text{ }\mu\text{N}$. From these seven measurements (spaced $40\text{ }\mu\text{m}$ apart) per sample, the first two (i.e., the experiments at 2100 and $1800\text{ }\mu\text{N}$) were disregarded to even further reduce the influence of drift. For the samples containing 30 wt% EHe, the indentation experiments performed at $1500\text{ }\mu\text{N}$ and for the 2 s unloading time experiment also that at $1200\text{ }\mu\text{N}$ exceeded the tip area function calibration range, and were therefore not analyzed either. Before quasistatic experiments in “open loop” mode, the tip was not lifted but loaded directly. The load function is described in Figure 6. For the “open loop” experiments, the nominal maximum loads ranged from 2800 to $400\text{ }\mu\text{N}$ (steps of $400\text{ }\mu\text{N}$) for the 0, 18, and 30 wt% EHe copolymers. Because of the significant compliance of the 48 wt% EHe copolymer, lower load levels were chosen, namely 1400 to $200\text{ }\mu\text{N}$ with steps of $200\text{ }\mu\text{N}$.

Load-displacement responses were analyzed using the method of Oliver and Pharr^[8] by fitting the unloading response from 0.95 to $0.20 \cdot P_{\text{max}}$ with the conventional power law form to obtain the slope at the start of the unloading S . E_i is obtained using Equation 1 and taking $\beta = 1$, $E_{\text{diamond}} = 1140\text{ GPa}$, $\nu_{\text{diamond}} = 0.07$ and $\nu_{\text{sample}} = 0.4$.

The loss tangent $\tan \delta$ of the copolymers was determined using the TriboIndenter nanoDMA module, whereby an oscillating load (nominally $10\text{ }\mu\text{N}$) was superimposed over the quasistatic load (nominally $300\text{ }\mu\text{N}$). The loss tangent $\tan \delta$ is calculated from the phase lag between the applied load oscillation and the resulting

displacement oscillation,^[8,16,21] which was between 0.7 and 2.3 nm in amplitude. The average and standard deviation were obtained from three or four experiments on each duplicate sample, so in total seven or eight measurements, are reported.

General-purpose polystyrene (PS) with a number-averaged molar mass M_n of $95\text{ kg} \cdot \text{mol}^{-1}$ and a polydispersity index of 1.33 [as determined by gel permeation chromatography (GPC)] was supplied by Shell. The PS was dissolved in toluene (Biosolve LTD). From this 9 wt% solution, several spots were deposited onto a glass slide that was placed on a heating plate at ≈ 95 °C. No extensive deposition of material at the edge of the spot (the so-called “coffee-drop” effect^[1,22]) was observed. The glass slide with polystyrene spots was heated to 110 °C under reduced pressure (estimate: $<5\text{ mbar}$) in a Heraeus Vacutherm oven. The sample was allowed to cool slowly overnight under reduced pressure.

The polystyrene film thicknesses were measured using a Focale Zoomsurf 3D optical interferometer with a $5\times$ objective. DSI was conducted using a 2D transducer and a Berkovich (trigonal pyramid) diamond indenter. Various load levels were used. After loading in 10 and 10 s hold at P_{max} unloading took place in 1 s. A Poisson's ratio of 0.35 was used in the calculation of E_{PS} .^[23] Imaging of the residual imprints with the TriboIndenter was conducted at a scan velocity of either 6.0 or $6.4\text{ }\mu\text{m} \cdot \text{s}^{-1}$ and a setpoint of $2\text{ }\mu\text{N}$. For imaging, the same Berkovich indenter probe was used as for the indentation experiment.

Imaging of two residual imprints was conducted by tapping mode atomic force microscopy (AFM) using an NT-MDT Solver P47 SMENA AFM. Commercial tapping mode tips (MikroMasch) with a typical force constant of $11\text{ N} \cdot \text{m}^{-1}$ were used.

3. Results and Discussion Regarding Assumptions 1 and 2

3.1. Random Et/EHe Copolymers

At the glass transition, the mechanical properties of polymers change: the elastic modulus decreases drastically and the loss tangent passes through a maximum.^[24] These changes in the mechanical behavior are investigated on amorphous random copoly(2-oxazoline)s that are at room temperature only slightly below their T_g . These copoly(2-oxazoline)s were prepared by a living cationic ring opening polymerization at a monomer-to-initiator ratio of 100 using methyl tosylate as the initiator. A detailed description of the synthesis and the chemical characterization of these copolymers is reported elsewhere (Table 1).^[20]

The EHe units (Figure 1) have the same number of carbon and hydrogen atoms in the side-chain as the 2-nonyl-2-oxazoline units discussed in ref.^[25] However, the spatial arrangement of the atoms is different. The absence of a melting peak in the DSC traces shows that EHe does not crystallize, in contrast to poly(2-alkyl-2-oxazoline)s with linear alkyl side-chains longer than four carbon atoms.^[26] The ethyl groups racemically attached to the heptyl side chains impede alignment of the heptyl chains and thereby prevent crystallization.^[20]

Table 1. Characteristics of the EHe-Et random copolymers determined by ^1H NMR spectroscopy,^[20] GPC,^[20] and DSC.

^1H NMR		GPC ^{a)}		DSC
EHe		\bar{M}_n	PDI	T_g
[mol%]	[wt%]	[g · mol ⁻¹]		[°C]
0	0	17 700	1.18	59
10	18	14 400	1.21	45
18	30	15 200	1.21	35
32	48	15 700	1.19	27 ^{b)}
38	55	16 300	1.20	24
46	63	16 900	1.21	16
100	100	16 900	1.13	-3

^{a)} Eluent: *N,N*-dimethylacetamide with 2.1 g · L⁻¹ LiCl, PS calibration standards; ^{b)} Obtained from a fit of T_g as function of wt% EHe.

The EHe homopolymer was sticky at ambient temperature, which is related to its low glass transition temperature. The (co)polymers containing up to 63 wt% EHe were dissolved in chloroform and dropcast, resulting in accurately positioned, regularly shaped polymer spots. After drying, DSI was conducted on these materials at reduced humidity (5.2% RH) and room temperature. Various measurement protocols were employed:

1. quasistatic DSI with loading in 10 s, 10 s hold, unload in 2 s (load control);
2. quasistatic DSI with loading in 10 s, 10 s hold, unload in 0.4 s (load control);
3. quasistatic DSI with loading-unloading-reloading-unloading-reloading scheme (open loop);
4. dynamic DSI at various frequencies.

3.2. Effect of the Unloading Rate

Selected load-displacement responses are shown in Figure 2. The indentation moduli E_i obtained from the Oliver and Pharr analysis of the unloading responses of the Et:EHe copolymers decrease with increasing EHe content, as shown in Figure 3. Since the large decrease in the stiffness of glassy polymers at their glass transition sets in gradually,^[24] E_i starts to decrease with increasing EHe content due to the smaller distance to T_g . (As a side note, it is mentioned that the number of entanglements per chain may be small due to the modest chain length. Therefore, the rubbery plateau modulus in the range of ≈ 10 MPa usually exhibited

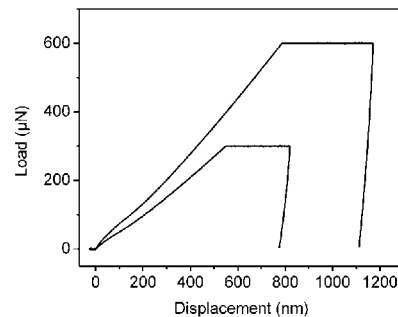


Figure 2. Load-displacement responses for the 30 wt% EHe copolymer, employing an unloading time of 0.4 s.

by amorphous polymers above their T_g may be absent for these materials.)

Indentation experiments were performed on the copolymers employing unloading times of either 0.4 or 2 s. The indentation moduli E_i obtained for both unloading times agree relatively well for the (co)polymers containing up to 18 wt% EHe (Figure 3). However, for the copolymer containing 30 wt% EHe, E_i obtained employing the two unloading times differ. For the 30 wt% EHe copolymer, the displacement rate upon unloading in 2 s is only one tenth of the creep rate during the preceding hold period (Table 2). Therefore, the 2 s unloading response is significantly influenced by creep. If the unloading is not predominantly elastic, application of the Oliver and Pharr procedure results in unreliable E_i values,^[10,13] as also shown by the different E_i values obtained employing both unloading times for the

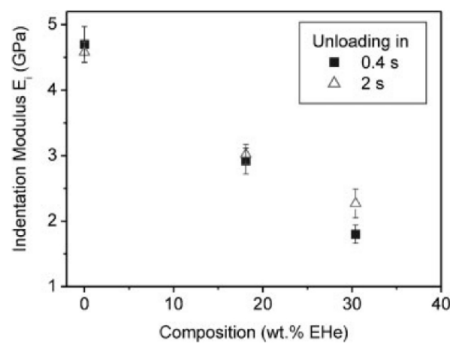


Figure 3. Indentation moduli obtained for Et-*r*-EHe random copolymers employing an experimental protocol with unloading in 2 or 0.4 s. As discussed in the text, E_i obtained for the 30 wt% EHe copolymer by unloading in 2 s is not reliable.

Table 2. Approximate ratio of the initial unloading displacement rate to the creep rate at the end of the hold time. The ratio was evaluated from the last ≈ 1 s of the hold time and the first 0.1 s of the unloading for the indentation experiment performed at 1500 μ N. The indenter moves during hold at constant load into the material, while during elastic unloading, the material pushes the indenter back, resulting in a displacement rate with the opposite sign. For readability reasons, the minus sign of the displacement rate ratio is not shown.

EHe [wt%]	Displacement rate ratio	
	Unloading in 0.4 s	Unloading in 2 s
0	84	13
18	22	4
30	4	0.1

30 wt% EHe (Figure 3). In contrast, the analysis results from unloading responses showing displacement rate ratios ≥ 4 (Table 2) appear to be only negligibly influenced by creep, as shown by the agreement in the obtained moduli in Figure 3: analysis of load-displacement responses exhibiting a ratio of only four already resulted in the same E , as quicker unloading experiments on the same material.^b So our criterion on the displacement rate ratio adopted in ref.^[15] seems to be rather effective in minimizing the influence of creep on the analysis results.

Figure 4 shows that fitting of the 2 s unloading response of the 30 wt% EHe copolymer, i.e., the data influenced significantly by creep, resulted in highly deviating power values that were far outside the range expected for the contact of a cone onto an elastic surface. This shows that the power value can be used as an indicator for influence of creep on the analysis.

3.3. Viscous Response and Adhesion

The third quasistatic loading protocol that was applied is outlined in Figure 5. This protocol included a 10 s hold at maximum load, partial unloading to 40% thereof combined with subsequent reloading, followed by a second unloading/reloading cycle. This loading protocol resulted in the

^b It is not likely that for the 18 wt% EHe copolymers the initial slope S resulting from the fit to the 2 s unloading response is affected by creep. The indentation experiments were performed at various levels of P_{\max} , resulting in different indentation depths h_{\max} . The plot of S as function of h_{\max} overlapped for both unloading times, indicating that creep can be neglected. Even if S would be affected by creep, the overall effect on the determined E is negligible as a too high slope S mathematically also results in an increase in the contact depth and, thus, in the contact area, Equation 2.

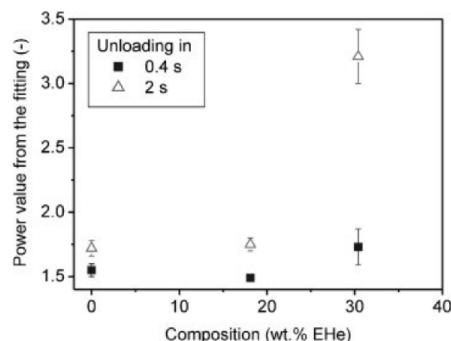


Figure 4. Average and variation in the power law values for all analyzed indentation experiments (so: all employed P_{\max}) for each sample unloading time combination, i.e., for each datapoint presented in Figure 3.

load-displacement responses shown in Figure 6. In contrast to the load-displacement responses shown in Figure 2 obtained under “load control”, the load-displacement responses shown in Figure 6 were obtained using the “open loop” mode. While in the load-control mode a feedback assures that the desired load is applied onto the sample surface, in the “open loop” mode part of the force applied electrostatically to the drive plate in the transducer is used to elastically deform the springs inside the transducer.^[27] Therefore, the actual load applied onto the sample surface is the nominal load minus a certain amount

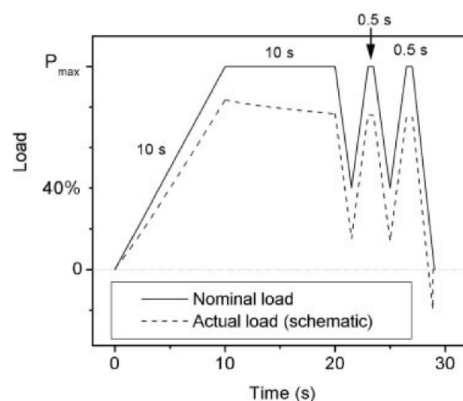


Figure 5. Protocol employed to obtain the load-displacement responses shown in Figure 7. The partial unload and reload took place in 1.5 s each and final unloading took place in 2 s. The actual load depends on the deformation of the transducer springs, which depends, in return, on the mechanical properties of the material.

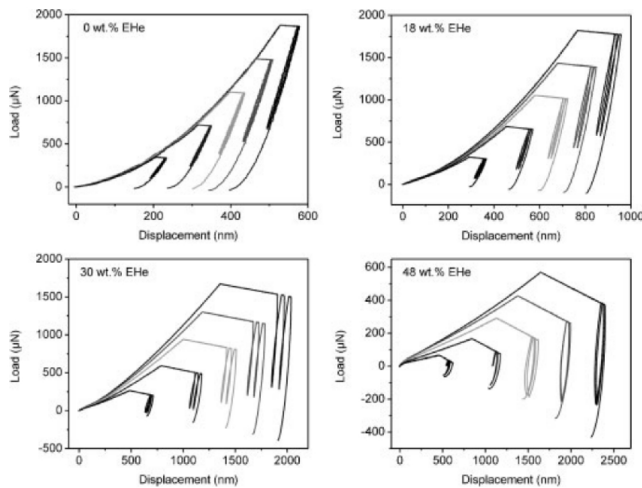


Figure 6. Loading/unloading/reloading experiments on Et:EHe random copolymers. Data acquired when the tip was not in contact with the material surface (after final unloading and for the 48 wt% EHe also during several unloading/reloading cycles) has been removed.

that depends on the displacement of the indenter probe (dashed line in Figure 5). For indentation experiments performed in open-loop the load may even be negative, which means that the indenter pulls on the sample material.

Figure 6 shows that with increasing EHe content, i.e., with decreasing distance to the glass transition:

1. the displacement, in particular the displacement during the hold period, increases;
2. the curvature of the loading response decreases;
3. the overlap between the various loading responses for the same material decreases;
4. the overlap between the unloading and reloading responses decreases;
5. a smaller part of the total displacement recovers during unloading;
6. the negative load at the end of the (final) unloading increases.

The first five observations are mainly caused by the increased viscous response. Furthermore, the first, second, and fifth observation are partly attributable to a decrease of the yield stress, resulting in a larger plastic deformation. Here, it is noted that the yield stress depends on the timescale of testing, i.e., on the viscosity,^[28] so both causes mentioned above are related.

Decreasing overlap between the various loading responses for the same material, listed as third observation, is a clear expression of the time-dependent mechanical behavior.^[5,7,17] As the loading was conducted in 10 s irrespective of P_{\max} , the various loading responses in Figure 6 represent different loading rates. The loadings to the smaller P_{\max} allow more time for viscous deformation upon loading to the same load P . For the Et homopolymer, the lowest P_{\max} experiment resulted in a maximum displacement at the end of the loading of 205 nm, at a load of 345 μN . At the same load of 345 μN , the highest loading rate experiment exhibited a displacement of 200 nm. The displacement value of 205 nm is only 3% higher than the latter value. However, for the 18, 30, and 48 wt% EHe copolymers, the difference increases due to time-dependent deformation. For these materials, the displacement for the lowest loading rate exceeds the displacement at the same load employing the highest loading rate by 17, 49, and 180%, respectively.

For a perfectly elastic-plastic material, the reloading response should coincide with the preceding unloading response. This material behavior is a key assumption of the Oliver and Pharr method.^[1,8,14] The extent to which this assumption is violated can be assessed by comparing the slope of the unloading and the reloading responses (Figure 6). For materials where the loading and unloading responses are difficult to discern in Figure 6, one unload/reload cycle is shown in Figure 7. The difference between the loading and the reloading slope increases with increasing amount of EHe. This demonstrates that the viscous contribution to these responses increases. However, the increasing difference between the loading and the unloading response with increasing EHe content should not solely be attributed to the increased time-dependent behavior, as with increasing EHe content the unloading is performed effectively to lower loads, due to the so-called "open loop" experimental protocol.

Selected unloading responses were fitted using the power law equation. For selected reloading responses, the last ≈ 0.7 s of the reloading segment were fitted using the power law as well, whereby the power value was restricted to be equal to or larger than 1. From these fits, the slope at P_{\max} was obtained, which is a key parameter for the calculation of E_i as shown by Equation 2. Typically, the slopes upon reloading were for the 0, 18, and 30 wt% EHe

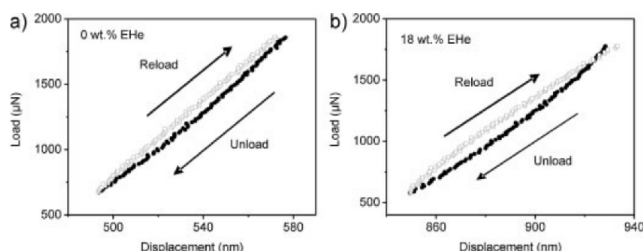


Figure 7. Unloading and reloading responses for (a) 0 and (b) 18 wt% EHe copolymers at the same nominal load (the highest loads shown for these materials in Figure 6).

copolymers ≈ 10 , 30, or 70% smaller than those obtained upon unloading, respectively. A high slope for the unloading response results in a high E_i (Equation 2). This is in line with the relatively high E_i obtained for the 30 wt% EHe copolymer obtained upon unloading in 2 s (Figure 3). The increasing deviation between the unloading and reloading slopes indicates that the assumption that the unloading is governed by the elastic response becomes more and more problematic upon approaching the glass transition.

Figure 6 shows that the negative load (pull-off force) at the end of the final unloading increases with increasing EHe content. Indentation experiments at higher P_{max} on the same copolymer result in larger pull-off forces, as the higher load results in deeper indents and, therefore, a larger contact area between the indenter probe and the material. From the negative load upon unloading, the work of adhesion can be obtained. For this calculation, also the contact area at the moment that this negative load is largest is required. This analysis is usually performed employing a large radius sphere.^[9,10] Even though the contact area at the maximum negative load is not known, the observed negative force prior to loss of contact indicates substantial probe/copolymer adhesion. Large adhesion between the tip and the sample, and concomitant friction, will affect the load-displacement response. The observed increase in pull-off force with increasing EHe content indicates that also the assumption that adhesion and friction are negligible turns more and more problematic for these copolymers with decreasing distance to the glass transition.

3.4. The Loss Tangent as a Function of Composition and Frequency

Visco-elastic properties of polymers can be studied by subjecting the polymer to a small-amplitude cyclic deformation. At the glass transition of an amorphous polymer, the dissipation of the mechanical energy of such a cyclic deformation is maximum.^[24,29] The ratio of the viscous response to the elastic response is called the loss

tangent, $\tan \delta$. For polymers, a time/temperature superposition principle applies: an increase of the test frequency has a similar effect as a decrease of the temperature during testing.^[24,29] Therefore, the loss tangent changes with the test frequency. For materials close to their glass transition, the change in the loss tangent with test frequency is large.

Dynamic experiments can be performed by DSI, as well.^[8,25,29] Hayes et al.^[29] have measured $\tan \delta$ of polycyanurate, epoxy, polyvinyl acetate, and propylene as a function of both testing frequency and temperature by dynamic

DSI. In variation to their work where the measurement temperature was varied, in the current investigation the “distance” to the glass transition is varied by changing the chemical composition of the tested material. In Figure 8, $\tan \delta$ is presented for selected Et:EHe copolymers. (It is noted that adhesion also may affect the dynamic DSI response. Therefore, the $\tan \delta$ value of the 55 wt% EHe copolymer may be less accurate than that at lower wt% EHe.) In agreement with theory, Figure 8 shows that with decreasing distance to the glass transition, the loss tangent increases.

The loss tangent increases to higher values than observed for the Et:Non copolymers discussed in ref.^[25] This can be attributed to the formation of small crystallites for the Et:Non random copolymers and the absence thereof for the Et:EHe random copolymers. Such crystallites stiffen the material, resulting in a more elastic response. Figure 9 shows that with increasing test frequency the energy dissipation decreased. Furthermore, not only for 20 Hz (Figure 8) but also for other frequencies, $\tan \delta$ increased with decreasing distance to the glass transition, here corresponding to increasing EHe content.

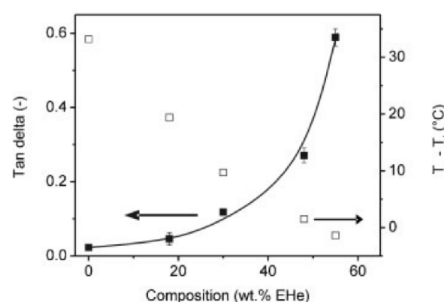


Figure 8. Loss tangent obtained at a test frequency of 20 Hz as a function of composition for Et:EHe random copolymers. The difference between the glass transition temperature as observed by DSC and the temperature during testing ($T_t = 25^\circ\text{C}$) is indicated as well.

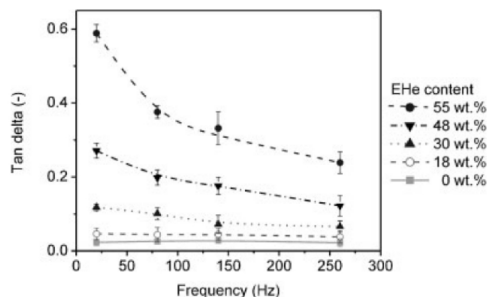


Figure 9. The loss tangent as a function of testing frequency and chemical composition.

4. Results and Discussion Regarding Assumption 3

Although cracking at the indent corners allows evaluation of the fracture toughness for, in particular, ceramics and hard metals,^[6] this cracking should be avoided during indentation experiments aiming at obtaining elastic properties. Cracking of the material around the indent or at the indent corners invalidates the Oliver and Pharr method.^[6] Residual indentation imprints can be imaged in order to investigate whether cracking occurred. This topologic imaging can be performed by scanning the indenter tip over the polymer surface.^[27] However, it should be verified whether this imaging is sensitive enough to identify the occurrence of cracking. The question whether the absence of cracks at the indent corners in the topographic image proves that these cracks are really absent will be addressed in this section.

Polystyrene is well-known for its localized deformation, in particular after physical ageing.^c This strain localization, which is attributable to the large extent of strain softening for aged PS followed by only modest strain hardening,^[30] may cause the material to exhibit cracking during the indentation experiment. Therefore, PS was chosen for the current investigation. Several spots of PS were deposited onto a glass slide. Subsequently, the glass slide containing the PS spots was heated under reduced pressure to 110 °C, which is 10 °C above the glass transition temperature of PS, and slowly cooled. During cooling, physical ageing can take place. Subsequently, indentation experiments were performed and several indents were imaged with the indenter tip. However, no cracking was observed. In order to investigate whether this is due to insufficient instrument sensitivity, imaging by AFM (tapping mode) was conducted

^c It is noted that wear of the Berkovich probe may change the sensitivity.

on two of these indents. The AFM tips are much sharper than the indenter tips, and this instrument is designed to be very sensitive for surface topology. Moreover, AFM provides the possibility of phase imaging, which is a very sensitive tool for observation of structural changes at the surface. However, also with this instrument no cracking at the indent corners was observed (Figure 10). In the close-up phase image at one of the corners (Figure 10d), some line-shaped features are observed originating from the indent corner. These are probably attributable to orientation in the material and/or local strain-hardening of the polymer induced by the indentation.

The samples were subjected to several heat treatments consisting of heating above their glass transition and subsequent cooling to room temperature at various cooling rates. After only one of these heat treatments (again: heating to 110 °C under reduced pressure followed by slow cooling), cracks were observed upon imaging with the TriboIndenter at the corners of the indents on one of the two investigated PS spots. The indentation load-displacement responses for both spots are shown in Figure 11. The topography images obtained by imaging with the TriboIndenter are shown in Figure 12.

An important observation is that the indenter equipped with a Berkovich probe is capable of identifying the presence of cracks.^c Secondly, extensive cracking is observed, while the differences in the load-displacement responses are only modest (Figure 11). The differences in the stiffness at the start of the unloading (Figure 13a) and in E_i (Figure 13b) are also relatively small.

The presence or absence of cracking is the main cause for the difference between the load-displacement responses shown in Figure 11. However, it is not the only cause for the difference between the load-displacement, as this difference in cracking behavior itself indicates that the mechanical properties (yield stress, extent of strain localization, stress at break, etc.) of spot A and spot B were not exactly equal. In this context it is noted that the non-cracking sample was $\approx 60 \mu\text{m}$ thick, while the PS spot exhibiting cracking was $\approx 45 \mu\text{m}$ thick. Possibly, in the thicker sample a tiny amount of toluene remained that did not yet evaporate. Alternatively, there might be some stress in the PS due to the thermal expansion mismatch between the PS and the glass substrate, where the differing thickness resulted in differing stress levels. However, ascribing in first approximation the difference between the indentation responses obtained on spot A and spot B to the occurrence of cracking, it is observed that cracking resulted in:

1. a larger displacement at the same load P_{max} ;
2. a higher slope S at the start of the unloading (Figure 13a);
3. a somewhat lower E_i (Figure 13b).

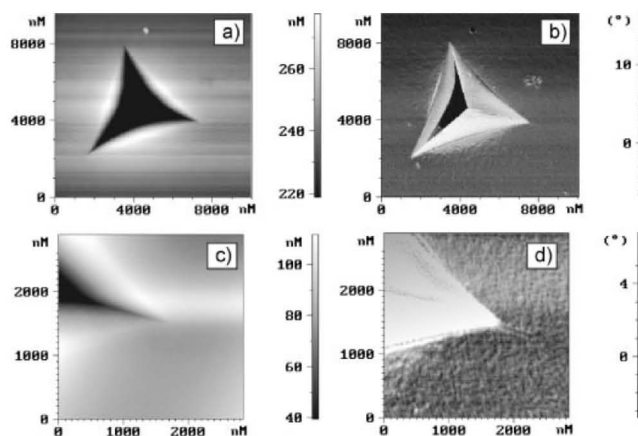


Figure 10. AFM (a) height and (b) phase image of a residual indent on polystyrene; (c) and (d) are the height and phase image of a second, smaller-area scan at one of the corners. Z-height scale is reduced to increase the visibility of possible cracks.

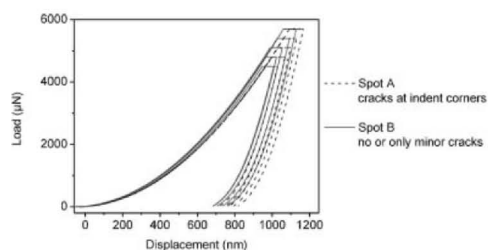


Figure 11. The indentation load-displacement responses for two PS spots with identical thermal history, one exhibiting cracking and the other exhibiting no or only minor cracking.

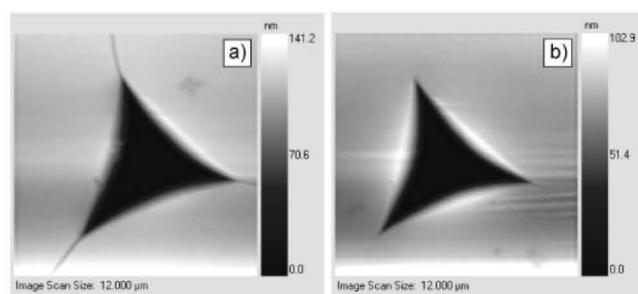


Figure 12. Surface topology obtained by imaging with the Tribolindenter of the indents resulting after the indentations at a maximum load of 5400 µN. (a) Significant cracking is observed for spot A (the corresponding load-displacement response is shown dashed in Figure 11), while (b) on spot B only a minor crack is observed (solid line in Figure 11). The Z-scale is reduced to improve the visibility of possible cracks.

By the cracking, elastic strain in the PS adjacent to the indenter probe is dissipated, resulting in a decreased resistance to deformation during the indentation experiment and, therefore, deeper indents. The loss of the elastic strain also decreases the ability of the material to push the indenter back during the unloading step of the indentation experiment, resulting in a reduced displacement during unloading and, therefore, a higher slope at the start of the unloading. As the loss of elastic strain is not accounted for in the Oliver and Pharr analysis, E_i obtained for the spot A samples is not reliable. It is noted that the difference between E_i obtained from indentations exhibiting cracking and indentations not exhibiting cracking is only modest, as mathematically the effect of the larger slope S is counteracted by the larger contact area A_c , as shown

by Equation 2.

Interestingly, the cracking was not shown by any abrupt events in the loading responses such as pop-ins. This is in agreement with the observation that on the polystyrene spot exhibiting cracking, cracks were already observed after indentations employing only modest loads P_{rmax} . Already after indentation at a P_{rmax} of 2700 µN, cracking was observed (although at only one of the indent corners), which may indicate a gradual, continuous crack-growth process.

5. Conclusion

It was shown that amorphous, non-crosslinked polymers of relatively low molar mass close to their glass transition may give rise to unreliable results when the unloading responses are analyzed using the protocol proposed by Oliver and Pharr. Due to substantial time-dependent deformation, the assumption that the unloading is predominantly elastic may become problematic. Increasing the unloading rate improved the reliability of the analysis results. It was demonstrated that the criterion that the unloading displacement rate should exceed the creep rate by a factor of 5 is suited to minimize influence of creep on the obtained E_i values. Also the value for the power of the fit to the unloading

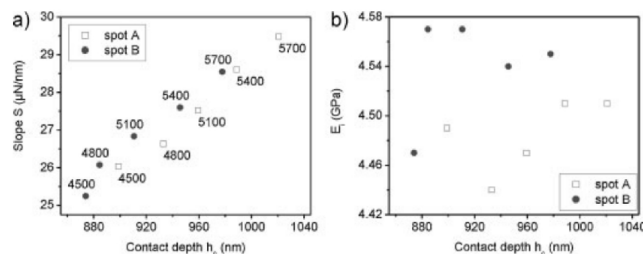


Figure 13. Analysis results of the load-displacement responses shown in Figure 12. (a) Slope S at the start of the unloading. For easy comparison with Figure 12, P_{\max} is annotated (b) indentation moduli E_f . The values obtained for spot A, which exhibited cracking, are unreliable.

response can be used as a quick and convenient indicator whether creep influenced the unloading response.

Unloading and subsequent reloading confirmed that the assumption that the unloading response is elastic becomes problematic if the material is tested only just below its T_g . Moreover, the pull-off force, where the indenter probe breaks loose from the sample surface, indicates that the extent of adhesion is no longer negligible for materials close to their glass transition. Therefore, apart from the creep, also the increased adhesion and tip-sample friction reduce the accuracy of the analysis results for such copolymers tested very close to, or above, their T_g .

The different dynamic mechanical response of the various copolymers was related to the differences between their respective glass transition temperature and the testing temperature. The frequency and composition dependency of the loss tangent of the studied random Et:EHe copolymers was in agreement with that expected based on the DSC results.

A key assumption to the analysis of quasistatic indentation responses is that no cracking occurs around the indent or at the indent corners. The imaging facility of the indentation instrument equipped with a Berkovich tip seems to be sufficiently sensitive to determine whether cracking occurred. Cracks could be visualized that had resulted in only modest changes in the load-displacement response.

Acknowledgements: This research forms part of the research program of the Dutch Polymer Institute (DPI, project 496, technology area HTE). S. Jacobs and M. W. M. Fijten are gratefully acknowledged for synthesizing the poly(2-oxazoline).

Received: March 18, 2012; Published online: July 17, 2012; DOI: 10.1002/mame.201200094

Materials
Views
www.MaterialsViews.com

Macromol. Mater. Eng. 2013, 298, 78–88
© 2013 WILEY-VCH Verlag GmbH & Co. KGaA, Weinheim

Macromolecular
Journals

87

Keywords: cracking; creep; elastic properties; indentation; polymers

- [1] J. M. Kranenburg, C. A. Tweedie, K. J. Van Vliet, U. S. Schubert, *Adv. Mater.* **2009**, *21*, 3551.
- [2] L. Cheng, X. Xia, L. E. Scriven, W. W. Gerberich, *Mech. Mater.* **2005**, *37*, 213.
- [3] J. M. J. den Toonder, Y. Ramone, A. R. van Dijken, J. G. J. Beijer, G. Q. Zhang, *J. Electron. Packag.* **2005**, *127*, 267.
- [4] C. G. N. Pelletier, J. M. J. Den Toonder, L. E. Govaert, N. Hakiri, M. Sakai, *Philos. Mag.* **2008**, *88*, 1291.
- [5] M. L. Oyen, R. F. Cook, *J. Mater. Res.* **2003**, *18*, 139.
- [6] A. C. Fischer-Cripps, *Nanoindentation*, 2nd edition Springer-Verlag, New York **2004**.
- [7] H. G. H. van Melick, A. R. van Dijken, J. M. J. den Toonder, L. E. Govaert, H. E. H. Meijer, *Philos. Mag. A* **2002**, *82*, 2093.
- [8] W. C. Oliver, G. M. Pharr, *J. Mater. Res.* **1992**, *7*, 1564.
- [9] W. C. Oliver, G. M. Pharr, *J. Mater. Res.* **2004**, *19*, 3.
- [10] M. R. VanLandingham, J. S. Villarrubia, W. F. Guthrie, G. F. Meyers, *Macromol. Symp.* **2001**, *167*, 15.
- [11] D. C. Webster, *Macromol. Chem. Phys.* **2008**, *209*, 237.
- [12] C. A. Tweedie, D. G. Anderson, R. Langer, K. J. Van Vliet, *Adv. Mater.* **2005**, *17*, 2599.
- [13] G. Feng, A. H. W. Ngan, *J. Mater. Res.* **2002**, *17*, 660.
- [14] Y.-T. Cheng, C.-M. Cheng, *Mater. Sci. Eng., R* **2004**, *44*, 91.
- [15] J. M. Kranenburg, C. A. Tweedie, R. Hoogenboom, F. Wiesbrock, H. M. L. Thijs, C. Hendriks, K. J. Van Vliet, U. S. Schubert, *J. Mater. Chem.* **2007**, *17*, 2713.
- [16] K. L. Johnson, K. Kendall, A. D. Roberts, *Proc. R. Soc. A* **1971**, *324*, 301.
- [17] Y. Y. Lim, M. M. Chaudhri, *Philos. Mag.* **2004**, *84*, 2877.
- [18] M. Mata, J. Alcalá, *J. Mech. Phys. Solids* **2004**, *52*, 145.
- [19] H. G. H. van Melick, O. F. J. T. Bressers, J. M. J. den Toonder, L. E. Govaert, H. E. H. Meijer, *Polymer* **2003**, *44*, 2481.
- [20] K. Kempe, S. Jacobs, H. M. L. Lambermont-Thijs, M. M. W. M. Fijten, R. Hoogenboom, U. S. Schubert, *Macromolecules* **2010**, *43*, 4098.
- [21] S. A. Syed Asif, K. J. Wahl, R. J. Colton, *Rev. Sci. Instrum.* **1999**, *70*, 2408.
- [22] R. D. Deegan, O. Bakajin, T. F. Dupont, G. Huber, S. R. Nagel, T. A. Witten, *Nature* **1997**, *389*, 827.
- [23] B. J. Briscoe, L. Fiori, E. Pelillo, *J. Phys. D: Appl. Phys.* **1998**, *31*, 2395.

- [24] R. J. Young, P. A. Lovell, *BT Introduction to Polymers*, 2nd edition Chapman & Hall, London **1991**.
- [25] M. W. M. Fijten, J. M. Kranenburg, H. M. L. Thijs, R. M. Paulus, B. M. van Lankvelt, J. de Hullu, M. Springintveld, D. J. G. Thielen, C. A. Tweedie, R. Hoogenboom, K. J. Van Vliet, U. S. Schubert, *Macromolecules* **2007**, *40*, 5879.
- [26] R. Hoogenboom, M. W. M. Fijten, H. M. L. Thijs, B. M. van Lankvelt, U. S. Schubert, *Des. Mon. Polym.* **2005**, *8*, 659.
- [27] Hysitron Inc., *Feedback Control Users Manual*, v1.0.
- [28] T. A. P. Engels, L. E. Govaert, G. W. M. Peters, H. E. H. Meijer, *J. Polym. Sci., Part B: Polym. Phys.* **2006**, *44*, 1212.
- [29] S. A. Hayes, A. A. Goruppa, F. R. Jones, *J. Mater. Res.* **2004**, *19*, 3298.
- [30] H. E. H. Meijer, L. E. Govaert, *Macromol. Chem. Phys.* **2003**, *204*, 274.

P3 A systematic investigation of the effect of side chain branching on the glass transition temperature and mechanical properties of aliphatic (co-)poly(2-oxazoline)s

Kristian Kempe, Erik F.-J. Rettler, Renzo M. Paulus, Anette Kuse,
Richard Hoogenboom, Ulrich S. Schubert,

Polymer **2013**, *54*, 2036-2042.



A systematic investigation of the effect of side chain branching on the glass transition temperature and mechanical properties of aliphatic (co-)poly(2-oxazoline)s

Kristian Kempe^{a,b,1}, Erik F.-J. Rettler^{a,b,c}, Renzo M. Paulus^{a,b}, Anette Kuse^a, Richard Hoogenboom^{d,**}, Ulrich S. Schubert^{a,b,c,*}

^aLaboratory of Organic and Macromolecular Chemistry (IOMC), Friedrich-Schiller-University Jena, Humboldtstr. 10, 07743 Jena, Germany

^bJena Center for Soft Matter (JCSM), Friedrich-Schiller-University Jena, Philosophenweg 7, 07743 Jena, Germany

^cDutch Polymer Institute (DPI), John F. Kennedylaan 2, 5612 AB Eindhoven, The Netherlands

^dSupramolecular Chemistry Group, Department of Organic Chemistry, Ghent University, Krijgslaan 281 S4, B-9000 Ghent, Belgium

ARTICLE INFO

Article history:

Received 17 August 2012

Received in revised form

9 January 2013

Accepted 11 January 2013

Available online 22 January 2013

Dedicated to Prof. Dr. Axel H. E. Mueller on the occasion of his 65th birthday.

Keywords:

Low glass transition temperature

Poly(2-oxazoline)s

Branched polymers

ABSTRACT

The synthesis of a new branched 2-oxazoline monomer, namely 2-(3-ethylpentyl)-2-oxazoline is described. Microwave-assisted cationic ring-opening polymerization allows the synthesis of well-defined homopolymers as well as copolymers when copolymerized with 2-ethyl-2-oxazoline (EtOx). The systems obtained are investigated with regard to their thermal and mechanical properties. In order to elucidate structure–property correlations, these copolymers are compared to copolymers of EtOx with two other branched monomers, namely 2-(1-ethylpentyl)-2-oxazoline and 2-(3-ethylheptyl)-2-oxazoline comprising a different branching position or length of the main side chain, respectively. It is observed that the influence of the branching position on the glass transition temperature and mechanical properties is significantly higher than the length of the side chain. Furthermore, copolymerizations with EtOx are presented which enable the alteration of the thermal and mechanical properties showing a linear decrease of the glass transition temperatures as well as a decrease of the elastic modulus with increasing weight percentage of the branched monomers.

© 2013 Elsevier Ltd. All rights reserved.

1. Introduction

Low glass transition temperature (T_g) materials are of significant interest in everyday life. They possess broad application possibilities, such as in car tires, engine mountings, adhesives and inflatable boats [1]. At their usage temperature such materials show rubberlike properties, *i.e.* they are amorphous compounds with T_g 's below the operating temperature. Furthermore, from a more scientific point of view these kinds of materials might improve the phase separation of block copolymer segments [2,3]. Therefore, the

interest in new designer systems exhibiting such properties is of significant interest.

The cationic ring-opening polymerization (CROP) of 2-substituted 2-oxazolines, which was first reported in 1966 by four independent research groups [4–7], represents a suitable polymerization technique for the synthesis of well-defined (co-) polymers with distinct properties due to relatively simple variation possibility of the polymer side chains enabling adjustable polymer properties [8–11]. In recent years, poly(2-oxazoline)s (POxs) with various side groups and properties were prepared and studied ranging from alkyl- and aryl-substituents to more advanced functionalities, such as different fluorinated [12–14], amino [15], aldehyde [16], alkene [17–19], alkyne [20], and sugar groups [21]. In particular, the polymerization of 2-(*n*-alkyl)-2-oxazoline was extensively investigated with regard to their polymerization behavior as well as the thermal and surface properties of the resulting polymers [22]. In these studies, POxs with linear side chains containing up to five carbon atoms were found to exhibit amorphous behavior. However, recently the semi-crystalline character of poly(2-butyl-2-oxazoline) and poly(2-propyl-2-oxazoline) was described, which was attributed to side chain and main chain

* Corresponding author. Laboratory of Organic and Macromolecular Chemistry (IOMC), Friedrich-Schiller-University Jena, Humboldtstr. 10, 07743 Jena, Germany. Tel.: +49 3641 948 200/01; fax: +49 3641 948 202.

** Corresponding author. Tel.: +32 92644482.

E-mail addresses: richard.hoogenboom@ugent.be (R. Hoogenboom), ulrich.schubert@uni-jena.de (U.S. Schubert).

¹ Current address: Nanostructured Interfaces and Materials group, Department of Chemical & Biomolecular Engineering, The University of Melbourne, Parkville, Victoria 3010, Australia.

crystallinity, respectively [23]. Moreover, even the crystallization behavior of poly(2-ethyl-2-oxazoline) (PEtOx) when kept above the cloud point temperature was reported [24]. In any case POxs with aliphatic side chains containing more than five carbon atoms represent semi-crystalline polymers with melting temperatures at about 150 °C.

It is well known, that the melting temperature (T_m) and glass transition temperature (T_g) of a polymer can be influenced by certain parameters. Particularly the nature of the side chain plays an important role: the longer the side chain the lower the T_g due to the higher flexibility of the polymer, as it is reported for different lengths of poly(*n*-alkyl methacrylates) [25]. Only the 1-position of the side chain has a negative influence on the molecular motion of the polymer whereas a further elongation acts as a softener. In addition, branching of the side chain can influence the temperature transitions in different ways. On the one hand T_g can increase due to an increase of the steric hindrance caused by the more rigid branched alkyl substituent [26]. On the other hand further substituents can lower the packing density by pushing neighboring chains apart. Furthermore, branching of the side chain can suppress the crystallization of the polymer. Since POxs show a decrease of T_g with increasing number of carbon atoms only for $n = 1$ to 5, i.e. longer polymers only revealed a T_m , the plasticization effect of a long side chain could not be exploited to further lower the glass transition temperature. This drawback was recently overcome by the introduction of an ethyl branching group in the side chain of poly(2-heptyl-2-oxazoline) resulting in a polymer with a T_g of -6 °C [27].

Up to date only a few more branched poly(2-oxazoline)s are known. Poly(2-(*i*-propyl)-2-oxazoline) (PiPropOx) and poly(2-(*i*-butyl)-2-oxazoline) (PiButOx) are semi-crystalline with $T_m > 200$ °C contrary to their linear analogs indicating an influence of the branching methyl group [7]. Furthermore, the synthesis of 2-(*tert*-butyl)-2-oxazoline was reported [28], but a detailed characterization suffered so far from the low solubility of the respective polymer, and the polymer could not be synthesized at all, respectively [29]. Still, the scope of the branched POxs has to be expanded in order to gain new insights in the effect of branching.

In previous works of our group [23,30,31], depth-sensing indentation (DSI) has proven itself as a very suitable tool to determine the mechanical properties of POx homo- and copolymers, in particular when only small amounts of material are available and thus, macroscopic tests like tensile or compression tests are unapplicable. Furthermore, the high-throughput capabilities of this technique allow for automated screening of large numbers of different materials in a short time period, making it ideal for comparative studies of similar materials. In our previous study on POx homopolymers with linear side-chains, it was found that the elastic modulus strongly depends on the number of carbon atoms within the linear side-chain.

Here, we report a systematic investigation of the effect of side-chain branching in aliphatic POx. A new branched 2-oxazoline monomer, namely 2-(3-ethylpentyl)-2-oxazoline (3EPOx), is presented, which allows evaluation of the influence of the position of the ethyl group in the side chain and the main side-chain length when compared to the known 2-(1-ethylpentyl)-2-oxazoline (EPOx) and 2-(3-ethylheptyl)-2-oxazoline (EHOx), respectively. To this end, the microwave-assisted homopolymerization of 3EPOx as well as the copolymerizations of 3EPOx and EPOx with EtOx are described. The homopolymers of all three monomers as well as their copolymers with EtOx were compared in view of their thermal behavior. Furthermore, samples exhibiting a T_g above room temperature were subjected to depth-sensing-indentation studies in order to elucidate and compare their elastic moduli.

2. Experimental section

2.1. Materials

1-Bromo-2-ethylbutane, *n*-butyllithium and *N,N,N',N'*-tetramethylethylenediamine (TMEDA) were purchased from Sigma-Aldrich and were used as received. 2-Methyl-2-oxazoline, 2-ethyl-2-oxazoline and methyl tosylate were obtained from Acros and were distilled to dryness over barium oxide (BaO) and stored under argon. 2-(1-Ethylpentyl)-2-oxazoline was synthesized as reported previously [32].

2.2. General methods and instrumentation

The Initiator Sixty single-mode microwave synthesizer from Biotage, equipped with a noninvasive IR sensor (accuracy: $\pm 2\%$), was used for polymerizations under microwave irradiation. Microwave vials were heated overnight to 110 °C and allowed to cool to room temperature under argon before usage. All polymerizations were carried out with temperature control. Gas chromatography (GC) was measured on an Interscience Trace gas chromatograph with a Trace Column RTX-5 connected to a PAL autosampler. Size exclusion chromatography (SEC) measurements were performed on an Agilent system equipped with a diode array detector and a refractive index detector. Two PSS SDV (5 μm pore size) columns were placed in series. DMA with 5 mmol of LiCl was used as eluent at 1 mL/min flow rate, and the column oven was set to 50 °C. Molar masses were calculated against polystyrene standards. ^1H NMR spectra were recorded on a Bruker AC 300 MHz spectrometer at room temperature, with CDCl_3 as the solvent. The chemical shifts are given in ppm relative to the signal from residual non-deuterated solvent. For the MALDI measurements an Ultraflex III TOF/TOF apparatus (Bruker Daltonics, Bremen, Germany) equipped with a Nd:YAG laser and a collision cell was used. All spectra were measured in the positive reflector or linear mode. The instrument was calibrated prior to each measurement with an external PMMA standard from PSS Polymer Standards Services GmbH (Mainz, Germany). Thermal transitions were determined on a DSC 204 F1 Phoenix by Netzsch under a nitrogen atmosphere from -100 – 220 °C with a heating rate of 10 K/min and 20 K/min and a cooling rate of 40 K/min (for the calculations only the third heating curve of three runs was considered). The depth-sensing indentation tests were performed on a Hysitron TriboIndenter with a conospherical diamond indenter tip of approximately 4.7 μm radius. In a typical experiment, the tip was loaded up to a maximum force of 1500 μN and consecutively unloaded. To diminish the influence of the material's time-dependent behavior, very short times for each segment have been chosen. Thus, the loading was performed in 0.5 s, the unloading in 0.1 s. The mechanical properties were derived from the unloading curve, applying the method proposed by Oliver and Pharr [33]. The reduced moduli (E_r) were converted into indentation moduli (E_i) assuming a Poisson's ratio of 0.4 according to:

$$E_i = \frac{1 - \nu_{\text{sample}}^2}{1 - \frac{1 - \nu_{\text{indenter}}^2}{E_{\text{indenter}}}} \quad (1.1)$$

where ν is the Poisson's ratio of the respective material. The values for the diamond indenter tip ($\nu_{\text{indenter}} = 0.2$ and $E_{\text{indenter}} = 1200$ GPa) have been used from the literature [34]. Values have been averaged over 16 measurements for each material. All measurements have been performed in an automated run overnight.

2.3. Monomer synthesis

2-(3-Ethylpentyl)-2-oxazoline (3EPOx): A solution of 12.67 g (0.109 mol) TMEDA in 375 mL THF was cooled to $-78\text{ }^{\circ}\text{C}$ under an argon atmosphere. Within 40 min 41.25 mL *n*-butyl–lithium (2.5 M in hexane) were added and the solution was stirred for 60 min. Subsequently, 9.28 g (0.109 mol) 2-methyl-2-oxazoline (MeOx) were added dropwise and stirring was continued for another 2 h at $-78\text{ }^{\circ}\text{C}$. After the addition of 14.86 g (0.09 mol) 1-bromo-2-ethylbutane, the solution was allowed to warm to room temperature overnight. The reaction was quenched after 24 h with 180 mL methanol and the solvents were evaporated under reduced pressure. The residue was dissolved in 180 mL chloroform and 180 mL NaHCO_3 solution and the aqueous phase was extracted three times with 60 mL chloroform. The combined organic phases were washed with water and brine. After drying over MgSO_4 , the solvent was removed under reduced pressure and the crude product was purified by distillation ($62\text{ }^{\circ}\text{C}$, 5.2×10^{-2} Torr) to yield 5.4 g (0.032 mol, 29%) (3EPOx).

$^1\text{H NMR}$ (250 MHz, CDCl_3 , $25\text{ }^{\circ}\text{C}$): $\delta = 0.84$ (t, 6H, CH_3), 1.22 (m, 1H, CH), 1.29 (m, 4H, CH_2CH_3), 1.59 (m, 2H, $\text{NCOCH}_2\text{CH}_2$), 2.23 (m, 2H, $\text{NCOCH}_2\text{CH}_2$), 3.81 (t, 2H, CNCH_2), 4.21 (t, 2H, COCH_2). $^{13}\text{C NMR}$ (100 MHz, CDCl_3 , $25\text{ }^{\circ}\text{C}$): $\delta = 10.7$ (CH_3), 25.02, 25.47, 28.88, 40.22, 32.42, 38.5 (CH/CH_2), 54.35 (CNCH_2), 67.1 (COCH_2), 169.04 (CNCH_2). HR-MS (ESI+): calcd for $\text{C}_{10}\text{H}_{19}\text{NO} + \text{H}^+$: 170.1539, found: 170.1541.

2.4. Microwave-assisted homopolymerization of 3EPOx

A stock solution containing initiator (methyl tosylate), monomer (3EPOx) and solvent (acetonitrile) was prepared. The monomer concentration was adjusted to 1 M, and a monomer-to-initiator-ratio of 60 was used. The stock solution was divided over seven polymerization vials that were capped under argon. For the calculation of the conversion, three t_0 -samples were taken. The vials were heated to $140\text{ }^{\circ}\text{C}$ for different times in the microwave synthesizer. After cooling, the reaction was quenched by addition of 50 μL water. GC and SEC samples were prepared to determine the monomer conversion and the polymer molar masses, respectively. For the calculation of the monomer conversion, the polymerization solvent was used as internal standard.

2.5. Microwave-assisted copolymerization of EtOx and branched comonomer: preparation of the statistical copolymers for detailed property studies

Copolymers (EtOx/EHOx, EtOx/3EPOx, EtOx/EHOx) with a total monomer-to-initiator-ratio of 100 with 10% increments were prepared. A polymerization solution containing initiator, appropriate amounts of monomers and solvent was irradiated in the microwave for a pre-calculated time (based on the homopolymerization kinetics) to reach full conversion. The full consumption of both monomers as well as the monomer ratios incorporated in the final polymer were assured by $^1\text{H NMR}$ spectroscopy and the resulting copolymer was either precipitated in ice-cold diethyl ether or dried under reduced pressure to remove the residual monomer and solvent.

2.6. Film preparation and indentation measurements

Prior to the indentation measurements, small amounts (~ 20 mg) of each material were dissolved in chloroform and subsequently dropcasted onto Teflon[®]-coated 12-well microscopy glass slides. These glass slides are generally used for biological arrays, as the Teflon[®]-coating prevents the dropcasted solution from spreading out over a larger area.

After drying overnight, the samples were heated above T_g for several hours under reduced pressure to remove solvent residues.

3. Results and discussion

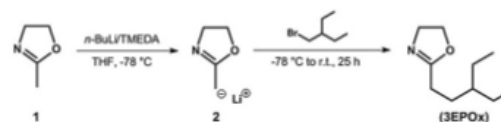
3.1. Monomer synthesis

The new monomer, 2-(3-ethylpentyl)-2-oxazoline (3EPOx), was synthesized according to a general procedure recently published for the synthesis of 2-substituted 2-oxazolines [16]. In contrast to the synthesis of 2-(1-ethylpentyl)-2-oxazoline (EPOx) [32], which was obtained starting from the corresponding acid chloride, 3EPOx represents the product of the nucleophilic attack of the deprotonated 2-methyl-2-oxazoline (MeOx) onto 1-bromo-2-ethylbutane (Scheme 1). Thus, this monomer can be synthesized in a straightforward one-pot procedure including the generation of the nucleophile using *n*-butyllithium (*n*-BuLi) and *N,N,N',N'*-tetramethylethylenediamine (TMEDA) as well as the addition of 1-bromo-2-ethylbutane. Here, it is noteworthy that several trials failed to synthesize the monomer with the ethyl branch in the 2-position of the side chain. Most likely, rearrangements of the corresponding 2-bromohexane compound to more stable systems prevent the reaction.

3.2. Homopolymerization of 3EPOx

As already demonstrated by the homopolymerization of EHOx and EPOx, branched 2-oxazolines are able to undergo a living CROP showing a similar behavior as their linear analogs. Both monomers exhibit a living character under appropriate conditions, as indicated by the absence of chain transfer and termination reactions or only limited extent of these side reactions, respectively. The living manner of the polymerization is crucial in order to enable the synthesis of well-defined block and statistical copolymer structures. 3EPOx was also polymerized applying the optimized and nowadays frequently used conditions for the microwave-assisted CROP of 2-oxazolines, i.e. methyl tosylate as initiator, acetonitrile as solvent and a polymerization temperature of $140\text{ }^{\circ}\text{C}$. Under these conditions a linear increase of the $\ln([M]_0/[M]_t)$ with time was observed demonstrating a constant concentration of propagating species indicative of a living polymerization mechanism of the monomer. The resulting first-order kinetic plot is shown in Fig. 1 left. The almost perfect linear fit of the data ($R^2 = 0.99$) indicates the high reproducibility of the microwave-assisted polymerization since each data point represents a separate polymerization reaction. The linear increase in the molar mass with conversion further supports the living character of the polymerization (Fig. 1 right). The polymers showed reasonable polydispersity index (PDI) values which are slightly higher (up to 1.4) in particular for higher conversions indicating the occurrence of some side reactions.

In order to confirm the molecular composition of the polymers obtained, matrix-assisted laser desorption/ionization time-of-flight (MALDI-TOF) mass spectrometry studies were conducted of the early kinetic samples with molar masses lower than 3000 g mol^{-1} (Fig. 2, left). The expanded section of the mass spectrum (Fig. 2,



Scheme 1. Schematic representation of the reaction scheme for the synthesis of 2-(3-ethylpentyl)-2-oxazoline (3EPOx).

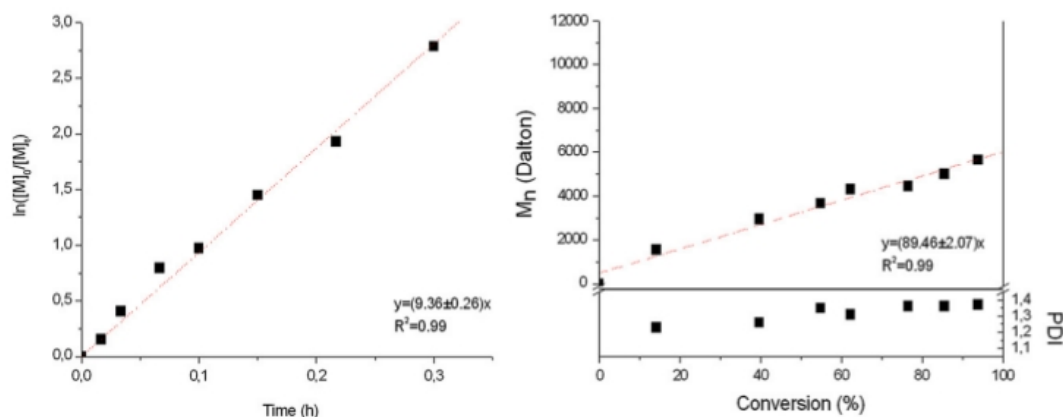


Fig. 1. Homopolymerization of 3EPOx (1 M) under microwave irradiation in acetonitrile at 140 °C using methyl tosylate as initiator. Left: First-order kinetic plot. Right: M_n and PDI value against conversion plot for the kinetic screening determined by SEC (dotted lines represent the linear regression).

right) reveals an exact agreement of the isotopic pattern of the calculated and the measured signals. In addition, the signal of the proton-initiated polymer resulting from chain transfer reactions can be assigned. The latter shows a higher intensity than the actual product, which might indicate the occurrence of significant chain transfer reactions at the early stage of the polymerization.

3.3. Copolymerizations with 2-ethyl-2-oxazoline (EtOx)

Due to the controlled character of their homopolymerizations all three monomers, EHOx, EPOx and 3EPOx, are suitable for copolymerization with other 2-oxazolines. In fact, EPOx and EHOx were already used for the synthesis of (block) copolymers demonstrating their potential for copolymerizations. To study the tunability of the glass transition temperature as well as the elastic modulus of these systems the copolymerization with EtOx was chosen (Scheme 2). A series of copolymers was synthesized of both comonomers having different ratios of monomers using 10 mol% increments of EPOx and 3EPOx, respectively. Because the copolymerization of EHOx and EtOx was already reported only the copolymers showing T_g 's above room temperature were synthesized (mol% EHOx < 30) because these are suitable for depth-sensing indentation. All copolymerizations were performed under

microwave irradiation at 140 °C. The polymerizations were pushed in each case to full conversion in order to guarantee the targeted feed composition and to simplify the purification of the resulting copolymers. Thus, slightly higher PDI values were expected for the copolymers (Tables 1–3). However, the final monomer ratios as determined by ^1H NMR spectroscopy are in good agreement with the feed ratios. Prior to differential scanning calorimetry (DSC) and depth-sensing indentation (DSI) measurements, the copolymers were purified by extensive drying under reduced pressure at elaborated temperature. A complete overview of the copolymers obtained can be found in Table 1 (P(EPOx-*stat*-EtOx), Table 2 (P(3EPOx-*stat*-EtOx) and Table 3 (P(EHOx-*r*-EtOx).

3.4. Thermal transitions

The thermal properties of the PEPOx and P3EPOx homopolymers as well as of the copolymer series P(EPOx-*stat*-EtOx) and P(3EPOx-*stat*-EtOx) were determined by DSC and compared to the known PEHOx and P(EHOx-*r*-EtOx) system. PEPOx and P3EPOx exhibit the same number of carbon atoms in the side chain, the same branching group but different branching positions. Both polymers were found to be amorphous, *i.e.* revealing only a glass transition and no melting point. In a similar manner as for the

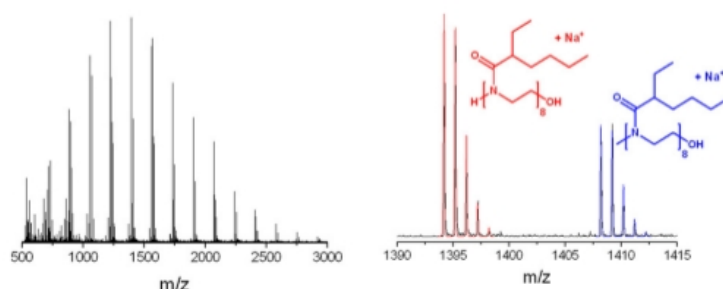
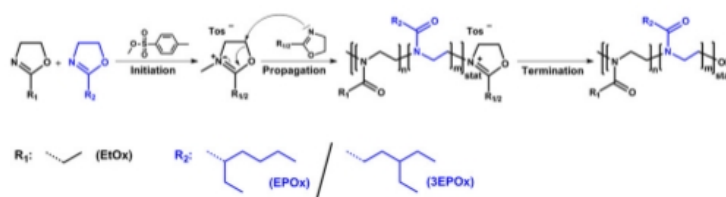


Fig. 2. Representative MALDI-TOF MS spectrum (matrix: DCTB; ionization salt: NaI; solvent: CHCl_3) of P3EPOx (left). In the expanded spectrum the signals are assigned to the according polymer structures encompassing the methyl (blue) and the proton (red) initiated polymers (right). (For interpretation of the references to colour in this figure legend, the reader is referred to the web version of this article.)



Scheme 2. Schematic representation of the mechanism of the cationic ring-opening copolymerization of 2-oxazolines.

PEHOx homopolymer the crystallinity of the polymers is suppressed in comparison to their linear analogs with the same number of carbon atoms in the side chain. Poly(2-heptyl-2-oxazoline) as well as poly(2-nonyl-2-oxazoline) are semi-crystalline polymers with T_m about 150 °C whereby remaining amorphous fractions are too small to detect a T_g by DSC. Thus, the incorporation of branching points in the side chain changes the thermal behavior from semi-crystalline to amorphous. Furthermore, the position of the branching point and the length of the side chain influence T_g significantly. In general, the ethyl side group lowers the T_g which is consistent with a decrease in the packing density associated with an easier molecular motion of the polymer. A direct comparison of PEPOx and P3EPOx demonstrates the importance of the branching position: PEPOx with the ethyl branch in 1-position of the side chain exhibits a glass transition at about 30 °C whereas P3EPOx with the ethyl branch in 3-position shows a much lower T_g at about 5 °C suggesting a lower packing density of the polymer in case of P3EPOx. Moreover, the branch position in 1-position hinders the backbone movement due to stronger steric hindrance causing a higher T_g . Additional information concerning the length of the main side chain was obtained from the difference between P3EPOx and PEHOx. Increasing the length of the main side chain while keeping the branching position constant results in a further decrease of the T_g to -6 °C. As a consequence, a linear order for the T_g was obtained: PEPOx > P3EPOx > PEHOx.

To study the effect of molecular composition on the thermal properties, P(EPOx-*stat*-EtOx) and P(3EPOx-*stat*-EtOx) copolymers with 10 mol% increments branched monomer were synthesized. In either case the difference of the T_g between the two comonomers allows the alteration of the glass transition temperature by varying the monomer composition. A linear behavior was observed for both copolymer series. As can be seen from Fig. 3, the T_g of the copolymers are linearly decreasing with increasing weight percent of

the branched monomers. Again it can be seen that the incorporation of the EHOx alters the T_g significantly and decreases the T_g value faster than EPOx and 3EPOx [35]. However, in each case an increasing amount of branched side chains causes a lowering of the packing density of the polymer chains by pushing neighboring chains apart which is consistent with a decrease of the glass transition temperature. To conclude, all three series show a nearly perfect linear relationship enabling a fine-tuning of the thermal properties not only by choosing the sort of branched monomer but also by synthesizing copolymers with varying compositions.

3.5. Mechanical properties

The mechanical properties of the homo- and copolymers were investigated by DSI measurements. Fig. 4 shows selected examples of load-displacement responses obtained during the indentation experiments of the P(EPOx-*stat*-EtOx) series. As can be clearly seen from the maximum indentation depths, the materials become softer with increasing comonomer content. This holds true for all three series, as the EtOx (due to its higher T_g) always represents the 'hard' component in the copolymer.

Fig. 5 shows the indentation moduli of the investigated copolymer series. Within each library, the moduli linearly decrease with increasing comonomer content. This is not surprising, regarding the linear decrease in the glass transitions shown in Fig. 3. As the difference between room temperature and T_g decreases, the polymer chains gain mobility. At the point where T_g is lower than room temperature, all materials will flow and exhibit no significant differences in the moduli [31]. Therefore, such samples have been excluded from the indentation experiments.

Table 1

Molecular characteristics and selected properties of the P(EPOx-*stat*-EtOx) copolymer series (T_g = glass transition temperature, E_i = indentation modulus).

EPOx ^a			M_n^b (g mol ⁻¹)	PDI ^b	T_g^c (°C)	E_i^d (GPa)
Mol% _{theor.}	Mol% _{exp.}	wt% _{exp.}				
0	0	0	12,000	1.41	58.7	3.25
10	11	18	9500	1.2	55.7	3.68
20	19	29	10,300	1.12	50.3	3.48
30	30	42	10,100	1.22	46.2	2.81
40	41	55	13,800	1.17	40.3	2.68
50	50	63	10,000	1.43	38.3	2.48
60	61	73	7100	1.52	36.3	2.19
70	74	83	7000	1.67	35.4	1.89
80	83	89	4800	1.47	32.7	1.76
90	88	93	5200	1.48	31.8	1.54
100	100	100	5800	1.55	30.3	1.40

^a Determined using ¹H NMR spectroscopy.

^b SEC results (eluent: *N,N*-dimethylacetamide with 2.1 g L⁻¹ LiCl; PS standards).

^c From DSC measurements.

^d From DSI measurements.

Table 2

Molecular characteristics and selected properties of the P(3EPOx-*stat*-EtOx) copolymer series (T_g = glass transition temperature, E_i = indentation modulus).

3EPOx ^b			M_n^c (g mol ⁻¹)	PDF	T_g^d (°C)	E_i^e (GPa)
Mol% _{theor.}	Mol% _{exp.}	wt% _{exp.}				
0	0	0	12,000	1.41	58.7	3.25
10	11	17	7900	1.18	50.6	3.44
20	25	36	5400	1.43	41.4	2.89
30	33	45	6400	1.48	38.0	2.83
40	42	53	6800	1.54	31.0	2.51
50	52	65	4800	1.58	23.1	^a
60	68	78	4200	1.58	18.5	^a
70	77	85	5300	1.46	19	^a
80	85	91	4700	1.58	12.3	^a
90	93	96	5300	1.58	7.5	^a
100	100	100	5500	1.44	2.6	^a

^a Samples with a T_g below room temperature were excluded from the indentation measurements.

^b Determined using ¹H NMR spectroscopy.

^c SEC results (eluent: *N,N*-dimethylacetamide with 2.1 g L⁻¹ LiCl; PS standards).

^d From DSC measurements.

^e From DSI measurements.

Table 3

Molecular characteristics and selected properties of the P(EHOx-*r*-EtOx) copolymers with glass transition temperatures above room temperature (E_i = indentation modulus).

EHox ^a			M_n^b (g mol ⁻¹)	PDI ^b	E_i^c (GPa)
Mol% _{theor}	Mol% _{exp}	wt% _{exp}			
0	0	0	12,000	1.41	3.25
10	11	20	9600	1.15	3.37
20	21	35	10,100	1.16	2.91
30	33	49	11,300	1.16	2.78

^a Determined using ¹H NMR spectroscopy.

^b SEC results (eluent: *N,N*-dimethylacetamide with 2.1 g L⁻¹ LiCl; PS standards).

^c From DSI measurements.

When comparing the different libraries with each other, it could be observed that upon changing the position of the ethyl-group in the side-chain from the 1- to the 3-position, the effect on the mechanical properties is more prominent than upon elongating the main side-chain by another ethyl-unit consistent with the T_g observations. This may be due to the steric hindrance of the branched side-chain. Considering the number of stiff 'junction' points per repeating unit, the P(EPOx-*stat*-EtOx) only has one between the main chain and the two side chains (considering one ethyl- and one butyl- side-chain starting from the branching point), while the P(3EPOx-*stat*-EtOx) has two junction points, one between main and side-chain and one where the side-chain branches. It has to be mentioned that the total number of carbon atoms in the side-chain is the same in both cases.

When comparing the P(3EPOx-*stat*-EtOx) with the P(EHOx-*r*-EtOx), the moduli do not significantly differ, contrary to the difference in the glass transitions. As the steric hindrance is already high due to the second junction point, an increase in one of the secondary side-chains does not significantly increase the interchain distance any further.

The unexpectedly lower modulus of the pure EtOx is a result of the hygroscopicity of that particular sample. As previous studies have shown [23], EtOx shows a significant water-uptake from the surrounding atmosphere. The incorporated water causes a swelling of the polymer by increasing the interchain volume, thus increasing chain flexibility which, in turn, results in a lower elastic modulus. In our previous study, the modulus of a dried PEtOx was found around 4.5 GPa, however, in that study, a polymer with approx. 60 repeating units was investigated.

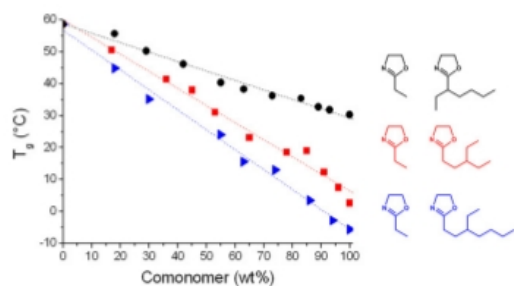


Fig. 3. Dependence of the glass transition of the P(EtOx-*stat*-EPOx) (●; $R^2 = 0.982$) and the P(EtOx-*stat*-3EPOx) (■; $R^2 = 0.985$) copolymer on the weight percent of EPOx and 3EPOx, respectively. For comparison reasons the P(EtOx-*r*-EHOx) (▲; $R^2 = 0.993$) series was added [35]. Dotted lines represent the linear fit of the data points (R^2 can be regarded as a measure for the standard deviation, whereby it represents both the standard deviation in the polymer composition as well as the DSC measurements; assuming ideal mixing of the polymer segments).

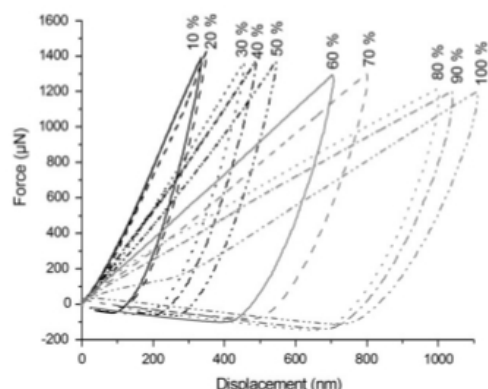


Fig. 4. Load-displacement curves obtained from the indentation experiments on the P(EPOx-*stat*-EtOx) series. EPOx content is increasing from left to right.

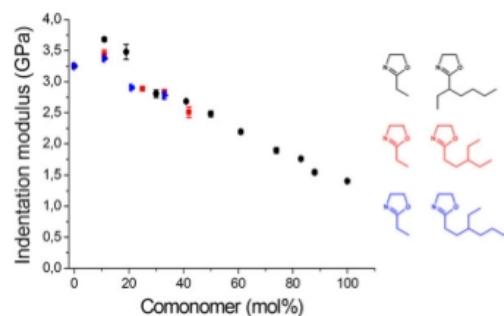


Fig. 5. Indentation moduli of the investigated copolymer systems: P(EtOx-*stat*-EPOx) (●), P(EtOx-*stat*-3EPOx) (■), P(EtOx-*r*-EHOx) (▲). Error bars show one standard deviation over at least 16 measurements and may be smaller than the symbols.

4. Conclusions

In conclusion, new insights in the effect of side chain branching of poly(2-oxazoline)s were presented. By means of a new branched 2-oxazoline monomer, the influence of the branching position as well as the length of the main side chain in the respective POx was elucidated. To this end, homopolymers and copolymers of the new branched 2-oxazoline were systematically compared to two other branched systems with regard to their thermal behavior and elastic modulus. All copolymers (branched 2-alkyl-2-oxazoline/EtOx) showed a linear decrease of the glass transition temperature possessing decays depending on the kind of the branched comonomer. Copolymers with glass transition temperatures above room temperature were applied to depth-sensing indentation measurements which demonstrated a decreasing elastic modulus with increasing percentage of the branched 2-oxazoline comonomer consistent with a softening of the material. In both, thermal as well as mechanical studies, it was found that changing the position of the ethyl-group in the side-chain from the 1- to the 3-position causes a more prominent change in properties than by elongating the main side-chain by another ethyl-unit clearly demonstrating that the branching position has a stronger effect on the chain mobility.

These results motivate the study of polymers with even more complex side chain branching which might yield new interesting properties. Furthermore, the usage of these monomers for new block copolymer systems is currently under investigation.

Acknowledgments

The authors thank the Dutch Polymer Institute (DPI, Technology area HTE) and the Thueringer Kultusministerium (grant no. B715-07011 and B515-07008) for financial support. K.K is grateful for the Alexander Humboldt foundation for financial support. R.H. acknowledges the Ghent University for support via the Concerted Research Actions (project BOF11/GOA/023). Furthermore, we thank Anja Baumgärtel for MALDI-TOF MS measurements.

References

- [1] Saccomandi G, Ogden RW. *Mechanics and thermomechanics of rubberlike solids*. Wien: Springer; 2004.
- [2] Huang H, Chung B, Jung J, Park H-W, Chang T. *Angew Chem Int Ed* 2009;48:4594–7.
- [3] Nardin C, Hirt T, Leukel J, Meier W. *Langmuir* 2000;16:1035–41.
- [4] Tomalia DA, Sheets DP. *J Polym Sci Part A: Polym Chem* 1966;4:2253–65.
- [5] Seeliger W, Thier W. *Angew Chem Int Ed* 1966;5:612–7.
- [6] Kagiya T, Narisawa S, Maeda T, Fukui K. *J Polym Sci Part C: Polym Lett* 1966;4:441–5.
- [7] Bassiri TG, Levy A, Litt M. *J Polym Sci Part C: Polym Lett* 1967;5:871–9.
- [8] Hoogenboom R. *Angew Chem Int Ed* 2009;48:7978–94.
- [9] Makino A, Kobayashi S. *J Polym Sci Part A: Polym Chem* 2010;48:1251–70.
- [10] Schlaad H, Diehl C, Gress A, Meyer M, Demirel AL, Nur Y, et al. *Macromol Rapid Commun* 2010;31:511–25.
- [11] Adams N, Schubert US. *Adv Drug Deliv Rev* 2007;59:1504–20.
- [12] Lobert M, Thijs HML, Erdmenger T, Eckardt R, Ulbricht C, Hoogenboom R, et al. *Chem Eur J* 2008;14:10396–407.
- [13] Miyamoto M, Aoi K, Saegusa T. *Macromolecules* 1989;22:3540–3.
- [14] Ivanova R, Komenda T, Bonne TB, Ludtke K, Mortensen K, Pranzas PK, et al. *Macromol Chem Phys* 2008;209:2248–58.
- [15] Cesana S, Auernheimer J, Jordan R, Kessler H, Nuyken O. *Macromol Chem Phys* 2006;207:183–92.
- [16] Taubmann C, Luxenhofer R, Cesana S, Jordan R. *Macromol Biosci* 2005;5:603–12.
- [17] Gress A, Volkel A, Schlaad H. *Macromolecules* 2007;40:7928–33.
- [18] Kempe K, Hoogenboom R, Schubert US. *Macromol Rapid Commun* 2011;32:1484–9.
- [19] Cai GF, Litt MH. *J Polym Sci Part A: Polym Chem* 1996;34:2679–88.
- [20] Luxenhofer R, Jordan R. *Macromolecules* 2006;39:3509–16.
- [21] Kempe K, Weber C, Babiuch K, Gottschalk M, Hoogenboom R, Schubert US. *Biomacromolecules* 2011;12:2591–600.
- [22] Hoogenboom R, Fijten MMW, Thijs HML, Van Lankvelt BM, Schubert US. *Des Monomers Polym* 2005;8:659–71.
- [23] Rettler EFJ, Lambermont-Thijs HML, Kranenburg JM, Hoogenboom R, Unger MV, Siesler HW, et al. *J Mater Chem* 2011;21:17331–7.
- [24] Guner PT, Miko A, Schweinberger FF, Demirel AL. *Polym Chem* 2012;3:322–4.
- [25] Rogers SS, Mandelkern L. *J Phys Chem* 1957;61:985–90.
- [26] Tsuchida S, Tadano K, Yano S. *Polym Bull* 1996;37:97–101.
- [27] Kempe K, Jacobs S, Lambermont-Thijs HML, Fijten MMW, Hoogenboom R, Schubert US. *Macromolecules* 2010;43:4098–104.
- [28] Kempe K, Lobert M, Hoogenboom R, Schubert US. *J Comb Chem* 2009;11:274–80.
- [29] Huber S, Jordan R. *Colloid Polym Sci* 2008;286:395–402.
- [30] Kranenburg JM, Thijs HML, Tweedie CA, Hoepfener S, Wiesbrock F, Hoogenboom R, et al. *J Mater Chem* 2009;19:222–9.
- [31] Rettler EFJ, Kranenburg JM, Lambermont-Thijs HML, Hoogenboom R, Schubert US. *Macromol Chem Phys* 2010;211:2443–8.
- [32] Kempe K, Baumgaertel A, Hoogenboom R, Schubert US. *J Polym Sci Part A: Polym Chem* 2010;48:5100–8.
- [33] Oliver WC, Pharr GM. *J Mater Res* 1992;7:1564–83.
- [34] <http://www.sp3inc.com/diamond.htm>.
- [35] T_g data of P(EHOx-r-EtOx) were taken from Ref. [27].

P4 Water uptake of poly(2-*N*-alkyl-2-oxazoline)s: Temperature-dependent FTIR spectroscopy and two-dimensional correlation analysis

Erik F.-J. Rettler, Miriam V. Unger, Richard Hoogenboom, Heinz W. Siesler,
Ulrich S. Schubert,

Appl. Spectrosc. **2012**, *10*, 1145-1155.

Water Uptake of Poly(2-*N*-Alkyl-2-Oxazoline)s: Temperature-Dependent Fourier Transform Infrared (FT-IR) Spectroscopy and Two-Dimensional Correlation Analysis (2DCOS)

Erik F.-J. Rettler,^{a,b,c,d} Miriam V. Unger,^e Richard Hoogenboom,^{a,b} Heinz W. Siesler,^e Ulrich S. Schubert^{a,b,c,d,*}

^a Laboratory of Macromolecular Chemistry and Nanoscience, Eindhoven University of Technology, P.O. Box 513, Den Dolech 2, 5600 MB Eindhoven, The Netherlands

^b Dutch Polymer Institute (DPI), John F. Kennedylaan 2, 5612 AB Eindhoven, The Netherlands

^c Laboratory of Organic and Macromolecular Chemistry (IOMC), Friedrich-Schiller-Universität Jena, Humboldtstrasse 10, 07743 Jena, Germany

^d Jena Center for Soft Matter (JCSM), Friedrich-Schiller-Universität Jena, Humboldtstrasse 10, 07743 Jena, Germany

^e Department of Physical Chemistry, University of Duisburg-Essen, Schuetzenbahn 70, 45117 Essen, Germany

A library of poly(2-oxazoline)s with varying length of the alkyl side-chain has been investigated by variable-temperature Fourier transform infrared (FT-IR) spectroscopy. These polymers are suitable for studies of structure–property relationships as their cationic ring-opening polymerization and the relatively facile monomer synthesis enable a control of the molecular structure. In this contribution, the number of carbon atoms in the linear side-chain is systematically varied from a short methyl to a long nonyl group. Previous studies showed that the sample library can be split in two groups: poly(2-oxazoline)s with a short side-chain (methyl-, ethyl-, and isopropyl-) exhibit hygroscopic behavior, while those with longer side-groups (butyl- and longer) were found to be semi-crystalline. To gain further insight into the mechanisms of hydrogen bonding and crystallization, temperature-dependent infrared (IR) spectroscopy has been applied in the current study. The processes involved have been monitored by generalized two-dimensional correlation spectroscopy (2DCOS) and perturbation-correlation moving-window two-dimensional correlation spectroscopy (PCMW2D) in the C=O stretching region around 1645 cm⁻¹. These advanced analysis techniques provided valuable additional information on the material behavior during heating. As water is removed from the samples in the course of the heating process, it was possible to clearly distinguish between “loosely associated” and hydrogen-bonded water. Furthermore, the melting process of the semi-crystalline samples could be depicted. For the poly(2-isopropyl-2-oxazoline) even a crystallization process could be monitored in the temperature range between glass transition and melting.

Index Headings: Poly(2-oxazoline)s; Water uptake; TGA; Hydrogen bonding; Crystallinity; Temperature-dependent FT-IR-spectroscopy; Fourier transform infrared spectroscopy; Generalized 2D correlation spectroscopy; 2DCOS; Perturbation-correlation moving-window 2D correlation spectroscopy.

INTRODUCTION

Due to their relatively facile monomer synthesis, poly(2-oxazoline)s have regained major interest in the last decades.¹ As has been shown, the material properties are mainly governed by the length and type of side-chain. Thus, by copolymerizing different 2-oxazoline monomers, the material properties can be fine-tuned to different application requirements.^{2–5}

Received 8 March 2012; accepted 13 June 2012.

* Author to whom correspondence should be sent. E-mail: ulrich.schubert@uni-jena.de.
DOI: 10.1366/12-06650

As a result of their structural similarities with polypeptides, poly(2-oxazoline)s have received significant attention for biomedical applications.^{1,6} Their high biocompatibility and thermo-responsiveness make them ideal model compounds for drug-delivery applications. Furthermore, due to the stealth effect found for poly(2-ethyl-2-oxazoline), their use as immunosuppressors has been discussed.^{5,7} A short review on the biomedical applications as an alternative to polyethylene glycol (PEG) can be found in Ref. 8.

In previous studies,^{9–11} we investigated the properties of poly(2-oxazoline)s under idealized and ambient conditions. A significant water-uptake was observed for materials with short side-chains, significantly altering the mechanical properties of the materials, whereas semi-crystalline behavior was found for samples with longer side-chains. In 1988, Lichkus et al. investigated the hydrogen bonding interactions in blends with different ratios of poly(2-ethyl-co-methacrylic acid).¹² The authors determined the fraction of “free” carbonyl groups from peak-fitting results in the carbonyl region. Later in 1996, Cai et al. used a similar approach in a series of decenyl/heptyl oxazoline copolymers to determine the ratio of hydrogen-bonded/“free” carbonyl groups.³ Thus, as hydrogen bonding interactions were reported for both hygroscopic and semi-crystalline samples, we aimed to gain further insight into the processes involved. Therefore, the initial temperature-dependent infrared (IR) measurements from our previous study¹¹ have been further evaluated by generalized two-dimensional correlation spectroscopy (2DCOS) and perturbation-correlation moving-window two-dimensional correlation spectroscopy (PCMW2D).

2DCOS, first proposed by Noda^{13–15} in 1993, represents a powerful procedure to investigate the spectral intensity fluctuation under a specific perturbation such as temperature, time, concentration, etc. In 2D correlation spectroscopy, the spectral intensities are plotted for two spectral variables, generally wavenumbers. 2DCOS creates a pair of synchronous $\Phi(\nu_1, \nu_2)$ and asynchronous $\Psi(\nu_1, \nu_2)$ 2D correlation spectra where the spectral variables ν_1 and ν_2 are wavenumbers. The synchronous 2D correlation intensity represents the overall similarity or simultaneous changes between two separate spectral variables during variation of an external perturbation (here increasing temperature). The asynchronous 2D correlation spectrum monitors variations in spectral intensities that are

not synchronously correlated. By application of Noda's rules,^{13,15,16} the sequential order of the events causing these spectral intensity variations can be determined.

On the other hand, PCMW2D is a relatively new analytical tool developed by Morita et al.¹⁷ in 2006. Its basic principles are based on the conventional moving-window 2D correlation spectroscopy proposed by Thomas and Richardson.¹⁸ The PCMW2D correlation method provides pairs of synchronous and asynchronous spectra that are plotted in a 2D map between a spectral variable (here, wavenumber) axis and a perturbation (here, temperature) axis. One of the advantages of this method is that a typical transition (such as melting point or crystallization temperature) of a spectral intensity variation can be visualized in the PCMW2D correlation spectra. Another important advantage is that complicated spectral intensity variations of overlapping bands or peak shifts along the perturbation direction can be detected. For example, in one of our previous studies,¹⁹ we analyzed the impact of annealing on the properties of poly(3-hydroxybutyrate) (PHB) by variable-temperature Fourier transform infrared (FT-IR) spectroscopic measurements in the $\nu(\text{C}=\text{O})$ region in combination with 2DCOS and PCMW2D analyses. It was found that further crystallization takes place between 30 and 120 °C and the melting temperature could be determined to be 180 °C by a sharp change to a broad $\nu(\text{C}=\text{O})$ absorption band, which is characteristic of the amorphous phase.

The present study focuses on vibrations in the carbonyl stretching region of the investigated poly(2-oxazoline)s. It has been demonstrated that the C=O functionality is involved in hydrogen bonding in cases where the material shows significant water uptake.¹¹ Furthermore, this band has a very high peak intensity and represents a superposition of an amorphous and a crystalline shoulder (for samples where crystallinity could be detected), making it ideal for monitoring the mentioned processes.

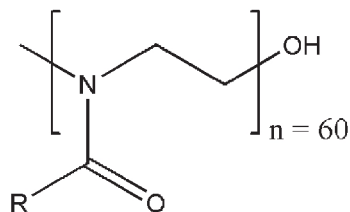
Thus, based on the combination of 2DCOS and PCMW2D, we attempted to derive an overall scenario for the structural changes of poly(2-*N*-alkyl-2-oxazoline)s as a function of temperature. Furthermore, these methods will assist in the assignment of the different states of the $\nu(\text{C}=\text{O})$ vibrational mode during the heating process due to the intensity increase and decrease of selected wavenumber regions with temperature.

EXPERIMENTAL

Synthesis. The different poly(2-alkyl-2-oxazoline)s were prepared by microwave-assisted cationic ring-opening polymerization in acetonitrile. Methyl tosylate was used as initiator with a monomer to initiator (M/I) ratio of 60, resulting in relatively well-defined (PDI < 1.3) poly(2-oxazoline)s with ~60 repeating units. The investigated polymers are depicted in Scheme 1; the abbreviations used in the text are listed in Table I. The synthesis is described elsewhere in full detail.²⁰

Thermogravimetric Analysis. Prior to the thermogravimetric analysis (TGA), the samples were stored in a water-saturated atmosphere overnight to enable water uptake. The saturated samples were then weighed into TGA crucibles and measured in a Netzsch TG 209 F1 instrument. The samples were heated up to 900 °C at a heating rate of 10 °C/min.

Temperature-Dependent FT-IR Investigations. Sample Preparation. The poly(2-oxazoline)s were dissolved in chloroform (p.a. quality from Fisher Scientific, used without further



SCHEME 1. Schematic representation of the chemical structure of the investigated poly(2-alkyl-2-oxazoline)s. Side-chains R are listed in Table I.

TABLE I. Schematic representation of the chemical structures of the investigated poly(2-alkyl-2-oxazoline)s and their respective abbreviations.

Poly(2-alkyl-2-oxazoline)s as depicted in Scheme 1, side-chain R =	Abbreviation
-CH ₃	MeOx
-C ₂ H ₅	EtOx
-C ₃ H ₇	PropOx
-CH(CH ₃) ₂	<i>i</i> -PrOx
-C ₄ H ₉	ButOx
-CH ₂ -CH(CH ₃) ₂	<i>i</i> -ButOx
-C ₅ H ₁₁	PentOx
-C ₆ H ₁₃	HexOx
-C ₇ H ₁₅	HeptylOx
-C ₉ H ₁₉	NonOx

purification) and drop-cast onto KBr pellets until a suitable thickness for recording an FT-IR spectrum with good signal-to-noise-ratio was achieved. The MeOx was dissolved in deionized water instead, due to its low solubility in chloroform, but treated equally in the following steps. All samples were dried under reduced pressure overnight. Subsequently, the pellets were kept in a closed compartment in a water-saturated atmosphere overnight to allow for water uptake by the materials.

FT-IR Measurements. For the actual measurements, a second KBr pellet was placed onto the sample to prevent possible melt-flow of the sample film at higher temperatures. The KBr sandwich was fixed on a heating block within the beam path of the spectrometer. The temperature (controlled with a Hotset RR 210) was increased in steps of 5 °C from 30 °C to at least 200 °C (max. 235 °C for *i*-ButOx, depending on the melting behavior of the individual sample), allowing a period of 5 min time for temperature equilibration at each step. After the heating run, cooling of the samples was performed in the same stepwise manner. The spectra were recorded on a Bruker IFS 28 FT-IR/FT-NIR spectrometer by co-adding 32 scans for each spectrum with a spectral resolution of 4 cm⁻¹.

Generalized 2DCOS and PCMW2D Spectroscopy. Baseline correction was performed using the rubber-band method (standard method implemented in the Bruker OPUS software) for all FT-IR spectra in the $\nu(\text{C}=\text{O})$ wavenumber regions before calculation of the 2D correlation. The generalized 2D correlation analysis was applied using 2D Shige software (Kwansei-Gakuin University, Japan; <http://sci-tech.ksc.kwansei.ac.jp/~ozaki/2Dshige.zip>) developed by Shigeaki Morita and in a further step plotted by Wavemetrics Igor Pro 6.22 software in order to obtain 2D correlation maps with good

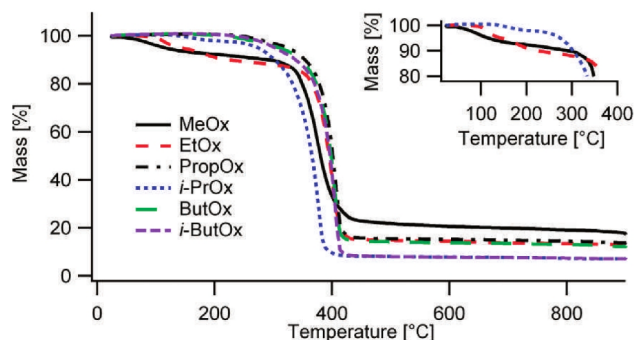


Fig. 1. TGA analysis of the investigated hygroscopic poly(2-oxazoline)s in the temperature range from 30 to 700 °C. The inset shows the enlarged view of the weight loss for the three most hygroscopic samples.

quality and clarity. In the 2D contour maps, the red colored regions are defined as positive correlation intensities, while the blue colored ones indicate negative intensities.

Perturbation-correlation moving-window two-dimensional correlation analysis is expressed as a pair of synchronous and asynchronous correlation spectra plotted between a spectral variable axis and a perturbation variable axis. The FT-IR spectral datasets from each heating cycle were treated with this method and further correlation was calculated using the 2D Shige software with window size ($2m + 1 = 5$). Similarly, the contour maps were plotted using Igor Pro with the same colors defined as in the 2DCOS analysis.

RESULTS AND DISCUSSION

Thermogravimetric Analysis. Figure 1 shows the TGA results of the investigated poly(2-oxazoline)s after equilibration in a humid atmosphere. Polymer degradation is characterized by a large mass loss between 300 and 400 °C for all samples. Furthermore, for MeOx, EtOx, and *i*-PrOx, smaller mass losses were observed due to the evaporation of water. This confirms earlier water-uptake measurements¹¹ that also showed these samples to be hygroscopic. For the MeOx, the mass loss starts at the lowest temperature and decreases continuously until decomposition of the sample, suggesting a strong interaction of the polymer with water molecules. The mass loss in the EtOx sample starts later and also continuously decreases until degradation. Two steps in the curve can be identified, ascribed to loosely bound and hydrogen-bonded water. For the *i*-PrOx, the mass loss is less significant, pointing out a lower hygroscopicity of the material. Furthermore, the onset of the mass loss is at around 130 °C, where DSC investigations (data not shown) have shown an exothermic peak, resulting from crystallization of the sample. Demirel et al.²¹ already pointed out the importance of small amounts of water for the crystallization of *i*-PrOx.

Therefore, the TGA results allow a rough differentiation between hygroscopic and non-hygroscopic samples. In comparison with the DSC results from our previous study,¹¹ TGA is also not sensitive enough to detect the water loss in the PropOx sample, where the IR spectra showed a small but detectable peak shift of the C=O band towards higher

wavenumbers with decreasing water content. As our previous studies have shown, the full width at half-maximum (FWHM) values of this peak are more sensitive towards changes in the material upon variation of the temperature. Therefore, the samples have been divided into two groups, namely hygroscopic and semi-crystalline samples, based on the behavior deduced from the IR spectroscopic results.

Hygroscopic Samples. This group contains only materials with very short side-chains: the MeOx, EtOx, PropOx, and *i*-PrOx. The short side-chains of these polymers cannot fully shield the polar amide groups, yielding hydrophilic materials that are hygroscopic. As seen by the TGA measurements, these samples show a more or less severe water uptake.

More detailed information can be gained from the temperature-dependent FT-IR spectra. Figures 2A and 2B show the FT-IR spectra and their second derivatives of MeOx and PropOx at 30 °C and at the highest investigated temperature. These data reveal that there are at least two absorption bands in the 1750 to 1550 cm^{-1} region. One band is located at 1635 cm^{-1} ; this absorption band is intense at 30 °C, but its intensity slightly decreases during the temperature increase and can be assigned to the $\delta(\text{OH})$ vibrational mode of water. As it can still be observed at temperatures above 100 °C, it is assigned to water that is strongly bound to the polymer, presumably by hydrogen bonding with the C=O functionality, as proposed in Ref. 10. On the other hand, an absorption band at about 1650 cm^{-1} becomes the dominant absorption at the highest temperature and can be assigned to the $\nu(\text{C}=\text{O})$ absorption band of the amorphous regions of the respective polymer. Based on the second derivatives displayed in the top of Figs. 2A and 2B a further absorption band is detectable, showing only a small shoulder at about 1618 cm^{-1} at 30 °C. This absorption band completely disappears with increasing temperature. This latter absorption band is also assigned to the water deformation mode, but, as it is significantly weaker than the one found at 1636 cm^{-1} , it is assigned to weakly associated water molecules that are not involved in strong hydrogen bonding interactions with the polymer C=O functionalities and might be present as a second hydration layer.

2DCOS and PCMW2D Analysis. For a more detailed analysis of the water uptake behavior of the hygroscopic samples as a function of temperature, 2DCOS and PCMW2D

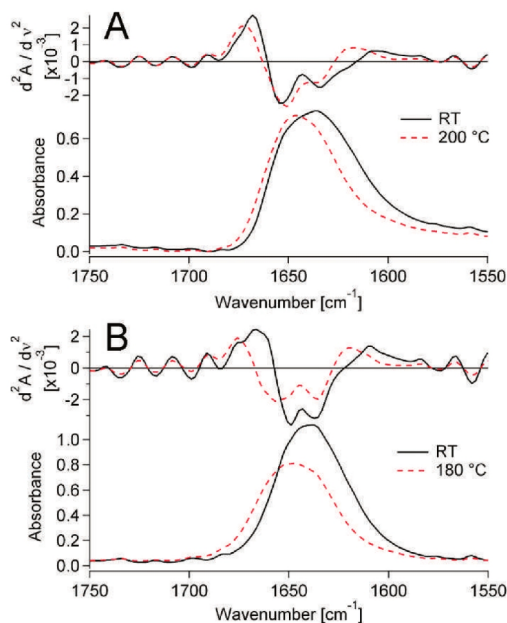


Fig. 2. FT-IR spectral variations in the carbonyl region of (A) MeOx and (B) PropOx (top: second derivatives, bottom: FT-IR spectra).

correlation spectroscopy have been applied to each spectral data set. First the results of MeOx in the temperature range from 30 to 200 °C will be discussed. Figure 3 shows the synchronous (A) and asynchronous (B) 2D correlation spectra of the wavenumber region 1700 to 1600 cm^{-1} . In the synchronous 2DCOS spectrum, two auto peaks at about (1664, 1664) and (1623, 1623) cm^{-1} and a negative cross-peak at (1664, 1623) cm^{-1} are observed, representing the inverse correlation of the polymer's C=O functionality with water. This simply corresponds to the evaporation of hydrogen-bonded water, which causes a decrease in the water peak and, simultaneously, an increase of the C=O intensity due to strengthening of the C=O bond.

The asynchronous 2DCOS spectrum (Fig. 3B) provides additional information. The spectrum shows two positive cross-peaks at about (1614, 1631) and (1631, 1660) cm^{-1} , which characterize the correlation of three highly overlapped components in the 1700 to 1600 cm^{-1} wavenumber region, namely loosely associated water (1614 cm^{-1}), hydrogen-bonded water (1631 cm^{-1}), and the C=O absorption band (1660 cm^{-1}). By application of Noda's rules, the sequential order of the structural changes during the temperature increase can be determined. It can be concluded that the absorption intensities change in ascending order with increasing temperature as follows (the symbol < means "changes prior to"):

$$(1614 < 1631 < 1660)\text{cm}^{-1}$$

The correlation between the two different water bands (1614 and 1631 cm^{-1}) suggests an equilibrium between loosely

associated and hydrogen-bonded water within the polymer, with the loosely associated water removed first by the heat treatment. Furthermore, only the hydrogen-bonded water (1631 cm^{-1}) shows a correlation with the carbonyl band (1660 cm^{-1}). This result suggests that weak interactions of loosely associated water and hydrogen-bonded water molecules disappear before the hydrogen-bonded water molecules are removed from the sample. As discussed above, the TGA analysis does not allow distinguishing between the two different states of water, as only a smooth slope of the TGA curve is visible for the MeOx, while the curve for the EtOx clearly shows two distinct steps resulting from loosely associated and hydrogen-bonded water, respectively. This may be the result of the higher hygroscopicity of the MeOx compared to the EtOx. As in the saturation period prior to the measurement, much more water is attracted than is required for hydrogen bonding; the mass loss in the TGA shows a continuous decrease in the MeOx sample. In the EtOx material, with less associated water, the slope of the curve results in sharper transitions due to the water loss. This confirms the high sensitivity of 2DCOS analysis towards structural changes within the materials.

Figure 3C shows the synchronous PCMW2D correlation spectrum of the MeOx $\nu(\text{C}=\text{O})$ region calculated from the FT-IR spectra recorded in the temperature range from 30 to 200 °C. Similar to the 2DCOS evaluation, positive and negative correlation areas are represented by red and blue, respectively. In contrast to the 2DCOS plots, the PCMW2D correlation spectra allow us to visualize the perturbation (here, temperature) on the y-axis. At low temperatures the spectrum shows two peaks around 1660 and 1616 cm^{-1} , resulting from the $\nu(\text{C}=\text{O})$ and $\delta(\text{H}_2\text{O})$ vibration modes, respectively. The water peak at 1616 cm^{-1} is decreasing with increasing temperature, while the carbonyl peak is increasing, representing the process of water removal from the sample. In the raw spectra, this results in a peak-shift of the $\nu(\text{C}=\text{O})$ band towards higher wavenumbers as the C=O bond is strengthened due to the removal of water. This peak-shift is the cause of the spreading of the peaks in the PCMW2D spectra.

As the 2DCOS spectra have already shown, two types of water can be distinguished: loosely associated and hydrogen-bonded water molecules. As can be seen from the PCMW2D spectrum, the loosely associated water is being removed at low temperatures (negative peak), resulting in a strengthening of the carbonyl bond. At high temperatures (~ 150 °C), another water peak is found, resulting from the removal of the strongly hydrogen-bonded water molecules. Also, this peak is accompanied by an increasing peak in the carbonyl region; however, the intensity is much lower due to the lower amount of hydrogen-bonded water in the sample. Similar behavior has been found for the other hygroscopic samples as well.

Since both PropOx and *i*-PrOx also exhibit crystalline behavior, besides being hygroscopic, they are discussed in more detail in the section on the semi-crystalline samples.

Semi-Crystalline Samples. As discussed previously,¹¹ the crystalline behavior found for these poly(2-alkyl-2-oxazoline)s is a consequence of alignment and close packing of the polymer side-chains (with the exception of *i*-PrOx, where main-chain crystallinity is supposed). As MeOx and EtOx did not show crystalline behavior, it was concluded that the methyl and ethyl side-chains are too short to align and form crystalline domains. As a consequence, this second group of semi-crystalline samples contains all samples with a linear propyl- or

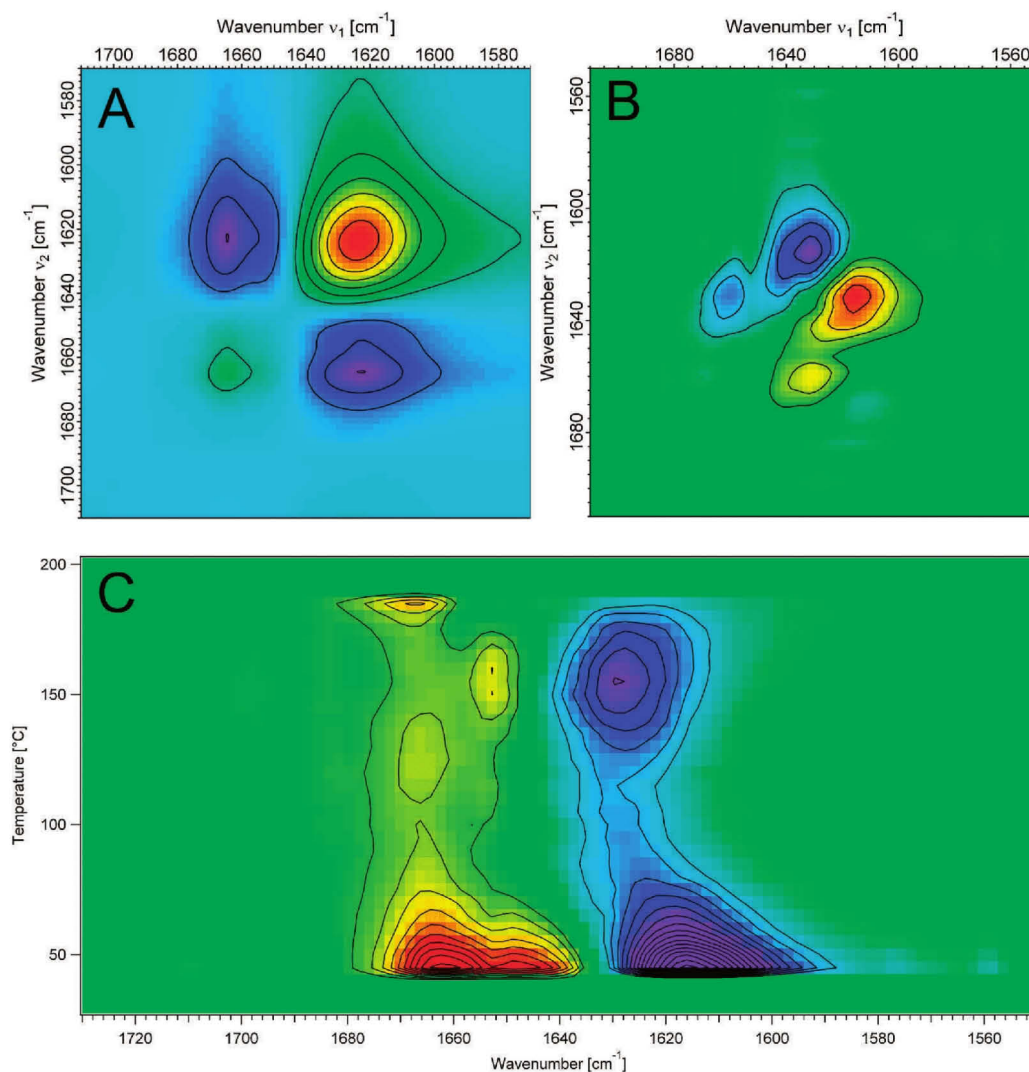


Fig. 3. (A) Synchronous, (B) asynchronous correlation spectra, and (C) synchronous PCMW2D correlation spectrum of the MeOx $\nu(\text{C}=\text{O})$ region calculated from the FT-IR spectra collected in the temperature range from 30 to 200 °C. Red indicates positive, blue indicates negative peak intensity.

longer side-chain, as well as the *i*-PrOx. Figure 4 exemplarily shows the FT-IR spectra of NonOx (A) and *i*-PrOx (B) in the carbonyl region, as well as their second derivatives, as examples of the semi-crystalline group. ButOx through HeptylOx and *i*-ButOx show similar behavior to NonOx.

As can be seen, the spectra at room temperature show a dominant peak at $\sim 1645 \text{ cm}^{-1}$ for both samples that is much sharper and more symmetric than the peak in the MeOx. For the *i*-PrOx, one spectrum at 120 °C is also shown. The

crystallization of this sample during the heating process can be followed by a sharpening of the C=O band, as well as an increase in peak maximum (compare Fig. 6 in Ref. 11). As seen in Fig. 4, the band at 120 °C is already sharper and slightly shifted to higher wavenumbers compared to the RT spectrum. The shift is a result of the hygroscopicity of the sample as discussed above.

The NonOx is considered to be fully crystallized at the beginning of the measurement, as its T_g is far below room

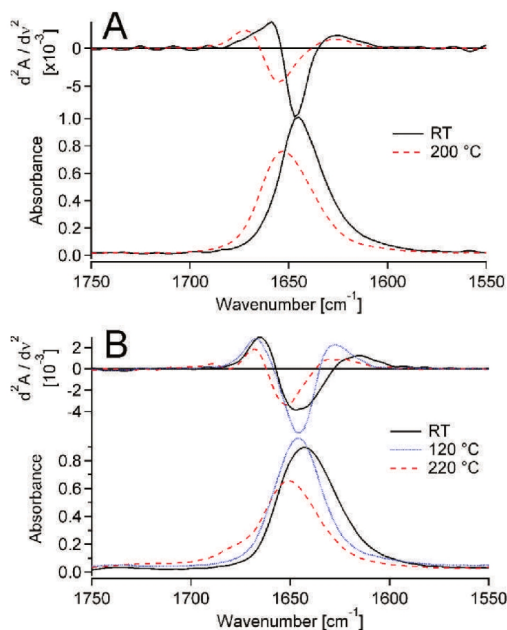


Fig. 4. FT-IR spectral variations in the carbonyl region of (A) NonOx and (B) *i*-PrOx (top: second derivatives, bottom: FT-IR spectra).

temperature and the preparation allowed for enough time for chain realignment.

At high temperatures, the crystalline part of the C=O peak ($\sim 1645 \text{ cm}^{-1}$) disappears, while the broad amorphous shoulder increases ($\sim 1655 \text{ cm}^{-1}$). Similar results can be detected in the second-derivative spectra (top of Figs. 4A and 4B).

2DCOS and PCMW2D analysis. PropOx. Figure 5 displays the 2D correlation spectra of PropOx. The synchronous 2DCOS spectrum (A) shows two pairs of auto peaks at (1627, 1627) and (1660, 1660) cm^{-1} , corresponding to water and to the amorphous polymer matrix. The related cross-peak is negative, indicating an increase in one band at the cost of the other one, as a consequence of the removal of water during the heat treatment, as already discussed for MeOx.

The asynchronous 2DCOS spectrum (Fig. 5B) shows three peaks. The peak resulting from associated water at 1619 cm^{-1} correlates positively with a second water peak of hydrogen-bonded water at 1635 cm^{-1} , indicating that the loosely associated water is changing prior to the hydrogen-bonded water. The second peak at (1619, 1664) cm^{-1} indicates a negative correlation between water and the amorphous regions of the polymer. As a result of the negative cross-peak in the synchronous 2DCOS spectrum, the sign of the (1619, 1664) cm^{-1} peak has to be reversed. Thus, it shows that the variations in the water band occur before the changes of the $\nu(\text{C}=\text{O})$ band of the amorphous polymer regions. The third peak at (1646, 1660) cm^{-1} indicates that the crystalline regions of the polymer change prior to the amorphous domains.

The PCMW2D analysis depicted in Fig. 5C shows two

peaks at low temperatures, starting from the very beginning. The peak at $\sim 1660 \text{ cm}^{-1}$ corresponds to the amorphous matrix of the polymer and slightly increases with increasing temperature, while the second peak at $\sim 1625 \text{ cm}^{-1}$ corresponds to the decreasing water deformation band. As the water is removed from the sample during heating, the high-wavenumber wing of the carbonyl band, which is characteristic of the amorphous regions of the polymer, is increasing. In comparison to the MeOx, however, the decrease of the water band is much lower in PropOx. Furthermore, as only one water peak is observed, we cannot discriminate between hydrogen-bonded and loosely bonded water. At very high temperatures, another decreasing peak is shown due to melt-flow of the sample. This resulted in a large-scale intensity loss over the whole region.

NonOx. Figure 6 displays the 2D correlation spectra of NonOx. The synchronous 2DCOS spectrum (A) identifies two auto peaks at (1643, 1643) and (1660, 1660) cm^{-1} , corresponding to the $\nu(\text{C}=\text{O})$ absorption bands of the crystalline and the amorphous regions of the polymer. The corresponding cross-peak is negative, indicating opposite spectral changes as a function of temperature increase.

The asynchronous 2DCOS spectrum shows one positive and one negative cross-peak corresponding to a correlation between associated water and the C=O groups in the crystalline domains (1631, 1643 cm^{-1}), as well as a correlation between water and the C=O groups in the amorphous matrix (1631, 1662 cm^{-1}). According to the rules of Noda,^{13,15,16} changes in the amorphous matrix occur before the water is removed due to the increasing temperature. The changes in the crystalline domains occur last. At first glance, this may look contradictory to the findings of the PropOx and *i*-PrOx samples as the sequential order in these samples suggests a change in the crystalline domains occurring before changes in the amorphous matrix. But considering the T_g values of these samples, it becomes clear that both PropOx and *i*-PrOx are below their respective T_g at the beginning of the measurement, and thus the realignment of the crystalline domains is hindered until the experimental temperature exceeds the T_g of the polymer. As the NonOx is always above T_g , its chains can freely realign during the course of the whole measurement. It shall be noted that the peaks found in the asynchronous spectrum result from intensity changes in the corresponding peaks of the original spectra due to the melting of the sample and not from a peak shift like in the MeOx sample.

The perturbation-correlation moving-window analysis (Fig. 6C) shows only two peaks at temperatures above $150 \text{ }^\circ\text{C}$, corresponding to the melting of the crystalline domains. As expected, the peak corresponding to the amorphous matrix ($\sim 1662 \text{ cm}^{-1}$) sharply increases while the crystallinity-sensitive peak ($\sim 1643 \text{ cm}^{-1}$) decreases. Traces of water that are still present (as seen in the 2D correlation spectra) do not appear as peaks in the moving-window evaluation due to the low intensity. This view is supported by the almost symmetric shape of the $\nu(\text{C}=\text{O})$ band in Fig. 4, suggesting only a very small contribution of the water band to the low-wavenumber wing.

ButOx through HeptylOx show a behavior similar to that of NonOx, even though in the asynchronous spectra, the correlation between water and the amorphous domains can be obscured by an intense positive peak for the correlation between the crystalline and amorphous carbonyl absorp-

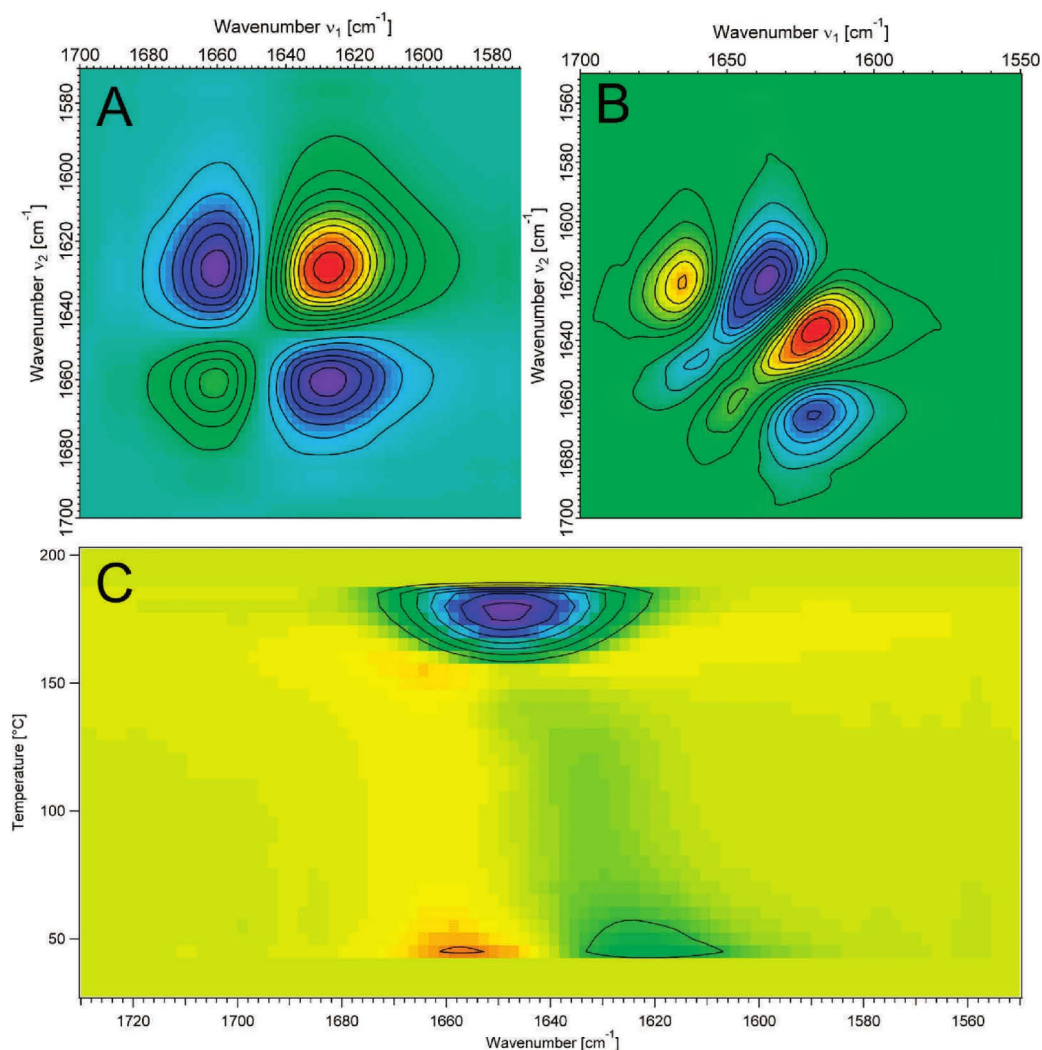


Fig. 5. (A) Synchronous and (B) asynchronous correlation spectra of the PropOx $\nu(\text{C}=\text{O})$ region calculated from the FT-IR spectra collected in the temperature range 30 to 170 °C. Spectra above 170 °C have been omitted from the calculation due to their low overall intensity caused by melt-flow of the sample. (C) Synchronous PCMW2D correlation spectrum in the temperature range 30 to 200 °C. Red indicates positive, blue indicates negative peak intensity.

tions. The sequential order in all semi-crystalline samples is therefore: water < crystalline regions < amorphous domains.

i-PrOx. The 2D correlation spectra of *i-PrOx* in the full temperature range contain too many peaks for a straightforward evaluation. Furthermore, several peaks of low intensity are obscured due to the dominance of others. Thus, the temperature range of the 2D correlation spectra has been split according to the processes taking place. For that reason, first the temperature

range from 30 to 150 °C will be discussed, where the spectral changes can be observed due to a further crystallization of *i-PrOx*. Finally, the 2DCOS analysis will be applied for the 150 to 220 °C temperature range, indicating mainly the melting behavior of *i-PrOx*.

Figure 7 shows the 2D correlation spectra of *i-PrOx*. In the temperature range from 30 to 150 °C, the synchronous spectrum (A) displays three distinct auto peaks at (1631, 1631), (1645, 1645), and (1656, 1656) cm^{-1} , corresponding to

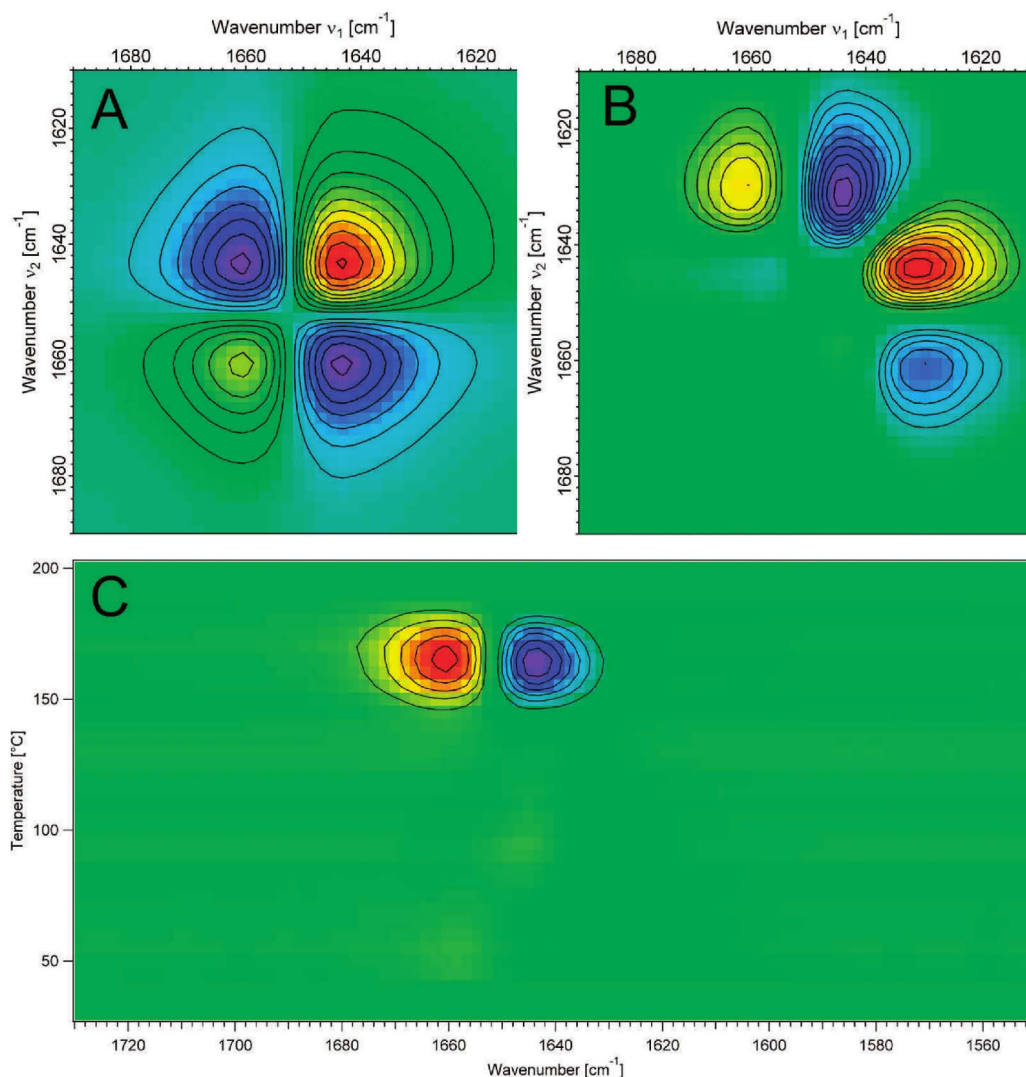


FIG. 6. (A) Synchronous, (B) asynchronous correlation spectra, and (C) synchronous PCMW2D correlation spectrum of the NonOx $\nu(\text{C}=\text{O})$ region calculated from the FT-IR spectra collected in the temperature range from 30 to 200 $^{\circ}\text{C}$. Red color indicates positive, blue color indicates negative peak intensity.

the $\delta(\text{H}_2\text{O})$ band and the $\nu(\text{C}=\text{O})$ band of the crystalline and amorphous regions of the polymer, respectively. Negative cross-peaks can be found at (1625, 1645) and (1643, 1658) cm^{-1} , reflecting the inverse correlation between water and the amorphous regions and between the amorphous and the crystalline regions. This is not surprising as the water is removed from the sample due to the heating, thereby strengthening the $\text{C}=\text{O}$ bond of the amorphous regions. The second peak results from the crystallization of the *i*-PrOx. From

the differential scanning calorimetry (DSC) curve (data not shown), an exothermic peak could be attributed to crystallization of the *i*-PrOx, now resulting in a signal increase of the crystalline $\nu(\text{C}=\text{O})$ band at the cost of the corresponding band of the amorphous regions in the synchronous 2D correlation spectrum. The asynchronous spectrum (B) in this temperature range shows two negative and three positive peaks. Due to the negative cross-peaks in the synchronous spectrum, the signs of both negative peaks in the asynchronous spectrum have to be

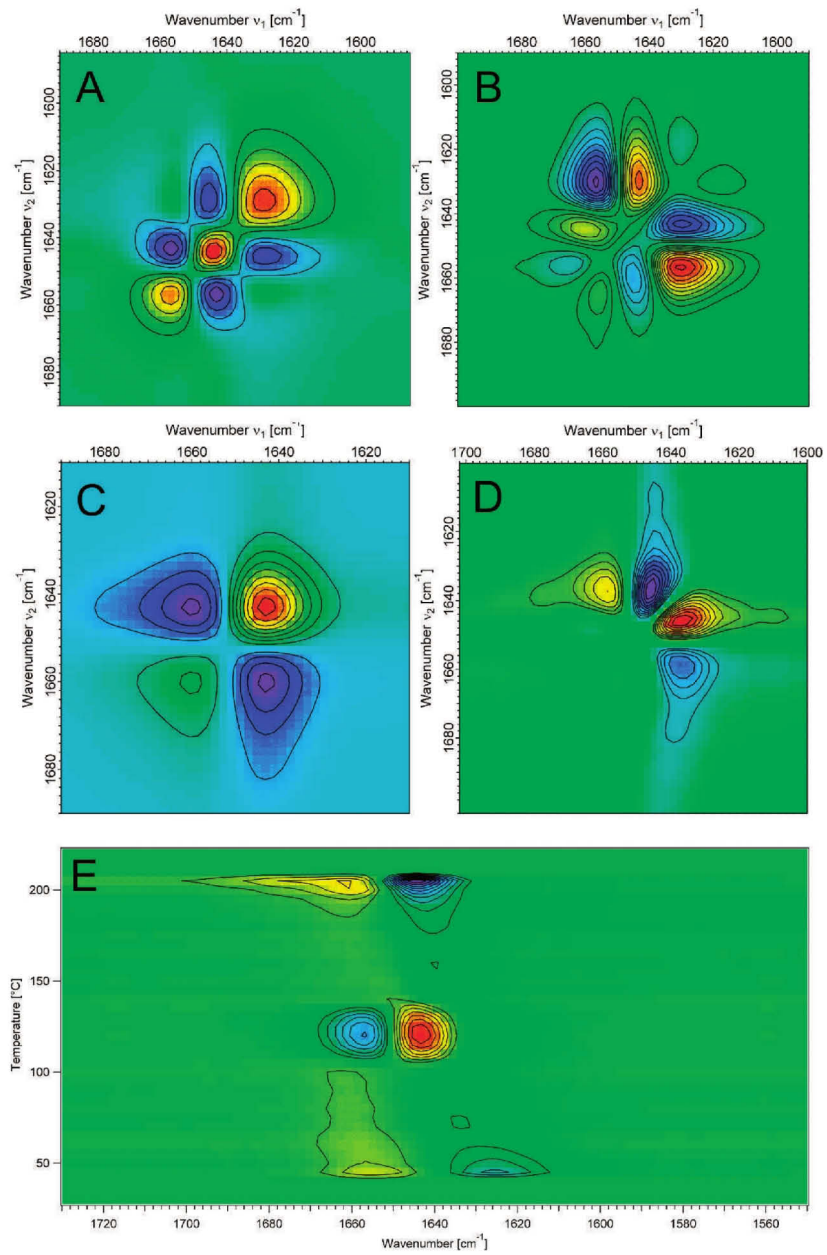


FIG. 7. (A) Synchronous, (B) asynchronous correlation spectra of the *i*-PrOx $\nu(\text{C}=\text{O})$ region in the temperature range from 30 to 150 °C; (C) synchronous and (D) asynchronous correlation spectra in the temperature range 150 to 220 °C; (E) synchronous PCMW2D correlation spectrum; calculated from the FT-IR spectra. Red indicates positive, blue indicates negative peak intensity.

reversed. Thus, the asynchronous spectrum yields the following peaks: (1618, 1629), (1629, 1643), (1629, 1656), (1645, 1658), and (1654, 1664) cm^{-1} . The combination (1618, 1629) indicates an exchange between loosely bound and hydrogen-bonded water (as found for the other hygroscopic samples), where the loosely bound water changes before the hydrogen-bonded water. The (1629, 1643) and (1629, 1656) peaks show the interaction between hydrogen-bonded water and the C=O groups in the crystalline and the amorphous domains, respectively. The peak at (1645, 1658) represents the transformation of amorphous into crystalline C=O functionalities due to recrystallization. The last peak at (1654, 1664) seems to be an artifact resulting from the peak shift of the carbonyl band due to the loss of water, as no other peaks are expected at higher wavenumbers than the amorphous C=O.

Figures 7C and 7D depict the 2D correlation spectra in the temperature range from 150 to 220 °C. The synchronous spectrum displays two auto peaks and one negative cross-peak. The auto peaks at (1643, 1643) and (1660, 1660) cm^{-1} correspond to the crystalline and amorphous domains of the polymer. The corresponding cross-peak at (1643, 1660) cm^{-1} is negative, indicating an increase in one band while the other one decreases. It clearly results from the melting of the sample; thus, the band due to the amorphous regions is increasing at the cost of the crystallinity-sensitive band.

The asynchronous spectrum shows a positive peak at (1639, 1648) and a negative one at (1648, 1658). According to the rules of Noda, again the negative sign of the peak at (1648, 1658) cm^{-1} has to be reversed. Thus, also here, the sequential order of water < crystalline regions < amorphous regions is obtained.

The PCMW2D analysis of the *i*-PrOx is shown in Fig. 7E. It shows three sets of peaks over the temperature range of the heat treatment. In the very beginning water is removed from the sample, resulting in a negative peak centered at about 1626 cm^{-1} . This is accompanied by an increase of the carbonyl absorption (broad positive peak around 1656 cm^{-1}). At temperatures between 105 and 140 °C, the second pair of peaks appears. As the peak (\sim 1660 cm^{-1}) abruptly decreases, another peak (\sim 1643 cm^{-1}) strongly increases. This is a clear visualization of the crystallization process of *i*-PrOx, as the C=O groups in amorphous domains are converted into crystalline ones.

The third pair of peaks starts at temperatures around 185 °C and is attributed to the melting of the sample. Here, the peaks are centered again at 1660 and 1643 cm^{-1} , but the signs are reversed because crystalline material is now converted to amorphous domains as discussed already for the NonOx.

CONCLUSION

Generalized two-dimensional correlation spectroscopy and perturbation-correlation moving-window two-dimensional correlation spectroscopy was successfully applied to the temperature-dependent FT-IR spectra datasets of water-saturated poly(2-oxazoline)s, significantly expanding a previous study.¹¹ This allowed visualization and a better understanding of the sequence of the processes of hydrogen bonding between water and the polymer as well as the recrystallization and melting of the polymer. For samples with a short side-chain (MeOx through PropOx and *i*-PrOx), hygroscopic behavior has been found, resulting in hydrogen bonding interactions of water molecules with the C=O functionalities of the polymer. This is

in agreement with stepwise weight losses found in the TGA curves and (previously published) water uptake measurements.

For samples with longer side-chains, crystalline behavior could be found. The melting of the samples at high temperatures resulted in a conversion of crystalline into amorphous regions. Contrary to the original spectra, which do not allow differentiation between the $\nu(\text{C}=\text{O})$ absorption of the crystalline and amorphous regions of the polymer, 2DCOS and PCMW2D were able to resolve these two peaks, as well as the water deformation band, which is obscured in the original spectra.

With the *i*-PrOx polymer, one sample has been found in which a crystallization process could be monitored between T_g and T_m . The DSC trace of this sample showed an exothermic peak in the first heating run, already indicating crystallization. This could now be clearly resolved in the PCMW2D data as a simultaneous increase and decrease of the corresponding $\nu(\text{C}=\text{O})$ absorptions of the crystalline and amorphous regions, respectively.

The presented results will greatly increase the understanding of the processes of hydrogen bonding and crystallization in poly(2-oxazoline)s. Furthermore, it was shown that the application of two-dimensional correlation analyses allowed the investigation of highly overlapping peaks in the infrared spectrum, where conventional analysis failed.

ACKNOWLEDGMENTS

This research forms part of the research programme of the Dutch Polymer Institute (DPI), technology area HTE, projects #502 and #604. MU thanks the Dr. Jost-Henkler-Stiftung (Düsseldorf, Germany) and the Japan Society for the Promotion of Science (JSPS) for financial support.

1. N. Adams, U.S. Schubert. "Poly(2-oxazoline)s in biological and biomedical application contexts". *Adv. Drug Delivery Rev.* 2007. 59: 1504-1520.
2. J.-S. Park, K. Kataoka. "Precise control of lower critical solution temperature of thermosensitive poly(2-isopropyl-2-oxazoline) via gradient copolymerization with 2-ethyl-2-oxazoline as a hydrophilic comonomer". *Macromolecules*. 2006. 39: 6622-6630.
3. G. Cai, M.H. Litt. "Synthesis and characterization of poly(N-acyl or N-aroyl ethylenimines) containing various pendant functional groups. II. Copolymers with pendant hydroxyl groups". *J. Polym. Sci., Part A: Polym. Chem.* 1996. 34: 2689-2699.
4. M.W.M. Fijten, J.M. Kranenburg, H.M.L. Thijs, R.M. Paulus, B.M. Van Lankvelt, J. De Hullu, M. Springintvelt, D.J.G. Thielen, C.A. Tweedie, R. Hoogenboom, K.J. Van Vliet, U.S. Schubert. "Synthesis and structure-property relationships of random and block copolymers: A direct comparison for copoly(2-oxazoline)s". *Macromolecules*. 2007. 40: 5879-5886.
5. R. Hoogenboom. "Poly(2-oxazoline)s: A polymer class with numerous potential applications". *Angew. Chem. Int. Ed.* 2009. 48: 7978-7994.
6. H. Schlaad, C. Diehl, A. Gress, M. Meyer, A.L. Demirel, Y. Nur, A. Bertin. "Poly(2-oxazoline)s as smart bioinspired polymers". *Macromol. Rapid. Commun.* 2010. 31: 511-525.
7. Y.S. Park, Y.S. Kang, D.J. Chung. "Formation and blood compatibility of thin layers of hyperbranched polymers on polyurethane films". *e-Polymers*. 2002. no.016.
8. K. Knop, R. Hoogenboom, D. Fischer, U.S. Schubert. "PEG in drug delivery: Pros and cons as well as potential alternatives". *Angew. Chem. Int. Ed.* 2010. 49: 6288-6308.
9. E.F.-J. Rottler, J.M. Kranenburg, H.M.L. Lambertmont-Thijs, R. Hoogenboom, U.S. Schubert. "Thermal, mechanical and surface properties of poly(2-N-alkyl-2-oxazoline)s". *Macromol. Chem. Phys.* 2010. 211: 2443-2448.
10. J.M. Kranenburg, C.A. Tweedie, R. Hoogenboom, F. Wiesbrock, H.M.L. Thijs, C.E. Hendriks, K.J. Van Vliet, U.S. Schubert. "Elastic moduli for a diblock copoly(2-oxazoline) library obtained by high-throughput screening". *J. Mater. Chem.* 2007. 17: 2713-2721.
11. E.F.-J. Rottler, H.M.L. Lambertmont-Thijs, J.M. Kranenburg, R. Hoogenboom, M.V. Unger, H.W. Siesler, U.S. Schubert. "Water uptake of poly(2-

- N-alkyl-oxazoline)s: Influence of crystallinity and hydrogen bonding on the mechanical properties". *J. Mater. Chem.* 2011. 21: 17331-17337.
12. A.M. Lichkus, P.C. Painter, M.M. Coleman. "Hydrogen bonding in polymer blends. 5. Blends involving polymers containing methacrylic acid and oxazoline groups". *Macromolecules.* 1988. 21: 2636-2641.
 13. I. Noda. "Generalized two-dimensional correlation method applicable to infrared, Raman, and other types of spectroscopy". *Appl. Spectrosc.* 1993. 47: 1329-1336.
 14. I. Noda, A.E. Dowrey, C. Marcott, G.M. Story, Y. Ozaki. "Generalized two-dimensional correlation spectroscopy". *Appl. Spectrosc.* 2000. 54: 236-248.
 15. I. Noda, Y. Ozaki. "Principle of Two-dimensional Correlation Spectroscopy". In: I. Noda, Y. Ozaki, editors. *Two-dimensional Correlation Spectroscopy—Applications in Vibrational and Optical Spectroscopy*. Chichester, UK: John Wiley and Sons, 2004. Pp. 15-38.
 16. Q. Jia, N. Wang, Z. Yu. "An insight into sequential order in two-dimensional correlation spectroscopy". *Appl. Spectrosc.* 2009. 63: 344-353.
 17. S. Morita, H. Shinzawa, I. Noda, Y. Ozaki. "Perturbation-correlation moving-window two-dimensional correlation spectroscopy". *Appl. Spectrosc.* 2006. 60: 398-406.
 18. M. Thomas, H.H. Richardson. "Two-dimensional FT-IR correlation analysis of the phase transitions in a liquid crystal, 4'-n-octyl-4-cyanobiphenyl(8CB)". *Vib. Spectrosc.* 2000. 24: 137-146.
 19. M. Unger, S. Morita, H. Sato, Y. Ozaki, H.W. Siesler. "Variable-temperature Fourier transform infrared spectroscopic investigations of poly(3-hydroxyalkanoates) and perturbation-correlation moving-window two-dimensional correlation analysis. Part I: Study of non-annealed and annealed poly(2-hydroxybutyrate) homopolymer". *Appl. Spectrosc.* 2009. 63: 1027-1033.
 20. R. Hoogenboom, M.W.M. Fijten, H.M.L. Thijs, B.M. van Lankvelt, U.S. Schubert. "Microwave-assisted synthesis and properties of a series of poly(2-alkyl-2-oxazoline)s". *Design. Monom. Polym.* 2005. 8: 659-671.
 21. A.L. Demirel, M. Meyer, H. Schlaad. "Formations of polyamide nanofibers by directional crystallization in aqueous solution". *Angew. Chem. Int. Ed.* 2007. 46: 8622-8624.

P5 UV-induced crosslinking of the polybutadiene domains in lamellar polystyrene-block-polybutadiene block copolymer films – An in-depth study

Erik Rettler, Tobias Rudolph, Andreas Hanisch, Stephanie Hoepfener, Markus Retsch, Ulrich S. Schubert, Felix H. Schacher,

Polymer **2012**, 53, 5641-5648.



UV-induced crosslinking of the polybutadiene domains in lamellar polystyrene-*block*-polybutadiene block copolymer films – An in-depth study

Erik F.-J. Rettler^{a,b,c}, Tobias Rudolph^{a,b}, Andreas Hanisch^d, Stephanie Hoeppener^{a,b}, Markus Retsch^e, Ulrich S. Schubert^{a,b,c,*}, Felix H. Schacher^{a,b,*}

^a Laboratory of Organic and Macromolecular Chemistry (IOMC), Friedrich-Schiller-University Jena, Humboldtstr. 10, 07743 Jena, Germany

^b Jena Center for Soft Matter (JCSM), Friedrich-Schiller-University Jena, Philosophenweg 7, 07743 Jena, Germany

^c Dutch Polymer Institute (DPI), John F. Kennedylaan 2, 5612 AB Eindhoven, The Netherlands

^d Macromolecular Chemistry II, Universität Bayreuth, Universitätsstraße 30, 95440 Bayreuth, Germany

^e Physical Chemistry–Polymeric Systems, Universität Bayreuth, Universitätsstraße 30, 95440 Bayreuth, Germany

ARTICLE INFO

Article history:

Received 5 August 2012

Received in revised form

27 September 2012

Accepted 28 September 2012

Available online 6 October 2012

Keywords:

Block copolymers

Crosslinking

Depth-sensing indentation

ABSTRACT

We present an in-depth study of the UV-induced crosslinking of the polybutadiene domains in lamellar polystyrene-*block*-polybutadiene (PS-*b*-PB) block copolymer films. The crosslinking process is followed by a combination of depth-sensing indentation, Raman spectroscopy, and differential scanning calorimetry (DSC) investigations. Indentation assesses changes in the mechanical properties of the overall polymer films while Raman experiments directly monitor the consumption of the PB double bonds. Immediately after a short UV exposure, a loose network is formed and the glass transition temperature increases, whereas changes in the mechanical properties of the materials require far longer hardening times. We show that both processes are strongly affected by the amount of crosslinker (Lucirin-TPO[®]) added (within a range of 5 to 50 wt. % with respect to the PB fraction of the material).

© 2012 Elsevier Ltd. All rights reserved.

1. Introduction

Different synthetic approaches allow for the control over molar mass, functionality, composition, and architecture of polymeric materials. This applies to both homo- and copolymers. In particular block copolymers are of great interest due to the covalent linkage of at least two blocks of monomers in a sequential manner.

The incompatibility of different constituting segments in block copolymers typically leads to microphase separation in the bulk [1]. Different morphologies have been observed, including lamellae, cylindrical, or gyroidal structures, most often determined by the volume fractions of the respective segments or the interaction between adjacent compartments [2–4]. Such systems can be further modified or transferred into the solution state by the selective crosslinking of one of the blocks, as has been shown, e.g., for the polybutadiene (PB) compartment of polybutadiene-*block*-poly(2-vinylpyridine)-*block*-poly(*tert*-butyl methacrylate) (PB-*b*-P2VP-*b*-PtBMA) triblock terpolymers [5,6]. In general, the ability of

block copolymers and related materials to form well-defined nanostructures with different morphologies and tunable periodicity or size is probably the main driving force for the intense research interest in this field over the past decades [7–9].

Different methods for the controlled crosslinking of polymeric materials containing, e.g., vinyl bonds were investigated within the last years. Most commonly, radical crosslinking or so-called cold vulcanization processes are used. Radical initiators usually decompose upon irradiation or heating, generating radicals which initiate the crosslinking of adjacent polymer chains [10]. In that respect, Decker and coworkers studied the UV-induced crosslinking of polystyrene-*block*-polybutadiene-*block*-polystyrene (SBS) triblock copolymers using a variety of photoinitiators [11] as well as the use of multifunctional thiols or acrylate-based crosslinkers to accelerate the network formation within such films [12].

Another possibility is to selectively crosslink one domain of the bulk structures of AB diblock copolymer or ABC triblock terpolymers, followed by swelling in non-selective solvents and sonication-assisted dissolution into core-crosslinked micellar structures. In that way, Müller and coworkers were able to realize *Janus micelles*, cylinders, and discs from polystyrene-*block*-polybutadiene-*block*-polymethacrylate triblock terpolymers (SBM, the last block is poly(methyl methacrylate) and SBT), where the T

* Corresponding authors. Laboratory of Organic and Macromolecular Chemistry (IOMC), Friedrich-Schiller-University Jena, Humboldtstr. 10, 07743 Jena, Germany.

E-mail addresses: ulrichschubert@uni-jena.de (U.S. Schubert), felix.schacher@uni-jena.de (F.H. Schacher).

resembles poly(*tert*-butyl methacrylate) [13,14]. On the other hand, such processes have also been realized in thin films [15] or in solution, where either core or corona in block copolymer nanostructures (micelles) could be selectively crosslinked [16–18].

Among the multitude of block copolymers and related systems, PS/PB systems comprise a rather versatile class of materials where many different architectures (block, graft, and star-shaped systems) and compositions have already been synthesized. All these different materials feature a great variety of properties, turning them into probably the most intensively investigated block copolymer combination, especially with regard to possible applications in rubber technology [19]. Herein, one important aspect is the mechanical and thermal properties under different environmental conditions. If necessary, additives can be used to improve and fine-tune the material characteristics according to the requirements of the specific application. As polybutadiene still contains remaining double bonds, such materials offer the possibility of post-processing steps such as crosslinking by sulphur additives or UV irradiation. In case of crosslinking reactions, the vinyl groups in the side chain of 1,2-PB are far more reactive if compared to their 1,4-PB analogues.

Concerning the mechanical properties, Adhikari et al. investigated the effect of different morphologies in PS-*b*-PB block copolymers and compared the results with blends of the respective homopolymers [20]. This study was extended to composite materials of SBS triblock copolymers and particles of different dimensionalities as fillers using microhardness indentation testing in a more recent publication [21]. In general, the most common methods used for the mechanical characterization of these rubbers are tensile testing [20], microhardness indentation [20,21] and rheology [22]. All these methods require comparatively large quantities of material, sometimes limiting the applicability for materials produced in small scale.

Force microscopy methods clearly possess an advantage here, as only small sample areas are investigated, as shown by Chizhik et al. for the micromechanical properties of several solution-cast polymer thin films [23]. A similar approach was used by Blach et al. to monitor the degradation of polyisoprene (PI) under UV irradiation by force spectroscopy [24]. However, in both cases mainly the sample surface has been investigated. As an alternative, Raghavan et al. combined force microscopy (AFM) and dynamic mechanical analysis (DMA) during the annealing of PS/PB polymer blends to assess the mechanical properties of the resulting materials [25]. In this case, also auto-crosslinking took place during the annealing treatment at 80 °C due to oxidation.

Tsou et al. investigated the mechanical properties of several formulations of two different elastomers by dynamic indentation at different degrees of crosslinking and in relation to the depth of indentation [19]. The main advantage of this technique is that it requires only very small amounts of sample material. In general, the method can be performed on polymer thin films or any kind of bulk material fixed on a substrate, as long as it provides a flat, smooth surface. In this method, a measurement probe of known geometry is pushed into the material up to a defined force (or a certain displacement) and then the probe is retracted. During this procedure, both force and displacement are recorded, resulting in force–displacement or indentation curves. With certain assumptions on the material tested, the mechanical properties of the sample can be calculated from these indentation curves [26].

Herein, we present a detailed investigation of the UV-induced crosslinking process of a polystyrene-*block*-polybutadiene (PS-*b*-PB) diblock copolymer film. Crosslinking was performed through the incorporation of a suitable UV-photoinitiator into solution-cast films of a PS₅₁-*b*-PB₄₉^{73.3} diblock copolymer. The subscripts represent the weight fractions of the corresponding segments and the

superscript the overall molar mass in kg/mol. The influence of different amounts of crosslinker on the crosslinking efficiency was studied using Raman spectroscopy, depth-sensing indentation (DSI) measurements, and differential scanning calorimetry (DSC) for various irradiation times.

This work has been inspired by recent efforts on the sonication-assisted dissolution of various PB-containing triblock terpolymers [3,5]. Especially for materials exhibiting cylindrical bulk morphologies, in some cases spherical micelles were observed as side products, hinting towards incomplete crosslinking of the PB domains on the timescale of our experiments (1–5 h). Our aim was not only to achieve network formation (i.e. the generation of insoluble “gel” material) but also to monitor the conversion of the remaining double bonds of PB and to study the mechanical properties of the material at different stages of crosslinking.

2. Experimental part

2.1. Synthesis

The block copolymer, PS₅₁-*b*-PB₄₉^{73.3}, was synthesized by sequential living anionic polymerization in THF at low temperatures. First, styrene (14.28 g, 0.14 mol) in THF (600 mL) was initiated by the addition of *sec*-butyl lithium (0.2 mL of a 1.4 M solution in hexane, 0.28 mmol) at –70 °C. The reaction was allowed to proceed for 15 min before 1,3-butadiene (14.83 g, 0.27 mol) was added using a pre-cooled burette and the reaction was warmed to 15 °C. At this temperature the polymerization was continued for additional 3 h before the reaction was terminated using degassed isopropanol.

The subscripts denote the weight fractions of the corresponding blocks and the superscript is the molar mass in kg/mol. Under these conditions, approximately 90% of 1,2-PB is generated [3]. The molar mass of the first block, PS, was determined by size exclusion chromatography with THF as eluent using PS standards for calibration. For the second block, PB, the molar mass was estimated by comparing the respective signals in ¹H NMR spectroscopy. The corresponding SEC traces are shown in Fig. 1 and the molecular characteristics of the employed material are as follows: the precursor, PS, has a molar mass (M_n) of 37.400 g/mol and a narrow molar mass distribution (PDI) of 1.02. The diblock copolymer, PS₅₁-*b*-PB₄₉^{73.3}, has a molar mass (M_n) of 73.300 g/mol and a PDI of 1.02. The corresponding degrees of polymerization (DPs) are 374 for PS and 660 for PB, respectively and the formation of a lamellar bulk morphology can be expected according to the volume fractions of the constituting segments.

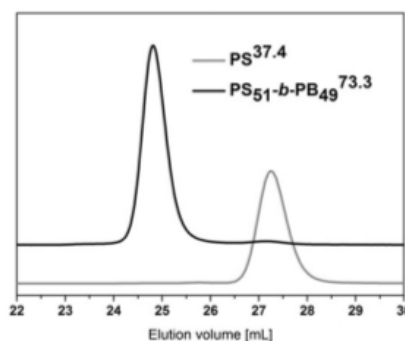


Fig. 1. THF-SEC traces for the precursor PS^{37.4} (solid grey line) and the PS₅₁-*b*-PB₄₉^{73.3} diblock copolymer (solid black line).

2.2. Sample preparation

Small amounts (50 to 100 mg) of PS₅₁-*b*-PB₄₉^{73,3} were weighed into glass vials. Referring to the weight fraction of the PB segment, the corresponding amounts of the UV-photoinitiator, Lucirin-TPO[®] (5, 10, 20, 30, 40 and 50 wt. %), were added to the diblock copolymer. The mixture was then dissolved in 1 mL chloroform and drop-casted onto gold-coated 12-well microscopy glass slides and allowed to dry in the dark overnight. The film thickness was approximately 200 μm. The gold-coating was produced by vapour deposition and was necessary to achieve a good signal-to-noise ratio during the Raman measurements. The general measurement cycle was performed in the following order for each time specified: the sample was first investigated by Raman spectroscopy (content of vinyl groups), afterwards analysed by depth-sensing indentation (DSI), followed by 1 h of irradiation in a Höppler UVACube 100 (equipped with a 100 W mercury lamp). The distance between sample and the light source was approximately 15 cm. All measurements have been performed on the same specimen.

For the polymer sample containing 20 wt. % of TPO, the measurement procedure was following the same cycle except that 12 different sample films have been drop-casted on the same glass slide. After the indentation measurements, the respective specimen was removed from the glass slide with a scalpel and the polymer film was subjected to differential scanning calorimetry (DSC) measurement.

2.3. Optical profilometry

The film thickness of the samples was determined with a Wyko NT 9100 optical profilometer from Veeco.

2.4. Depth-sensing indentation

The measurements were performed on a Hysitron TriboIndenter with a conospherical diamond indenter tip of approximately 4.7 μm radius. In a typical experiment, the tip was loaded up to a maximum force of 2500 μN in 1 s, then held at this load for 10 s and consecutively unloaded in 1 s. The measurements were performed in 'open-loop' mode, meaning that no force feedback is applied on the tip which would be used to compensate the time-dependant behaviour of the material. Instead, the hold period at maximum load is introduced to minimize the influence of the time-dependant behaviour of the investigated material on the unloading segment. The reduced moduli (E_r) were derived from the unloading curve, utilizing the method proposed by Oliver and Pharr [27]. The indentation moduli, E_i , were calculated from the E_r values according to Equation (1):

$$E_i = \frac{1 - \nu_{\text{sample}}^2}{E_r - \frac{1 - \nu_{\text{indenter}}^2}{E_{\text{indenter}}}} \quad (1)$$

where ν is the Poisson's ratio of the respective material. For the investigated samples, a Poisson's ratio of 0.36 has been assumed (as the average value from each of the two pure components according to the weight fractions) [28,29].

2.5. Raman spectroscopy

The Raman spectra were recorded on an Avalon Instruments RamanStation with a 300 mW infrared laser (wavelength: 785 nm). A special lens for thin film applications was used for the measurements. As UV-Vis measurements have shown, the

photoinitiator does not show absorption peaks above ~410 nm. Thus, it can be safely assumed that the laser in the Raman spectrometer did not induce decomposition of the UV-photoinitiator or further crosslinking of the diblock copolymer.

2.6. Differential scanning calorimetry (DSC)

The DSC thermograms were recorded on a Netzsch DSC 204 F1 instrument equipped with an autosampler in an automated run under nitrogen atmosphere. The samples were heated from 70 °C to 200 °C at a heating rate of 20 °C min⁻¹, then cooled to -70 °C at 40 °C min⁻¹ and again heated to 200 °C at 20 °C min⁻¹. The glass transition temperatures were determined from the second heating cycle. Midpoint values have been used for the evaluation.

2.7. Atomic force microscopy (AFM)

The AFM images have been recorded with a NanoScope IIIa Multimode instrument (Veeco) in semi-contact mode. MicroMasch NSC 35 cantilevers have been used for the investigations.

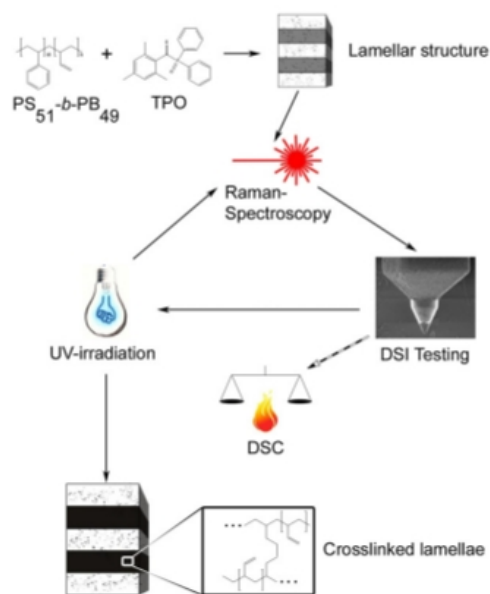
2.8. Small angle X-Ray scattering (SAXS)

SAXS measurements on drop-cast films from PS₅₁-*b*-PB₄₉^{73,3} were performed on a Bruker AXS Nanostar (Bruker, Karlsruhe, Germany), equipped with a microfocus X-ray source (Incoatec μSCu E025, Incoatec, Geesthacht, Germany), operating at $\lambda = 1.54 \text{ \AA}$. A pinhole setup with 750 μm, 400 μm, and 1000 μm (in the order from source to sample) was used and the sample-to-detector distance was 107 cm. Samples were mounted on a metal rack and fixed using tape. The scattering patterns were corrected for the beam stop and the background (Scotch tape) prior to evaluations.

3. Results and discussion

The aim of this work was to follow the crosslinking of the polybutadiene domains in microphase-separated block copolymer structures via a suitable method combination. We used a polystyrene-*block*-polybutadiene (PS₅₁-*b*-PB₄₉^{73,3}, the subscripts denote the weight fraction of the respective segment and the superscript corresponds to the overall number average molar mass in kg/mol) block copolymer as a model system. This, to our opinion, can be directly compared to literature examples where the PB segment of block co- and terpolymers has been selectively crosslinked in so-called bulk templating processes [5,6,14]. The block copolymer was synthesized using sequential living anionic polymerization in THF at low temperatures, generating mainly 1,2-PB, and exhibits a narrow molar mass distribution of 1.02.

Films of the diblock copolymer, PS₅₁-*b*-PB₄₉^{73,3}, were prepared on glass slides by drop-casting from solutions in chloroform. As a crosslinker, Lucirin-TPO[®] was chosen, as acylphosphine oxides are known to undergo fast photolysis (decolouration of THF solution within 15 min) and generate very reactive radicals, rendering this class of photoinitiators particularly efficient [30]. Both PS₅₁-*b*-PB₄₉^{73,3} and the equivalent amount of crosslinker (0–50 wt. %, calculated according to the fraction of PB) were dissolved, drop-casted onto the respective substrate and dried in the dark overnight. Any preference of the TPO crosslinker for either the PS or the PB phase is difficult to estimate. The average film thickness was around 200 μm as determined by optical profilometry. The dried films were first analysed using Raman spectroscopy (reference for the determination of the amount of vinyl groups) and then subjected to depth-sensing indentation (DSI) measurements. Afterwards, the specimen was irradiated for 1 h with UV-light (the UV-lamp was equipped with a quartz filter, i.e. a cut-off at 300 nm



Scheme 1. Schematic representation of the crosslinking procedure for the PS₅₁-b-PB₄₉^{73.3} diblock copolymer and the respective methods used for the investigations. The material exhibits a lamellar morphology, any preference of the TPO crosslinker for one of the two blocks is difficult to estimate. After irradiation, a dense network is formed within the PB domains.

to avoid additional unwanted crosslinking of PS). This cycle was repeated until the sample showed no further changes according to its indentation modulus, which we assume to represent the maximum crosslinking that can be reached. For the sample with 20 wt. % TPO, the film was removed after each irradiation step and separately analysed by DSC to determine the T_g of the material. Scheme 1 shows an overview on the film preparation, the diblock copolymer structure/morphology, and the different techniques used for the investigation of the film morphology or for monitoring the crosslinking procedure.

According to the weight fractions, a lamellar morphology can be anticipated for PS₅₁-b-PB₄₉^{73.3}. We therefore first used atomic force microscopy (AFM) for one representative specimen of the material on a glass slide. As can be seen in Fig. 2, a lamellar

structure with a spacing of approximately 53 ± 6 nm is obtained. The height image is shown in Fig. 2A, whereas Fig. 2B shows the corresponding phase image (Fig. 2C shows a higher magnification; the two parallel grey bars represent the domain spacing and the white bar spans over ten sequences of AB lamellae). The lamellae show a tendency to broaden in the outer part of the spherical phase separated areas and the images show both parallel and perpendicular orientation of the lamellae with respect to the underlying substrate. The herein used indentation-tip with a size of approximately $4.7 \mu\text{m}$ is a factor of approximately 100 larger if compared to the domain spacing of the block copolymer bulk morphology with 53 nm.

Both domain spacing and the overall morphology were further confirmed using small angle X-ray scattering experiments (Fig. 3). The characteristic peaks for lamellae at integer multiples of the first order peak are visible. The relative reflex positions 1 : 2 : 3 : 4 : 5 are related to the [100] : [200] : [300] : [400] : [500] reflections. From the SAXS measurements, the long period was calculated to $d_{\text{LAM}} = 50 \pm 3$ nm (with $q_n = 0.0128 \text{ \AA}^{-1}$ for [100], $q_n = 0.0256 \text{ \AA}^{-1}$ for [200], and $q_n = 0.0369 \text{ \AA}^{-1}$ for [300]; an error of approximately 5% was taken into account due to the rather broad reflections observed in SAXS) and is in good agreement with the results obtained from AFM ($d_{\text{LAM, AFM}} = 53 \pm 6$ nm).

The indentation experiments were performed in three consecutive segments: first, application of the load (A), followed by a hold at maximum load (B), and finally release of the load (C). These segments can be clearly distinguished from the indentation curves in Fig. 4 (the letters A, B, and C represent the corresponding segments of the measurement). During the hold segment, the indentation depth increases while the load decreases. This is the result of the material's time-dependant behaviour under constant force. As can be seen, the maximum indentation depth decreases with increasing irradiation time and the slope of the unloading curve is getting steeper. Both effects indicate a toughening of the material caused during the crosslinking process.

Furthermore, during the hold segment, the time-dependant behaviour of the block copolymer can be visualized as the indentation-tip continues to penetrate into the material, while the (nominal) force is held constant. This results in an increase in indentation depth with a simultaneous decrease in the (measured) force during the hold segment. This observation may be first interpreted as tip-sample adhesion, but this can be excluded, as at the end of the unloading segment no significant negative forces are measured (which would be expected for the polymer sticking on the tip while the latter is being retracted).

With increasing irradiation time, this effect significantly decreases, visible through smaller differences of both force and displacement at the beginning and the end of each hold segment. As the unloading curve is used for the calculation of the elastic

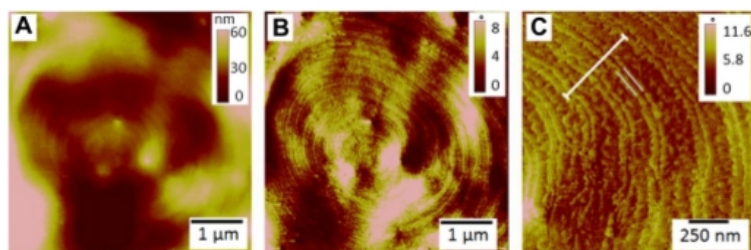


Fig. 2. AFM investigations of a block copolymer film containing 5 wt. % crosslinker: A) tapping mode height, B) phase image, C) shows a higher magnification, the two grey bars indicate the domain spacing; the averaged thickness of the lamellae is 53 ± 6 nm.

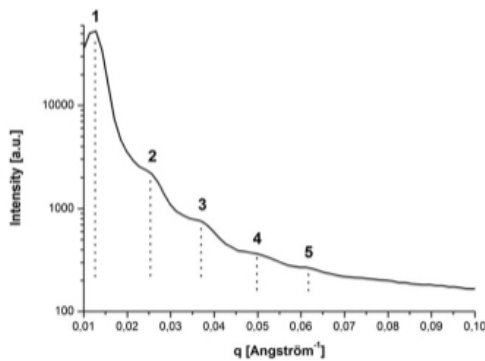


Fig. 3. SAXS pattern obtained for a drop-cast film of the $PS_{51}\text{-}b\text{-}PB_{49}^{73.3}$ diblock copolymer.

modulus, increasing slopes result in higher moduli for the material after longer irradiation times. Fig. 5 depicts the indentation moduli for $PS_{51}\text{-}b\text{-}PB_{49}^{73.3}$ with different amounts of TPO over the course of stepwise irradiation up to a total of 11 h; the corresponding indentation moduli are listed in Table 1. In general, an increase of the indentation modulus by a factor of 10 can be seen for all used photoinitiator concentrations. Exemplarily, for 20 wt. % TPO the respective values range from 0.4 GPa in the beginning to 3.97 GPa after 11 h. As a comparison, pure PS ($M_n = 30,000$ g/mol, PDI = 1.05) films did not show significant changes in modulus after 10 h of irradiation under identical conditions (native: 4.2 ± 0.1 GPa, irradiated: 4.5 ± 0.2 GPa).

If films without any additional TPO are investigated, the hardening of the PB due to auto-crosslinking starts after 6–7 h of irradiation, visible through changes in the materials properties. As shown by Decker et al. [11,12], the initial formation of crosslinks occurs within a few seconds after irradiation, although without immediate changes in the mechanical properties [30]. Therefore, the initially formed network is only loosely crosslinked. The material still behaves like a rubber while, after several hours,

the material is fully crosslinked and should rather be compared to a thermoset.

While the incorporation of 5 wt. % TPO (short dashes) does not show a significant difference if compared to the sample without TPO (dash-dotted line), significant changes in the materials properties for the samples with higher amounts (10% (dashed curve), 20% (black curve), and 30% CL (dark grey diamonds)) can be already seen after 2–3 h. In particular, the initial modulus is doubled after ~7 h of irradiation without and with only 5 wt. % TPO, while it takes only ~3 h for the 10–30% samples. In case of even higher amounts of CL added (40% (light grey diamonds) and 50% (light grey crosses)) the mechanical reinforcement is apparent already after the first hour of crosslinking. This may be explained by an initiation period where radicals are formed and mainly intra-chain crosslinking occurs, until their concentration in the material is high enough to form crosslinks. A simplified depiction of this process, showing both intra- (right hand part) and inter-chain crosslinking (left hand side), is presented in Scheme 2.

After the initiation period, the material undergoes a transition in which crosslinks are formed. Apparently, the initiation period is concentration dependant, i.e. shortens with increasing amount of crosslinker in the block copolymer films. While the incorporation of only 5 wt. % CL does not show a significant difference to the auto-crosslinking of the pure polymer, for higher percentages, the effect becomes more pronounced. For the 40 and 50 wt. % samples, the initiation period is no longer detectable; however, such high amounts of crosslinker are not practical and were only investigated to gather information about the onset of the crosslinking process.

The radicals then migrate until they react with a double bond in one of the polymer chains, forming a larger macro-radical. These macro-radicals can either undergo recombination reactions or lead to intra- or inter-chain crosslinking. Intra-chain crosslinking will not significantly increase the elastic modulus of the material, as new bonds are only formed within the same polymer chain, forming ring-structures which mainly retain the degrees of freedom regarding chain movement and realignment. The toughening of the material can be attributed to inter-chain crosslinking, as a dense polymer network with lower degrees of freedom is formed. This causes the moduli to increase rather sharply during the transition and afterwards level off to a plateau value which we correlate with fully crosslinked rubber domains.

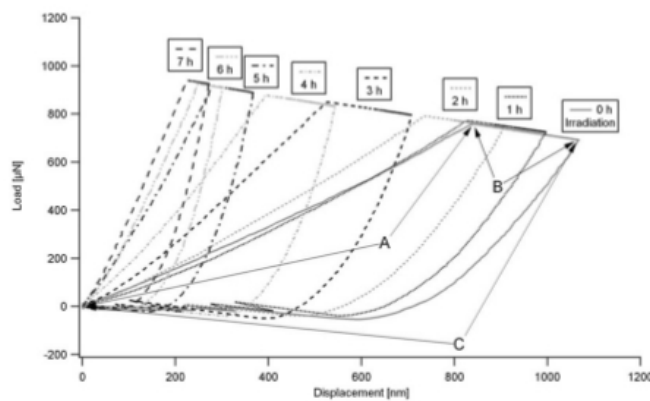


Fig. 4. Representative depth-sensing indentation responses (application of the load (A), followed by a hold at maximum load (B), and finally release of the load (C)) of $PS_{51}\text{-}b\text{-}PB_{49}^{73.3}$ block copolymer films with 20 wt. % TPO after different irradiation times.

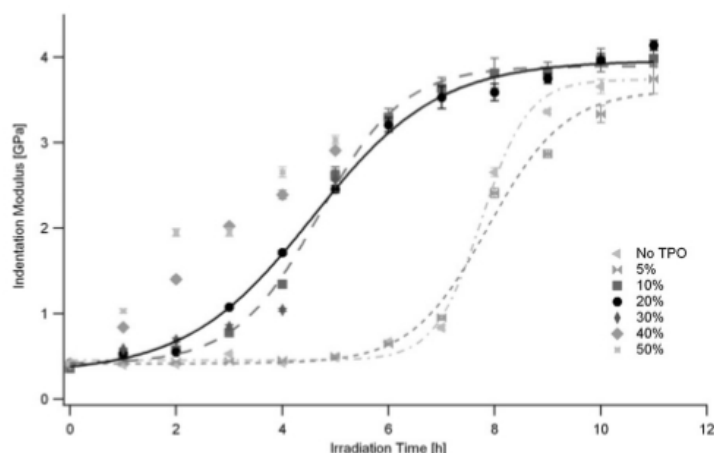
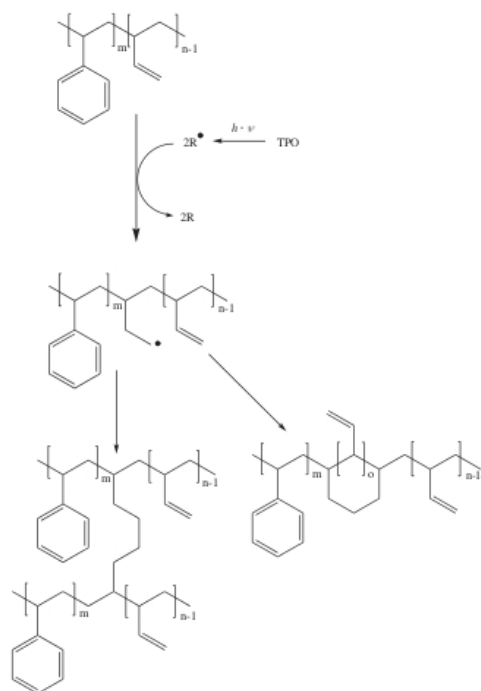


Fig. 5. Development of the indentation moduli during the stepwise irradiation of $PS_{51}\text{-}b\text{-}PB_{49}^{73,3}$ with different amounts of TPO; lines represent sigmoidal fits for the obtained datapoints and error bars refer to one standard deviation among 16 measurements each and may be smaller than the symbols.

For the samples containing 40 and 50 wt. % crosslinker, the increase in the modulus values is linear, as the formation of radicals probably exceeds both their migration and reaction rate. As the concentration of TPO in the polymer is comparatively high, also the concentration of radicals formed in the very beginning of the irradiation is high. Assuming that the UV-photoinitiator, Lucirin-TPO, is evenly distributed over the whole block copolymer film, the polybutadiene immediately reacts upon radical formation, forming a new macro-radical. As the total amount of C=C functionalities exceeds the number of radicals, it can be assumed that recombination reactions are less likely to occur if compared to inter-chain crosslinking. Hence, the formerly entangled block copolymer chains form a densely crosslinked network and exhibit a higher elastic modulus.

Fig. 6 shows the normalized intensity ratio of the peak areas of the C=C band and the aromatic C–H valences as measured by Raman spectroscopy. The aromatic C–H valences are assumed to not take part in the crosslinking process and can therefore be used as an internal standard. As can be seen, the intensity of the C=C band linearly decreases with increasing irradiation time. Contrary

to the results from the mechanical testing, no initiation period is found. Both findings support the assumption that the formation of radicals is continuous and slow if compared to the reaction step. Furthermore, any intramolecular crosslinking occurring also



Scheme 2. Crosslinking of the PB domains in films of $PS_{51}\text{-}b\text{-}PB_{49}^{73,3}$ induced via photolysis of an UV-photoinitiator, Lucirin-TPO[®].

Table 1
Indentation moduli of the investigated films of $PS_{51}\text{-}b\text{-}PB_{49}^{73,3}$ with different amounts of TPO as depicted in Fig. 3.

Time [h]	Indentation modulus [GPa] ^a						
	0% Cl ^b	5%	10%	20%	30%	40%	50%
0	0.4	0.36	0.36	0.42	0.41	0.41	0.42
1	0.4	0.43	0.5	0.53	0.59	0.84	1.03
2	0.41	0.44	0.57	0.55	0.69	1.4	1.95
3	0.53	0.44	0.78	1.07	0.84	2.02	1.95
4	0.43	0.45	1.34	1.71	1.04	2.39	2.65
5	0.49	0.5	2.61	2.45	2.56	2.91	3.03
6	0.67	0.65	3.29	3.21			
7	0.84	0.95	3.63	3.53			
8	2.65	2.41	3.81	3.59			
9	3.36	2.87	3.81	3.75			
10	3.66	3.33	3.96	3.96			
11	3.93	3.74	3.98	4.13			

^a Determined via depth-sensing indentation.

^b Added amount of crosslinker (Lucirin-TPO[®]) with respect to the overall weight of the PB segments.

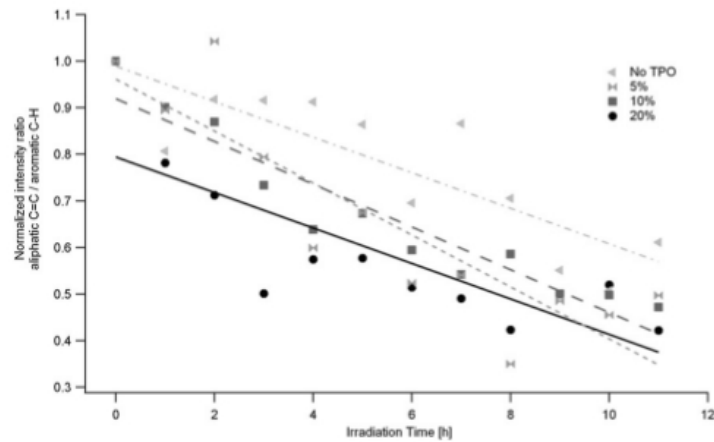


Fig. 6. Decrease of the normalized Raman signal of the C=C stretching vibration for different amounts of CL during crosslinking. Lines are added as a guide to the eye.

decreases the amount of C=C functionalities without significantly altering the elastic modulus of the material.

Fig. 7 shows a comparison of all measured properties of a 20 wt. % sample over the course of the crosslinking process. This amount of added crosslinker can be nicely compared to earlier work on the bulk crosslinking of SBT or BVT samples [5,14]. As can be seen, both the Raman signal and the T_g values show already a significant change after the first hour of irradiation, hinting towards loose network formation. The onset of the material hardening can be observed after about 3 h of irradiation.

Furthermore, the T_g values increase from $-5\text{ }^\circ\text{C}$ to roughly $30\text{ }^\circ\text{C}$ with increasing irradiation time (and crosslinking of the material) and finally, after around 8 h, no T_g can be detected. This is in accordance with the indentation experiments, as the 20 wt. % sample is significantly hardened after ~ 6 h, indicating a high degree of crosslinking. At this state, the PS-*b*-PB rather behaves like a thermoset. The glass transition temperature determined initially corresponds to the PB domains, as mainly 1,2-polybutadiene is present and the T_g of the styrene block is expected to be above $100\text{ }^\circ\text{C}$.

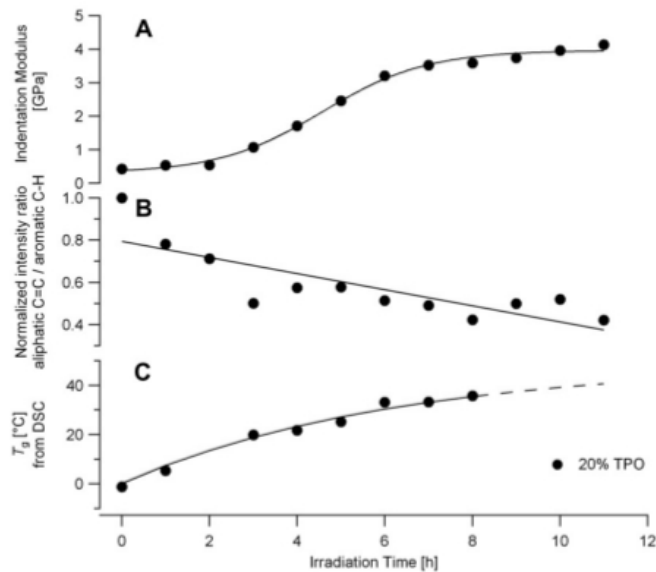


Fig. 7. Development of the crosslinking process for a sample with 20 wt. % CL content. A: Indentation Modulus; B: Normalized Raman signal of the C=C stretching vibration; C: Shift of the glass transition temperature during crosslinking; A and B are reproduced for clarity. Lines are added as a guide to the eye.

4. Conclusion

We show that the UV-assisted crosslinking of the polybutadiene block in drop-cast films of PS₅₁-*b*-PB₄₉^{73.3} diblock copolymers with a lamellar bulk morphology can be studied via a combination of depth-sensing indentation, Raman scattering and DSC measurements. The pendant vinyl groups form a loose network after a short irradiation period where the material still behaves like a rubber. After several hours of UV exposure, a dense network is formed, significantly hardening the block copolymer films, shown by the shift of the glass transition temperature as well as significant changes in the material's modulus. Raman spectroscopy was used to monitor the consumption of the C=C bonds during the crosslinking procedure.

For the system investigated here, the incorporation of 10–20 wt. % of crosslinker (Lucirin-TPO[®]) represents an optimum amount and complete crosslinking/consumption of the vinyl groups of the PB domains can be reached within 10 h of irradiation. With regard to AB diblock copolymer or ABC triblock terpolymers bulk templating approaches reported in literature, our study implies that longer irradiation times might be necessary to achieve full crosslinking of, e.g., the PB domains (in our own studies we used 1–2 h up to now) [3,5]. On the other hand, varying degrees of crosslinking might lead to different swelling degrees of the crosslinked domains in non-selective solvents, which is desirable if further chemical modifications are targeted.

Acknowledgements

This research forms part of the research programme of the Dutch Polymer Institute (DPI), Technology area HTE, projects #502 and #604. F. H. Schacher is grateful to the FCI for a fellowship and also to the Thuringian Ministry for Education, Science and Culture (TMBWK, grant #B515-10065, ChaPoNano), U. S. Schubert and F. H. Schacher thank the Thuringian Ministry for Education, Science and Culture (TMBWK, grants #B514-09051, NanoConSens, and #B515-11028, SWAXS-JCSM) for financial support. We also thank Markus J. Barthel for the synthesis of the PS homopolymer.

References

- [1] Bates FS, Fredrickson GH. *Phys Today* 1999;52(2):32–8.
- [2] Auschra C, Stadler R. *Macromolecules* 1993;26(9):2171–4.
- [3] Schacher F, Yuan J, Schobert HG, Müller AHE. *Polymer* 2010;51(9):2021–32.
- [4] Hadjichristidis N, Iatrou H, Pitsikalis M, Pispas S, Avgeropoulos A. *Prog Polym Sci* 2005;30(7):725–82.
- [5] Schacher FH, Rudolph T, Drechsler M, Müller AHE. *Nanoscale* 2011;3(1):288–97.
- [6] Walther A, Goldmann AS, Yelamanchili RS, Drechsler M, Schmalz H, Eisenberg A, et al. *Macromolecules* 2008;41(9):3254–60.
- [7] Abetz V, Simon P. In: Abetz V, editor. *Phase behaviour and morphologies of block copolymers block copolymers I*, vol. 189. Berlin/Heidelberg: Springer; 2005. p. 125–212.
- [8] Schacher FH, Rupar PA, Manners I. *Angew Chem Int Ed* 2012;51:7898–921.
- [9] Kim H-C, Park S-M, Hinsberg WD. *Chem Rev* 2009;110(1):146–77.
- [10] Akiba M, Hashim AS. *Prog Polym Sci* 1997;22(3):475–521.
- [11] Decker C, Viet TNT. *Macromol Chem Phys* 1999;200(2):358–67.
- [12] Decker C, Viet TNT. *Macromol Chem Phys* 1999;200(8):1965–74.
- [13] Walther A, Müller AHE. *Soft Matter* 2008;4(4):663–8.
- [14] Walther A, André X, Drechsler M, Abetz V, Müller AHE. *J Am Col Surg* 2007;129(19):6187–98.
- [15] Sperschneider A, Schacher F, Gawenda M, Tsarkova L, Müller AHE, Ulbricht M, et al. *Small* 2007;3(6):1056–63.
- [16] O'Reilly RK, Hawker CJ, Wooley KL. *Chem Soc Rev* 2006;35(11):1068–83.
- [17] Jiang X, Luo S, Armes SP, Shi W, Liu S. *Macromolecules* 2006;39(18):5987–94.
- [18] Schacher F, Walther A, Ruppel M, Drechsler M, Müller AHE. *Macromolecules* 2009;42(10):3540–8.
- [19] Tsou AH, Westwood AD, Schulze JS, Herbert EG. *Rubber Chem Technol* 2004;77(4):678–90.
- [20] Adhikari R, Michler GH. *Prog Polym Sci* 2004;29(9):949–86.
- [21] Adhikari R, Khatri SK, Adhikari S, Michler GH, Calleja JFB. *Macromol Symp* 2010;290(1):166–74.
- [22] Cook RF, Koester KJ, Macosko CW, Ajbani M. *Polym Eng Sci* 2005;45(11):1487–97.
- [23] Chizhik SA, Huang Z, Gorbunov VV, Myshkin NK, Tsukruk VV. *Langmuir* 1998;14(10):2606–9.
- [24] Blach JA, Watson GS, Busfield WK, Myhra S. *Polym Int* 2002;51(1):12–20.
- [25] Raghavan D, Gu X, Nguyen T, VanLandingham M, Karim A. *Macromolecules* 2000;33(7):2573–83.
- [26] Fisher-Cripps AC. *Nanoindentation*. New York: Springer-Verlag; 2004. p. 266.
- [27] Oliver WC, Pharr GM. *J Mater Res* 1992;7(6):1564–83.
- [28] Fo Fy GA, Savin GN. *Mech Compos Mater* 1965;1(1):106–10.
- [29] Greaves GN, Greer AL, Lakes RS, Rouxel T. *Nat Mater* 2011;10(11):823–37.
- [30] Decker C, Zahouily K, Decker D, Nguyen T, Viet T. *Polymer* 2001;42(18):7551–60.

P6 Water uptake of poly(2-*N*-alkyl-2-oxazoline)s: Influence of crystallinity and hydrogen-bonding on the mechanical properties

Erik F.-J. Rettler, Hanneke M. L. Lambermont-Thijs, Johannes M. Kranenburg, Richard Hoogenboom, Miriam V. Unger, Heinz W. Siesler, Ulrich S. Schubert,

J. Mater. Chem. **2011**, *21*, 17331–17337.

Water uptake of poly(2-*N*-alkyl-2-oxazoline)s: influence of crystallinity and hydrogen-bonding on the mechanical properties

Erik F.-J. Rettler,^{abcd} Hanneke M. L. Lambermont-Thijs,^a Johannes M. Kranenburg,^{ab} Richard Hoogenboom,^{ab} Miriam V. Unger,^e Heinz W. Siesler^e and Ulrich S. Schubert^{abcd}

Received 3rd June 2011, Accepted 15th August 2011

DOI: 10.1039/c1jm12541a

Poly(2-oxazoline)s are suitable materials to study structure–property relationships as their preparation by a living cationic ring-opening polymerization procedure and the relatively facile monomer synthesis allow accurate control over the molecular structure. In this contribution, the number of carbon atoms in the linear side-chain is systematically varied from a short methyl- to a long nonyl-group. As some of the materials are known to be hygroscopic, the effect of water uptake on the mechanical properties is investigated in detail. The combination of water uptake measurements, FT-IR spectroscopy and indentation revealed that only the samples with very short side-chains show significant hygroscopicity, while samples with longer side-chains exhibit crystalline behavior. Furthermore, depending on the polymer structure, it could be differentiated between side-chain and main-chain crystallinity.

Introduction

Poly(2-oxazoline)s have regained major interest in the past few decades, due to their relatively facile monomer synthesis and great variability in properties, such as water solubility and crystallinity. As these properties are mainly governed by the type and length of the side-chains, they can be easily fine-tuned by copolymerizing various 2-oxazoline monomers.^{1,2}

As can be seen from recent reviews, poly(2-oxazoline)s also have received significant attention for biomedical applications^{3–5} due to their structural similarities with polypeptides, high biocompatibility and thermo-responsiveness, making them ideal compounds for drug delivery devices. Also, possibilities for the use as immunosuppressors have been discussed.^{4,6} A recent review on the biomedical applications of poly(2-methyl-2-oxazoline) and poly(2-ethyl-2-oxazoline) and a comparison as an alternative to PEG has been discussed in ref. 7.

Lichkus *et al.* have investigated the hydrogen-bonding interaction of poly(2-ethyl-2-oxazoline) in blends of different ratios with poly(ethylene-co-methacrylic acid).⁸ The authors

determined the fraction of “free” carbonyl-groups from peak-fitting results in the carbonyl region. Later, Cai and Litt used a similar approach to determine the ratio of hydrogen-bonded/“free” carbonyl-groups in a series of decenyl/heptyl oxazoline copolymers.⁹

Earlier work from our group¹⁰ has focused on the material properties under idealized conditions, minimizing water uptake of the samples by working under dry conditions. Also the behavior of several oxazoline copolymers at different levels of humidity has been investigated.¹¹ For applications in the biomedical sector, materials should ideally retain their properties also under ambient conditions. Thus, the aim of this study is to elucidate the mechanical properties of the materials in relation to their water uptake behavior under ambient conditions. The obtained results will also be related to the polymer crystallinity based on temperature-dependent FT-IR spectroscopy.

Results and discussion

Water uptake

The macroscopic water uptake as a function of relative humidity was evaluated for a range of poly(2-oxazoline)s by analyzing the mass change. The polymers investigated in this study are shown in Table 1. Fig. 1 depicts the weight change of the investigated oxazolines due to water uptake from a humid environment. Only MeOx and EtOx show significant hygroscopicity, displaying weight changes of 62% and 37% at 90% relative humidity, respectively. Moderate water uptake (9% weight change) has also been found for a sample with an isopropyl side-chain, thus hinting that also structural parameters play a role for the hygroscopic behavior and not merely the number of carbon

^aLaboratory of Macromolecular Chemistry and Nanoscience, Eindhoven University of Technology, P.O. Box 513, Den Dolech 2, 5600 MB Eindhoven, The Netherlands. E-mail: ulrich.schubert@uni-jena.de; Fax: +49 3641 948202

^bDutch Polymer Institute (DPI), John F. Kennedylaan 2, 5612 AB Eindhoven, The Netherlands

^cLaboratory of Organic and Macromolecular Chemistry (IOMC), Friedrich-Schiller-Universität Jena, Humboldtstrasse 10, 07743 Jena, Germany

^dJena Center for Soft Matter (JCSM), Humboldtstrasse 10, 07743 Jena, Germany

^eDepartment of Physical Chemistry, University of Duisburg-Essen, Schuetzenbahn 70, 45117 Essen, Germany

Table 1 Schematic representation of the chemical structures of the poly(2-*N*-alkyl-2-oxazoline)s used in this investigation and their respective abbreviations

R=	Abbreviation
-CH ₃	MeOx
-C ₂ H ₅	EtOx
-C ₃ H ₇	PropOx
-CH(CH ₃) ₂	<i>i</i> -PrOx
-C ₄ H ₉	ButOx
-C ₅ H ₁₁	PentOx
-C ₆ H ₁₃	HexOx
-C ₇ H ₁₅	HeptylOx
-C ₉ H ₁₉	NonOx

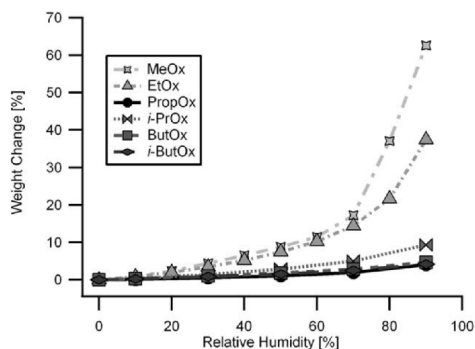


Fig. 1 Weight change as a function of relative humidity at 30 °C due to water uptake of the investigated polymers.

atoms in the side-chain. As discussed earlier,¹² the weight change in the hygroscopic polymers is non-linear due to the entropy-hindered formation of a first hydration shell. By forming hydrogen-bonds with the associated water molecules, the polymer chains adapt a new conformation which is more favorable to additional water uptake. Thus, subsequent hydration shells are formed more easily. The polymers with a propyl- or longer linear side-chain do not exhibit hygroscopic behavior. Their weight change is in all cases less than 5% at 90% relative humidity.

Temperature-dependent FT-IR investigations

To gain an insight into the molecular interactions with varying temperature of water-saturated polymers, FT-IR measurements were performed. Two important phenomena could be observed by the temperature-dependent IR-measurements: hydrogen-

bonding and melting processes. Both could be assessed by the observation of the dominant carbonyl absorption ($\sim 1645\text{ cm}^{-1}$).

Hydrogen-bonding

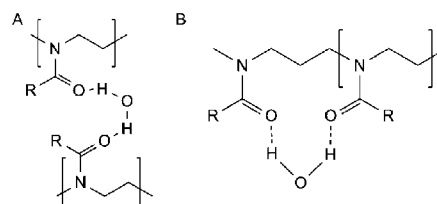
As the samples were saturated with water prior to the measurements, the associated water evaporates during the measurement due to the increasing temperature. This is observed by a shift of the peak maximum of the carbonyl band towards higher wavenumbers^{13,14} as well as the decrease of the water stretching band in the 3500 cm^{-1} region.

As illustrated in Scheme 1, the carbonyl group can take part in hydrogen-bonding processes, which weakens the $\nu(\text{C}=\text{O})$ absorption band (lower wavenumbers). With decreasing amount of associated water, the $\nu(\text{C}=\text{O})$ band becomes stronger, thus the peak maximum shifts to higher wavenumbers.

This peak shift ($8\text{--}10\text{ cm}^{-1}$) can be observed in all samples that showed hygroscopic behavior, but not in the samples with butyl- or longer side-chains. It has also been found for the PropOx, which does not show a significant weight change in the water uptake measurements, thus, the FT-IR analysis seems to be more sensitive in detecting the water association behavior than the macroscopic thermal gravimetric analyses. Fig. 2 depicts the temperature induced peak shift of the carbonyl region for the MeOx as an illustrative example. Furthermore, during the cooling of the EtOx, the peak maximum shifts back to lower wavenumbers by only 6 cm^{-1} , thus proving that the additional peak-shifting resulted from the hydrogen-bonding with water. Butyl- and longer side-chains seem to shield the $\text{C}=\text{O}$ bond from being accessed by water. These samples show no significant water uptake and also no significant shift of the carbonyl peak in the IR-spectrum.

Crystallinity

Previous work revealed endothermic peaks in the differential scanning calorimetric (DSC) heating runs of samples with a butyl- or longer *n*-alkyl side-chain.¹⁰ Furthermore, for ButOx, PentOx and *i*-PrOx, small exothermic peaks between T_g and the endothermic peaks have been observed. We attributed these transitions to melting and crystallization (ButOx, PentOx and *i*-PrOx) processes of the samples, thus terming them (semi-)crystalline without further evidence. Polarized optical microscopy did not reveal Maltese Cross patterns as would be expected for crystalline domains within the material, but this could also be due to a small crystallite size. This is in agreement with the



Scheme 1 Proposed mechanism for hydrogen-bonding in poly(2-oxazoline) chains, (A) low amount of water and small side-group R; (B) saturated conditions.

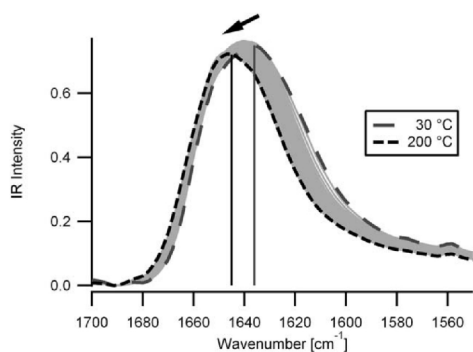


Fig. 2 Peak shift in the FT-IR spectrum of the water-saturated MeOx sample during heating (carbonyl region only).

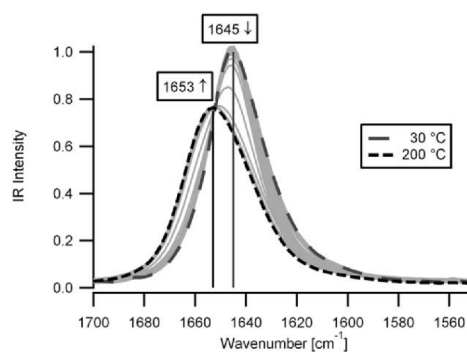


Fig. 4 Temperature-dependent FT-IR-spectra of water-saturated NonOx during heating (carbonyl region only).

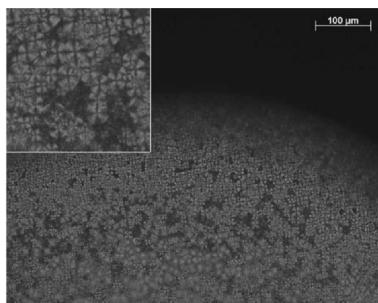


Fig. 3 Polarized optical microscopy image of the edge of a MeOx sample after two years of storage at ambient conditions (see ref. 16). Inset dimensions are 100 μm squared.

observations of Cai and Litt,¹⁵ who proved by scattering experiments that at least the HeptylOx and samples with longer side-chains are semi-crystalline.

Nonetheless after a long time of storage under ambient conditions, Maltese Cross patterns were observed for MeOx as depicted in Fig. 3.¹⁶

As MeOx only has a very short side-chain, it may be concluded that the crystallization process observed here results from an alignment of the main-chains. Demirel *et al.*¹⁷ have observed main-chain crystallization for *i*-PrOx. The authors examined the crystallization process by AFM, DSC and XRD techniques and concluded that the crystallization was caused by alignment of the dipolar amide-groups. They also emphasized the importance of incorporated water to increase the backbone mobility and, thereby, allow for chain alignment.

In analogy to Fig. 2, Fig. 4 shows the development of the NonOx carbonyl-peak during heating. Two features can be directly distinguished: at 30 °C, the carbonyl region is dominated by a sharp peak at $\sim 1645\text{ cm}^{-1}$, while at 200 °C, the broad absorption at $\sim 1653\text{ cm}^{-1}$ is dominant. At temperatures above 150 °C, the 1645 cm^{-1} absorption loses intensity until it disappears in the shoulder of the 1653 cm^{-1} peak. This corresponds

well with the endothermic peak of the NonOx found in the DSC (149.1 °C). Similar behavior is found for PropOx through HeptylOx as well.

Fig. 5 depicts the full-width-at-half-maximum (FWHM) of the carbonyl absorptions of the investigated samples. The values have been obtained by peak-fitting a Gaussian profile to the carbonyl band (linear baseline ~ 1535 to 1776 cm^{-1}) from which the FWHM was calculated.

For the investigated samples with a propyl through pentyl or isopropyl side-chain, an increase in the peak maxima at 1645 cm^{-1} is observed during heating. For the samples that also show exothermic peaks in the DSC response, this behavior is attributed to (further) crystallization of the material. The increase in the peak maximum should not be confused with a loss of water (found for the MeOx through PropOx and *i*-PrOx), which can be followed by the decrease of the water stretching vibration around $\sim 3500\text{ cm}^{-1}$. It may be easily confused from only observing the FWHM values, as both processes will decrease the FWHM value, but only the crystallization will increase the peak maximum as well.

Fig. 5 shows that after an initial decrease (which may arise either from the loss of associated water, or from crystallization of the sample), the FWHM values stay almost constant until approximately 150 °C. This temperature corresponds well with the endothermic peaks found in the DSC.¹⁰ At 150 °C, the FWHM values increase sharply and eventually level off. This increase, indicating a broadening of the peak, is usually observed during melting of (semi-)crystalline materials.^{13,14} During the cooling of the samples, the FWHM values for the semi-crystalline poly(2-oxazoline)s sharply decrease at around 135 °C due to the sharpening of the carbonyl-peak upon crystallization. Data for the EtOx and PropOx heating above 165 °C could not be calculated due to the low quality of the spectra caused by an undesired flow of the material between the KBr discs at high temperatures. As these samples do not show endothermic peaks in the DSC response, no increase in the FWHM is expected.

A special case is found in the *i*-PrOx sample. Having a T_g of $\sim 67\text{ °C}$, it is not brought to full crystallization during the preparation. As can be seen from Fig. 6, the FWHM sharply decreases around 115 °C which is caused by peak-sharpening due

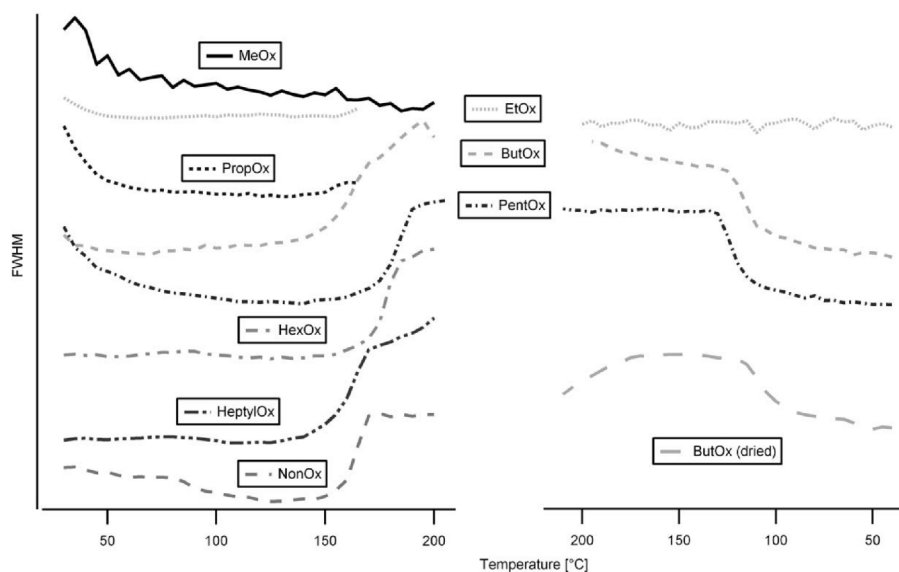


Fig. 5 Full-width-at-half-maximum values of the carbonyl absorptions of the investigated poly(2-oxazolines) during heating (MeOx through NonOx) and cooling (EtOx, ButOx, PentOx and dried ButOx). The values are shifted for better separation.

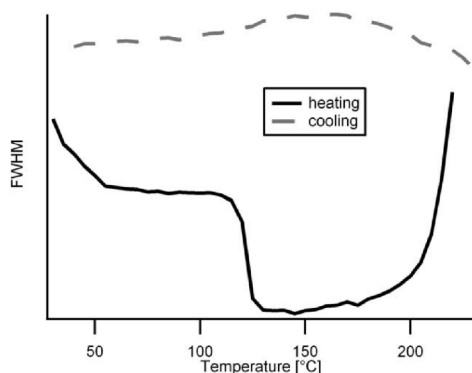


Fig. 6 Full-width-at-half-maximum of the carbonyl absorption of the *i*-PrOx sample during heating and cooling.

to further crystallization of the sample. During the cooling, there are no sharp transitions, pointing out that crystallization is slow compared to the time-frame of the experiment.

Mechanical properties

Fig. 7 shows typical load-displacement responses for MeOx, EtOx and HeptylOx in both dry (~5% RH) and ambient conditions (~40% RH). From these responses it is observed that the hygroscopic poly(2-oxazolines) are significantly softer at ambient conditions compared to low humidity conditions: the

slope of the loading response is less steep and the material creep during the hold time is significantly increased. For the non-hygroscopic samples, the differences between the indentation responses at low humidity are smaller: the slopes during loading and the extent of creep during the hold time at low and ambient humidity do not differ as much as for the hygroscopic samples.

The negative loads observed at the end of the unloading for the HeptylOx and especially the EtOx result from tip-sample adhesion. This tip-sample adhesion may influence the load-displacement response at the start of the unloading, which is used for the calculation of the elastic modulus. However, based on the work of Zhao *et al.*¹⁸ and the relevant parameters for the experiments discussed here, we estimate that the influence of adhesion on our data is negligible.

The mechanical properties of the investigated poly(2-oxazolines) have already been discussed for idealized conditions.¹⁰ For comparison, the data have been reproduced in Fig. 8, together with the new results under ambient conditions. Under ambient conditions, the indentation moduli significantly drop by almost 50% for the hygroscopic materials, while for the semi-crystalline materials, the decrease is very small to negligible. As discussed previously, the general trend within the library is related to the glass transition temperatures of the materials and to the presence of crystallinity.

Fig. 8 shows that at ambient conditions the trend is the same as under dry conditions. The measurements have been performed at room temperature. Therefore, MeOx through PropOx are still in the glassy state, while the T_g of the rest of the library is at (for ButOx) or below room temperature. The lower values for the indentation moduli (E_i) of the hygroscopic samples can be

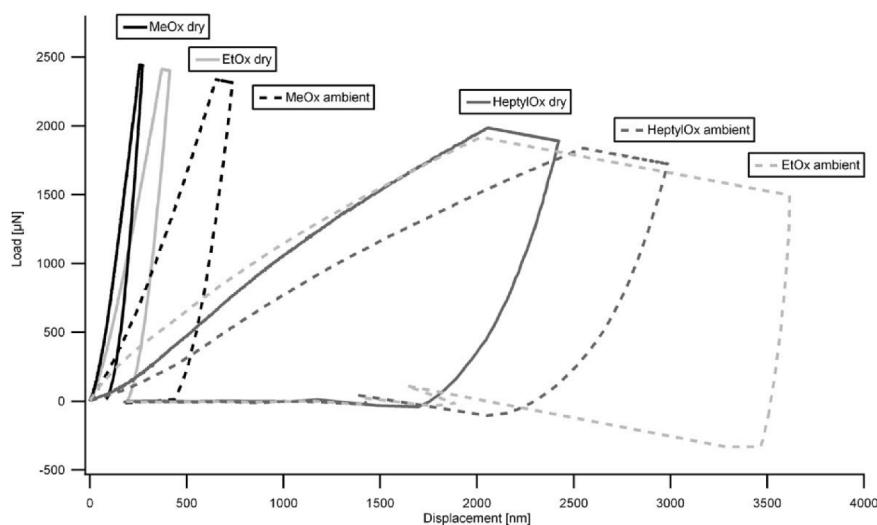


Fig. 7 Selected indentation curves for MeOx, EtOx and HeptylOx in dry (RH ~5%) and ambient atmosphere (RH ~40%), measured at high loads.

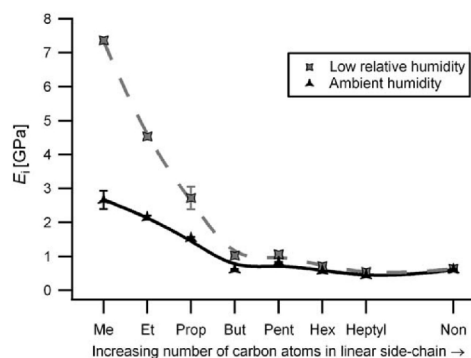


Fig. 8 Indentation moduli of poly(2-oxazoline)s with linear side-chains at low and ambient humidity. The error bars represent one standard deviation of the measurements and may be smaller than the symbols. The lines are added to guide the eye only.

explained by a plasticising effect of the incorporated water. The moisture taken up from the environment causes a swelling of the polymers, thus increasing the interchain volume. This results in a higher flexibility of the polymer chains. Therefore, the elastic modulus of the material is decreased.

Furthermore it can be seen that the MeOx exhibits an unusually high modulus of ~7.4 GPa at low humidity and drops to ~2.7 GPa at ambient conditions. This behavior at low humidity may be explained by traces of water still present in the MeOx even after the drying procedure or by water uptake of the material from the remaining ~5% humidity. Due to their low amount, water molecules may hydrogen-bond with two C=O

functionalities from different poly(2-oxazoline) chains (Scheme 1A), thus providing additional interaction between neighbouring polymer chains and therefore increasing the material stiffness.

Experimental

Synthesis

The different poly(2-alkyl-2-oxazoline)s have been prepared by microwave-assisted cationic ring-opening polymerization in acetonitrile. Methyl tosylate was used as initiator with a monomer to initiator (*M/I*) ratio of 60, resulting in relatively well-defined (*PDI* < 1.3) poly(2-oxazoline)s with ~60 repeating units. A schematic representation can be found in Table 1. The synthesis is described elsewhere.¹⁹

Water uptake

The water uptake measurements were performed on a Q5000 SA thermogravimetric analyzer from TA Instruments. Both sample and reference pans were enclosed in a humidity and temperature controlled chamber. A dried nitrogen gas flow was split in two paths, one passing through a water-saturation chamber. The desired relative humidity in the sample chamber was adjusted by mixing proper proportions of both the dry and the wet N_2 stream (regulated by mass-flow controllers). The temperature was kept constant at 30 °C and was controlled by Peltier elements. The measurements have been performed according to the protocol described by Thijs *et al.*¹²

Temperature-dependent FT-IR investigations

For the temperature-dependent IR-measurements, the samples were dissolved in chloroform (p.a. quality from Fisher Scientific, used without further purification), except for the MeOx sample,

which was dissolved in deionized water due to its low solubility in chloroform. The solutions were dropcast onto KBr discs and dried under reduced pressure. The discs were kept in a humid atmosphere overnight to allow for water uptake by the materials. For the measurements, a second KBr disc was placed onto the sample to prevent a possible melt-flow of the sample films at higher temperatures. The KBr-“sandwich” was clamped onto a heating block in the beam path of the spectrometer. The temperature (controlled with a Hotset RR 210) was increased in steps of 5 °C from 30 to at least 200 °C (max. 235 °C for ButOx, depending on the melting behavior of the individual sample), allowing a period of 5 min time for temperature equilibration at each step. After the heating run, cooling of the samples was performed in the same stepwise manner. The spectra were recorded on a Bruker IFS 28 FT-IR/FT-NIR-spectrometer. 32 scans were co-added for each spectrum with a spectral resolution of 4 cm⁻¹.

Mechanical properties

To prepare the samples for the indentation measurements, the poly(2-oxazolines) were dissolved in chloroform (except for the MeOx which was dissolved in deionized water because of its low solubility in chloroform) and dropcast onto 12-well Teflon-coated microscopy glass slides using an Analytik Jena FasTrans automated pipetting station. The Teflon coating prevents the solution from spreading over a too large area. These sample films were dried under reduced pressure at 45 °C over two weeks to remove the solvent residues.

The mechanical properties of the samples were measured with a Hysitron TriboIndenter, the employed measurement protocol can be found elsewhere.¹⁰ The reduced moduli (E_r) were derived from the unloading segment, utilizing the analysis method proposed by Oliver and Pharr.²⁰ Values are averaged from at least five measurements each. The indentation moduli (E_i) were calculated from the reduced moduli, assuming a Poisson's ratio ν_{sample} of 0.4, according to:

$$E_{i,\text{sample}} = \frac{1 - \nu_{\text{sample}}^2}{1/E_{r,\text{sample}} - (1 - \nu_{\text{indenter}}^2)/E_{\text{indenter}}} \quad (1)$$

For the measurements at low humidity, the sample compartment of the TriboIndenter was purged with dried air to lower the humidity that the samples were exposed to. Measurements were started after equilibration at 5 ± 1% RH, measured with a Testo 608-H2 hygrometer.

For the measurements at ambient humidity, the samples were simply stored for two weeks at ambient conditions after the drying procedure. During the measurements the ambient humidity was within 40 ± 5% RH.

Conclusion

By applying temperature-dependent FT-IR-spectroscopy and depth-sensing indentation, it was possible to explain the mechanical properties of a library of poly(2-oxazolines) with varying alkyl side chain length under the influence of water uptake and to relate them to the sample's hygroscopic behavior determined by water uptake measurements. At ambient conditions, the water-saturated samples exhibit lower moduli due to

a plasticising effect of the incorporated water.²¹ The water molecules hydrogen-bond to the polymer as shown by FT-IR-spectroscopy. At low humidity, however, small amounts of water still present in the dried MeOx may increase the material's modulus as they give rise to additional interactions between neighbouring polymer chains. The extreme case of this behavior is found in supramolecular polymers, where hydrogen-bonding is the driving force for the formation of crosslinks.²²

Furthermore, crystalline behavior of the carbonyl-band was shown for poly(2-oxazolines) with a linear side-chain of at least three carbon atoms' length. All FT-IR-spectroscopic results are based on the observation of the C=O bond, which represents the “junction point” between the side-chains and the polymer backbone. Therefore, it can be concluded that crystalline behavior found for the C=O vibration results from side-chain crystallization for ButOx and longer side-chains (which correlates with the melting peaks found in the DSC), whereas for shorter side-chains, the crystalline behavior is caused by an alignment of the polymer backbones. The crystallization of *i*-PrOx, ButOx and PentOx is slower than for longer alkyl side-chains, as shown by the exothermal peak in the DSC, indicating that during the first cooling run, the crystallization was not complete.

For very small side-chains (MeOx through *i*-PrOx), main-chain crystallization can occur. Moisture absorbed from the surrounding air provides the mobility necessary for this crystallization process and may be incorporated into the crystallites. The main-chain crystallization of MeOx was a slow process, as the Maltese Cross patterns were only observed after prolonged storage (months). The FT-IR results give rise to the conclusion that even the PropOx is slightly crystalline, as it shows a similar increase in the carbonyl peak maximum as samples with a longer side-chain. However, no melting peak in the DSC response could be observed. As the PropOx also does not show significant hygroscopicity, the necessary chain mobility for crystallization may result from the lower glass transition temperature (37.8 °C) compared to the MeOx (71.8 °C) and EtOx (59.2 °C).

A more detailed investigation on the side-chain crystallization processes of poly(2-oxazolines) will be given by generalized two dimensional correlation spectroscopy in a future contribution.

Acknowledgements

This research forms part of the research programme of the Dutch Polymer Institute (DPI), projects #449, #496, #502 and #604. MU thanks the Dr Jost-Henkel-Stiftung (Düsseldorf, Germany) and the Japan Society for the Promotion of Science (JSPS) for financial support. EFJR thanks Dr Joachim Loos for the helpful discussions about side-chain crystallinity of poly(2-oxazolines), which initiated this study.

References

- 1 J.-S. Park and K. Kataoka, *Macromolecules*, 2006, **39**, 6622–6630.
- 2 R. Hoogenboom, H. M. L. Thijs, M. J. H. C. Jochems, B. M. van Lankvelt, M. W. M. Fijten and U. S. Schubert, *Chem. Commun.*, 2008, 5758–5760.
- 3 N. Adams and U. S. Schubert, *Adv. Drug Delivery Rev.*, 2007, **59**, 1504–1520.
- 4 C. R. Becer, R. Hoogenboom and U. S. Schubert, *Angew. Chem., Int. Ed.*, 2009, **48**, 4900–4908.

- 5 H. Schlaad, C. Diehl, A. Gress, M. Meyer, A. L. Demirel, Y. Nur and A. Bertin, *Macromol. Rapid Commun.*, 2010, **31**, 511–525.
- 6 Y. S. Park, Y. S. Kang and D. J. Chung, *e-Polymers*, 2002, no. 016.
- 7 K. Knop, R. Hoogenboom, D. Fischer and U. S. Schubert, *Angew. Chem., Int. Ed.*, 2010, **49**, 6288–6308.
- 8 A. M. Lichkus, P. C. Painter and M. M. Coleman, *Macromolecules*, 1988, **21**, 2636–2641.
- 9 G. Cai and M. H. Litt, *J. Polym. Sci., Part A: Polym. Chem.*, 1996, **34**, 2689–2699.
- 10 E. F.-J. Rettler, J. M. Kranenburg, H. M. L. Lambermont-Thijs, R. Hoogenboom and U. S. Schubert, *Macromol. Chem. Phys.*, 2010, **211**, 2443–2448.
- 11 J. M. Kranenburg, C. A. Tweedie, R. Hoogenboom, F. Wiesbrock, H. M. L. Thijs, C. E. Hendriks, K. J. Van Vliet and U. S. Schubert, *J. Mater. Chem.*, 2007, **17**, 2713–2721.
- 12 H. M. L. Thijs, C. R. Beecer, C. Guerrero-Sanchez, D. Fournier, R. Hoogenboom and U. S. Schubert, *J. Mater. Chem.*, 2007, **17**, 4864–4871.
- 13 J. Dechant, *Ultrarotspektroskopische Untersuchungen an Polymeren*, Akademie-Verlag, Berlin, 1972.
- 14 H. W. Siesler and K. Holland-Moritz, *Infrared and Raman Spectroscopy of Polymers*, Marcel Dekker, Inc., New York, 1980.
- 15 G. Cai and M. H. Litt, *J. Polym. Sci., Part A: Polym. Chem.*, 1996, **34**, 2701–2709.
- 16 J. M. Kranenburg, *Depth-Sensing Indentation and High-Throughput Experimentation on Polymers and Elastomers*, PhD thesis, Technische Universiteit Eindhoven, 2009.
- 17 A. L. Demirel, M. Meyer and H. Schlaad, *Angew. Chem., Int. Ed.*, 2007, **46**, 8622–8624.
- 18 Y.-P. Zhao, X. Shi and W. J. Li, *Rev. Adv. Mater. Sci.*, 2003, **5**, 248–253.
- 19 R. Hoogenboom, M. W. M. Fijten, H. M. L. Thijs, B. M. van Lankvelt and U. S. Schubert, *Des. Monomers Polym.*, 2005, **8**, 659–671.
- 20 W. C. Oliver and G. M. Pharr, *J. Mater. Res.*, 1992, **7**, 1564–1583.
- 21 S. Ito, M. Hashimoto, B. Wadgaonkar, N. Svizero, R. M. Carvalho, C. Yiu, F. A. Rueggeberg, S. Foulger, T. Saito, Y. Nishitani, M. Yoshiyama, F. R. Tay and D. H. Pashley, *Biomaterials*, 2005, **26**, 6449–6459.
- 22 S. Sivakova, D. A. Bohnsack, M. E. Mackay, P. Suwanmala and S. J. Rowan, *J. Am. Chem. Soc.*, 2005, **127**, 18202–18211.

P7 Preparation of polyurethane elastomers (PUEs) in a high-throughput workflow

Laszlo I. Majoros, Bernard Dekeyser, Nancy Haucourt, Pieter Castelein, Johan Paul, Johannes M. Kranenburg, Erik F.-J. Rettler, Richard Hoogenboom, Ulrich S. Schubert,

J. Polym. Sci., Part A: Polym. Chem. **2011**, *49*, 301–313.

Preparation of Polyurethane Elastomers (PUEs) in a High-Throughput Workflow

LÁSZLÓ I. MAJOROS,¹ BERNARD DEKEYSER,² NANCY HAUCOURT,² PIETER CASTELEIN,³ JOHAN PAUL,³ JOHANNES M. KRANENBURG,¹ ERIK RETTLER,⁴ RICHARD HOOGENBOOM,¹ ULRICH S. SCHUBERT^{1,4}

¹Laboratory of Macromolecular Chemistry and Nanoscience, Eindhoven University of Technology, P.O. Box 513, 5600 MB Eindhoven, The Netherlands

²International Development Center, Recticel N.V., Damstraat 2, B-9230 Wetteren, Belgium

³Flamac, a division of SIM, Strategic Initiative on Materials in Flanders, Technologiepark 903, B-9052 Zwijnaarde, Belgium

⁴Laboratory of Organic and Macromolecular Chemistry (IOMC), Friedrich-Schiller-University Jena, Humboldtstr. 10, D-07743 Jena, Germany

Received 30 June 2010; accepted 17 September 2010

DOI: 10.1002/pola.24397

Published online 29 November 2010 in Wiley Online Library (wileyonlinelibrary.com).

ABSTRACT: High-throughput experimentation (HTE) represents a promising and versatile approach for polyurethane (PU) research as a tool to rapidly screen and characterize a large number of samples in an automated way. To realize a unique HTE workflow for the research and development of PU elastomers (PUEs), the use of parallel automated formulation and coating platforms at Flamac were explored. To evaluate the applicability of HTE for PUEs, four different PU systems were investigated with different reactivities and viscosities. All prepared PUEs were evaluated by conventional physical testing methods measuring the E-modulus, tensile-elongation and the hardness properties revealing similar trends as conventionally prepared PUEs indicating the viability of the HTE approach. In addition, the properties of the PUEs were also investigated

using downscaled microtensile bars as well as depth-sensing indentation, again, revealing similar trends. With this proof of principle study, we demonstrated for the first time that HTE can also be extended to polymeric materials based on high reactive and viscous raw materials in combination with complex technologies. The reported results provide a basis for the use of HTE approaches for preparing, screening and characterizing large numbers of PUEs for R&D purposes. © 2010 Wiley Periodicals, Inc. *J Polym Sci Part A: Polym Chem* 49: 301–313, 2011

KEYWORDS: depth-sensing indentation; high performance coatings; high-throughput experimentation; mechanical properties; polyurethane elastomers (PUEs)

INTRODUCTION Combinatorial research represents a dynamic field, which was originally developed in the pharmaceutical industry. After a fast progress, high-throughput experimentation (HTE) techniques have also been extended to other research fields such as materials science for the development of new polymers and catalysts.^{1–14}

The application of combinatorial methods for the development of organic coatings is extensively reported by Chisholm et al.^{15–19} In most cases, the starting materials are liquid and, thus, can be easily transferred by a liquid handling robot²⁰ which is utilized for the production of arrays of liquid coatings.²¹ Other research groups^{22,23} and companies^{24–26} also invested significant efforts to develop advanced HTE techniques to identify new coating solutions. Nowadays, these processes include many independent chemical variables and parameters as well as many time-consuming steps.

Recently, we reported high-throughput approaches to accelerate investigations on the preparation of polyurethane (PU) pre-

polymers.^{27,28} In this contribution, a concept is reported for the high-throughput preparation and screening of polyurethane elastomer (PUE) samples that are mainly applied within the automotive industry as covering materials for dashboards, cup holders, ashtrays, door panels and interior parts of cars. Other applications include usage as encapsulation materials for car windows or other electrical parts. Depending on the raw materials, recipes, preparation and moulding conditions of PUEs, large property variations are accessible in the final products,^{29,30} thus automation of their preparation process is essential for a fast and sustainable research.

The raw materials for the preparation of PUEs are very viscous and reactive. Therefore, their handling requires a highly flexible and fast high-throughput tool. Nowadays, these non-cellular PU materials are mainly processed in a manual way enabling the preparation of a maximum of 20 elastomer samples per day per person which does not allow a fast innovation. The growing markets and demands for new PU

Correspondence to: U. S. Schubert (E-mail: ulrich.schubert@uni-jena.de, www.schubert-group.com)
Journal of Polymer Science: Part A: Polymer Chemistry, Vol. 49, 301–313 (2011) © 2010 Wiley Periodicals, Inc.



FIGURE 1 Overview of the high-throughput formulation platform at Flamac.

materials are pushing the companies towards the use of high-throughput technology as the key approach to discover and develop new polymer products faster than before.

In this contribution, we report a proof of principle study for a high-throughput workflow for PUEs consisting of three independent units: (a) a compounding platform for the preparation of isocyanate and polyol blends, (b) a coating platform for a two component reactive system and (c) a physical testing unit. The designed equipment should be able to cope with high viscosities and a large number of raw materials, as well as with 20 to 30 s reaction time counting from the moment of mixing of the two blends. In an ideal case, the same platform should also be applicable for the preparation and testing of cellular PU materials.³¹ Although there are scientific contributions in the field of HTE applied to PU systems,^{32,33} to the best of our knowledge, this is the first reported high-throughput method for highly reactive PU elastomer research.

EXPERIMENTAL

Materials

Polyurethane Elastomers

Elastomer systems PUE1, PUE2, PUE4 were based on a trifunctional ether polyol while PUE3 was based on an OH-prepolymer obtained from Recticel N.V. (Belgium).

The solvents *N*-methylpyrrolidone (NMP) and acetone were used for cleaning purpose. All chemicals (polyol, isocyanate, catalysts, etc.) were used as received without further purification. The applied formulation recipe is the property of Recticel N.V. (Belgium).

High-Throughput Instrumentation and Workflow

The high-throughput formulation (Fig. 1) and coating platforms (Fig. 2) at Flamac (Zwijnaarde, Belgium)³⁴ developed in close collaboration with HTE AG (Heidelberg, Germany)³⁵ were used for the preparation of the selected PUEs. The two workstations, controlled by the automation software suite

hteControl™, had to be synchronized to prepare PUEs in an automated way under well-defined reaction conditions.

The formulation platform is equipped with a robotic arm and with a gripper mounted on a linear track for flexible sample transfer in combination with an individual bar coding system for the vessels, as well as a storage facility for the empty or filled vessels. The viscosity range for weight based dispensing of formulations without cross contamination is 17 to 8300 mPa s. The dispensing range was available from 50 mg to 100 g with an accuracy of 0.5% to 1%. Accurate dispensing of the raw materials was realized by a mini spool valve (Techcon Systems, CA), an olive TE 14GA needle (Miyachi Europe BV, Eindhoven, The Netherlands) and seven bar nitrogen pressure on the containers. Mixing of the dispensed materials in the glass vessels was performed by an overhead mixer with a maximum speed of 2000 rpm. After each mixing step the impeller was cleaned in a brush bath filled with different solvents and dried by compressed air. The formulation platform consisted of three independent dispense modules with nine containers each with a maximum volume of 600 mL. With this current workflow, 50 to 100 formulations per day could be realized depending on the complexity of the preparation procedure.

The coating platform for high speed applications was equipped with a specially designed heated mould and a round shaped bar coater for the preparation of the PUEs using a doctor blade process. This step was realized by a powerful articulated robot arm which enables fast processes for high reactive materials such as PUs. The mould for the doctor blade process was preheated to 65 °C before the coating step started. Optionally, the prepared elastomers could be stored in a substrate hotel (6 storage racks, 120 hotel positions). After 10 min curing time, the elastomers were removed from the mould and placed for 7 days at room temperature for final curing. The mould applied had to be manually cleaned after each elastomer preparation. The



FIGURE 2 Detailed view of the high-throughput coating platform at Flamac.

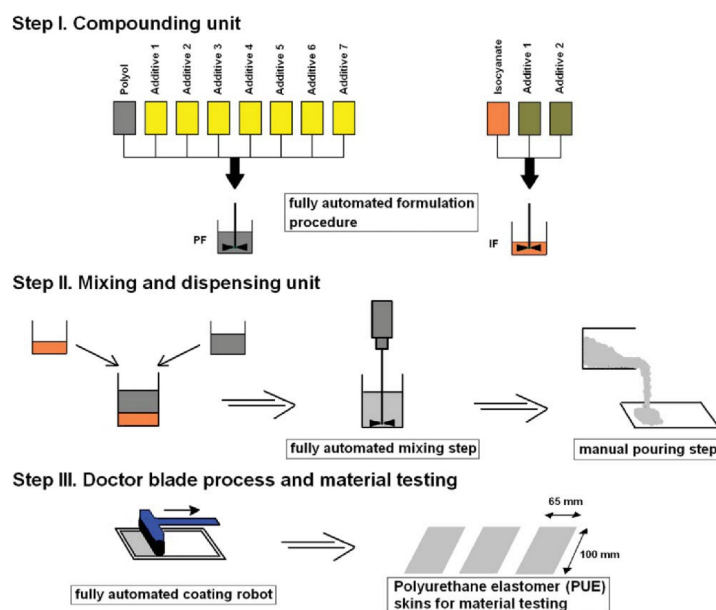


FIGURE 3 Schematic representation of the developed workflow for the PUE preparation.

temperature (20 °C) and the relative humidity of the laboratory were kept constant.

PUEs Preparation in a High-Throughput Workflow

Manually prepared, ready-to-use materials (formulations) including all components were provided to Flamac for the HTE to focus on the most challenging steps, namely the mixing of the two reactive formulations and the coating process (see Fig. 3). It is strongly believed that these steps are the most crucial in the whole high-throughput workflow for preparing PUEs. The polyol formulation (PF) was manually prepared in a 1 L beaker made out of polypropylene and the compounds were weighed together in the same order as listed in Table 1.

After adding all materials manually into the beaker an overhead mixer at a speed of 6000 rpm was used to prepare a homogeneous, highly viscous mixture. Similarly, the isocyanate formulation (IF) was also prepared manually in a 1 L polypropylene beaker according to the recipe stated in Table 1. These ready-to-use formulations were delivered to Flamac, filled into the dispense modules on the formulation workstation and finally pressurized under 7 bar nitrogen. The polyol formulations containing solid particles (e.g., water scavengers) were continuously mixed by an overhead mixer at 500 rpm to keep it homogeneous. Fresh materials were prepared for the high-throughput experiments and all containers, valves and tubing were daily changed after the experiments. Before each dispensing procedure, a purge step was

applied for both PF and IF into a waste container to avoid cross contamination and inhomogeneity during dispensing.

To start the high-throughput preparation of the PUEs, the robot arm mounted on a linear track moved the vessels to the dispensing station on a balance after the bar coding step. First the PF and secondly the IF was dispensed gravimetrically into the vessels. In our PU formulations, the reaction between the two reactive formulations started solely when the mixing step was applied since no significant chemical reaction took place on the surface of the two layers without efficient mixing. In a next step the robotic arm placed the vessel in a specially designed nest with a lift system. This vessel contained the two mixtures layered on top of each other. Afterwards, the polymerization was started by mixing the two components in the vessel with an overhead mixer of the formulation platform exactly for 10 s at 2000 rpm. The developed lift system with a nest facilitated the fast manual removal of the vessel as well as the pouring of the mixture on the preheated mould of the coating platform. From the moment when the mixing started until the pouring step, the required processing time was ~25 s. The doctor blade process was carried out afterwards by the precisely synchronized robot arm of the coating platform with a round shaped bar coater. After 10 min curing time (demould time), the prepared elastomer with a dimension of $100 \times 65 \times 1$ mm was removed from the mould. The round shaped bar coater was washed automatically but the stainless steel mould had to be cleaned and dried manually before the next experiments

TABLE 1 Formulation and Selected Properties of the Four Investigated PUEs Systems

Properties	Materials	PUE1	PUE2	PUE3	PUE4
Polyol Formulation (PF)	Component 1 (g)	81	81	60	66
	Component 2 (g)	–	–	20	–
	Component 3 (g)	4	6	6	6
	Component 4 (g)	4	4	4	4
	Component 5 (g)	0.25	0.25	0.25	0.25
	Component 6 (g)	5.5	5.5	5.5	5.5
	Component 7 (g)	0.5	0.5	0.5	0.5
	Component 8 (g)	6	6	6	6
	Component 9 (g)	0.3	0.3	0.3	0.3
	Total (g)	101.625	103.625	104.55	88.625
	Used amount of PF (g) for one PUE (high-throughput way prepared)	8.27	7.87	7.92	6.78
IOH value of PF (mg KOH/g)		166	194	190	221
Viscosity of PF (mPa.s)		874	905	1892	965
Isocyanate Formulation (IF)	Component 1 (g)	51.2	51.2	51.2	51.2
	Component 2 (g)	–	–	–	15
	Component 3 (g)	0.22	0.22	0.22	0.22
	Component 4 (g)	0.5	0.5	0.5	0.5
	Total (g)	51.92	51.92	51.92	66.92
	Used amount of IF (g) for one PUE (high-throughput way prepared)	3.73	4.13	4.07	5.22
NCO value of IF (%)		27.6	27.6	27.6	20.7
Viscosity of IF (mPa.s)		1172	1172	1172	2453
Index		100	100	100	100
Fiber time ^a (s)		42	35	30	35

^a Fiber time = Time from the moment of mixing of the two reactive formulations until the materials can form fibers by pulling it with a

glass rod. It gives an impression about the reactivity of the system.

could be started. In this manner, in total 40 PUEs (PUE1, PUE2, PUE3, PUE4) have been prepared (4 systems; for each system 10 identical samples) in a reduced dimension (see schematic representation of the entire workflow in Fig. 3).

During the entirely automated operation, the only manual step was the pouring step. At this stage of our research, we particularly focused on proving the concept of the preparation of PUEs in a high-throughput manner, which goal could

FORMULATION PLATFORM

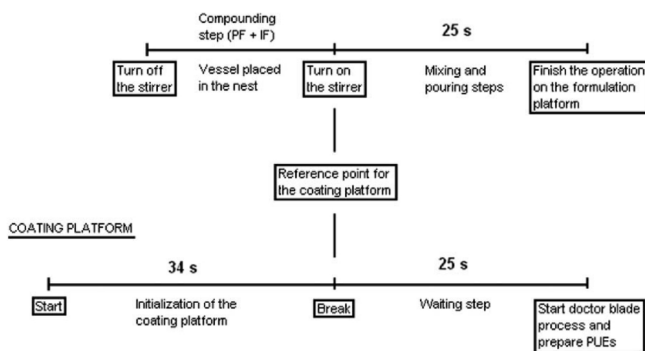


FIGURE 4 Synchronization of the two platforms.

TABLE 2 Summary of the Physical Testing Methods of the Prepared PUEs

Type of Sample	Physical Test	Standards	Dimensions of the Test Specimen (mm)	Number of Measurements
PUEs prepared in a high-throughput way	Tensile strength (N/mm ²) and elongation at break (%)	ASTM D1708	38 × 15 × 1 (microtensile specimen)	3
	E-Modulus (MPa)	ASTM D790-I B	50.8 × 12.7 × 1 (microtensile specimen)	3
	IRHD	DIN ISO 48		5
PUEs prepared in a conventional way	Tensile strength (N/mm ²) and elongation at break (%)	ASTM D1708	38 × 15 × 1 (microtensile specimen)	3
	E-Modulus (MPa)	ASTM D790-I B	50.8 × 12.7 × 1 (microtensile specimen)	3
	IRHD	DIN ISO 48		5
PUEs prepared in a conventional way	Tensile strength (N/mm ²) and elongation at break (%)	DIN 53504 S1	115 × 25 × 3 (conventional specimen)	3

be reached without the development of a high cost automated pouring unit.

Synchronization of the Two High-Throughput Platforms

In general, the formulation and the coating platforms are functioning independently from each other. For our purpose, the use of the two separate platforms in one workflow was essential to deal with the very fast reaction (30 s reaction time), and therefore, synchronization of the formulation and the coating platforms had to be performed (see the time line of the synchronization in Fig. 4). First of all, the overhead stirrer was completely turned off during the compounding step of the two formulations (PF and IF). After the vessel was placed in the nest by the robotic arm and ready for mixing, the stirrer was turned on again. Turning on the stirrer was the reference point for the coating platform and, from this moment on (starting point), the software of the coating platform was started after 25 s. Due to the fact that initialization of the coating platform required 34 s, the robot system was ready for the coating application after 59 s. As a next step, the mixing was started on the formulation platform, which together with the pouring step required 25 s. To be on time for the doctor blade process using the coating robot (SIAS robot), a 25 s waiting step was introduced. This synchronization enabled sequential operation on the two platforms and eliminated the possible source of errors (e.g., small time delays) of the manual pouring step.

Conventional PUEs Preparation

To compare the macroscopic mechanical properties of the PUEs prepared in a high-throughput manner, chemically equal PUEs have also been prepared in a manual, conventional way. The same batches of the ready-to-use raw materials were used for the preparation of the samples. In this case, the PF was weighed on an analytical balance in a 1 L polypropylene cup and premixed for 10 s at 4000 rpm with an overhead mixer. The appropriate amount of PF was filled in a 50 mL syringe, injected into the polyol formulation and then mixed further for 10 s at 4000 rpm with the same mixer. The well-mixed reactive mixture (with ~35 s gelling time) was poured onto a preheated (65 °C) mould and the doctor blade process was applied to obtain 40 pieces of PUEs (4 systems; for each system 10 identical samples) with a conventional dimension

of 13.5 × 40 × 0.3 cm. The mixing to pouring required 25 s. The total amounts of samples are between 153 g and 156 g depending on the system used, see Table 1.

Physical Analysis of PUEs

The tensile-elongation (tensile strength and elongation at break) macroscopic properties of the PUEs were determined according to ASTM D1708, the bending test (E-modulus) according to ASTM D790-I B and IRHD (International Rubber Hardness Degrees) according to DIN ISO 48. Four different systems have been defined (PUE1, PUE2, PUE3, PUE4) and ten pieces of PUEs have been prepared for each system, thus, in total 40 pieces of PUEs have been obtained by high-throughput preparation and 40 pieces of PUEs by conventional elastomer preparation, respectively. On each PUE, three times tensile strength, three times bending and 5 times IRHD measurements have been consecutively performed and the average values were calculated for comparison. The dimensions of the reduced sized specimen (microtensile) are summarized in Table 2.

For comparison, the PUEs prepared in a conventional way were also tested according to the same standards using the microtensile specimens. All dimensions of the test specimens and the number of measurements are detailed in Table 2.

Finally, the tensile-elongation properties of the conventionally prepared PUEs were also measured according to test methods DIN 53504 S1 using conventional specimens. These results were compared with the values obtained using microtensile specimens.

In many cases, the characterization of the prepared samples is considered to be the bottleneck of a high-throughput workflow. To overcome this problem, we have implemented depth-sensing indentation measurements into our workflow to validate this characterization tool for these types of PUEs. The measurements were solely performed for PUEs prepared in a high-throughput way using a Hysitron TriboIndenter (Minneapolis, MN) with a conospherical diamond tip of ~4.7 μm radius.^{36–38} The machine was calibrated with a fused quartz standard. A load-hold-unload pattern of 10-1-10 s was used up to a maximum displacement of 1000 nm in the sample materials. The samples were measured in a high-throughput approach. All 40 samples were glued at regular



FIGURE 5 Fluid container equipped with overhead stirrer for storage of the formulations (PF and IF). [Color figure can be viewed in the online issue, which is available at wileyonlinelibrary.com.]

positions onto glass substrates, which were fixed to the sample stage by reduced pressure. Gluing and setting-up the experiment took ~ 1 and 3 hours, respectively. The indentation measurements were carried out in an automated run overnight. In total, 480 indents were made, six per sample on two different positions per sample. The analysis method proposed by Oliver and Pharr³⁶ was applied to calculate the reduced modulus from the unloading curves.

RESULTS AND DISCUSSION

Optimization Procedures for the Formulation Platform

Nowadays, all steps of the conventional PU elastomer preparation are carried out manually in the R&D process. All components of the polyol formulation (PF) and isocyanate formulation (IF) are weighed together and mixed separately by a dynamic mixer. At first, the PF has to be premixed and the IF is quickly added. After 10 s mixing, the material is manually poured onto a prepared mould, which is either open or closed and mostly heated. The total processing time is ~ 30 s. The de-moulding time strongly depends on the formulation but it takes generally ~ 10 min.

In this contribution, we discuss a high-throughput workflow for PU research using two individual platforms for mixing and dispensing as well as coating. This setup was investigated to develop and to prove the high-throughput preparation concept for different PU elastomers. To be able to handle and process fast PU reactions that could reach a gelling time in 25 to 30 s, almost all steps of the workflow had to be slightly modified or optimized.

Potential sources of errors in a high-throughput workflow can arise during the liquid handling and the processing (coating) steps. For the liquid handling step, problems might occur due to inaccurate dispensing, isocyanate incompatibility, inefficient mixing of the raw materials and cross-contamination in particular when using viscous materials.³⁹ During

the processing step, attention should be paid to avoid slow pouring, inadequate surface coverage, variability in film thickness as well as poor curing.²¹ The system should cope with all these challenges to develop a robust HTE setup.

To realize such a fast, automated and robust high-throughput workflow, we have developed and optimized the following modules: the pneumatically driven nest enabling fast removal of the vessel after the mixing step, the flat-bottom glass vessels with straight wall for the mixing of the two reactive formulations, an effective mixing impeller allowing complete homogenization of the formulations and, finally, the specially designed mould for the PUE preparation.

Due to the fact that the PF contains solid particles (e.g., water scavengers) which could sediment within 20 min, a continuous mixing of this dispersion was an absolute requirement during the HTE operation. Without mixing, the dispensed material might not fulfil the exact criteria of the formulation and the morphology as well as properties of the prepared samples might vary significantly. For this reason, the ready-to-use materials were stored in special 600 mL fluid containers (Fig. 5). The mixing speed was set to 500 rpm, which ensured acceptable homogeneity as verified by the solid particle content measurements of the upper and lower parts of the viscous mixture after one day. In addition, to ensure the quantity of the dispensed formulations and to minimize the air contact during the process, the dead volume from the tubing and valve was rinsed by dispensing into the waste before each dispense step. With this setup, a sampling accuracy could be reached within 3 wt % for both formulations.

To keep the vessel in place during mixing of the reactive mixture after the weighing step, a pneumatic lift system with a nest was applied (Fig. 6). The vessel was transferred automatically into the nest by the robotic arm. The pneumatic drive allowed fast removal of the vessel by fast sinking of the nest before the pouring step.

The next module that was optimized was the 20 mL vessel with straight wall design, which enabled the use of a mixing impeller with 19 mm diameter in a 22 mm diameter vessel. Inhomogeneity of the reactive mixture could result in unreacted material (mainly polyol) on the surface of the

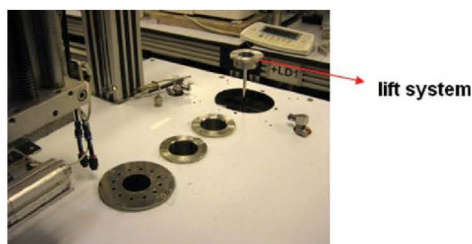


FIGURE 6 Photo of the pneumatic driven lift system for the vessels containing the reactive mixture. [Color figure can be viewed in the online issue, which is available at wileyonlinelibrary.com.]



FIGURE 7 Images of the round shaped bar coater (left) and the mould equipped with heated substrate holder (right). [Color figure can be viewed in the online issue, which is available at wileyonlinelibrary.com.]

prepared PUEs, which should be avoided since this can dramatically influence the macroscopic properties of the materials. An even more crucial point in this mixing step was found to be the efficient mixing close to the walls of the vessels. This was solved by reducing the difference between the diameter of the impeller and the diameter of the vessels as much as possible, in particular for highly viscous materials. Thus, the specially designed vessels ensured efficient mixing at the walls by the impeller and simplified the pouring process of the viscous mixtures since there was no physical barrier for pouring the liquid. As a result, the maximum amount of mixed material could be poured onto the mould and used for the doctor blade process. In this manner, the surface of the mould was almost entirely covered with elastomer to obtain PUEs in a rectangle shape (dimension: $100 \times 65 \times 1$ mm).

The mixing of the reactive formulations was carried out by an overhead mixer of the formulation platform. Next to the newly designed straight-wall vessels, a specially designed axial disc impeller was used for the experiments, which allowed fast and effective mixing of the raw materials within 10 sec. After the impeller was immersed into the mixture, the mixer started to turn on with an acceleration time of 2 s to reach 2000 rpm. The system required additional 2 s for the deceleration of the mixer reaching 0 rpm. In fact, the effective mixing was performed for 6 s at full speed. To obtain the highest efficiency during this limited time interval,

the impeller was moved to the lowest position in the vessel and then the mixing was performed in an oscillation mode between two set points, that is, the mixer was moved up 4 times and down 3 times. The mixer was stopped at the upper point about 2 mm deep in the mixture allowing fast removal of the vessels.

Optimization Procedures for the Coating Platform

The doctor blade experiments were performed with a round-shaped bar coater (Fig. 7, left) and a preheated mould (Fig. 7, right). Therefore the mould was placed in a heated substrate holder, which was reposed in the vacuum table. The thermal heater was adjusted to 95 °C to ensure 65 °C at the



FIGURE 8 PUEs prepared using the high-throughput workflow.



FIGURE 9 Conventional test specimen for physical characterization according to norm DIN 53504 S1 (left); microtensile specimen for the physical characterization according to norm ASTM D1708 (right).

TABLE 3 Comparison of the Macroscopic Properties Measured Using Microtensile Specimen for the PUEs Prepared in a High-Throughput Way and Conventional Test Bars for the PUEs Obtained in a Manual Way

Manner of PUEs Preparation	High-Throughput	Conventional, Manual	High-Throughput	Conventional, Manual
Type of test specimen	Microtensile	Conventional	Microtensile	Conventional
Standards	ASTM D1708	DIN 53504 S1	ASTM D1708	DIN 53504 S1
Macroscopic properties	Elongation at break (%) /standard deviation/		Tensile strength (N/mm²) /standard deviation/	
PUE1	75 /5.1/	82 /6.6/	4.0 /0.4/	4.8 /0.22/
PUE2	79 /4.4/	88 /4.4/	5.4 /0.3/	6.7 /0.26/
PUE3	82 /12.2/	86 /9.4/	6.2 /0.4/	6.6 /0.27/
PUE4	81 /6.5/	83 /5.3/	5.7 /0.4/	6.2 /0.17/

surface of the mould. This temperature is required to imitate and replicate the conventional preparation of the PUEs.

Before the start of the coating process, the table was manually placed in the starting position. During the coating process (doctor blade), the table was automatically moved at 100 mm/s speed. A pause was introduced after the coating process to finalize the curing process. Afterwards, the bar coater was moved to the solvent bath where it was cleaned with NMP. The mould had to be cleaned manually after each shot as mentioned previously. Eight prepared PUEs with a dimension of 100 × 65 × 1 mm are shown in Figure 8.

Discussion of the Results Obtained by Physical Testing

To be able to analyze the PUEs prepared in a high-throughput manner, the dimension of the tensile test specimens had to be reduced as depicted in Figure 9. The miniaturization of the samples was a key issue, because the same trends should be identified with both types of specimens. To perform the same physical testing of PUEs obtained in the high-throughput workflow and by conventional methods, additional physical testing norms had to be determined for screening the samples with microtensile specimens. For the comparison of the samples, the same macroscopic properties were measured such as E-modulus, elongation at break, tensile strength and IRHD for elastomers obtained in the conventional way and in the high-throughput manner using the

same standards (test methods) with the same sample sizes (microtensile specimen, 38 × 15 × 1 mm).

Table 3 shows a comparison between the tensile-elongation properties obtained by microtensile (38 × 15 × 1 mm) and the conventional test bars (115 × 25 × 3 mm). Several measurements have been performed to evaluate the difference between the two test methods. In this case, two different international standards have been applied using chemically the same kind of high-throughput manner as well as conventional way prepared PUEs, respectively. The experimental data were collected for each system (PUE1-PUE4) in Table 3.

These experimental data were the average values of the measurements on 30 specimens which were prepared from 10 identical PUEs by die-cutting three specimens from each identical elastomer skin. Thus, 30 data points have been averaged resulted in the data given in Table 3 and compared for each PUE (PUE1-PUE4) system. A very good correlation could be obtained between microtensile and conventional test bars (Table 3) demonstrating the possibility to reduce the dimension of the prepared PUE samples without influencing the macroscopic properties of the material. This observation is important for the preparation of PUEs by a high-throughput workflow: the miniaturization of the samples had certain advantages, such as faster and more reliable

TABLE 4 Overview of the Measured Physical Parameters of PUE1

Standards	Number of Tests	Physical Test	PUE1			
			Manner of Preparation	Average	Standard Deviation	Relative Standard Deviation (%)
ASTM 790-IB	30	E-modulus (MPa)	Conventional	24	2.0	8
	30	E-modulus (MPa)	High-throughput	26	4.7	18
ASTM D1708	30	Elongation at break (%)	Conventional	74	10.4	14
	30	Elongation at break (%)	High-throughput	75	8.5	11
	30	Tensile strength (N/mm ²)	Conventional	3.7	0.3	8
	30	Tensile strength (N/mm ²)	High-throughput	4.0	0.7	17
DIN ISO 48	50	IRHD	Conventional	81	2.2	3
	50	IRHD	High-throughput	81	2.5	3

TABLE 5 Overview of the Measured Physical Parameters of PUE2

PUE2						
Standards	Number of Tests	Physical Test	Manner of Preparation	Average	Standard Deviation	Relative Standard Deviation (%)
ASTM 790-IB	30	E-modulus (MPa)	Conventional	47	6.2	13
	30	E-modulus (MPa)	High-throughput	55	9.0	16
ASTM D1708	30	Elongation at break (%)	Conventional	78	10.6	14
	30	Elongation at break (%)	High-throughput	76	9.6	13
	30	Tensile strength (N/mm ²)	Conventional	5.2	0.4	9
	30	Tensile strength (N/mm ²)	High-throughput	5.4	0.3	6
DIN ISO 48	50	IRHD	Conventional	87	2.0	2
	50	IRHD	High-throughput	87	2.8	3

preparation of the PUEs, simpler automation of the physical testing method and the requirement of smaller amounts of raw materials, which is accompanied by a reduced environmental impact and cost saving.

The same raw material batches have been used for the parallel preparation of the elastomers in a conventional way and in a HTE approach with the same output number (4×10 elastomers). In this way, the comparison and evaluation of the physical parameters of these two sets of elastomers were most reliable. For each PU system, 10 pieces of PUEs have been prepared, thus, at the end of the high-throughput workflow, 40 pieces of PUEs have been obtained, analyzed and compared with the same number of conventionally prepared elastomers. For each of the 10 samples prepared from each formulation, three samples have been taken for the physical testing (E-modulus, elongation at break and tensile strength), resulting in 30 measurements for each type of test. For IRHD test, each individual samples have been measured five times resulting in 50 data points. The results of the physical testing are summarized in Tables 4–7.

The average values were in each case calculated by measuring three samples per prepared PUE meaning that three specimens were prepared for bending test (E-modulus), three specimens for tensile-elongation (tensile strength and

elongation at break tests) and five specimens for IRHD measurements by die-cutting.

The obtained results showed that the two different ways of PUE preparation were comparable demonstrating that similar PUEs could be prepared in a high-throughput manner allowing acceleration of the research and development of these kinds of materials. For each PUE system, ten times the same elastomers were prepared in the same way. By investigating the average values of the mechanical properties (E-modulus, elongation at break, tensile strength and IRHD) of the conventional and the high-throughput PUEs, it can be noted that the values were in the same range revealing the same trends. The standard deviation of these experimental data was below 13.7 and the relative standard deviation (RSD) revealed less than 17%. It should be noted that all data were used for the calculation of the average values and no outliers were omitted to validate the overall concept related to the high-throughput preparation of PUEs. The validity of the HTE approach will be illustrated by comparison of some of the PUEs. The main difference between PUE1 and PUE2 was the amount of crosslinker used. In total, 50% more crosslinker was applied in PUE2 to modify the formulation and, thus, the elasticity decreased significantly. Indeed, this phenomenon could be clearly seen from the E-modulus value

TABLE 6 Overview of the Measured Physical Parameters of PUE3

PUE3						
Standards	Number of Tests	Physical Test	Manner of Preparation	Average	Standard Deviation	Relative Standard Deviation (%)
ASTM 790-IB	30	E-modulus (MPa)	Conventional	51	4.1	8
	30	E-modulus (MPa)	High-throughput	71	11.9	17
ASTM D1708	30	Elongation at break (%)	Conventional	81	8.3	10
	30	Elongation at break (%)	High-throughput	85	13.7	16
	30	Tensile strength (N/mm ²)	Conventional	5.2	0.3	5
	30	Tensile strength (N/mm ²)	High-throughput	6.2	0.6	9
DIN ISO 48	50	IRHD	Conventional	88	2.3	3
	50	IRHD	High-throughput	89	2.3	3

TABLE 7 Overview of the Measured Physical Parameters of PUE4

Standards	Number of Tests	Physical Test	PUE4			
			Manner of Preparation	Average	Standard Deviation	Relative Standard Deviation (%)
ASTM 790-IB	30	E-modulus (MPa)	Conventional	48	7.1	15
	30	E-modulus (MPa)	High-throughput	59	9.8	16
ASTM D1708	30	Elongation at break (%)	Conventional	76	7.9	10
	30	Elongation at break (%)	High-throughput	81	11.2	14
	30	Tensile strength (N/mm ²)	Conventional	5.2	0.3	7
DIN ISO 48	30	Tensile strength (N/mm ²)	High-throughput	5.7	0.5	8
	50	IRHD	Conventional	87	2.5	3
	50	IRHD	High-throughput	88	1.7	2

which served as indication for the detection of differences between the elastomers systems.

In some cases, significant trends were randomly observed independent from the type of measurement (e.g., tensile strength or elongation at break) and from the type of PUE (PUE1, PUE2, PUE3, PUE4). Therefore it has been decided that none of the data should be disregarded to provide a full picture about the material properties and the correlation. In addition, the macroscopic mechanical properties of the PU samples are significantly depending on the sampling location on the elastomer skin, that is, from which location of the skin the samples are taken for analyses.

A crucial parameter for validating the high-throughput workflow is the reactivity of the PU system. The higher the reactivity, the shorter the gelling time, which requires faster han-

dling of the reacting mixture. Our setup for the automated preparation of complex PU elastomer systems was found to be applicable with a gelling time above 30 s. Even though the gelling time, that is, the reactivity of the systems significantly decreased from PUE1 to PUE3 (see Table 1), all PUEs have been obtained with a full surface coverage and without incomplete curing.

The most important observation was that the same trends could be found for the PUEs prepared conventionally and by HTE (Tables 4–7). Figure 10 shows the comparison between the conventional versus the high-throughput data to reinforce our statements regarding the trends in macroscopic properties observed for each PUE system. This observation facilitates the high-throughput screening of a large number of PUEs in a short labour time. After certain trends are

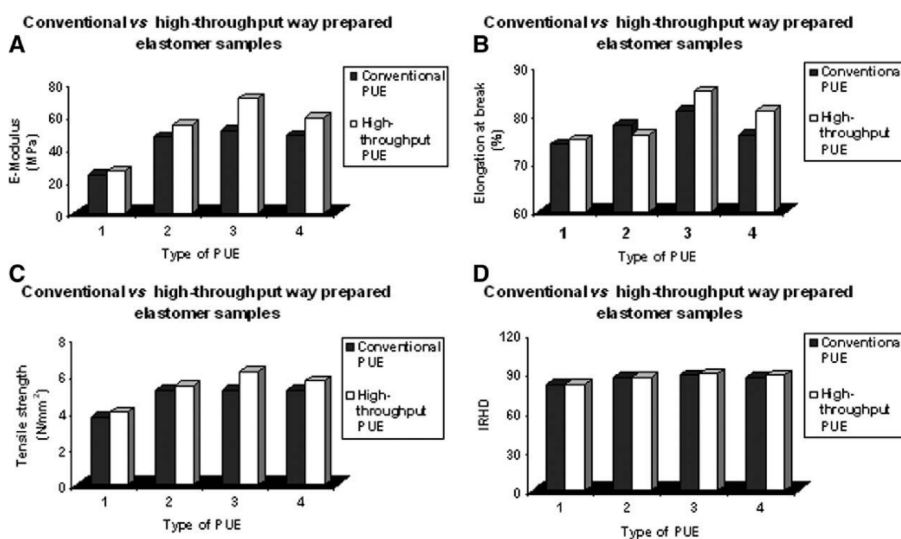


FIGURE 10 Correlation of the results between conventional versus high-throughput way prepared elastomer samples.

TABLE 8 Comparison of the Depth-Sensing Indentation Results with Those Obtained by Physical Test Methods Using Standard ASTM 790-IB with Microtensile Specimen (50.8 × 12.7 × 1 mm)

Measurement	Conventional Physical Testing (ASTM 790-IB) Microtensile Specimen (50.8 × 12.7 × 1 mm)			Depth-Sensing Indentation		
	E-Modulus (MPa) ^a	Standard Deviation	Relative Standard Deviation (%)	Reduced Modulus (MPa) ^b	Standard Deviation	Relative Standard Deviation (%)
PUE1	26	4.7	18	205	64.7	32
PUE2	55	9.0	16	270	65.5	24
PUE3	71	11.9	17	380	94.8	25
PUE4	59	9.8	16	273	46.7	17

^a The data are an average value of 30 measurements analyzed by conventional physical testing methods using microtensile specimen.

^b The data are an average value of 120 measurements analyzed by depth-sensing indentation experiments.

obtained by comparison of the data from the screening of thousands of PUEs, the most promising and versatile leads possessing special macroscopic properties can be further developed and optimized by conventional techniques. We believe that the high-throughput workflows can accelerate the R&D of these materials independently from the complexity of the formulation.

The final part of this study focused on fast physical characterization of the PUEs from HTE by depth-sensing indentation. The sample preparation for the indentation as well as the measurement itself could be carried out in one night for all 40 PUEs prepared in the workflow demonstrating that such mechanical tests will not be a bottleneck in the complete high-throughput workflow. In the future, our goal is to change entirely to depth-sensing indentation as a first screening tool for PUEs prepared in a high-throughput manner to predict the macroscopic properties. Nevertheless, it is believed that the conventional physical analysis cannot be excluded, but it should be used in the next stage of development after an initial, profound screening of the elastomers.

In Table 8, the E-modulus obtained by a conventional test method (bending test, standard ASTM 790-IB) and the reduced modulus obtained by depth-sensing indentation measurement are compared. As it can be directly observed, the indentation

values differ by an order of magnitude from those measured by the conventional testing method see also Figure 11.

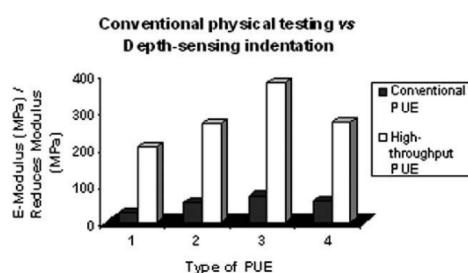
Herewith, we should note that the obtained values from physical testing methods are no real true material properties but depend on many facts, such as testing conditions, cure state of the material and so forth. In general, the values obtained from indentation experiments were found to be higher than those from bending tests. This is probably due to material creep and to pile-up around the indent. Creep results in a too high stiffness S obtained from the unloading response (eq. 1), and therefore a too high E_r . Pile-up results in an increased contact area. In the mathematical analysis of the measurements, this phenomenon was not taken into account since the amount of pile-up cannot be easily quantified (eq. 1).

$$E_r = \frac{\sqrt{\pi}}{2 \cdot \sqrt{A_c}} \cdot S \quad (1)$$

A_c = contact area, S = stiffness obtained from the unloading response.

Due to the pile-up, the area was underestimated (it was actually larger than the one that was used for the calculation of this value). As a result, the calculated reduced modulus was overestimated. Since we could not estimate this overshoot, it is assumed that the pile-up depends on the modulus of the materials and, thus, it will not affect the observed trends. In addition, the surface roughness might influence the results. In the current measurements the mould sides of the samples were used for indentation, which were smooth enough not to influence the indentation as revealed by interference microscopy.

In general, the indentation data represented the same trends as the results obtained by conventional physical testing for the modulus. Even small deviations in the macroscopic properties, for example, PUE2 versus PUE4 could be detected with this technique. As it was previously discussed, the most important advantage of HTE is the identification of certain trends in the comparison of various PUEs to identify the most promising leads which might be further evaluated and optimized. Moreover, it is generally accepted that during the primary screening a rough characterization of the physical

**FIGURE 11** Correlation between conventional physical testing versus depth-sensing indentation data.

parameters and the identification of the general trends is often sufficient.⁴⁰

CONCLUSIONS

In this study, the high-throughput preparation of PUEs has been discussed. The raw materials of these systems are highly viscous and reactive compounds and their processing is rather complex from a technology point of view. Furthermore, a fully automated high-throughput workflow which contains only one manual pouring step has been described. With this setup it was possible to prepare PUEs with a gelling time of 30 s, which requires fast processing and, thus, shows the proof of concept.

In total four different PUE systems have been tested preparing ten identical pieces from each to validate the robustness of this workflow. Furthermore, the PUEs from HTE have been compared with those prepared in a conventional (manual) way and it was found that the results represent the same trends. In addition, depth-sensing indentation measurements have been introduced into the high-throughput strategy to develop a complete workflow from compounding up to fast characterization. A good correlation between the results measured by conventional physical testing and depth-sensing indentation has been obtained. Thus, these results provide an unprecedented basis to further develop high-throughput approaches for high viscous and reactive materials.

In the present study, we have introduced this first-generation high-throughput workflow, but we are confident that most of the limiting steps of the current setup, such as the pouring and the curing steps, can be further optimized and developed. In fact, we believe that HTE will revolutionize PU research providing even more reliable results excluding several potential sources of errors. Since the fashion of the preparation of PUEs was very close to the conventional way of preparation, the demonstrated strategy will also allow easy up-scaling of the developed materials while stimulating new products in the commercial production of PUEs by allowing fast process optimization.

The authors thank the European Union Research Funding (Marie Curie Host Fellowship, FP6) for financial support and Flamac for the collaboration. They also thank the CombiTeam of Recticel N.V. (Belgium) for the fruitful discussions and physical testing measurements.

REFERENCES AND NOTES

- Potyrailo, R. A.; Olson, D. R.; Medford, G.; Brennan, M. J. *Anal Chem* 2002, 74, 5676–5680.
- Meier, M. A. R.; Schubert, U. S. *J Mater Chem* 2004, 14, 3289–3299.
- Hoogenboom, R.; Wiesbrock, F.; Leenen, M. A. M.; Maier, M. A. R.; Schubert, U. S. *J Comb Chem* 2005, 7, 10–13.
- Wiesbrock, F.; Hoogenboom, R.; Leenen, M.; van Nispen, S. F. G. M.; van der Loop, M.; Abeln, C. H.; van der Berg, A. M. J.; Schubert, U. S. *Macromolecules* 2005, 38, 7957–7966.
- Hoogenboom, R.; Schubert, U. S. *Macromol Rapid Commun* 2007, 28, 368–386.
- Meier, M. A. R.; Hoogenboom, R.; Schubert, U. S. *Macromol Rapid Commun* 2004, 25, 21–33.
- Jandeleit, B.; Schaefer, D. J.; Powers, T. S.; Turner, H. W.; Weinberg, W. H. *Angew Chem Int Ed* 1999, 38, 2494–2532.
- Hoogenboom, R.; Fijten, M. W. M.; Brändli, C.; Schroer, J.; Schubert, U. S. *Macromol Rapid Commun* 2003, 24, 98–103.
- Webster, D. C. *Macromol Chem Phys* 2008, 209, 237–246.
- Potyrailo, R. A.; Takeuchi, I. *Meas Sci Technol* 2005, 16, 1–4.
- Ekin, A.; Webster, D. C. *J Comb Chem* 2006, 9, 178–188.
- Rojas, R.; Harris, N. K.; Piotrowska, K.; Kohn, J. *J Polym Sci Part A: Polym Chem* 2009, 47, 49–58.
- Le Notre, J.; Touzani, R.; Lavastre, O.; Bruneau, C.; Dixneuf, P. H. *Adv Synth Catal* 2005, 347, 783–791.
- Bray, C. L.; Tan, B.; Wood, C. D.; Cooper, A. I. *J Mater Chem* 2005, 15, 456–459.
- Potyrailo, R. A.; Chisholm, B. J.; Olson, D. R.; Brennan, M. J.; Molaison, C. A. *Anal Chem* 2002, 74, 5105–5111.
- Chisholm, B. J.; Potyrailo, R. A.; Shaffer, R.; Cawse, J. N.; Brennan, M. J.; Molaison, C. A. *Prog Org Coat* 2003, 47, 112–119.
- Chisholm, B. J.; Potyrailo, R. A.; Cawse, J. N.; Shaffer, R.; Brennan, M. J.; Molaison, C. A. *Prog Org Coat* 2003, 47, 120–127.
- Potyrailo, R. A.; Chisholm, B. J.; Morris, W.; Cawse, J. N.; Flanagan, W.; Hassib, L.; Molaison, C. A.; Ezbiatsky, K.; Medford, G.; Reitz, H. *J Comb Chem* 2003, 5, 472–478.
- Chisholm, B. J.; Stafslie, S. J.; Christianson, D. A.; Gallagher-Lein, C.; Daniels, J. W.; Rafferty, C.; Wal, L. V.; Webster, D. C. *Appl Surf Sci* 2007, 254, 692–698.
- www.symyx.com.
- Chisholm, B. J.; Christianson, D. A.; Webster, D. C. *Prog Org Coat* 2006, 57, 115–122.
- Hewes, J. D.; Bendersky, L. A. *Appl Surf Sci* 2002, 189, 196–204.
- Potyrailo, R. A.; Olson, D. R.; Medford, G.; Brennan, M. J. *Anal Chem* 2002, 74, 5676–5680.
- www.dowcoatingsolutions.com.
- www.bayermaterials.com.
- www.basf-coatings.com.
- Majoros, L. I.; Dekeyser, B.; Hoogenboom, R.; Fijten, M. W. M.; Haucourt, N.; Schubert, U. S. *J Polym Sci Part A: Polym Chem* 2009, 47, 3729–3739.
- Majoros, L. I.; Dekeyser, B.; Hoogenboom, R.; Fijten, M. W. M.; Geeraert, J.; Haucourt, N.; Schubert, U. S. *J Polym Sci Part A: Polym Chem* 2010, 48, 570–580.
- Furukawa, M. *Recent Res Cevel Macromol Res* 1998, 3, 89–103.

- 30** Rosthauser, J. W.; Haider, K. W.; Steinlein, C.; Eisenbach, C. D. *J Appl Polym Sci* 1997, 64, 957–970.
- 31** Majoros, L. I.; Dekeyser, B.; Hoogenboom, R.; Haucourt, N.; Schubert, U. S. Concept of a High Throughput Workflow Designed for Polyurethane Elastomer Discovery. Fifth International Conference on Combinatorial and High Throughput Materials Science, Kloster Seeon, Germany, 29 September–2 October 2008.
- 32** Wingkono, G. A.; Meredith, J. C. *Polym Biomed Appl ACS Symp Series* 2008, 977, 299–309.
- 33** Sormana, B. J. L.; Meredith, J. C. *Macromolecules* 2004, 37, 2186–2195.
- 34** www.flamac.be.
- 35** www.hte-company.com.
- 36** Oliver, W. C.; Pharr, G. M. *J Mater Res* 1992, 7, 1564–1583.
- 37** Van Landingham, M. R.; Villarrubia, J. S.; Guthrie, W. F.; Meyers, G. F. *Macromol Symp* 2001, 167, 15–43.
- 38** Kranenburg, J. M.; Van Duin, M.; Schubert, U. S. *Macromol Chem Phys* 2007, 208, 915–923.
- 39** Hoogenboom, R.; Schubert, U. S. *J Polym Sci Part A: Polym Chem* 2003, 41, 2425–2434.
- 40** Iden, R.; Schrof, W.; Hädeler, J.; Lehmann, S. *Macromol Rapid Commun* 2003, 24, 63–72.

**P8 Thermal, mechanical, and surface properties of
poly(2-*N*-alkyl-2-oxazoline)s**

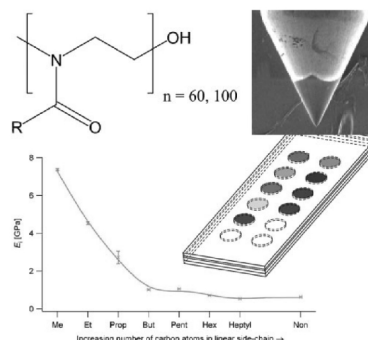
Erik F.-J. Rettler, Johannes M. Kranenburg, Hanneke M. L. Lambermont-Thijs, Richard
Hoogenboom, Ulrich S. Schubert,

Macromol. Chem. Phys. **2010**, *211*, 2443–2448.

Thermal, Mechanical, and Surface Properties of Poly(2-*N*-alkyl-2-oxazoline)s

Erik F.-J. Rettler, Johannes M. Kranenburg, Hanneke M.L. Lambermont-Thijs, Richard Hoogenboom, Ulrich S. Schubert*

Thermal, mechanical, and surface properties of a library of poly(2-oxazoline)s are investigated. These polymers are suitable to study structure/property relationships as their cationic ROP and the relative facile monomer synthesis allow for control over the molecular structure. The number of carbon atoms in the linear side-chain is systematically varied from methyl to nonyl. Relations between chemical structures, thermal transitions, surface energies, and elastic moduli are discussed. It is shown that the mechanical and thermal properties of the polymers depend on the presence of a crystalline phase in the material. The amorphous polymers reveal a decrease in the reduced moduli along with a decrease in their respective glass transition temperature with increasing length of the side-chain.



Introduction

Considering the large number of monomers available, and the variation in chain length and polymer architectures that can be achieved, a vast amount of different polymers can be synthesized. For copolymers also the block sequence in the polymer chain can be varied, extending this potential structural variation even more. It is therefore no surprise

that combinatorial approaches, originally stemming from pharmaceutical research, have found their way into polymer research as well.^[1–3] The search for a polymer exhibiting the desired properties often requires extensive screening without guaranteeing success. However, the information obtained from such screenings also allow to study and, hopefully, to understand the relationship between the properties of the material and its structure.

Since combinatorial approaches utilizing automated platforms have facilitated and accelerated organic synthesis, an even larger variety of monomers is nowadays easily accessible. These basic “building units” can be assembled to form a tremendously large variety of (co-)polymers in different shapes and architectures, all with different material properties.

Since high-throughput synthesis techniques are already frequently used in polymer chemistry, we also aim at implementing efficient approaches for the characterization of the resulting material libraries, focusing on the determination of structure/property relationships. In this way, we aim at a full high-throughput experimentation (HTE) cycle

E. F.-J. Rettler, J. M. Kranenburg, H. M. L. Lambermont-Thijs, R. Hoogenboom, U. S. Schubert
Laboratory of Macromolecular Chemistry and Nanoscience, Eindhoven University of Technology, P.O. Box 513, Den Dolech 2, 5600 MB Eindhoven, The Netherlands
E. F.-J. Rettler, J. M. Kranenburg, U. S. Schubert
Dutch Polymer Institute (DPI), John F. Kennedylaan 2, 5612 AB Eindhoven, The Netherlands
E. F.-J. Rettler, U. S. Schubert
Laboratory of Organic and Macromolecular Chemistry (IMOC), Friedrich-Schiller-Universität Jena, Humboldtstrasse 10, 07743 Jena, Germany
Fax: +49 3641 94 8202; E-mail: ulrich.schubert@uni-jena.de

for synthesis and characterization where the structure/property information gathered by the characterization can be used to design the next combinatorial experiment.

Depth-sensing indentation (DSI) has been proven to be a versatile technique for the high-throughput characterization of the mechanical properties of polymeric materials, as it is fast and requires only small amounts of materials as well as it provides a means of measuring brittle materials, where the sample preparation for standardized tensile or compression testing is more than challenging.^[4,5]

In this characterization technique, a stiff measurement probe is driven into the sample material while both the force exerted by the probe and the displacement of the probe into the sample material are recorded. While the application of the force (loading) causes elastic and plastic deformation of the material, the release of the force (unloading) is often predominantly elastic. In that case, the elastic modulus can be obtained from the unloading response.^[5–8]

Poly(2-oxazoline)s have been chosen to serve as a model system because their synthesis allows for a good control over the main chain length and over the side-group. Earlier work on 2-oxazoline copolymers showed that the mechanical properties strongly depend on the side-chains: the type of side-chain governed the glass transition temperature of the polymer, as well as the presence of crystallinity, and, therefore, the modulus of elasticity of the resulting material.^[9–14] Furthermore, the mechanical properties also depend on the humidity of the surrounding atmosphere. For some poly(2-oxazoline)s, small amounts of water still present in the samples at low humidity induce hydrogen bonding and/or polar interactions between the polymer chains, resulting in relatively high elastic moduli.

In the current work, the thermal and mechanical properties as well as the surface properties of linear poly(2-oxazoline)s are investigated in a high-throughput approach and structure/property relationships are discussed in detail.

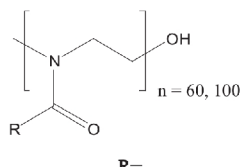
Experimental Part

Synthesis

The different poly(2-alkyl-2-oxazoline)s have been prepared by microwave-assisted cationic ring-opening polymerization in acetonitrile, using methyl tosylate as initiator, resulting in the polymers depicted in Table 1. The details of the synthesis can be found elsewhere.^[15]

The thermal properties have been investigated on two polymer libraries prepared with a monomer-to-initiator (M/I) ratio of 100 and 60, resulting in ≈ 100 and ≈ 60 repeating units, respectively. The surface energies have been investigated on the $M/I = 100$ series, while the indentation experiments were performed on the $M/I = 60$ series samples. Typical values of the polydispersity index

Table 1. Schematic representation of the chemical structures of the poly(2-alkyl-2-oxazoline)s used in this investigation and their respective abbreviations.

	Abbreviation
$-\text{CH}_3$	MeOx
$-\text{C}_2\text{H}_5$	EtOx
$-\text{C}_3\text{H}_7$	PropOx
$-\text{C}_4\text{H}_9$	ButOx
$-\text{C}_5\text{H}_{11}$	PentOx
$-\text{C}_6\text{H}_{13}$	HexOx
$-\text{C}_7\text{H}_{15}$	HeptylOx
$-\text{C}_9\text{H}_{19}$	NonOx

(PDI) are ≈ 1.2 for the $M/I = 100$ and ≈ 1.1 for the $M/I = 60$ series, respectively.

Thermal Properties

The thermal behavior of the materials was investigated by differential scanning calorimetry (DSC) using a Netzsch 204 F1 instrument in an automated run. The materials were subjected to three subsequent heating/cooling cycles. After cooling from 200 to -100°C at $10\text{K}\cdot\text{min}^{-1}$, the melting temperatures (T_m) were obtained from the second heating run ($10\text{K}\cdot\text{min}^{-1}$). Subsequently, the sample was cooled and heated again (both at $40\text{K}\cdot\text{min}^{-1}$, from -100 to 200°C) to determine the T_g . Peak values of T_m are used, while for the determination of T_g , midpoint values are reported.

Mechanical Properties

Prior to the measurements of the mechanical properties, the materials were dissolved in chloroform (except for the MeOx which was dissolved in deionized water because of its low solubility in chloroform) and drop-cast onto 12-well Teflon-coated microscopy glass slides using an Analytik Jena FasTrans automated pipetting station. The Teflon coating prevented the solution from spreading over a too large area. These sample libraries were dried under reduced pressure at 45°C over 2 weeks to remove the solvent residues.

The mechanical properties of the samples were measured with a Hysitron TriboIndenter, using a conospherical diamond indenter tip of $\approx 4.7\mu\text{m}$ radius. The indentation measurements were performed for each material employing a measurement protocol of 10 s loading, 10 s hold at maximum load and unloading in 1 s in the force range of 2100–2500 μN . All measurements were performed in a single automated run in less than 3 h. The reduced

moduli (E_i) were derived from the unloading segment, utilizing the analysis method proposed by Oliver and Pharr.^[6] Values are averaged from at least five measurements each. The indentation moduli (E_i) were calculated from the reduced moduli, using a Poisson's ratio ν of 0.4, according to

$$E_{i,\text{sample}} = \frac{(1-\nu_{\text{sample}}^2)}{\left(\frac{1}{E_{r,\text{sample}}} - \frac{1-\nu_{\text{indenter}}^2}{E_{\text{indenter}}}\right)} \quad (1)$$

The sample compartment of the TriboIndenter was purged with dried air prior to the measurements to lower the humidity the samples were exposed to. The measurements were started after equilibration of the relative humidity (RH) at $5 \pm 1\%$.

Surface Energies

For the surface energy measurements, thin films of the polymers were prepared by spin-coating of chloroform solutions ($20 \text{ mg} \cdot \text{mL}^{-1}$) of each polymer. A WS-400/500 spin-coater from Laurell Technologies Corp. was used at 1000 rpm for 90 s. Annealing of the spin-coated samples was conducted in a laboratory oven at the given temperatures overnight. The samples were allowed to cool slowly to room temperature prior to the contact angle measurements.

The contact angles have been measured using an automated OCA 30 instrument from Dataphysics. From the contact angles of ethylene glycol and diiodomethane, the surface energies have been calculated using Neumann's equation of state.^[16,17] Measurements have been performed with drop volumes of $1 \mu\text{L}$ (diiodomethane) and $3 \mu\text{L}$ (ethylene glycol), respectively, on four different spots for each coating.

Results and Discussion

Thermal Properties

Figure 1 shows the DSC response of the investigated polymers. Glass transitions can be found for the MeOx

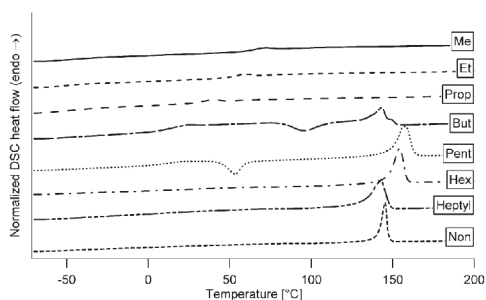


Figure 1. DSC response (second heating cycle) of the investigated poly(2-oxazoline)s ($M/I = 60$).

through the PentOx samples. For ButOx through NonOx, endothermal peaks around $150 \text{ }^\circ\text{C}$ were observed. Since these peaks only occur within the polymers with longer side-chains, they are attributed to side-chain crystallization. While the glass transition temperatures constantly decrease with increase in length of the side-chain (MeOx through PentOx), the melting temperatures of the semi-crystalline polymers (ButOx through NonOx) stay constant around $150 \pm 10 \text{ }^\circ\text{C}$, thus showing that T_m is independent of the side-chain length. Up to the PropOx sample no melting peaks were observed, indicating that a minimum length of the side-chain is required to induce crystallization further evidencing the side-chain crystallization and that the MeOx, EtOx, and PropOx samples are completely amorphous, while the rest of the library is semi-crystalline.

For the ButOx and PentOx, exothermal peaks have been found in the temperature regime between T_g and T_m . These peaks are attributable to the recrystallization process of a polymer which had been given insufficient time to fully crystallize during the preceding cooling step. Thus, upon crossing T_g in the next heating step, polymer chain segments become mobile enough to continue the crystallization process, resulting in the exothermal peaks.

Figure 2 shows a comparison of the characteristic transition temperatures of both series ($M/I = 60$ and $M/I = 100$) of the poly(2-oxazoline)s. In agreement with earlier work^[15] the glass transition temperatures of the polymers show a linear decrease throughout the library with increasing length of the linear side-chain.

The samples prepared with a M/I ratio of 60 show the same trend as the ones prepared with a ratio of 100. With increase in length of the side-chain, the material's T_g is lowered due to the increased distance between the polymer main chains. Longer side-chains will result in a larger free volume of the amorphous phase of the material, a reduced packing density and therefore a reduced steric hindrance of the chains, thus increasing the segmental mobility and decreasing the T_g values.^[9]

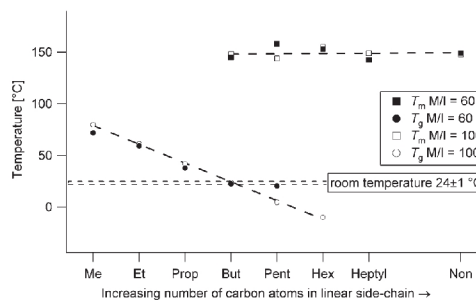


Figure 2. Thermal properties of the investigated poly(2-oxazoline)s (T_m : peak values, T_g : midpoint). Lines are linear fits to the data points.

On the other hand for the samples with a butyl or with longer side-chains, the effect of crystallinity on the glass transition temperatures starts to play a role. According to Struik^[18] and Mizuno et al.^[19] a larger crystalline volume fraction in a semi-crystalline polymer disturbs the amorphous phase, increasing the materials T_g . This may be the reason for the deviation of the PentOx in the $M/I = 60$ series from the general trend, since for the $M/I = 100$ series, the overall crystalline volume fraction is lower due to the longer main chains. For the materials with a hexyl or longer side-chains, no T_g values could be determined, which may be caused by their large crystalline volume fraction. The T_g of the $M/I = 60$ HexOx sample would be expected between 0 °C and room temperature, since the length of the side-chain increases, thus decreasing the T_g , while, on the other hand, the crystalline volume fraction increases further, increasing the T_g (both compared to the PentOx sample). As already indicated in Figure 1, the melting temperatures stay constant in a range of ± 10 °C.

Mechanical Properties

Figure 3 shows examples of the load-displacement responses obtained from the indentation experiments. The load/hold/unload segments can be observed clearly for each sample. Due to the experimental settings (so called "open-loop"), the load decreases during the hold period. Thus, the deviation seen here results from material creep under the applied load. The MeOx, EtOx, and PropOx are relatively stiff, however, the PropOx shows significant time-dependent responses to the mechanical deformation (as do the other samples with longer side-chains). This is due to the lower difference of the measurement temperature to the T_g . With increase in length of the side-chain, the samples become softer (as seen by the lower maximum load), as the T_g is constantly decreasing. From the indentation curves, one can clearly distinguish the samples being measured above or below their respective T_g . The interchange in the

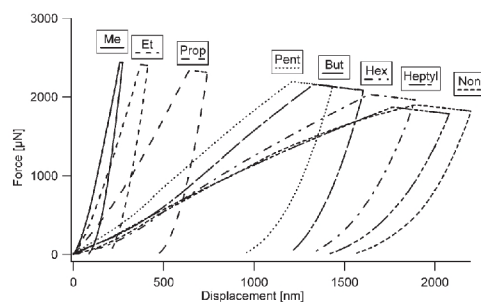


Figure 3. Indentation responses of the investigated poly(2-oxazoline)s with $M/I = 60$, obtained at high loads.

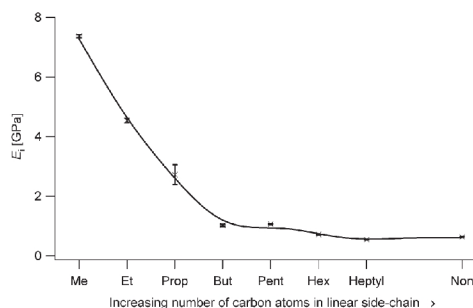


Figure 4. Indentation moduli of the poly(2-oxazoline)s with $M/I = 60$. The error bars show one standard deviation of the measurements and may be smaller than the symbols. The line is inserted to guide the eye only.

indentation responses of the ButOx and PentOx samples within the trend may be due to impurities in the sample material, such as residual solvent that can plasticize the material.

Upon increasing the length of the alkyl side-chain from methyl- to butyl-, the modulus of elasticity, E_i , decreases almost linearly (Figure 4). This is related to the decrease in T_g of the samples (Figure 2). As the distance between their T_g and room temperature decreases, E_i decreases as well. When the material is tested below T_g , the polymer is in the glassy state. Motion of the chains is severely restricted. Upon reaching T_g , the mechanical properties change drastically. Brownian motion is enabled for longer chain segments, resulting in a higher flexibility of the polymer chains and therefore lower moduli.

The dependency of E_i on the side-chain length is also related to the phases present in the material. The MeOx, EtOx, and PropOx samples are in the glassy state when probed at room temperature, while the polymers with the longer side-chains are semi-crystalline and measured above their respective T_g . The value of their reduced moduli of ≈ 0.8 GPa is common for polymers tested between their glass transition and melting temperatures.^[20] The ButOx sample consists at the testing temperature (24 ± 1 °C) of a crystalline and an amorphous phase very close to its T_g (≈ 23 °C), resulting in a similar reduced modulus as the polymers with longer side-chains.

Surface Energies

Earlier work on oxazoline di- and triblock copolymers has shown a dependency of the surface energy on the presence of a block with a long alkyl side-group.^[13,16] If such a block was present in the copolymer, the contact angles were considerably higher and the surface energies were significantly lower than without. This is attributed to

preferential orientation of the nonyl side-chains to the surface of the sample material which makes the surface more hydrophobic, thus increasing the contact angles.^[12,13] In the aforementioned references, only the MeOx, EtOx, and NonOx blocks were investigated as the linear side-chains, although preliminary results for an incomplete library of side-chain lengths were also previously reported.^[15] This work takes these investigations further, as the length of the side-chains is systematically increased throughout the sample library. Figure 5 shows the surface energies calculated from the surface angles using Neumann's equation of state for the investigated library of increasing side-chains. With the given T_g at approximately room temperature, again, the ButOx sample marks the change in material property. All samples that are measured above their respective T_g show low surface energies, due to segregation of the longer side-chains to the surface, which is favored by the higher flexibility of the polymer chains as T_g is at or below room temperature. The samples that are measured below the T_g are frozen and cannot orient the side-chains to the surfaces, resulting in exposure of both side and main chains to the surface and, thus, a higher surface energy.

Upon annealing at different temperatures, this critical side-chain length is shifted to shorter side-chains. During annealing, the temperature is raised sufficiently to let even the propyl side-chains segregate to the surface. This already starts from an annealing temperature of 30 °C, even though the glass transition temperature (≈ 38 °C) is not yet reached. Still, the MeOx and EtOx do not show this behavior. Even at annealing temperatures of 90 °C (data not shown), no further shift is observed, pointing out that the methyl and ethyl side-chains are too short to fully cover the surface. The C=O bond in the side-chain (Table 1) contributes to the high surface energies. This group makes the polymer surface more hydrophilic. In the polymers with the longer side-chains, the C=O bonds are shielded from the polymer surface by the side-chains, however, for the MeOx through

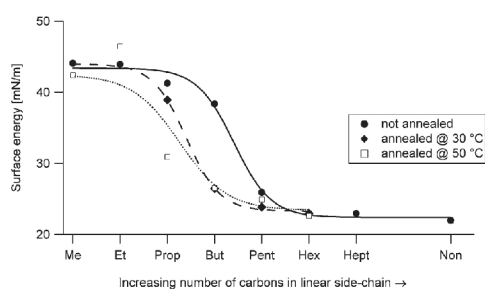


Figure 5. Surface energies of the investigated poly(2-oxazoline)s with $M/I = 100$. The lines are sigmoidal fits to the data points.

PropOx samples, the side-chains are too short to effectively shield the C=O bonds.

Conclusion

In this contribution, we have investigated the thermal, surface, and mechanical properties of a systematic library of poly(2-oxazoline)s with increasing length of the linear side-chains. We used combinatorial preparation and measurement techniques to diminish possible error sources and to provide reproducible results in a rapid manner. DSI was chosen as a tool for the determination of the mechanical properties of the samples, as it requires only small amounts of material and can be performed in an automated measurement run.

With these tools, structure/property relationships could be established. It was shown by means of DSI and DSC measurements that both the mechanical and thermal properties of the materials are related to the phases present in the material. The amorphous samples show a linear decrease in E_i with increasing side-chain length. This linear decrease is also found for the T_g values. For all of the investigated semi-crystalline poly(2-oxazoline)s, both E_i and T_m values are constant and independent of the length of the side-chain.

Furthermore, it was shown by contact angle measurements, that the surface energies of the semi-crystalline samples are much lower due to segregation of the side-chains to the surface, which makes the surface more hydrophobic. This segregation can be promoted by annealing the samples down to a minimum length of the side-chain of three carbon atoms, pointing out that the driving force for segregation to the surface is still sufficient for a side-chain of only three carbon atoms length. In contrast, four carbon atoms are required to induce side-chain crystallization.

Acknowledgements: This research forms part of the research program of the Dutch Polymer Institute (DPI), projects 449, 496, 502, and 604 (technology area HTE).

Received: June 12, 2010; Published online: October 13, 2010; DOI: 10.1002/macp.201000338

Keywords: indentation; mechanical properties; poly(2-oxazoline)s; surface energies; thermal properties

- [1] [1a] B. Jandeleit, D. J. Schaefer, T. S. Powers, H. W. Turner, W. H. Weinberg, *Angew. Chem., Int. Ed.* **1999**, *38*, 2494; [1b] R. Hoogenboom, *Angew. Chem., Int. Ed.* **2009**, *48*, 7978.
[2] N. Adams, U. S. Schubert, *Adv. Drug Delivery Rev.* **2007**, *59*, 1504.

- [3] D. C. Webster, *Macromol. Chem. Phys.* **2008**, *209*, 237.
- [4] C. A. Tweedie, D. G. Anderson, R. Langer, K. J. Van Vliet, *Adv. Mater.* **2005**, *17*, 2599.
- [5] J. M. Kranenburg, C. A. Tweedie, K. J. Van Vliet, U. S. Schubert, *Adv. Mater.* **2009**, *21*, 3551.
- [6] W. C. Oliver, G. M. Pharr, *J. Mater. Res.* **1992**, *7*, 1564.
- [7] A. C. Fisher-Cripps, *Nanoindentation*, 2nd edition, Springer-Verlag, New York 2004.
- [8] W. C. Oliver, G. M. Pharr, *J. Mater. Res.* **2004**, *19*, 3.
- [9] H. K. Reimschuessel, *J. Polym. Sci., Part A: Polym. Chem.* **1979**, *17*, 2447.
- [10] J. M. Kranenburg, C. A. Tweedie, R. Hoogenboom, F. Wiesbrock, H. M. L. Thijs, C. E. Hendriks, K. J. Van Vliet, U. S. Schubert, *J. Mater. Chem.* **2007**, *17*, 2713.
- [11] M. W. M. Fijten, J. M. Kranenburg, H. M. L. Thijs, R. M. Paulus, B. M. van Lankvelt, J. de Hullu, M. Springintveld, D. J. G. Thielen, C. A. Tweedie, R. Hoogenboom, K. J. Van Vliet, U. S. Schubert, *Macromolecules* **2007**, *40*, 5879.
- [12] M. Litt, J. Herz, *J. Colloid Interface Sci.* **1969**, *31*, 248.
- [13] J. M. Kranenburg, H. M. L. Thijs, C. A. Tweedie, S. Hoepfener, F. Wiesbrock, R. Hoogenboom, K. J. Van Vliet, U. S. Schubert, *J. Mater. Chem.* **2009**, *19*, 222.
- [14] M. Litt, F. Rahl, L. G. Roldan, *J. Polym. Sci., Part A-2* **1969**, *7*, 463.
- [15] R. Hoogenboom, M. W. M. Fijten, H. M. L. Thijs, B. M. van Lankvelt, U. S. Schubert, *Design. Monom. Polym.* **2005**, *8*, 659.
- [16] S. Wijnans, B.-J. de Gans, F. Wiesbrock, R. Hoogenboom, U. S. Schubert, *Macromol. Rapid Commun.* **2004**, *25*, 1958.
- [17] D. W. Kwok, A. W. Neumann, *Adv. Colloid Interface Sci.* **1999**, *81*, 167.
- [18] L. C. E. Struik, *Polymer* **1987**, *28*, 1521.
- [19] A. Mizuno, M. Mitsuiki, M. Motoki, *J. Agric. Food Chem.* **1998**, *46*, 98.
- [20] R. J. Young, P. A. Lovell, *Introduction to Polymers*, 2nd edition, Chapman & Hall, London 1991.